Atomistic simulation of magnesia, alumina, spinels and yttria

Sultana Yasmin

A dissertation submitted for the degree of
Doctor of Philosophy

Principal Supervisor: Dr Changming Fang

Supervisor: Professor Zhongyun Fan

RDA: Dr Isaac Chang

BRUNEL UNIVERSITY LONDON
UNITED KINGDOM

May 2022

Abstract

Magnesia, alumina, spinels and yttria are of considerable interest for their wide applications in various technological fields including electrochemistry, catalysis or microelectronics, aerospace, automotive, personnel protection, nuclear materials, chemicals, biomaterials, host material in rare-earth-doped lasers, etc [5-18, 36-39]. To increase the proper use of these minerals in various scientific applications it requires further understanding of the crystal structural, electronic, and optical properties in a systematic way. First-principles density functional theory (DFT) and molecular dynamics (MD) techniques have become popular as they allow us to retain an accurate description of electronic cohesion of the atoms/ions even including the dynamics associated with elevated temperatures [56, 57]. In this thesis first-principles DFT within the local density approximation (LDA) and generalized gradient approximation (GGA-PBE) was applied to study the crystal structural and electronic properties of MgO, Al_2O_3 (α-, θ-, and γ-Al_2O_3), $MgAl_2O_4$ and Y_2O_3. The electronic and optical properties of MgO and Al_2O_3 (α-, θ-, and γ-phases) are improved by state-of-art *GW0* approach over DFT.

For the γ-Al_2O_3, various existing models from the literature were examined. The distribution and interactions between cation and vacancies with all possible vacancy configurations were explored homogeneously. The present study concluded that the spinel type hexagonal γ-Al_2O_3 with Al vacancies at the octahedral sites is more stable rather than other models.

The composition-dependent structure and properties of the Al_2O_3 rich spinels in $MgAl_2O_4$ to γ-Al_2O_3 solid solution have been studied in this thesis. A formula $[Mg_{(1-x)}Al_x]_{Tet}[Al_{(2-x/3)}V_{x/3}]_{Oh}O_4$ (x = 0 to 1) was developed with distribution rules of cations, vacancies and anions in the defected structure in a systematic way.

The structural chemistry and electronic properties of MgO and γ-Al_2O_3 surfaces were studied in a systematic way in this thesis. The present study showed good indication of reliability of the method to study for complex surfaces.

The six different structures of Y_2O_3 (i.e., cubic, monoclinic, hexagonal, F-Er_2S_3-type monoclinic, α-Al_2O_3-type hexagonal, and fcc phases) have been discussed in detail with their chemical bonding and energetics. The calculations show that C-Y_2O_3 is the ground state phase.

The overall results in this thesis will help to resolve many properties of magnesia, alumina, spinels and yttria regarding the interpretation of numerous applications in various aspects.

Acknowledgements

I would like to convey my utmost gratitude to the persons who have helped and supported me throughout my PhD journey.

Firstly, I am thankful to Professor Zhongyun Fan, my supervisor and director of BCAST (Brunel Centre for Advanced Solidification Technology), for his guidance and giving me opportunity to be a part of his group over the years at the Brunel University London. I would like to thank my principle supervisor Dr. Changming Fang for all his help, valuable time and guidance in the last four years. I have been lucky to have such a great supervisor and without his cooperation, directions and patience all this might have been impossible. I am also thankful to Prof. Dr. Isaac Chang, my research development advisor (RDA), for his guidance and support over the years.

A special thank of mine goes to all the group members of theoretical research (Modelling and simulations) group at BCAST, Dr. Holly Alexandra Tetlow (left BCAST now), Dr. Bruno Lebon, Dr. Maaouia Souissi, Dr. Hua Men for their precious time and thoughtful suggestions, during this long PhD Journey.

Finally, I would like to acknowledge my funding sources, the Engineering and Physical Sciences Research Council (EPRSC) and Liquid Metal Engineering (LiME).

Personal acknowledgements

I would like to thank my husband Mr. Quazi Arif for his personal support, for being so patient, self-sacrificing, always giving me strength and hope. Also thankful to our beloved son Master Adib who always kept me cheer up when I felt tired. My simple thanks and gratitude will not be sufficient from them. I would like to special thank my parents and brothers who have supported me over

the years, have done their best to keep me out of trouble and got me through the hard times. Their constant love and support has been a source of lot of inspiration, courage and motivation to pursue my PhD. I also express many thanks to all of my friends at the Brunel University London for their companionship and making living here much more fun.

List of publications

[1] Changming Fang, Sultana Yasmin and Zhongyun Fan. Interfacial interaction and prenucleation at liquid-Al/γ-Al_2O_3{1 1 1} interfaces. J. Phys. Commun. 5, 015007 (2021).

[2] Sultana Yasmin, Changming Fang and Zhongyun Fan. Systematic study of γ-Al_2O_3 structure by first-principles' calculations: cation (Al^{3+}), anion (O^{2-}), vacancy distribution homogeneously and enhance the electronic and optical properties by *GW0* corrections. **[In preparation]**

[3] Sultana Yasmin, Changming Fang and Zhongyun Fan. Crystal structures and properties of Al_2O_3 rich spinels in $MgAl_2O_4$ to γ-Al_2O_3 solid solution by first-principles DFT and MD simulation. **[In preparation]**

[4] Sultana Yasmin, Changming Fang and Zhongyun Fan. Structural chemistry and electronic properties of MgO and γ-Al_2O_3 surfaces by first-principles DFT. **[In preparation]**

[5] Sultana Yasmin, Changming Fang and Zhongyun Fan. Crystal chemistry and properties of Y_2O_3 phases by first-principles DFT. **[In preparation]**

Contents:

Legends of Figures xii

Legends of Tables xx

Chapter One 1

Introduction: 1

1.1 Background of the magnesia, alumina, spinels, and yttria 1

1.2 Introduction of atomic simulation techniques 2

Chapter Two 5

Overarching aim 5

2.1 Uncertainty surrounding γ-Al_2O_3 spinel 5

2.2 Stability and structures of Y_2O_3 phases 9

2.3 Appropriate method to study the crystal chemistry 9

2.4 Aims and Objectives 10

Chapter Three 13

Literature Review 13

3.1 Magnesia (MgO) 13

3.2 Alumina (Al_2O_3) 14

3.2.1 α-Al_2O_3 15

3.2.2 θ-Al_2O_3 17

3.2.3 γ-Al_2O_3 18

3.2.4 Summary 22

3.3 Structural correlation between spinel $MgAl_2O_4$ and γ-Al_2O_3 22

3.4 Stability and structural properties of γ-Al_2O_3 surfaces 25

3.5 Crystal chemistry of Y_2O_3 phases 26

Chapter Four 28

Theoretical Methods 28

4.1 The Schrödinger equation and the Hamiltonian 28

4.2 First-principles density-functional theory (DFT) 30

4.2.1 The Hohenberg-Kohn (H-K) theorems 30

4.2.1.1 Theorem One 30

4.2.1.2 Theorem Two 31

4.2.2 Kohn-Sham (K-S) Approximation 31

4.2.3 The exchange-correlation functional 32

4.2.3.1 Local Density Approximation (LDA) 33

4.2.3.2 Generalized Gradient Approximation (GGA) 34

4.2.3.3 GGA-PBE 34

4.3 *GW* Approximation 35

4.3.1 Green's Function 36

4.3.2 *GW* correction to standard density functionals 40

4.4 Basis sets 42

4.4.1 *k*-point sampling 43

4.4.2 Pseudopotentials 44

4.5 Optical properties calculation 46

4.6 Molecular Dynamics 47

4.6.1 Canonical ensemble: NVT 48

4.6.1.1 Nosé-Hoover thermostat 48

4.7 The first-principles' code VASP 49

Chapter Five 51

Formation, stability, and properties of MgO and α-Al_2O_3 51

5.1 Introduction 51

5.2 Methods 52

5.2.1 Computational details 52

5.2.2 Formation energy 53

5.3 Results and discussions 54

5.3.1 Crystal chemistry of MgO and α-Al_2O_3 54

5.3.2 Electronic Properties by GGA-PBE 56

5.3.3 Accurate calculation of band gap by *GW0* correction 59

5.3.4 Optical properties 61

5.4 Conclusion 67

Chapter Six 68

Crystal chemistry and physical properties θ- and γ-Al_2O_3 68

6.1 Introduction 68

6.2 Methods 68

6.2.1 Computational details 68

6.2.2 Formation energy calculation 68

6.3 Results and discussions 70

6.3.1 Crystal structural properties 70

6.3.1.1 θ-Al_2O_3 70

6.3.1.2 γ-Al_2O_3 72

6.3.1.2.1 Structural model of γ-Al_2O_3 72

6.3.1.2.2 Formation, stability, and chemical bonding in different models 74

6.3.1.2.3 Distribution of vacancies between layers in the structure 80

6.3.1.2.4 Summary 82

6.3.2 Electronic properties by GGA-PBE 83

6.3.3 Accurate calculation of band gap by *GW0* correction 84

6.3.4 Optical properties 85

6.4 Conclusion 90

Chapter Seven 91

Crystal structures and properties of Al_2O_3 rich $MgO.nAl_2O_3$ spinels 91

7.1 Introduction 91

7.2 Methods 92

7.2.1 Structural model for $Mg_5Al_{18}Vac_1O_{32}$ models 92

7.2.2 Prepare different models of $[Mg_{(1-x)}Al_x]_{Tet}[Al_{(2-x/3)}V_{x/3}]_{Oh}O_4$ spinels 94

7.2.3 Computational details 95

7.2.4 Formation energy calculation 96

7.3 Results and discussions 96

7.3.1 Distribution of cations in $[Mg_{(1-x)}Al_x]_{Tet}[Al_{(2-x/3)}V_{x/3}]_{Oh}O_4$ 96

7.3.2 Formation, stability and chemical bonding in the series of $[Mg_{(1-x)}Al_x]_{Tet}[Al_{(2-x/3)}V_{x/3}]_{Oh}O_4$ spinels 97

7.3.3 Electronic properties of the $[Mg_{(1-x)}Al_x]_{Tet}[Al_{(2-x/3)}V_{x/3}]_{Oh}O_4$ spinels 100

7.3.4 *Ab initio* MD simulations of $[Mg_{(1-x)}Al_x]_{Tet}[Al_{(2-x/3)}V_{x/3}]_{Oh}O_4$ compounds 102

7.4 Conclusions 107

Chapter Eight 109

Structural chemistry and electronic properties of MgO and γ-Al_2O_3 surfaces 110

8.1 Introduction 110

8.2 Methods 112

8.2.1 Preparing MgO (001) and (111) Surfaces 112

8.2.2 Preparing hexagonal γ-Al_2O_3 (0001) Surfaces 115

8.2.3 Computational details 120

8.2.4 Calculate surface energies and surface relaxation energies 120

8.3 Results and discussions 121

8.3.1 MgO (001) and (111) surfaces 121

8.3.1.1 Energetics and local Structure 121

8.3.1.2 Electronic structure of MgO (111) surfaces 124

8.3.2 Hexagonal γ-Al_2O_3 (0001) surfaces 126

8.3.2.1 Energetics and local structure 126

8.3.2.2 Electronic structure for surfacial atoms/ions 130

8.4 Conclusion 131

Chapter Nine 133

Crystal chemistry and physical properties of Y_2O_3 133

9.1 Introduction 133

9.2 Methods 133

9.2.1 Structural models of Y_2O_3 133

9.2.2 Computational details 136

9.3 Results and Discussions 136

9.3.1 Energetics and chemical bonding of the Y_2O_3 phases 136

9.3.2 Electronic Properties of cubic Y_2O_3 139

9.4 Conclusions 141

Chapter Ten 142

Final Remarks 142

10.1 Conclusions 142

10.2 Future Work 145

References 146

Appendix 166

Legends of Figures:

Figure 3.1: Schematic structure of MgO with face centered cubic (fcc) lattice. Magnesium ions are octahedrally coordinated by oxygen ions. Red spheres represent oxygen atoms, yellow spheres are magnesium, and the oxygen octahedron is shown in light gray [73] 14

Figure 3.2: (a) Schematic structure of the hexagonal α-Al_2O_3 conventional unit cell where pink and red balls represent Al and O atoms, respectively [100]. (b) The Al-O bonds and (c) Polyhedra of ABAB stacking where, Al in blue polygons and O in red [101] 16

Figure 3.3: (a) Schematic structure of monoclinic θ-Al_2O_3 unit cell where blue and red balls represent Al (Al in pink polygons) and O atoms, respectively, (b) Al(tet)-O and (c) Al(oct)-O bonds [109] 17

Figure 3.4: Schematic representation of spinel type cubic γ-Al_2O_3 structure, where the green, blue and red balls represent the octahedral, tetrahedral coordinated Al atoms and O atoms respectively, the dotted black lines represent the unit cell of the cubic lattice [123] 19

Figure 3.5: Schematic structure of fcc $MgAl_2O_4$ conventional unit cell where red, green, and blue spheres represent O, Al and Mg atoms, respectively. Mg and Al ions are tetrahedrally (yellow polyhedra) and octahedrally (green polyhedra) coordinated by oxygen ions respectively [150] 23

Figure 3.6: Schematic representation of γ-Al_2O_3 along (1 1 1) axis, the octahedral and tetrahedral Al atoms are green and blue balls, while the oxygen atoms are red balls respectively, the dotted black lines represent the unit cell [139] 26

Figure 4.1: Schematic of Hedin's full set of equations (a) and Hedin's *GW* approximation (b, c). (a) All five quantities are iterated to self-consistency. (b) Self-consistent *GW* (sc*GW*), Γ is set to a single spacetime point and the remaining four quantities are determined self-consistently. (c) One iterates *G* to self-consistency in Equation (4.25b) but does not update W_0 [66] 42

Figure 4.2: The pseudopotentials V_{pseudo} replaces the Coulomb potential V and as a result the oscillating core wavefunctions ψ are replaced by the pseudo-wavefunctions ψ_{pseudo} which are smooth inside the core region 46

Figure 5.1: Schematic crystal structure of (a) fcc MgO unit cell, (b) and (c) the Mg-O and Al-O bonds, respectively, (d) hexagonal α-Al_2O_3 unit cell. The orange spheres represent Mg, the silvery Al and the red O. The labels Al1, Al2 in (d) represent the Al sublayers in the structure 52

Figure 5.2: The total (TDOS) and partial (PDOS) density of states of (a) MgO and (b) α-Al_2O_3 from GGA-PBE calculations 57

Figure 5.3: Calculated total density of states (TDOS) of (a) MgO and (b) α-Al_2O_3 using both GGA(PBE) and *GW0* functionals 60

Figure 5.4: The optical functions of MgO i.e., dielectric constants of real part $\varepsilon_1(\omega)$ and imaginary part $\varepsilon_2(\omega)$ from (a) experiment [213], (b) and (c) this theoretical work, (d) refractive index $n(\omega)$, (e) extinction coefficient $k(\omega)$, (f) absorption coefficient $\alpha(\omega)$, (g) conductivity $\sigma(\omega)$, reflectance from (h) experiment [213] and (i) this theoretical work, energy loss spectra from (j) experiment [213] and (k) this theoretical work respectively. The direct band gap at 4.9 (7.26) eV for GGA_PBE (*GW0*) is marked by a vertical green (red) line in Figure 5.4 (a) and (b) 62

Figure 5.5: The optical functions of α-Al_2O_3 structure from experimental work [218, 219] and the present GGA_PBE and GW0 calculations: Dielectric constants of (a) real part $\varepsilon_1(\omega)$, (b) imaginary part $\varepsilon_2(\omega)$, (c) refractive index $n(\omega)$, (d) extinction coefficient $k(\omega)$, (e) reflectivity $R(\omega)$, (f) absorption coefficient $\alpha(\omega)$, (g) conductivity $\sigma(\omega)$ and (h) energy loss spectra $L(\omega)$ 63

Figure 6.1: Schematic structure of lattice topology and polyhedra of the (a) monoclinic θ-Al_2O_3, where Al_{tet} and Al_{oct} bonded with four and six O anions respectively. The surrounding bond arrangements and the bond lengths are shown for (b) Al_{tet} and (c) Al_{oct}. The silvery spheres represent Al and dark blue O atom/ion 70

Figure 6.2: Different structural models for γ-Al_2O_3: (a) Model-1: $1a_p \times 1a_p \times 3a_p$ primitive (rhombohedral) supercell, (b) Model-2: $1a_0 \times 1a_0 \times 3a_0$ conventional fcc supercell, (c) Model-3: $1a_h \times 1a_h \times 1c_h$ hexagonal cell, (d) Model-4: $2a_h \times 2a_h \times 1c_h$ hexagonal supercell, (e) Model-5: Monoclinic non-spinel cell [145]. The green and silvery spheres represent the Al(tetrahedral) and Al(octahedral), and dark blue balls represent O atom/ion 74

Figure 6.3: The energetics of the structural models of γ-Al_2O_3 with respect to that of α-Al_2O_3 (Equation 6.3) 77

Figure 6.4: Formation energy difference, ΔE (eV/f.u.) for different γ-Al_2O_3 structural models as a function of volume ($Å^3$/f.u.) 77

Figure 6.5: Schematic crystal structure of (a) 2×2×1 hexagonal γ-Al_2O_3 supercell with Oh vacancies (160 atoms), (b) Al_{tet} (green) and (c) Al_{oct} (silver) bonded with four and six O anions, respectively. O atom/ion (dark blue) bonded with Al(oh/tet) cations by (d) CN-4 and (e) CN-3 [here, CN-Coordination Number] 78

Figure 6.6: Formation energy difference, ΔE (eV/f.u.) for different γ-Al_2O_3 structural models as a function of CN-4:CN-3 of O anion 78

Figure 6.7: Schematic crystal structure of spinel γ-Al_2O_3 with Oh vacancies for (a) Model-1: primitive (Rhombohedral) cell, (b) Model-3: hexagonal 1×1×1 unit cell, (c) Model-4: hexagonal 2×2×1 supercell. Al_{tet} (green) and Al_{oct} (silver) bonded with four and six O anions, respectively. The dark blue represents O atom/ion. The orange lines represent the axis of the unit cell. The labels Al_1, Al_2 and O represent the Al sublayers and O layer in the structure, respectively 81

Figure 6.8: Formation energy difference, ΔE (eV/f.u.) as a function of volume ($Å^3$/f.u.) for Primitive (Rhombohedral), Hexagonal (1×1×1) cell and Hexagonal (2×2×1) supercell of γ-Al_2O_3 structural models respectively with Oh vacancies distributed at different layers 81

Figure 6.9: The total and partial density of states of (a) monoclinic θ-Al_2O_3 and (b) hexagonal γ-Al_2O_3 crystal structure from GGA-PBE calculations 83

Figure 6.10: Schematic picture of the total density of states (DOS) of (a) θ-Al_2O_3 and (b) γ-Al_2O_3 structure using both GGA(PBE) and *GW0* functionals 85

Figure 6.11: The optical functions: Dielectric constants of (a) real part $\varepsilon_1(\omega)$, (b) imaginary part $\varepsilon_2(\omega)$, (c) refractive index $n(\omega)$, (d) extinction coefficient $k(\omega)$, (e) reflectivity $R(\omega)$, (f) absorption coefficient $\alpha(\omega)$, (g) conductivity $\sigma(\omega)$ and (h) energy loss spectra $L(\omega)$ of α-, θ- and γ-Al_2O_3 86

Figure 7.1: Schematic picture of (a) fcc $Mg_8Al_{16}O_{32}$ unit cell and 5 different structural models of $Mg_5Al_{18}Vac_1O_{32}$, (b) Model-1, (c) Model-2, (d) Model-3, (e) Model-4 and (f) Model-5. Orange, blue and red spheres represent the Mg, Al and O atoms respectively. Blue circles represent the vacancies at different sites in the unit cell 92

Figure 7.2: 2×2×1 hexagonal supercell models of $[Mg_{(1-x)}Al_x]_{Tet}[Al_{(2-x/3)}V_{x/3}]_{Oh}O_4$ for (i) x=0, (ii) x=0.125, (iii) x=0.25, (iv) x=0.50, (v) x=0.75, (vi) x=0.875, (vii) x=1, where orange, silver, green and dark blue balls represent Mg, Al, Vacancies and O atom/ions, respectively 95

Figure 7.3: The Formation energies (eV/f.u.) of the 5 different Models of $Mg_5Al_{18}Vac_1O_{32}$ unit cell 96

Figure 7.4: Variation of calculated (a) Formation energies, E_f (eV), (b) lattice constants and (c) average bond lengths (Å) of the optimized $[Mg_{(1-x)}Al_x]_{Tet}[Al_{2-x/3}V_{x/3}]_{Oh}O_4$ (x = 0.0, 0.125, 0.25, 0.5, 0.75, 0.875, 1.0) 98

Figure 7.5: The calculated total density of states (TDOS) and partial density of states (PDOS) of the $[Mg_{(1-x)}Al_x]_{Tet}[Al_{(2-x/3)}V_{x/3}]_{Oh}O_4$ spinels 100

Figure 7.6: Variation of calculated energy gap as a function of x in the $[Mg_{(1-x)}Al_x]_{Tet}[Al_{(2-x/3)}V_{x/3}]_{Oh}O_4$ spinels (x = 0 to 1) 101

Figure 7.7. The total-valence electrons energies of the $[Mg_{(1-x)}Al_x]_{Tet}[Al_{(2-x/3)}V_{x/3}]_{Oh}O_4$ (x = 0.0, 0.125, 0.25, 0.5, 0.75, 0.875, 1.0) system as a function of steps at 2000 *K* 103

Figure 7.8: Schematic picture of (a) normal spinel $MgAl_2O_4$ at 0 *K* and 0 *P*. (b) $MgAl_2O_4$ and (c) γ-Al_2O_3 supercells after *ab initio* MD simulation at 2000 *K*. The orange, silvery and red balls represent Mg, Al and O atoms/ions respectively. The black lines represent the axis of the unit cell 104

Figure 7.9: The radial distribution function *g(r)* as a function of atomic distances r (Å) of solid $[Mg_{(1-x)}Al_x]_{Tet}[Al_{(2-x/3)}V_{x/3}]_{Oh}O_4$ (x = 0.0 to 1) at 2000 *K* 105

Figure 7.10: Snapshots of (a) $MgAl_2O_4$ and (b) γ-Al_2O_3 during MD simulations. Green, silver, and red spheres are Mg, Al, and O atoms respectively. Mean squared displacements of Mg, Al, and O atoms in (c) $MgAl_2O_4$ and (d) γ-Al_2O_3 spinels 107

Figure 8.1: Schematic structure of (a) hexagonal γ-Al_2O_3 along its (0001) orientation and (b) the ABCABC stacking series. Al[Tet] and Al[Oh] bonded with four and six O anions, respectively. The green, silver and dark blue spheres represent the Al(Tet), Al(Oh) and O atom/ion respectively. The orange lines represent the axis of the unit cell. The labels Al1(Oh), Al2, O1 and O2 represent the Al sublayers and O layers in the structure, respectively 111

Figure 8.2: Configuration of (001) MgO surfaces. Subfigure (a) 1×1 fcc (conventional) bulk unit cell. MgO (001) surfaces of 3 atomic layers slab where (b) model-1: 15 Å vacuum, (c) model-2: 18 Å vacuum, (d) model-3: 20 Å vacuum and (e) model-4: 22 Å vacuum, thickness respectively. For (f) model-5: 6 atomic layers slab, (g) model-6: 8 atomic layers slab and (h) model-7: 10 atomic layers slab, respectively with 22 Å vacuum thickness. Orange and red balls represent Mg and O atoms, respectively 113

Figure 8.3: Configuration of (111) MgO surfaces. Subfigure (a) 1×1×1 hexagonal unit cell, (b) 2×2×4 supercell, (c) polar (111) surface slab contains atoms 1/4 of the slab and a vacuum ¾ of slab along c-direction. The subfigures (d) MgO (111)-Mg and (e) MgO (111)-O terminated defective surfaces 114

Figure 8.4: Side view of hexagonal γ-Al_2O_3 along (0001) surfaces. Subfigures: (a) 2×2×3 hexagonal bulk supercell, (b) polar surface slab contains 1/3 length of c-axis filled with the atoms and 2/3 of vacuum, (c) 1Al1(Oh) defective surface, (d) 2Al1(Oh) defective surface, (e) and (f) Three-dimensional schematic showing the nanopatterning based on the domain model 1Al1(Oh) and 2Al1(Oh) defective surfaces respectively 116

Figure 8.5: Configuration of side view of (a) polar surface slab used to prepare Al2(Oh_Tet) defective surfaces, (b) Al2(Tet1) defective surface, (c) Al2(Tet2) defective surface, (d) Al2(Oh) defective surface and (e) Al2(Oh_Tet) defective surface 118

Figure 8.6: Configuration of side view of (a) polar surface slab used to prepare O1 defective surfaces, (b) 1O1 defective surface, (c) 2O1 defective surface, (d) polar surface slab used to prepare O2 defective surfaces (e) 1O2 defective surface and (f) 2O2 defective surface 119

Figure 8.7: The variation of surface energy, γ_{surf} of MgO (001) surfaces as a function of (a) vacuum thickness and (b) slab thickness 121

Figure 8.8: The side view of the MgO (a) (111)-Mg and (b) (111)-O defective surfaces respectively before and after relaxations. Color legends: orange for Mg and red for O, black line for unit cell 124

Figure 8.9: The total (TDOS) and partial (PDOS) density of states for MgO (a) (111)-Mg defective and (b) (111)-O defective surfaces 125

Figure 8.10: The side view of hexagonal γ-Al_2O_3 (0001) (a) 1O2 and (b) Al2(Tet2) defective surfaces respectively. Atoms underneath the surfaces have been yellow colored for clarity. Color legends: red for O and light blue for Al.

128

Figure 8.11: The total (TDOS) and partial (PDOS) density of states for hexagonal (a) bulk γ-Al_2O_3 and (b) the most stable hexagonal γ-Al_2O_3 (0001)-1O2 defective surface. The Fermi level is set at 0 eV. 130

Figure 9.1: Schematic structure of the Y_2O_3 phases. Subfigure (a) cubic (80 atoms-$Y_{32}O_{48}$), (b) monoclinic (30 atoms-$Y_{12}O_{18}$), (c) hexagonal (5 atoms-Y_2O_3), (d) F-Er_2S_3-type monoclinic (20 atoms-Y_8O_{12}), (e) α-Al_2O_3-type hexagonal (30 atoms-$Y_{12}O_{18}$) and (f) fcc (10 atoms-Y_4O_6) Y_2O_3 unit cell. The green sphere represents Y atom and red sphere represents O atom. 135

Figure 9.2: Calculated total energies as a function of their volumes for the Y_2O_3 Phases. 137

Figure 9.3: Schematical coordination of Y by O and the related Y-O bond lengths (a) C-Y_2O_3, (b) M-Y_2O_3, (c) H-Y_2O_3, (d) F-Er_2S_3-type monoclinic-Y_2O_3, (e) α-Al_2O_3-type hexagonal-Y_2O_3 and (f) fcc-Y_2O_3. The green and red spheres represent Y and O atom respectively. 138

Figure 9.4: Total (black line) and partial (colored lines) density of states of the ground state C-Y_2O_3 phase. 140

Figure A.5.1: Calculated total energy as a function of volume for FCC MgO. Performing Birch-Murnaghan EOS (equation of state) fitting we estimate the bulk modulus for MgO is 166.294 *GPa* 166

Figure A.5.2: Calculated total energy as a function of volume for conventional hcp α-Al_2O_3 unit cell. Performing Birch-Murnaghan EOS (equation of state) fitting we estimate the bulk modulus is 250.5 *GPa* 167

Figure A.5.3: Convergence of the partially self-consistence *GW0* calculations for (a) fcc MgO and (b) hcp α-Al_2O_3 167

Figure A.6.1: The convergence of total energy with respect to the K-POINTS sampling for (a) θ-Al_2O_3 and (b) spinel hexagonal γ-Al_2O_3. From the Figure, 12×12×8 grid with 350 k-points for θ-Al_2O_3 and 8×8×6 grid with 114 k-points for spinel hexagonal γ-Al_2O_3 is sufficient to obtain convergence in both the total energy differences and the geometries for our investigated systems 167

Figure A.6.2: Calculated total energy as a function of volume for conventional monoclinic θ-Al_2O_3 unit cell. Performing Birch-Murnaghan EOS (equation of state) fitting we estimate the bulk modulus is 185.5 *GPa* 168

Figure A.6.3: Schematic structure of Model 1, Primitive (rhombohedral) γ-Al_2O_3 unit cell constructed from fcc spinel $MgAl_2O_4$ 168

Figure A.6.4: Schematic structure of Model 2, conventional fcc γ-Al_2O_3 supercell constructed from fcc spinel $MgAl_2O_4$ 168

Figure A.6.5: Schematic structure of (a) Model 3, hexagonal γ-Al_2O_3 unit cell and (b) Model-4, hexagonal γ-Al_2O_3 supercell constructed from fcc spinel $MgAl_2O_4$ 169

Figure A.6.6: Calculated total energy as a function of volume for conventional monoclinic γ-Al_2O_3 unit cell. Performing Birch-Murnaghan EOS (equation of state) fitting we estimate the bulk modulus is 209.73 *GPa* 169

Figure A.9.1: Calculated total energy as a function of volume for conventional cubic Y_2O_3 unit cell. Performing Birch-Murnaghan EOS (equation of state) fitting we estimate the bulk modulus is 154.7 *GPa* 169

Legends of Tables:

Table 2.1: Summary of previous experimental and computational models for the bulk structure of γ-Al_2O_3 5

Table 5.1: Comparison of calculated bulk properties (lattice parameters, formation energies, etc.) of fcc MgO and hcp α-Al_2O_3 with experiments and other DFT work 54

Table 5.2: The comparison of band widths and band gaps (eV) from GGA-PBE calculated results of fcc MgO and hcp α-Al_2O_3 with the previous theoretical and experimental data 58

Table 5.3: The comparison of widths and band gaps (eV) of fcc MgO and hcp α-Al_2O_3 by DFT-GGA(PBE) and *GW0* potential from our calculation with the previous experimental data 60

Table 5.4: The important optical parameters for MgO and α-Al_2O_3 compared with the previous theoretical and experimental results 64

Table 6.1: Crystallographic data for computed monoclinic θ-Al_2O_3 structure by GGA-PBE 71

Table 6.2: Comparison of calculated bulk properties of θ-Al_2O_3 crystals with experiments and other DFT work 71

Table 6.3: Relevant structural details including lattice parameters (input), symmetry, number of atoms and vacancies 74

Table 6.4: Calculated results (lattice parameters, volume, bulk modulus etc.) of our different structural models of γ-Al_2O_3 75

Table 6.5: The comparison of band widths and band gaps (eV) from GGA-PBE calculated results of monoclinic θ-Al_2O_3 and hexagonal γ-Al_2O_3 with the previous theoretical and experimental data 84

Table 6.6: The significant optical parameters for α-, θ- and γ-Al_2O_3 compared with the previous theoretical and experimental results 87

Table 7.1: Fractional coordinates of the substitute Al^{3+} in Mg^{2+} tetrahedral interstitial sites and vacancy sites for 5 different Models of $[Mg_5Al_3]_{Tet}[Al_{15}Vac_1]_{Oh}[O_{32}]$ unit cell 93

Table 7.2: Calculated crystallographic parameters and formation energies (E_f) of different compositions of $MgAl_2O_4$ to γ-Al_2O_3 (x = 0.0, 0.125, 0.25, 0.5, 0.75, 0.875, 1.0), where $d_{T\text{-}O}$ and $d_{Oh\text{-}O}$ denote the average bond lengths (Å) in tetrahedral (Mg/Al-O) and octahedral (Al-O) coordination, respectively 97

Table 8.1: Convergence of the surface relaxation energy for MgO (001) slabs with respect to the vacuum and slab thickness 122

Table 8.2: Calculated results of MgO (001), polar (111), defective (111)-Mg and defective (111)-O terminated surfaces 122

Table 8.3: Calculated surface energies of one polar smooth and 10 different hexagonal γ-Al_2O_3 along (0001) defective surfaces with 160 atoms slab size 126

Table 8.4: Calculate surface energy and slab size of the hexagonal γ-Al_2O_3 (0001)-1O2 defective surface and available theoretical results of α-Al_2O_3 (0001) [139] and $MgAl_2O_4$ (111)-O [171] 129

Table 9.1: Calculated bulk properties of the Y_2O_3 phases 136

Table 9.2: Comparison of the interatomic distances in Y_2O_3 structures 139

Table 9.3: Calculated electronic energy gap (E_g) in eV of C-Y_2O_3 140

Table A.5.1: Calculated physical properties of hcp Mg and fcc Al crystals at temperature of 0 *K* and a pressure of 0 *Pa* 166

Chapter One

Introduction:

In this thesis, first-principles calculations are applied to quantitatively predict the structural properties and interrelationships in detail of several metal oxides: magnesia, alumina, spinels, and yttria. This chapter will introduce the background and importance of these metal oxides in section 1.1. The atomic simulation techniques to study the crystal structure and properties will be introduced in section 1.2.

1.1 Background of the magnesia, alumina, spinels, and yttria

Magnesia and alumina are the most common minerals found in the earth's mantle [1-3]. Magnesia or magnesium oxide (MgO) is representative of the rocky materials comprising the mantles of terrestrial planets, such that its properties at high temperatures and pressures reflect the nature of planetary interiors [1]. It is an endmember of ferropericlase, (Mg, Fe)O which is thought to be the major non-silicate oxide of the earth's lower mantle, as well as super-earths (extra-solar planets with masses up to 10 times that of the earth) [1-4]. Alumina or aluminum oxide (Al_2O_3) occurs in nature in a variety of minerals, including boehmite, bayerite, corundum, diaspore, and gibbsite [2, 3]. Among the alumina polyforms, corundum (i.e., α-Al_2O_3) is the second hardest naturally occurring mineral [2].

Aside from being the major constituent of the outer crust of the earth, magnesia and alumina are of considerable interest for their wide applications in various technological fields including electrochemistry, catalysis or microelectronics, aerospace, automotive and personnel protection [5-18]. For example, in automotive industries, manufacturers start looking for lighter materials like aluminum and magnesium [6]. The automotive industry is currently gearing up to improve the performance and fuel economy at the same time the cost of their

products [19]. As a result, the demand for lightweight materials is increasing day by day, the magnesium and aluminum alloys have become the key materials in achieving a new era of lighter, more efficient vehicles [6]. The casting is an important process in the automotive industry to achieve fine-grain structures for alloys. In casting to enhance the nucleation process, the presence of a solid (catalytic) substrate nucleation is identified as heterogeneous and it promotes the nucleation process to get fine grain structure [7]. The recent experimental and theoretical observations revealed that alumina (includes α- and γ-Al_2O_3 phases), magnesia (MgO), and spinel $MgAl_2O_4$ have non-trivial influences on the mechanical performance of the cast parts and may act as potential nucleation sites to achieve effective grain refinement during the casting process [7, 20-22].

In recent years, another naturally occurring mineral Y_2O_3 [32, 33] has also attracted great research interest due to its diverse applications such as electronics, catalysts, photonics, nuclear materials, chemicals, biomaterials, host material in rare-earth-doped lasers, and substrate for superconductive thin films, etc [36-39]. It is known as starting material for the manufacture of YVO_4: Eu and Y_2O_3: Eu phosphors used to produce the red color in television tubes [39, 40]. In the aerospace field, Y_2O_3 has been used to improve the mechanical properties of the Fe–Cr–C alloy systems [41]. Therefore, a better understanding of MgO, Al_2O_3, $MgAl_2O_4$, and Y_2O_3 would stimulate further advances in many related applications.

1.2 Introduction of atomic simulation techniques

There has been a significant increase in the use of computational simulation methods within the scientific community over the last few decades to study crystal structure at the atomic level. Through a combination of the histrionic increase in computational processing power (a phenomenon described by Moore's Law [48]) and continuing algorithm development, atomic scale

modelling has become a valuable asset, providing a useful insight into the behaviour of atoms on a scale which often inaccessible to traditional experimental investigation.

Atomic simulations can be broken down into two categories, classical calculations, and quantum mechanical calculations. Classical calculations/simulations use empirically derived potential parameters to describe the interactions between ions at macroscopic levels [49]. For example, classical pair potential based on the Born model [50, 51] combined with long-range electrostatic interaction (Φ_{LR}) (also known as Coulomb interaction) [3] and the short-range interaction (Φ_{SR}) can be useful for predicting trends in atomic structure and defect processes as well as predicting macroscopic properties, such as the bulk modulus.

Quantum mechanics-based simulations such as electronic density functional theory (DFT) give a large quantity of information relating to the electronic structure of the system [52, 53] by solving the many-body Schrödinger equation [54]. For the simplest cases, quantum mechanical calculations are formally exact, however, as larger systems are studied various approximations have to be employed to make the calculations amenable. Among many atomic quantum mechanical simulation techniques, the first-principles molecular dynamics (FPMD) approach developed by Car and Parrinello [55], where they combined first principles (*ab initio*) DFT and MD to perform simulations of complex chemical systems become more popular now-a-days. The recent explosion in the popularity of first-principles methods is, to a large part, due to the success of DFT in providing a fairly accurate description of the ground state properties of materials at a reasonable computational cost [56, 57]. The parameter-free first principles DFT-MD is especially appealing as it allows us to retain an accurate description of the cohesion while including the dynamics of the atoms/ions associated with finite temperatures [56, 57]. Despite the success of DFT, it is

intrinsically a ground state theory, though the time-dependent versions of DFT are used increasingly to describe excited states in molecules and finite nanostructures [58]. One theory that goes beyond DFT for excited states in extended solids is the *GW* approximation [59–63]. The *GW* approximation to the one-electron self-energy, $\Sigma = iGW$, has been very successful in accounting for quasi-particle (QP) energies for a wide range of solids, as well as for isolated atoms and molecules [59-63]. Application of the *GW* approximation requires the input of initial guess QP energies and wave functions, which are generally taken from preparatory DFT calculations [64, 65]. Therefore, the *GW* approximation is characteristically referred to as a perturbation theory improvement to DFT [64, 65]. In recent years the DFT and *GW* become the methods of choice in chemistry, physics, and materials science to calculate the structural and electronic properties of many-body solids [64-66]. The detailed theoretical methods of the first principle DFT and *GW* are described in Chapter four.

Chapter Two

Overarching aim

This chapter will describe the principal aim of the thesis. The motivation with key open questions that are objective to address, formulate the relevant hypothesis are discussed. The appropriate methods that are believed applicable to the intended thesis are also discussed in this chapter.

2.1 Uncertainty surrounding γ-Al_2O_3 spinel

Despite the industrial significance, much uncertainty surrounds the precise structure of γ-Al_2O_3. At present the γ-Al_2O_3 is generally considered to have a cubic spinel-type structure [28] and additional cation vacancies have to occur at the cation sites in the γ-Al_2O_3 lattice to ensure the correct stoichiometry. The Al atoms occupy both tetragonal (Tet) and octahedral (Oh) sites created by the oxygen sublattice [28]. Therefore, the main uncertainty arises about whether vacancies can reside on either the T_d or O_h positions, as well as whether a random distribution of T_d and O_h vacancies can exist. The previous experimental and computational studies to determine the bulk structure of γ-Al_2O_3 are summarised in Table 2.1.

Table 2.1: Summary of previous experimental and computational models for the bulk structure of γ-Al_2O_3.

Spinel-like structure		
Experiment		
Author(s)	Method	Outcomes
E. J. W. Verwey (1935) [28]	XRD	Proposed γ-Al_2O_3 has a defective spinel structure, vacancies are mainly at octahedral sites.
H. Saafeld et. al (1965) [128]	XRD	Cubic spinel structure, vacancies to reside on tetrahedral sites.

C. S. John et al (1983) [129]	NMR	Cubic spinel structure, vacancies to reside on tetrahedral sites.
V. Jayaram et. al (1989) [130]	TEM	Determined vacancies to reside on tetrahedral sites.
R.-S. Zhou et. al (1991) [114]	XRD	Determined vacancies to reside on tetrahedral + octahedral sites.
J. Wang et. al (1999) [132]	XRD, NMR	Determined vacancies to reside on tetrahedral + octahedral sites.
C. Pecharromán et. al (1999) [131]	NMR, IR	Determined vacancies to reside on tetrahedral sites.
G. N. Kryukova et. al (2000) [127]	HREM	It was shown that the intrinsic feature of γ-Al_2O_3 structure is a presence of almost hexagonal closed loops formed due to the ordering of cation vacancies over octahedral positions on (110) and (111) planes.
L. Smročk et. al (2006) [122]	XRD	Cubic spinel structure, vacancies to reside on tetrahedral sites.
H. O. Ayoola et. al (2020) [123]	TEM	Determined cubic spinel structure, vacancies to reside on octahedral sites.
Theoretical		
Author(s)	Method	Outcomes
S. Blonski et. al (1993) [142]	Molecular dynamics using interatomic pair potentials	Determined vacancies to reside on tetrahedral sites.
Shang-Di Mo et. al (1997) [105]	Empirical pair potential calculation and first principles electronic structure studies	Cubic spinel structure $[(Al_8)_{tet}(Al_{13}V_3)_{oh}O_{32}]$ with 56 atoms, 3 vacancies at octahedral sites. The cation anion ratio 21:32.
F. H. Streitz et. al (1999) [137]	Interatomic pair potentials	Determined vacancies to reside in octahedral sites, but said tetrahedral vacancies possible
G. Gutiérrez et. al (2001) [138]	*ab initio* DFT (LDA)	Primitive (Rhombohedral) unit cell with 40 atoms, determined vacancies to reside in octahedral sites.
H. P. Pinto et. al (2004) [139]	*ab initio* DFT (GGA-PW91)	Primitive (Rhombohedral) unit cell with 40 atoms, determined vacancies to reside in octahedral sites.
E. Menéndez-Proupin et. al. (2005) [140]	*ab initio* DFT (LDA-USPP)	Primitive (pseudo-hexagonal) unit cell with 40 atoms, determined vacancies to reside in octahedral sites.

F. Maglia et. al (2008) [144]	DFT (LDA, using pair potentials)	Primitive (pseudo-hexagonal) unit cell with 160 atoms, determined vacancies to reside in tetrahedral + octahedral sites.
Y. Liu et. al (2014) [141]	First principle DFT, LDA, Fritz-Haber-Institute (FHI) pseudopotentials with Troullier-Martins scheme.	Hexagonal unit cell with 40 atoms, determined vacancies to reside in octahedral sites.
Non-spinel-like structure		
Experiment		
Author(s)	Method	Outcomes
G. Paglia et. al (2003) [134]	TEM, NMR	Proposed γ-Al2O3 with I41/amd space group symmetry, a maximal subgroup of Fd3m. a=5.616 Å, c=7.835 Å
V.P. Pakharukova et. al (2017) [135]	HRTEM, XRD.	Proposed tetragonally distorted structure
Theoretical		
M. Diagne et. al (2004) [145]	DFT, GGA-PW91	Compared spinel and non-spinel model and proposed non-spinel-based structure. (40 atoms cell).
G. Paglia et. al (2005) [146]	Empirical and First Principles Calculations	tetragonal *c* symmetry-based non-spinel model. (Unit cell contains 160 atoms, a=b=5.616 Å, c=7.835 Å)
A. R. Ferreira et. al (2011) [120]	The Gauge-Including Projector Augmented Wave (GIPAW) method, within the DFT GGA(PBE)	proposed the non-spinel model structure with *Fd3m* symmetry from Paglia *et. al*. Model (160 atoms).
M. F. Peintinger et. al (2014) [119]	Hybrid DFT functional PW1PW, exchange functional is a mixture of 20% Hartree-Fock (HF) and 80% PW91 exchange.	Compared spinel and non-spinel model and concluded diffraction patterns of non-spinel-based structure agree very well with experiment. For non-spinel model they proposed Paglia *et. al*. Model (160 atoms).
S. Blancka et. al (2020) [147]	DFT, GGA-PBE, mixed Guassian and plane wave approach (GPW)	Proposed non-spinel model (followed Digne *et. al*. Model-40 atoms).

As shown in Table 1, most works focused on simple structural models, such as primitive, face-centered cubic and hexagonal cell with two vacancies, and conventional cubic cell. These models exhibit beauty from physics: simple and small. However, in these models there are two weak points.

i) The vacancies distribute not in a homogeneous way. This causes unfavourable chemical bonding; and

ii) The distances between the vacancies might be too short. This may cause strong interaction between vacancies.

To overcome the above issues and get a reliable γ-Al_2O_3 structural model one needs to solve these questions:

i) distribution of the cations,

ii) vacancy-vacancy interaction, and

iii) local atomic coordination and chemical bonding?

Another issue is that in most of the theoretical work, the γ-Al_2O_3 structure developed from the cubic $MgAl_2O_4$ spinel crystal structural model by replacing $2Al^{3+}$ ions with $3Mg^{2+}$ ions in tetragonal sites [105, 137-142, 144]. Therefore, some intermediate structural models have also been possible from $MgAl_2O_4$ to γ-Al_2O_3 solid solution, but arise some questions:

i) the reasonable structural formula for the intermediate structural models,

ii) the distribution rules for the proportion of Al^{3+} ions and vacancies in tetrahedral (Tet) and octahedral (Oh) sites and

iii) the validity of the distribution rules of Al^{3+} ions.

The γ-Al_2O_3 surface structure is important for catalysis and solidification applications. To investigate the feasible γ-Al_2O_3 surface structure, the two main questions have to be solved:

i) is the polar surface stable for the system, and

ii) what are the structural models for the non-polar surfaces?

The solution to these questions will assist in the subsequent understanding of the surface structure of γ-Al_2O_3 and lead to the further development of many related applications.

2.2 Stability and structures of Y_2O_3 phases

The yttria (Y_2O_3) or yttrium oxide is another bixbyite type [$^{VI}A_2$][$^{IV}O_3$] mineral, which becomes the most research interest for many industrial applications [36-40]. According to the literature, this precious compound also could exhibit many structural polymorphisms such as cubic, monoclinic, hexagonal, and fcc [36-40, 176-180]. For such a growing number of uses for this oxide, the better understanding of Y_2O_3 is a prerequisite and the following questions need to be solved:

i) the possibility of different structural phases,

ii) the ground state phase,

iii) chemical bonding in the Y_2O_3 phases and

iv) the mechanical properties and electronic properties of the Y_2O_3 phases.

2.3 Appropriate method to study the crystal chemistry

Despite the valuable information one can obtain from the experiments, there are also phenomena and insights into the system hard to be interpreted due to the complexity of the system and the coupling of multiple interactions. Therefore, a theoretical approach beyond the experiment is crucial to predict the unobservable properties and improve the interpretation of the experimental data for atomic-level structural analysis. Quantum mechanics methods can be used to solve some of the problems and by applying different theoretical methods, most of the

molecular behavior can be predicted. For example, the structures and the relative energies of a molecule or solid can be calculated to obtain the knowledge of stable atomic structures of a system. The modeling of the structural properties by means of first-principles Density functional theory (DFT) calculation has become a very useful tool for understanding the properties of materials, from molecules, and crystalline solids to amorphous systems. Density functional theory (DFT) has been implemented in various computational codes, including VASP. The Vienna *Ab-initio* Simulation Package (VASP) uses a plane wave basis set [204]. The package includes the use of the Monkhorst Pack method to sample the Brillouin zone [204]. The self-consistency iteration approach is used to calculate the electronic Kohn-Sham ground state in VASP and is very efficient and robust. Therefore, in this thesis, the first-principal DFT and MD simulation by VASP code are used for structural analysis. The state-of-art *GW0* correction to the standard DFT functionals has been applied to improve the electronic and optical properties.

2.4 Aims and Objectives

The primary aim of the present work was to advance knowledge of and make new insights into the structure of γ-Al_2O_3. This study also comprises the relationships between the composition, structural and electronic properties of spinel $MgAl_2O_4$ to γ-Al_2O_3 solid solution. I also make efforts to study systematically the structural, electronic, and optical properties of magnesia, alumina, and yttria. To perform a detailed study of crystal structure and properties, the research program was divided into the following steps:

- First, study the crystal structural, electronic, and optical properties of MgO and α-Al_2O_3 by first-principles density functional theory (DFT) within the LDA and GGA(PBE) approximations to verify the methods. Then improve the electronic and optical properties by the state-of-art *GW* method.

- Investigate the occupations and distribution of cations at various sites in γ-Al_2O_3 and develop a structural model based on the spinel ($MgAl_2O_4$). Also, apply the *GW* approach to describe the electronic and optical properties of the developed γ-Al_2O_3 structure. Compare the crystal structural, electronic, and optical properties of θ-Al_2O_3 and γ-Al_2O_3 with α-Al_2O_3 in detail.
- Investigate the lattice variation of the transition compositions of MgO-rich spinel $MgAl_2O_4$ to Al_2O_3 rich γ-Al_2O_3 solid solution system. Also, study the influences of temperature effect on the stability of $MgAl_2O_4$ and γ-Al_2O_3 by first-principles MD simulation.
- Investigate the γ-Al_2O_3 surfaces. The polarity of the ionic oxide surfaces will be taken into account.
- Study the different phases of Y_2O_3 systematically using the first-principles Density Functional Theory (DFT).

The contents of the thesis are organized as follows:

Chapter three provides the literature review of the crystal structures and properties of MgO and Al_2O_3 (including α-, θ- and γ-Al_2O_3 phases), with stress on the γ-Al_2O_3 structure, problems associated with the correlation between spinels $MgAl_2O_4$ and γ-Al_2O_3, stability of γ-Al_2O_3 surfaces and different phases of Y_2O_3.

Chapter four gives details of the theoretical techniques i.e., first-principles density functional theory (DFT) including the local density approximation (LDA), generalized gradient approximation (GGA), *GW* approximation, basis sets with ***k***-point sampling, pseudopotentials, optical properties calculation techniques, molecular dynamics (MD) simulation technique, and VASP code.

Chapter five presents the results and discussion of the formation and stability of crystal structural, electronic, and optical properties of MgO and α-Al_2O_3

calculated by first-principles DFT within LDA and GGA(PBE) approximations. The resultant improved electronic and optical properties by *GW* approximation have also been discussed.

Chapter six presents the results and discussions of revisited existing structural models of γ-Al_2O_3 including their formation and stability with local chemical bonding in detail. This chapter also compares and discusses the structural, electronic, and optical properties of θ- and γ-Al_2O_3 phases with stable ground state α-Al_2O_3.

Chapter seven presents the study of composition-dependent structure and properties of the Al_2O_3 rich spinels $MgAl_2O_4$ to γ-Al_2O_3 solid solution, developing reasonable formula $[Mg_{(1-x)}Al_x]_{Tet}[Al_{(2-x/3)}V_{x/3}]_{Oh}O_4$ (x= 0 to 1) with distribution rules of cation and anion in the defected structure. The results with discussions are presented in detail. The influences of temperature effect on the stability of $MgAl_2O_4$ and γ-Al_2O_3 at elevated temperatures also be investigated and discussed using the first principle MD simulation technique.

Chapter eight presents a detailed analysis of structural chemistry and electronic properties of γ-Al_2O_3 surfaces. At first, the stability and atomic structure of MgO (001) and (111) surfaces have been studied. The methods were then applied to study the γ-Al_2O_3 surface analysis.

Chapter nine presents a detailed analysis of crystal chemistry and properties of Y_2O_3. Different phases of Y_2O_3 have been studied with their local chemical bonding and energetics. The electronic properties of the stable cubic Y_2O_3 phase have been discussed using the first-principles DFT within GGA-PBE and *GW* approximation.

Chapter ten presents the summary of the main conclusions and recommendations for future work.

Chapter Three

Literature Review

In Chapter one, we have seen that the magnesia, alumina and yttria have diverse applications in modern technology, such as, from nanoscale materials to automotive industries, medical instruments to armours, fuel reactors, etc [5-47]. New and demanding applications have generated intense interest to the knowledge of the crystal structural, electronic and optical properties of these oxides.

This chapter will briefly review the crystal structure and properties of MgO, Al_2O_3 (including α-, θ- and γ-Al_2O_3 phases), $MgAl_2O_4$ and different phases of Y_2O_3 from previous experimental and theoretical works in the literature [67-180]. Sub-section 3.2.3 will also raise the problems associated with determining the structural model of γ-Al_2O_3.

3.1 Magnesia (MgO):

Magnesia or magnesium oxide (MgO) has been considered as an ideal ionic crystal [67-72]. The crystal structure of MgO consists of a lattice of Mg^{2+} cations and O^{2-} anions held together by ionic bonding [Figure 3.1].

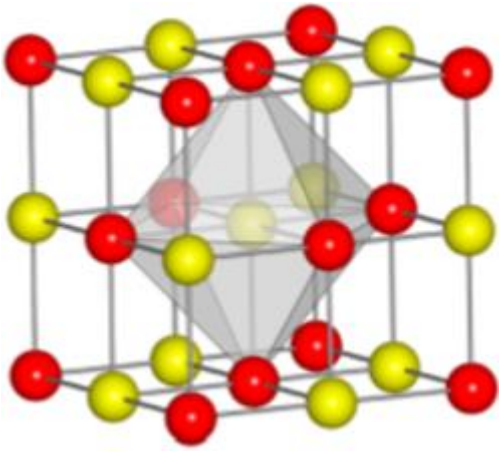

Figure 3.1: Schematic structure of MgO with face centered cubic (fcc) lattice. Magnesium ions are octahedrally coordinated by oxygen ions. Red spheres represent oxygen atoms, yellow spheres are magnesium, and the oxygen octahedron is shown in light gray [73].

The MgO has cubic rocksalt (NaCl) type structure at room temperature, belongs to space group *Fm3m* [74]. From experimental works by X-ray diffractometer (XRD) the obtained lattice parameter ranging from 4.210-4.220 Å [75-80], whereas the theoretical works include density functional theory (DFT) show the smaller lattice parameter (ranging from 4.125-4.190 Å) compared to experimental results [73, 81-87]. Using Ultraviolet spectroscopy Anderson obtained its bulk modulus is 162.2 GPa [79]. Whereas the theoretical results for the bulk modulus from DFT calculations are 156.0-182.0 GPa [81, 83-85, 88]. The electronic energy gap is 7.77 *eV* [80] and 7.8 *eV* [82] from Ultraviolet Spectroscopy and Reflection Electron Energy Loss Spectroscopy (REELS) experimental works respectively. But the electronic energy gaps from theoretical DFT calculations vary, 5.21 *eV* [85], 4.51 *eV* [86] and 4.835 *eV* [87]. Note that it is not unusual for a standard density-functional approximation to underestimate the band gap of a semiconductor or an insulator [58-66, 85]. Later J. G. Smith *et al* [73] and G. Cappellini *et al* [85] improved the band gap to 7.5 *eV* and 8.88 *eV* respectively by employing the Hedin's *GW* scheme for self-energy corrections over DFT.

The simple cubic crystal structure, atomic and electronic arrangement and well understood properties have resulted in MgO being utilized as a test material for many experimental analysis and computer simulations [67-88]. Therefore, in this thesis, MgO is used as a model system for testing calculation settings.

3.2 Alumina (Al_2O_3):

Alumina has a rich variety of crystal chemistry. Besides the stable phase α-Al_2O_3, alumina exhibits several different metastable polymorphs or transition phases at

elevated temperature, such as γ, κ, λ, η, θ, and χ alumina [10, 89-91]. All the metastable phases usually are formed prior to corundum, when an oxide is obtained via the dehydration process, and they can be stable up to 1100°C [90]. The sequence $\gamma \rightarrow \delta \rightarrow \theta \rightarrow \alpha$ occurs as the temperature increases when the alumina is obtained from either hydroxide (boehmite) or melt [89].

Among these alumina polymorphs, α- and θ- Al_2O_3 play an important role in the performance of the early oxidation of nickel–aluminium alloys in thermal barrier coatings (TBCs) [92-94]. The metastable θ- and γ-Al_2O_3 are used as catalyst and catalytic supports because of their lower surface energies [95]. To better understand the effect of metastable θ- and γ-Al_2O_3 on the performance of nucleation site, catalyst, catalytic supports, etc., knowledge about the crystal structural, electronic and optical properties is a prerequisite.

3.2.1 α-Al_2O_3:

The structure of the ground-state phase α-Al_2O_3 has been first reported by Linus Pauling in 1925 [96]. The α-Al_2O_3 belongs to the trigonal crystal system having a rhombohedral lattice with space group $R\bar{3}c$. The reported lattice parameter, a_{rh} = 5.13 Å and angle, α_{rh} = 55.10° [97]. The equivalent hexagonal cell has the lattice parameters, a_h = 4.760 Å and c_h = 12.995 Å obtained from XRD experiment by L. Lutterotti *et al* work [98]. The conventional unit cell [Figure 3.2 (a)] in the hexagonal representation contains six formula units (30 atoms) [99, 100]. The Al^{3+} cations, occupy two thirds of the octahedral interstices, i.e., they have six oxygen nearest neighbours and forms two sublayers along its (0001) axis [Figure 3.2 (a)]. There is thus only one coordination (octahedral) for Al^{3+} and one for O^{2-} anion with four surrounding Al^{3+} ions [Figure 3.2 (b)]. The oxygen sublattice follows hexagonal close packed (hcp) ABAB stacking [101] [Figure 3.2 (c)].

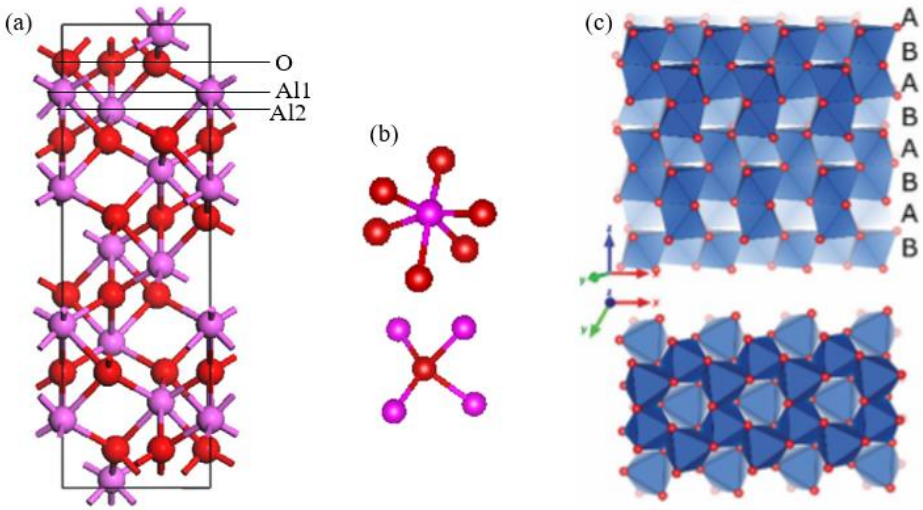

Figure 3.2: (a) Schematic structure of the hexagonal α-Al_2O_3 conventional unit cell where pink and red balls represent Al and O atoms, respectively [100]. (b) The Al-O bonds and (c) Polyhedra of ABAB stacking where, Al in blue polygons and O in red [101].

From X-ray diffractometer experiments, the bulk modulus is 254.4 *GPa* obtained by H. d'Amour *et al* [102]. N. Ishizawa *et al* observed the two independent Al-O bond lengths: 1.971 Å and 1.880 Å at 300*K* by means of XRD analysis [103]. R. H. French *et al* obtained the electronic energy band gap 9.57 *eV* from Vacuum Ultraviolet Spectroscopy (VUV) [104].

Many theoretical calculations have been performed including first-principles DFT to get inside into the crystal structural and electronic properties of α-Al_2O_3 [105-110]. The lattice parameters and bulk modulus from theoretical calculations [105-110] show close values (within ±5%) with experimental obtained results [100-104]. But the electronic band gap from theoretical calculations using DFT are 6.26 *eV* [105] and 6.60 *eV* [107] which are notably smaller (within 30%) than the experimental value 9.57 *eV* [104]. S. J. Mousavi *et al* investigated the electronic structure of α-Al_2O_3 by first-principles calculation in the framework of DFT and the full potential linearized augmented plane wave (FP-LAPW) with the Engle-Vosco approximation (EVA) and their calculated value for the band gap is

7.2 *eV* [108], which is 20% smaller than experimental result [104]. Using state-of-the art *GW* correction over DFT-LDA, T. Biswas *et al* improved the band gap to be 9.1 *eV* [110] which is in close agreement (within 5%) with the experimental band gap 9.57 *eV* [104].

3.2.2 θ-Al_2O_3:

The metastable θ phase of alumina (i.e., θ-Al_2O_3) transforms into α phase at about 1050°C, when the alumina is obtained from either hydroxide or melt [89, 90, 111]. Owing to its high crystallinity and clear X-ray diffraction pattern, its structure was first reported by J. D. Kohn *et al* work in 1957 [112]. The θ-Al_2O_3 structure belongs to the monoclinic crystal system with a space group of *C2/m* [113]. The monoclinic θ-Al_2O_3 unit cell is defined by the *a*, *b*, and *c* lattice parameters and the angle *β* between *a* and *c* axis [90, 109, 111-119] [Figure 3.3 (a)]. From XRD experiment G. Yamaguchi *et al* obtained the lattice parameters, *a*=11.813 Å, *b*=2.906 Å, *c*=5.625 Å and angle *β*=104.1^0 [113].

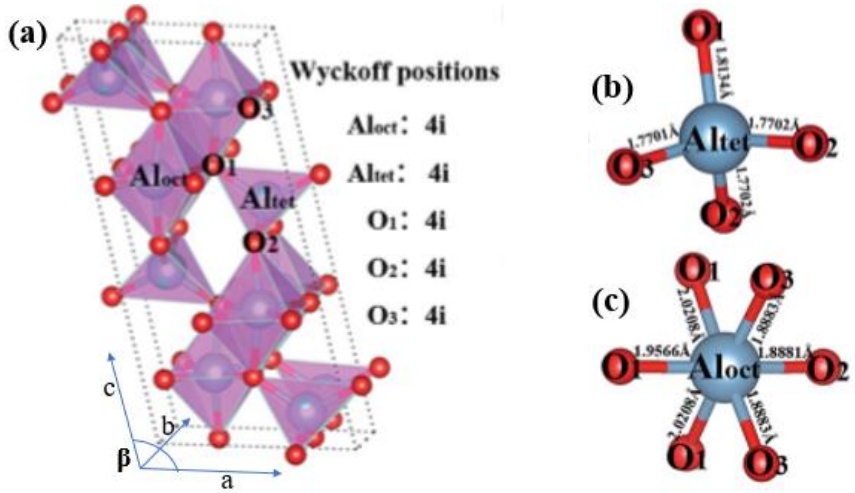

Figure 3.3: (a) Schematic structure of monoclinic θ-Al_2O_3 unit cell where blue and red balls represent Al (Al in pink polygons) and O atoms, respectively, (b) Al(tet)-O and (c) Al(oct)-O bonds [109].

The θ-Al_2O_3 structure can be described as a distorted cubic closest-packed array of oxygen anions in which the aluminum cations occupy one-eighth of the

tetrahedral interstices and half of the octahedral ones [109, 117, 118]. The crystal structure of θ-Al_2O_3 has been investigated by various experimental techniques, including x-ray and electron diffraction, scanning electron microscope (SEM), high-resolution transmission electron microscopy (HRTEM), and vibrational spectroscopy [113-116]. R. Franchy *et al* obtained the electron energy gap 7.4 *eV* using electron energy loss spectroscopy (EELS) [116]. On the theory side including DFT, the crystal structural and electronic properties of θ-Al_2O_3 have been investigated [90, 109, 117-119]. Z. Zhang *et al* calculated the bulk modulus using DFT within GGA(PBE) is 187.4 *GPa* [109]. S. -Di Mo *et al* calculated the electronic energy gap by DFT within the LDA is 4.98 *eV* [118]. Meanwhile M. F. Peintinger *et al* using the hybrid DFT method where exchange functional is a mixture of 20% Hartree–Fock (HF) and 80% PW91 exchange calculated the energy gap is 6.9 *eV* [119] which is 7% smaller than the experimental obtained value 7.4 *eV* [116]. Like α-Al_2O_3, θ-Al_2O_3 is an ordered phase, so its electronic and optical properties can be calculated unambiguously [118]. But in the case of the α phase there are experimental results available for several quantities, while such are absent for θ-Al_2O_3. Good understanding of the electronic and optical properties of θ-Al_2O_3 would certainly aid to many potential optoelectronic applications of this alumina phase such as solar energy devices, semiconductor industry etc.

3.2.3 γ-Al_2O_3:

Based on the literature, γ-Al_2O_4 is the first formed metastable phase when the alumina is obtained from either hydroxide (boehmite) or melt aluminium, even during the liquid-dealing and casting of Al-based melts [89-91]. γ-Al_2O_3 is regarded as one of most prominent material in various industrial applications such as, acting as an adsorbent, a catalyst and catalyst support [10–13, 120, 121]. The experimental observation revealed that this native oxide particle has nontrivial influences on the mechanical performances of the cast parts and may act as

heterogeneous nucleation sites during solidification processes of Al metals and Al- based alloys [7, 22, 91]. Significant applications of γ-Al_2O_3 imply that this material needs a clear description of its bulk structure as well the electronic and optical properties. Despite the vast amount of experimental and theoretical works into γ-Al_2O_3 have been done [28, 105, 107, 114, 119, 120-147] the fundamental questions about its accurate crystal structure with cation, anion and vacancy distributions are still in discussion.

In 1935 the crystal structure of γ-Al_2O_3 was first introduced as a defective cubic spinel with space group *Fd3m*, where the oxygen anions have the same cubic-close-packing arrangement as in spinel $MgAl_2O_4$ and the Al cations being coordinated both tetragonally and octahedrally by oxygen [Figure 3.4] [28, 89, 122, 123]. The lattice parameter of cubic spinel γ-Al_2O_3 structure is 7.938 Å from Smročk model using XRD experiments study [122].

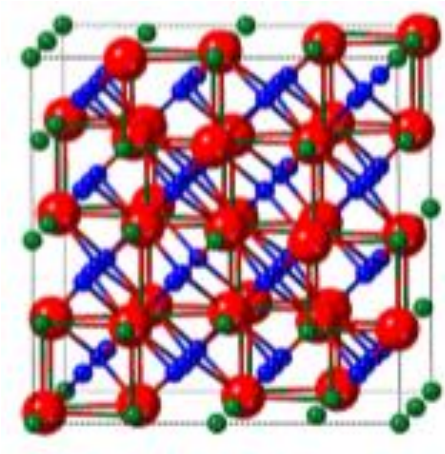

Figure 3.4: Schematic representation of spinel type cubic γ-Al_2O_3 structure, where the green, blue and red balls represent the octahedral, tetrahedral coordinated Al atoms and O atoms respectively, the dotted black lines represent the unit cell of the cubic lattice [123].

The crystal structure of an ideal spinel is cubic with chemical formula AB_2O_4, in which the A^{2+} divalent and B^{3+} trivalent cations occupying the tetrahedral (Tet) and octahedral (Oh) interstitial sites respectively and the ratio of cations to anions

is 3:4. But in the cubic γ-Al_2O_3 structure the ratio of cations to anions is 2:3. As a result, additional cation vacancies have to occur in the γ-Al_2O_3 unit cell to ensure the correct stoichiometry.

Based on the analysis from X-ray diffraction (XRD) [28], nuclear magnetic resonance (NMR) [124], Transition Electron Microscope (TEM) [123, 125] and High-Resolution Transmission Electron Microscope (HRTEM) [126, 127] experimental measurements, it was concluded that the vacancies reside mainly in octahedral sites. Meanwhile, other XRD [128], NMR [129, 131] and TEM [130] experimental studies suggested the preference of vacancies in tetrahedral sites. Based on NMR analysis a disordered structure having 60% of the vacancies at the tetrahedral sites and 40% at the octahedral sites have also been proposed [132]. From HRTEM studies, it was also shown that the intrinsic feature of γ-alumina structure is a presence of almost hexagonal closed loops formed due to the ordering of cation vacancies over octahedral positions on (1 1 0) and (1 1 1) planes [127]. Images of high-resolution transmission electron microscopy (HR-TEM) revealed that the γ-Al_2O_3 plates exhibit hexagonal shapes and are (1 1 1)-faceted [90, 133]. Considering tetragonally distorted structure later non-spinel model has also been proposed from TEM and NMR [134] and XRD [135] analysis. These experimental results might provide only statistically averaged structure because the atomic arrangements of Al vary in the γ-Al_2O_3 samples from different preparations. To get more accurate structural information, many theoretical approaches have been applied in γ-Al_2O_3. Several computational studies including first-principles DFT with different approximations (i.e., LDA, GGA-PW-91, GGA-PBE, pair potential, etc.) employed different unit cells observed preferential location of cation vacancies on octahedral sites [118, 136-141]. Using first-principles DFT with LDA and GGA(PW-91) approximations E. Menéndez-Proupin *et al* reported that optimized primitive structure of the spinel γ-alumina resulting in a kind of pseudo-hexagonal cell with octahedral vacancies

[140]. Vacancy ordering on tetrahedral sites is supported by the molecular dynamics (MD) simulation using interatomic pair potentials [142]. However, *ab initio* DFT within LDA produced calculations support vacancy distribution among both octahedral and tetrahedral positions [143, 144]. Applying DFT with different potentials and approaches (i.e., GGA-PW91, GGA-PBE, hybrid functionals, mixed Guassian and plane wave approach etc.) non-spinel model of γ-Al_2O_3 structure was also proposed [119, 120, 145-147]. Most of the theoretical work in the literature focused on simple models, such as primitive cell containing only 40 atoms ($Al_{16}O_{24}$) [136-144, 145, 147]. There are a few theoretical calculations using larger supercell models of γ-Al_2O_3 structure [119, 120, 144, 146]. There are also first-principles calculations for a non-spinel γ-Al_2O_3 model [119, 120, 146]. F. Maglia *et. al* used the pseudo-hexagonal larger supercell (160 atoms) of spinel γ-Al_2O_3 model, applied DFT with LDA based on pair-wise interatomic potentials [144]. They concluded that larger supercell of spinel γ-Al_2O_3 preferred random distribution of tetrahedral and octahedral vacancies [144].

Although, the previous experimental and theoretical studies have sheded light on the configuration of the oxygen sublattice, the uncertainty about the positions of the aluminium cations and vacancies within the unit cell is still a topic of continuing debate over the γ-Al_2O_3 structure. Without a clear description of pure bulk γ-Al_2O_3 structure, clarification of many experimental data will be difficult or even misleading. In this purpose, careful theoretical calculations on a well defined structural model of γ-Al_2O_3 can provide much of the missing information and can be used to accurately interpret the data for more complex and nonstoichiometric samples in material industries.

3.2.4 Summary:

As shown in the above subsections (i.e., 3.2.1-3.2.3), there are many experimental and theoretical efforts to describe the crystal structural and electronic properties of α-, θ- and γ-Al_2O_3 [89-147]. Though the calculated structural properties from theoretical DFT works of α-, θ- and γ-Al_2O_3 are in agreement with those obtained from experimental works, but large differences were observed for bulk modulus and electronic band gaps. Also, the chemical bonding nature in α-, θ- and γ-Al_2O_3 phases relates to their crystal structural, electronic and optical properties. The study of crystal structure with chemical bonding nature in detail as well electronic and optical properties of these alumina phases using a systematic procedure of computational investigation could open up many aspects in research industry. In the case of ground state α-Al_2O_3 there are experimental results available, while such are absent for metastable θ- and γ-Al_2O_3. Particularly for γ-Al_2O_3 there are controversy still exists over its crystal structure. Therefore, to resolve the uncertainty and properties of θ- and γ-Al_2O_3 it is prerequisite to acquire proper knowledge about these alumina phases.

3.3 Structural correlation between spinel $MgAl_2O_4$ and γ-Al_2O_3

$MgAl_2O_4$ is known as the prototype of the spinel group. It has the cubic structure with the space group *Fd3m* [148]. The O atoms are at 32e (point symmetry, 3*m*), the Mg atoms at 8a (point symmetry, 43*m*) and the A1 at 16d (point symmetry, 3*m*) [88]. The lattice parameter of spinel $MgAl_2O_4$ is 8.09 Å [149].

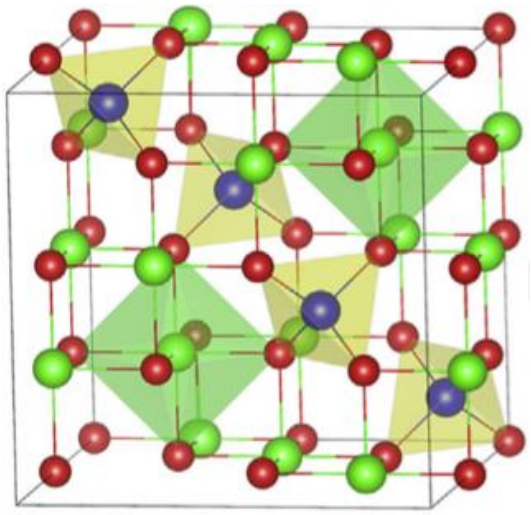

Figure 3.5: Schematic structure of fcc $MgAl_2O_4$ conventional unit cell where red, green, and blue spheres represent O, Al and Mg atoms, respectively. Mg and Al ions are tetrahedrally (yellow polyhedra) and octahedrally (green polyhedra) coordinated by oxygen ions respectively [150].

Following the ideal spinel structure AB_2O_4, in $MgAl_2O_4$ crystal structure the Mg cations occupy the A tetrahedral sites, and the Al cations occupy the B octahedral sites [148, 150] [Figure 3.5]. Spinel $MgAl_2O_4$ is the only ternary phase with a temperature below 1300 *K* in the MgO-Al_2O_3 phase diagram and does possess a spinel type solid solution MgO.$n$$Al_2O_3$ ($0.6 \leq n \leq 9.1$) [29]. Besides this, $MgAl_2O_4$, can be usually non-stoichiometric, with composition of MgO.$n$$Al_2O_3$ (here, $n > 1$) [151]. Such non-stoichiometric character makes them convenient to tune many properties by modifying their composition [152-154]. The non-stoichiometric MgO-n.Al_2O_3 (n = 1.2, 2.5) showed higher transmission of visible light than stoichiometric $MgAl_2O_4$ [152, 153].

In the literature, most of the theoretical models of γ-Al_2O_3 spinel like structure were based on the spinel $MgAl_2O_4$ cubic cell by substitute Al cations in both tetrahedral (Mg) and octahedral sites [136-144]. The previously mentioned [in subsection 3.2.3] cation vacancies are required to maintain the stoichiometry of γ-Al_2O_3. Moreover, the frames of both structures are based on distorted FCC O

sublattices. With the similar base structure there is a structural relationship between spinel $MgAl_2O_4$ and γ-Al_2O_3 which can be determined by substituting Al or Mg and cation vacancies.

The disordered $MgO{\cdot}nAl_2O_3$ spinel-type solid solution forms by two Al^{3+} ions substituting for every three of the Mg^{2+} ions (i.e., $3Mg^{2+}$<--> $2Al^{3+}$ replacements) to ensure the charge neutrality, which results in a vacant lattice sites and non-stoichiometric structure. So, both tetrahedral (Wyckoff site 8a) and octahedral interstices (Wyckoff site 16d) within the oxygen sublattice are occupied by more than one type of cations or vacancies. Despite plenty of studies on cation distributions in oxide spinels have been done in literature [29, 151-157], there is still a lack of knowledge about the local structure such as the distribution rules between Al^{3+} and Mg^{2+} cations and vacancies. From electron paramagnetic resonance (EPR) experimental data and MgO-x(Al_2O_3) samples ($1<x<3.4$), A. Ibarra *et al* have assumed the vacancy distribution in both octahedral and tetrahedral sites in non-stoichiometric structure [155]. Based on alumina-rich spinel ($MgO.nAl_2O_3$; $n\geq1$) first principle DFT studies in literature proposed a solid solution of $MgAl_2O_4$ and $Al_{8/3}O_4$ (i.e., γ-Al_2O_3) with the formula of $Mg_{(1-x)}Al_{2(1+x/3)}V_{x/3}O_4$ ($0\leq x\leq1$) [156, 157], where the Al^{3+} cations distribution in tetrahedral and octahedral interstitial sites are absent.

However, the complicated composition and the coupling effect between the two kinds of polyhedra (i.e., tetrahedra and octahedra) have brought about challenge for exploring such relationship for spinel-type compounds. As for a solid solution system, the distribution rules of ions can be found out by calculating as many configurations models as possible, comparing the energy difference with structural and electronic properties of those configurations, and thus the reasonable models can be screened out more efficiently [138]. Moreover, to gain insight into the crystal structure of the solid solution, it is also important to analyse the mechanisms behind the occupancy rules for ions.

3.4 Stability and structural properties of γ-Al_2O_3 surfaces

Considering the technological importance of γ-Al_2O_3, it is also a prerequisite to developing and understanding structural models for the surfaces of this metastable alumina phase. The surface of a material is an extension of its bulk, and many applications depend on its surface structure and properties, e.g., as ultra-hard coatings, microporous catalysts, and in electroluminescent flat-screen displays, etc [158]. γ-Al_2O_3 surfaces are found very active in the activation of C-H bonds of methane (CH_4) [159, 160]. A high-resolution TEM experiment has shown that the γ-Al_2O_3 particles have the (1 1 1) facets matching the same planes of Al grains in the pure Al melts and enhance the heterogeneous nucleation during solidification [22]. Therefore, adequate knowledge about γ-Al_2O_3 surface structure is a necessity for many extensive applications. However, the surface of γ-Al_2O_3 is very complicated and there is also controversy concerning the surface structure as the bulk [161-168].

The γ-Al_2O_3 has a cubic lattice with the Al cations being coordinated both tetragonally and octahedrally by O anions [28, 89, 122]. In the γ-Al_2O_3 along (1 1 1) orientation, O ions form two-dimensional (2D) distorted hexagonal sublattices and Al ions occupy the interstitial sites of the neighbouring O layers in two different ways. From Figure 3.6, at the Al(Oh) layer, which is below the O1 layer, the Al ions occupy two thirds of the octahedral sites [139]. The Al(Tet) layer below the O2 layer (Figure 3.6) is composed of three sublayers: a sublayer of octahedrally coordinated Al(Oh) or vacancies being sandwiched by two tetragonally coordinated Al(Tet) sublayers [Figure 3.6]. This implies that the smooth surfaces of γ-Al_2O_3 along (111) axis with an O termination or Al termination contain net charges, being polar which leads to an electric dipole moment in the direction perpendicular to the surface.

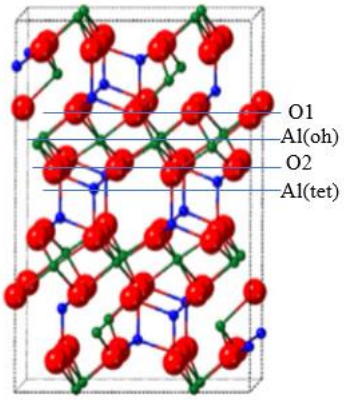

Figure 3.6: Schematic representation of γ-Al_2O_3 along (1 1 1) axis, the octahedral and tetrahedral Al atoms are green and blue balls, while the oxygen atoms are red balls respectively, the dotted black lines represent the unit cell [139].

But such polar surfaces are not stable for large crystal systems at ambient conditions [169-171]. Because bulk terminated polar surface has an infinite surface energy from alternating layers of oppositely charged ions produce a large dipole moment perpendicular to the surface [172]. To investigate feasible (111) surfaces, defective surfaces need to be constructed in a systematic way, as in the cases of oxides [168-171]. Thus γ-Al_2O_3 surface structure deserves to be examined with more possible configurations.

3.5 Crystal chemistry of Y_2O_3 phases:

Yttrium oxide also known as yttria (Y_2O_3) has attracted great research interest owing to its excellent properties which led to many attractive applications [36-47]. Experimental observations revealed that a small amount of yttrium doped influences both the properties and the microstructures of α-Al_2O_3, which is called yttrium effect [173, 174]. Though Yttria itself is a compound, it can be the end member of many pseudo-binaries: M_2O_3-Y_2O_3 (M=Al, La, B, etc.) [32].

The crystal structure of Y_2O_3 belongs to the bixbyite type $[^{VI}A_2][^{IV}O_3]$, which is body-centered cubic (bcc) [175]. The lattice parameter of yttria is 10.603 Å [176]. This compound could exhibit three different structural polymorphisms: cubic

(space group *Ia3*, No. 206), monoclinic (space group *C2/m*, No. 12) and hexagonal (space group *P3m1*, No. 164) structures, commonly known as C-Y_2O_3, M-Y_2O_3 and H-Y_2O_3 respectively [176-179]. Recently, based on TEM experiments S. Wang observed that fcc-Y_2O_3 is formed on MgO in liquid Mg alloys which might be a high-temperature phase [180]. To justify their observations, calculations on structural models with formation energies and bulk modulus in a systematic way are required. Based on the first-principles DFT calculations with structural and electronic properties, we may estimate the phase stability and transition of Y_2O_3.

Chapter Four

Theoretical Methods

This chapter introduces the methodology of density functional theory (DFT) in detail, as well as the state-of-art *GW* approach and MD simulation techniques used throughout this thesis. A brief introduction of each topic to specify what approximations are made and what basis functions are used is described in this chapter. First, we start with the basic concepts of the many-body Schrödinger equation [54] that governs the wave function of a quantum mechanical system.

4.1 The Schrödinger equation and the Hamiltonian

In quantum mechanics, the exact theory for a system of ions and interacting electrons is based on solving the many-body Schrödinger equation [54] of the form,

$$H\Psi([R_I; r_i]) = E\Psi([R_I; r_i]) \qquad \ldots\ldots\ldots\ldots\ldots\ldots \quad (4.1)$$

where, H is the Hamiltonian operator [181], which contains all of the kinetic and potential energy operators arising as a result of the ion-ion, electron-electron and ion-electron interactions, $\Psi([R_I; r_i])$ is the many-body wavefunction of the system and E is the eigen energy of the system. R_I and r_i are the position of the ion and electrons, respectively.

The total kinetic energy (KE) of the system can be written as the sum of the kinetic energies of each particle (ion or electron) in the many-body system from following equation [182],

$$KE = -\sum_I \frac{\hbar^2}{2M_I}\nabla_{R_I}^2 - \sum_i \frac{\hbar^2}{2m_e}\nabla_{r_i}^2 \qquad \ldots\ldots\ldots\ldots\ldots\ldots\ldots \quad (4.2)$$

Here, $\hbar$ is the Plancks's constant, M_I is the mass of the ion I, and m_e is the mass of the electron.

The total potential energy (*PE*) can be written from the interactions of the charges in a system using the following equation [182],

$$PE = -\sum_{iI} \frac{Z_I e}{|R_I - r_i|} + \frac{1}{2}\sum_{ij(j\neq i)} \frac{e^2}{|r_i - r_j|} + \frac{1}{2}\sum_{IJ(J\neq I)} \frac{Z_I Z_J}{|R_I - R_J|} \quad \ldots\ldots\ldots\ldots (4.3)$$

The $-\sum_{iI} \frac{Z_I e}{|R_I - r_i|}$ term in equation (4.3) represents the attraction between the electrons with its constituent ions, the $\frac{1}{2}\sum_{ij(j\neq i)} \frac{e^2}{|r_i - r_j|}$ and $\frac{1}{2}\sum_{IJ(J\neq I)} \frac{Z_I Z_J}{|R_I - R_J|}$ represents the repulsive term due to electron-electron and ion-ion interactions respectively in the system.

In the mass between ions and electrons as it is sensitive to consider the ions as moving very slowly and the electrons 'instantaneously' responding to any ionic motion [181]. By applying Born-Oppenheimer approximations [183], kinetic energies of the nuclei can be avoided and to discount the ion-ion interactions as this can be constant for any given electron. Taking these Born-Oppenheimer approximations [183] into account the Hamiltonian can be described by Equation (4.4),

$$H = -\sum_i \frac{\hbar^2}{2m_e} \nabla_{r_i}^2 + \sum_i V_{ion}(r_i) + \frac{1}{2}\sum_{ij(j\neq i)} \frac{e^2}{|r_i - r_j|} \quad \ldots\ldots\ldots\ldots\ldots (4.4)$$

where, $V_{ion}(r_i)$ is the ionic potential experienced by every electron, *i*.

Therefore, according to the Born-Oppenheimer approximation [183], it is only necessary to construct Ψ based on the electron positions. But in reality, this complicated many-particle Equation (4.4) is not separable into simpler single-particle equations because of the interaction term $\frac{1}{2}\sum_{ij(j\neq i)} \frac{e^2}{|r_i - r_j|}$ [184, 185].

Electronic Density-Functional Theory (DFT) provides an appealing method for solving the many-body Schrödinger Equation (4.1), being much more versatile, as it provides a way to systematically map the many-body problem with $\frac{1}{2}\sum_{ij(j\neq i)} \frac{e^2}{|r_i - r_j|}$, onto a single-body problem without $\frac{1}{2}\sum_{ij(j\neq i)} \frac{e^2}{|r_i - r_j|}$ [184,

185]. The core concept of DFT is to reformulate the problem in terms of the total density, ***n(r)***, of the electrons rather than by dealing with the many-body wavefunction, $\Psi(r_i)$ [184, 185]. DFT can be able to calculate electronic structure of many-body problem using spatially varying electron density ***n(r)***. The following section describes the DFT method in more detail.

4.2 First-principles density-functional theory (DFT)

First-principles density functional theory (DFT) is a method to determine the ground-state properties of a many-electron system by expressing its total energy as a functional of the electron density. DFT was first introduced by Hohenberg-Kohn and Kohn-Sham in two of the seminar papers in 1960s [184, 185]. Since then, the theory has attracted a lot of research interest in improving the adaption of the method for practical computational use. The real specialty of DFT is its favorable performance ratio compared with electron-correlated wave function-based methods such as Møller–Plesset perturbation theory or coupled cluster [186-188]. Thus, larger (and often more relevant) molecular systems can be studied with sufficient accuracy, thereby expanding the predictive power inherent in electronic structure theory [188-190]. As a result, DFT is now the most extensively used electronic structure method. The huge importance of DFT in physics and chemistry is evidenced by the 1998 award of the Nobel Prize to Walter Kohn 'for his development of the density- functional theory' [190]. DFT was formerly framed on basic two theorems of Hohenberg and Kohn (HK) [184].

4.2.1 The Hohenberg-Kohn (H-K) theorems

4.2.1.1 Theorem One:

The first Hohenberg-Kohn theorem states that if there are *N* interacting particles in a system and they are moving in an external potential $V_{ext}(r)$, is uniquely determined by the ground state particle density $\rho_0(r)$, except a constant. That mean there is a one-to-one mapping relation between the electron density and the

external potential, and every property of the many-body system is a functional of the ground state charge density [184].

Hence, the external potential $V_{ext}(r)$, and the total energy is a unique functional of the electron density $\rho(r)$:

$$E[\rho(r)] = \int \rho(r)V_{ext}(r)dr + F[\rho(r)] \qquad \ldots\ldots\ldots\ldots\ldots\ldots\ldots\ldots \quad (4.5)$$

4.2.1.2 Theorem Two:

The second Hohenberg-Kohn theorem establishes a variational principle for the total energy functional so that the ground state energy can be achieved by minimizing the energy over all possible densities, which is valid for any applied external potential [184]. Hence the density that minimises the total energy is the ground state density:

$$E[\rho(r)] \geq E_0[\rho_0(r)] \qquad \ldots\ldots\ldots\ldots\ldots\ldots\ldots\ldots \quad (4.6)$$

But the H-K theorem is an existence proof that the many electron wavefunction can be substituted by the electron charge density as a basic variable, it does not provide an explicit mathematical form [184, 185].

4.2.2 Kohn-Sham (K-S) Approximation

In 1965, Kohn-Sham proposed new approach to express the kinetic energy in terms of independent electron single particle wavefunctions [185]. This fictitious non-interaction electron system in an effective potential consisting of the external potential and the exchange correlation interaction is equivalent to the actual interacting system in the sense that it provides the same density. Then one arrives at the following set of equations, named the Kohn-Sham (K-S) equations

$$H_{eff}\psi_i(r) = \left(-\frac{1}{2}\nabla^2 + V_{eff}(r)\right)\psi_i(r) = \varepsilon_i\psi_i(r)$$

$$V_{eff}(r) = V_{ext}(r) + \int d^3r' \frac{\rho(r')}{|r-r'|} + V_{xc}[\rho(r)]$$

$$\rho(r) = \sum_i^{N_e} |\psi_i(r)|^2$$

…… (4.7)

Where, $V_{eff}(r)$ is the effective potential of the non-interacting system, $V_{ext}(r)$ is the external potential generated by the nuclei, $\rho(r)$ is the electron density, and $V_{xc}[\rho(r)] = \frac{\delta E_{xc}[\rho(r)]}{\delta\rho(r)}$ is the functional derivative of the exchange between the correlation energy $E_{xc}[\rho(r)]$ with respect to $\rho(r)$. Finally, once these equations are solved for $\rho(r)$ then the total ground state energy can be expressed as

$$E_0(r) = \sum_i n_i \varepsilon_i - \iint \frac{2\rho(r')}{|r-r'|} d^3r' - \int \frac{\delta E_{xc}[\rho(r)]}{\delta\rho(r)} d^3r + E_{xc}[\rho(r)] \quad \ldots\ldots (4.8)$$

Although the KS-DFT is in principle an exact theory, the exact exchange-correlation functional $E_{xc}[\rho(r)]$ is not known. So, if know the exact functional of $E_{xc}[\rho(r)]$ then one can solve the exact solution of the many electron system. Therefore, further approximations are required for generating a more accurate functional [186-188].

4.2.3 The exchange-correlation functional

Choosing the correct form of exchange-correlation functional $E_{xc}[\rho(r)]$ is important in order to reduce the error in the total ground state energy calculations. For this purpose, first, we should understand the physical meaning of $E_{xc}[\rho(r)]$. Let us consider an electron sitting in the electron cloud, which does not simply see an average charge density around itself. That is because the other electrons try to avoid this site due to the Pauli exclusion principle and electron repulsion as well. So, the region around that particular electron has a so-called exchange-correlation hole. And the exchange-correlation energy is basically the interaction of the electron with its surrounding exchange-correlation hole. In sorts, we can say that the exchange energy is the quantum mechanical energy resulting from the antisymmetry of the many-electron wavefunctions and the correlation energy is the dynamical interaction energy between electrons in a quantum system. Local

Density Approximation (LDA) [188] and Generalized Gradient Approximation (GGA) [191, 192] are two useful functional to obtain the exchange correlation energy, $E_{xc}[\rho(r)]$ in the ground state which are described in the following subsections 4.2.3.1-4.2.3.3.

4.2.3.1 Local Density Approximation (LDA)

The local density approximation (LDA) relates to the assumption that the exchange-correlation energy at each point in space depends only on the density at that point. I n a homogeneous electron gas, the density n is constant and the exchange correlation energy $E_{xc}[\rho(r)]$ has been calculated in various limits, e.g. at low density by Wigner [186] and high density by Gell-Mann and Brueckner [187], and interpolation formulas between these regimes exist. LDA starts from computing the ground state of the homogeneous electron gas as accurately as possible and then constructing the exchange-correlation energy per particle, $\varepsilon_{xc} = E_{xc}[\rho(r)]/N$ as a function of electron density $\rho(r) = N/V$ [188]. Then we apply the same expression at each point locally in the actual inhomogeneous system and by integration we get

$$E_{xc}^{LDA} = \int d^3r \rho(r) \varepsilon_{xc}(\rho(r)) \quad \ldots\ldots\ldots\ldots\ldots\ldots\ldots\ldots \quad (4.9)$$

The LDA exchange-correlation potential can be written as

$$V_{xc}^{LDA} = \frac{\partial(n\varepsilon_{xc})}{\partial n} \quad \ldots\ldots\ldots\ldots\ldots\ldots\ldots \quad (4.10)$$

Although the LDA is composed based on the assumption of a slowly varying density, it works remarkably well even for some realistic systems where the density is not slowly changing. This has been shown to be related to the fulfillment of certain sum rules [189]. LDA successfully predicts the total energy, lattice constant, equation of state and relaxations of atomic coordinates around defects and at surfaces within≈5% of accuracy [190]. Nevertheless, in the case of electronic excitation energy calculation LDA is unsuccessful because it is a theory for the ground state total energy, not for the excitations. The other problem

is that even for ground state properties, LDA may not succeed for systems which have localized electrons such as d and f electrons. It also fails near surfaces or for molecules and free atoms because the electron density changes too rapidly from a typical density inside the material to a low density outside. That is because the homogeneous electron gas is no longer a good approximation due to the large charge fluctuations [190].

4.2.3.2 Generalized Gradient Approximation (GGA)

In the LDA, we obtained the exchange correlation energy from the uniform electron gas expression at every point in space, but the charge density is nonuniform in the real system. Thus, the actual $E_{xc}[\rho(r)]$ can differ significantly from the LDA results. This difference can be expressed in terms of the gradient and higher spatial derivatives of the total charge density. So, generalized gradient approximation or GGA goes one step beyond LDA by taking the density and also its gradient at each point in space [191]. So, in the GGA we can write the exchange correlation energy in terms of the electron density and the electron density gradient $\nabla\rho(r)$ as

$$E_{xc}^{GGA} = E_{xc}[\rho(r), \nabla\rho(r)] \quad \ldots\ldots\ldots\ldots\ldots\ldots \quad (4.11)$$

This improves the exchange-correlation energy in situations when the density varies rapidly [191].

4.2.3.3 GGA-PBE

PBE by Perdew, Burke and Ernzerhof is a new version of GGA. The exchange energy of PBE approximation can be defined as an integral over the exchange density [192]

$$E_{xc}^{PBE} = \int d^3r\rho(r)\varepsilon_{xc}^{PBE}(\rho(r), s(r)) \quad \ldots\ldots\ldots\ldots\ldots\ldots \quad (4.12)$$

where, $s = |\nabla|/(2k_F\rho)$ is the reduced gradient with $k_F = (3\pi^2\rho)^{\frac{1}{3}}$.

The PBE exchange energy density is the product of LDA exchange and enhancement factor F_x^{PBE} which depends on $s(r)$, and is defined in explicitly PBE functional.

$$\varepsilon_x^{PBE}(\rho(r), s(r)) = \varepsilon_x^{LDA}\big(\rho(r)\big) \times F_x^{PBE}(s(r)) \quad \ldots\ldots\ldots\ldots\ldots \quad (4.13)$$

$$F_x^{PBE}(s) = -\frac{8}{9}\int_0^{\infty} y dy J^{PBE}(s, y) \quad \ldots\ldots\ldots\ldots\ldots\ldots \quad (4.14)$$

where, $J^{PBE}(s, y)$is the PBE exchange hole [204].

It has been shown that GGA-PBE gives a better description of the exchange-correlation hole and gives a more realistic account of energy barriers and adsorption energies for molecules [192]. Although GGA-PBE produces very good results for molecular geometries, ground state total energies and surface energies, though it is not clear that GGA-PBE is an improvement over LDA for all ground state properties. Therefore, for any calculation in DFT it is recommended to apply both LDA and GGA approximations and compare the results with available experimental works. LDA and GGA-PBE are basically designed to study ground state properties: there is no real justification to interpret the KS one-electron eigenvalues (ε_i of equation 4.8) as excitation energies, i.e. the energy to extract or add an electron to the system. They are usually not applicable for systems with strongly associated electrons and not completely self-interaction free. Thus, in the next section we will discuss Green's function methods as a tool to study both ground state and excited state properties of the many-body problem.

4.3 *GW* Approximation

The K-S eigenvalues cannot represent the quasiparticle band structure measured by direct and inverse photoemission because LDA and GGA including GGA-PBE suffer from an incomplete cancellation of artificial self-interaction and lack the discontinuity of the exchange-correlation potential with respect to the number of excited electrons [59, 193]. To overcome these deficiencies, the proper

addition of both dynamical and non-local effects by the *GW* approach was introduced to improve LDA and GGA results [193]. It was originally proposed by Hedin [59] and named after its construction of the electron self-energy from the Green's function (*G*) and the screened interaction (*W*).

4.3.1 Green's Function

Generally, the Green's function is known as a propagator or the probability amplitude for a particle to travel from position *r*, at time *t* to another position r' at time t' [66]. First, let us define field operators, $\psi^{\dagger}(r',t')$ and $\psi(r,t)$ as creation and extermination operators respectively written in the time dependent position basis. When these field operators functionate on an exact ground state wavefunction of *N* electron system $|N,0\rangle$ one will get *N*+1 or *N*−1 electron wavefunctions which are not necessarily in the ground. $\langle N,0|\psi(r,t)\psi^{\dagger}(r',t')|N,0\rangle$ defines a propagator $iG^{e}(rt,r't')$ for an extra electron transmitting from (r',t') to (r,t), in contrast, $\langle N,0|\psi^{\dagger}(r',t')\psi(r,t)|N,0\rangle = iG^{h}(r't',rt,)$ is a propagator measuring a missing electron (hole) which transmits from (r,t) to (r',t'). Thus, the one-electron Green's function can be written as [62]

$$\begin{aligned} iG^{e}(rt,r't') &= \langle N,0|T[\psi(r,t)\psi^{\dagger}(r',t')]|N,0\rangle \\ &= \langle N,0|\psi(r,t)\psi^{\dagger}(r',t')|N,0\rangle \; for\; t>t'. \\ &= -\langle N,0|\psi^{\dagger}(r',t')\psi(r,t)|N,0\rangle \; for\; t'>t \end{aligned} \qquad \ldots\ldots\ldots\ldots \quad (4.15)$$

Where, *T* is the time-ordering operator which rearranges operators from right to left after increasing time and includes a minus sign for every interchange of fermion operators. Let us consider the field operator in the Heisenberg representation is $\psi^{\dagger}(r,t) = e^{iHt}\psi^{\dagger}(r)e^{-iHt}$ and insert the closure relation into

equation (4.15). Also note that the limiting energy for injection of electrons or holes is the chemical potential μ. Thus, we can rewrite equation (4.15) as

$$iG(r,r',\tau) = \sum_n \langle N,0|\psi(r)|N+1,n\rangle\langle N+1,n|\psi^\dagger(r')|N,0\rangle e^{-iE_n\tau},\ \tau>0, E_n \geq \mu$$

$$= -\sum_m \langle N,0|\psi^\dagger(r')|N-1,m\rangle\langle N-1,m|\psi(r)|N,0\rangle e^{-iE_m\tau},\ \tau<0, E_m<\mu$$

…….. (4.16)

Where, $\tau = t - t'$, n and m represent quantum numbers to indicate the state, which is not the ground state, $E_n = E_n^{N+1} - E_0^N$ and $E_m = E_0^N - E_m^{N-1}$. Equation (4.16) can be Fourier-transformed into the frequency representation as

$$iG(r,r',\omega) = \int_{-\infty}^{\infty} iG\,(r,r',\tau)e^{i\omega t}d\tau$$

$$= \sum_n \left\langle N,0|\psi(r)|N+1,n\right\rangle \left\langle N+1,n|\psi^\dagger(r')|N,0\right\rangle \int_0^\infty e^{i(\omega-E_n+i\eta)\tau},\ E_n \geq \mu$$

$$= -\sum_m \left\langle N,0|\psi^\dagger(r')|N-1,m\right\rangle \left\langle N-1,m|\psi(r)|N,0\right\rangle \int_{-\infty}^0 e^{i(\omega-E_m-i\eta)\tau},\ E_m<\mu$$

…… (4.17)

The infinitesimal η ensures that $G(r,r',\omega)$ has the correct analytic properties.

If the quasiparticle amplitudes of any excited state *s* as

$$f_s(r) = \langle N,0|\psi(r)|N+1,s\rangle\ for\ E_s = E_s^{N+1} - E_0^N, E_s \geq \mu$$

$$f_s^*(r') = \langle N-1,s|\psi^\dagger(r')|N,0\rangle\ for\ E_s = E_0^N - E_s^{N-1}, E_s<\mu$$

……..…… (4.18)

and work out the integrals in the equation (4.17), then we get

$$G(r,r',\omega) = \sum_s \frac{f_s(r)f_s^*(r')}{\omega - E_s \pm i\eta} \text{ ……} \quad (4.19)$$

where the sum is over both electrons and holes and the ± signs correspond to electrons and holes respectively. And the poles of the Green's function represent the single-particle excitations or the quasiparticle energies [59].

Later, an explicit expression for the single-particle Green's function was developed by Hedin [59, 194]. Starting from the Heisenberg equation of motion for the field operator [66]

$$i\frac{\partial\psi(x)}{\partial t} = [\psi(x), H] \qquad \ldots\ldots\ldots\ldots\ldots\ldots\ldots \quad (4.20)$$

Where, x contains the variables: space (r), spin (σ), and time (t). The Hamiltonian, H is split into the non-interaction part H_0 and the interaction part.

$$H = \int dr\psi^{\dagger}(x)H_0(x)\psi(x) + \frac{1}{2}\int drdr'\psi^{\dagger}(r,t)\psi^{\dagger}(r',t)v(r,r')\psi(r',t)\psi(r,t)$$

$$\ldots\ldots\ldots\ldots\ldots\ldots\ldots\ldots \quad (4.21)$$

But the problem arises when second part in equation (4.21) inserted in equation (4.20) there involves a two-particle Green's function and includes all two-body correlations in the system, which in turn introduces the three-particle Green's function [66]. Applied iteratively, this procedure creates an infinite series of higher order Green's functions and in practice, however, the resulting recurrence relation for the n^{th} order Green's function is impossible to solve for large n [66]. Then, we must somehow decouple this part introducing the non-local, time-dependent self-energy $\bar{\Sigma}(x, x')$

$$\int dx^{"}\bar{\Sigma}(x,x^{"})G(x^{"},x') = -i\int dr^{"}v(r,r^{"})\langle N|T[\psi^{\dagger}(r^{"},t)\psi(r^{"},t)\psi(r,t)\psi(r',t')]|N\rangle$$

$$\ldots\ldots\ldots\ldots\ldots\ldots\ldots\ldots \quad (4.22)$$

and from the well-known equation (4.20), an equation of motion for the Green's function can be derived as

$$\left[i\frac{\partial}{\partial t} - H_0(x)\right]G(x,x') - \int dx^{"}\bar{\Sigma}(x,x^{"})G(x^{"},x') = \delta(x-x') \quad \ldots\ldots\ldots \quad (4.23)$$

One can put the average Coulomb interaction, V_H, into the non-interacting part, and the equation of motion for the Green's function can be written as

$$\left[i\frac{\partial}{\partial t} - H_0(x) - V_H(x)\right]G(x,x') - \int dx^{"}\Sigma\left(x,x^{"}\right)G\left(x^{"},x'\right) = \delta(x-x') \quad \ldots\ldots\ldots\ldots\ldots\ldots\ldots \quad (4.24)$$

The self-energy, $\Sigma = \bar{\Sigma} - V_H$ can be defined from the equation (4.24). Hedin used Schwinger's functional derivative method to derive a set of equations for the self-energy in terms of the screened Coulomb interaction [59, 62, 194]. The physical idea is that the electron-electron interaction can screened by itself. Because the screening reduces the interaction and expressing everything in the screened interaction will lead to a better-converging approximate method. In Hedin's equations, the exact self-energy is $\Sigma = iGW\Gamma$ [66]. With the replacement $\Gamma(1,2,3) = \delta(1,2)\delta(1,3)$, Hedin's approximation gives $\Sigma = iGW$, hence the name of the *GW* approximation [66]. Eventually, one can arrive at the set of equations [64, 66]

$\sum(1,2) = i\int d(3,4)G(1,4)W(1^{+},3)\Gamma(4,2,3) \quad : 1 \equiv (r_1,\sigma_1,t_1)$ ……..(4.25a)

$G(1,2) = G_0(1,2) + \int d(3,4)G_0(1,3)\sum(3,4)G(4,2)$ ……. (4.25b)

$W(1,2) = v(1,2) + \int d(3,4)v(1,3)P(3,4)W(4,2)$ …….. (4.25c)

$P(1,2) = -i\int d(3,4)G(2,3)\Gamma(3,4,1)G(4,2)$ ……. (4.25d)

$$\Gamma(1,2,3) = \delta(1,2)\delta(2,3) + \int d(4,5,6,7)\frac{\delta\sum(1,2)}{\delta G(4,5)}G(4,6)G(7,5)\Gamma(6,7,3) \quad \ldots\ldots\ldots\ldots\ldots\ldots \quad (4.25e)$$

where *W*, Γ and *P* are the screened Coulomb potential, the vertex function and the polarization function respectively.

These Hedin equations (4.25a-4.25e) can be solved self-consistently until the results of Green's function coincides with the starting one [194-196].

4.3.2 *GW* correction to standard density functionals

In practice the *GW* approximation is applied as a perturbation approach to calculate the excitation energy from KS-DFT eigenfunctions and eigenvalues [58-66, 193, 194]. In other words, it is just a one-shot correction to LDA. Although in previous section 4.3.1, quasi particle excitations were defined in terms of the poles of the Green's function, one can also introduce a quasiparticle wavefunction and energy. They obey the equation,

$$\left(-\frac{\nabla^2}{2} + V_{ext}(r) + V_H(r)\right)\phi_i(r) + \int dr' \Sigma\left(r, r', \varepsilon_i^{GW}\right)\phi_i(r, r') = \varepsilon_i^{GW}\phi_i(r)$$

…… (4.26)

Although it looks very similar to the K-S equation

$$\left(-\frac{\nabla^2}{2} + V_{ext}(r) + V_H(r)\right)\phi_i^{LDA}(r) + V_{xc}^{LDA}(r)\psi_i^{LDA}(r) = \varepsilon_i^{LDA}\psi_i^{LDA}(r)$$

…… (4.27)

Where the self-energy (Σ) is a non-local and energy-dependent operator in equation (4.26) and is not a Hermitian operator [193, 194], its energies can be complex. Their imaginary part (ε_i) represents the lifetime of the particle [193, 194]. Nevertheless, we can find solutions of equation (4.26) by means of perturbation theory if we assume the wavefunctions of equation (4.26) are the same as those in equation (4.27). Then one can correct DFT-LDA eigenvalues by a using first-order perturbation treatment [193]

$$\varepsilon_i^{GW} = \varepsilon_i^{LDA} + \langle\psi_i^{LDA}|\sum\left(r, r', \varepsilon_i^{GW}\right) - V_{xc}^{LDA}(r)|\psi_i^{LDA}\rangle \quad \text{……} \quad (4.28)$$

To summarize, equation (4.28) gives us the energy shift of the one-particle excitations from the K-S eigenvalues and the imaginary parts. Within the *GW*

approximation, by Fourier transforming equation (4.25a) over time, the self-energy $\sum$ is given as

$$\sum(r,r',\varepsilon) = \frac{i}{2\pi}\int d\varepsilon' e^{-i\delta\varepsilon'} G(r,r',\varepsilon+\varepsilon')W(r,r',\varepsilon') \quad \ldots\ldots\ldots\ldots \quad (4.29)$$

Where, ε is the dielectric function [66]. In the so-called one-shot G_0W_0, G can be approximated by the independent particle G_0

$$G_0(r,r',\varepsilon) = \sum_i \frac{\psi_i^{LDA}\psi_i^{LDA*}}{\varepsilon-\varepsilon_i^{LDA}\pm i\eta} \quad \ldots\ldots\ldots\ldots\ldots\ldots\ldots \quad (4.30)$$

By using the Random Phase Approximation (RPA), then the screened Coulomb interaction W can be estimated as W_0 [62]

$$W_0 = v\varepsilon^{-1} = v(1-vP)^{-1} \quad \ldots\ldots\ldots\ldots\ldots\ldots\ldots \quad (4.31)$$

Here, W_0 is expressed by a schematic notation and can be calculated from the bare Coulomb interaction v and the inverse dielectric function ε^{-1} via Equation (4.31). The commonly used G_0W_0 approach calculates G and W (and then the self-energy via Equation (4.25a)) based on the K-S eigenvalues ε_i^{LDA} and wave functions ψ_i^{LDA} from some form of DFT via Equation (4.30), where η is an infinitesimal positive number [64]. To introduce self-consistency beyond G_0W_0, two approaches can be employed [64]. The first one is the energy-only self-consistent approach, in which the eigenvalues are updated only in G (GW_0) or in both G and W (GW), while the QP wave functions are kept fixed at the K-S ones [64].

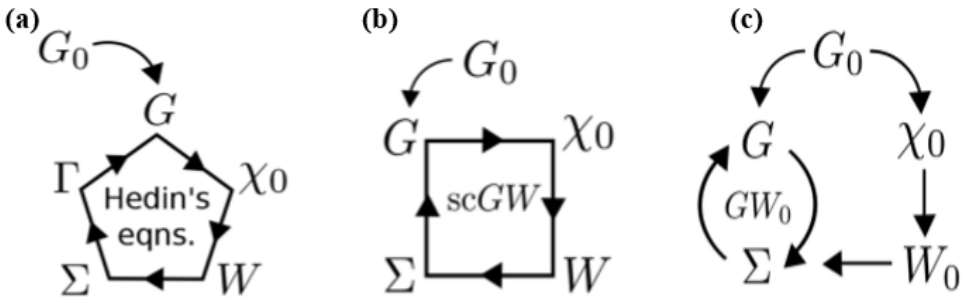

Figure 4.1: Schematic of Hedin's full set of equations (a) and Hedin's *GW* approximation (b, c). (a) All five quantities are iterated to self-consistency. (b) Self-consistent *GW* (sc*GW*), Γ is set to a single spacetime point and the remaining four quantities are determined self-consistently. (c) One iterates *G* to self-consistency in Equation (4.25b) but does not update W_0 [66].

The *GW* approximation is an enormous step forward from the K-S theory for calculating excitation energies [195, 196]. The results of *GW* approximations depend on other approximations made such as pseudopotentials to describe the interaction between valence and core electrons, and also depends on the accuracy of the starting point [195, 196].

4.4 Basis sets

Before solving the Kohn-Sham equations in DFT, first the form of the wavefunctions ψ_i must be chosen [197]. The wavefunction is extended into a set of basis functions, ϕ_j with coefficients c_{ij}

$$\psi_i = \sum_j c_{ij}\phi_j \qquad \ldots\ldots\ldots\ldots\ldots\ldots \qquad (4.32)$$

The type of the basis set is important because it affects how computationally expensive it is to converge the system with the required accuracy. The choice of the basis set is also dependent on the type of system. For a crystalline solid the basis set will obey Bloch's theorem since the system is periodic. Due to the periodicity the potential $V(\boldsymbol{r})$ will have the form

$$V(\boldsymbol{r}) = V(\boldsymbol{r} + \boldsymbol{\mathcal{R}}) \qquad \ldots\ldots\ldots\ldots\ldots\ldots \qquad (4.33)$$

Where, $\boldsymbol{\mathcal{R}} = n_1 \mathrm{a}_1 + n_2 \mathrm{a}_2 + n_3 \mathrm{a}_3$ is the direct lattice vector, with $\mathrm{a}_{1,2,3}$ the unit cell vectors of the system. Based on this the basis functions $\phi_{\boldsymbol{k}}(\boldsymbol{r}) = u_{\boldsymbol{k}} e^{i\boldsymbol{k}.\boldsymbol{r}}$ will satisfy the relation

$$\phi_{\boldsymbol{k}}(\boldsymbol{r} + \boldsymbol{\mathcal{R}}) = e^{i\boldsymbol{k}.\boldsymbol{\mathcal{R}}} u_{n\boldsymbol{k}}(\boldsymbol{r}) \qquad \ldots\ldots\ldots\ldots\ldots\ldots \qquad (4.34)$$

where $\boldsymbol{k}$ is the reciprocal space wave vector, $u_{\boldsymbol{k}}$ are arbitrary functions which obey the periodicity of the lattice and n is the band index. A set of plane waves fulfil this condition and are commonly used for a system with periodic boundary conditions [197]. Then the one-electron wavefunctions ψ_i can be expanded in them as

$$\psi_{i,\boldsymbol{k}}(\boldsymbol{r}) = \sum_{\boldsymbol{G}} c_{i,\boldsymbol{k}}(\boldsymbol{G}) e^{i(\boldsymbol{G}+\boldsymbol{k}).\boldsymbol{r}} \quad \ldots\ldots\ldots\ldots\ldots\ldots \quad (4.35)$$

Here, $\boldsymbol{G} = m_1\boldsymbol{b}_1 + m_2\boldsymbol{b}_2 + m_3\boldsymbol{b}_3$ is the reciprocal lattice vector and $c_{i,\boldsymbol{k}}(\boldsymbol{G})$are expansion coecients. The benefits of using plane waves is that they are orthogonal and Fast Fourier Transforms can be used in the calculation of the coefficients $c_{i,\boldsymbol{k}}(\boldsymbol{G})$. Though for large systems many plane waves are needed when using a plane wave basis set [66]. Therefore, plane waves are used in combination with pseudopotentials or the projector-augmented-wave methods [198] to approximate the effect of the core electrons [66]. The basic concept of pseudopotential is described in section 4.4.2.

4.4.1 *k*-point sampling

So far, the quantities discussed in above sections have been considered for an infinite $\boldsymbol{k}$-space sampling in the first Brillouin zone [199]. However, in practice the size of the $\boldsymbol{k}$-mesh should be limited. Also, in order to integrate a function over the Brillouin zone, specific number of $\boldsymbol{k}$-point sampling must be used. For example, the electron density is given by

$$\rho(\boldsymbol{r}) = \frac{1}{\Omega_{BZ}} \sum_n^{occ} \int_{BZ} |\psi_n(\boldsymbol{r})|^2 d^3\boldsymbol{k} \quad \ldots\ldots\ldots\ldots\ldots\ldots \quad (4.36)$$

where the sum is performed over all occupied states in the Brillouin zone and Ω_{BZ} is the volume of the Brillouin zone. In this case, only a finite number of $\boldsymbol{k}$-points are possible, and the number required depends on the system in question.

In terms of computational economy, for larger supercells a smaller $\boldsymbol{k}$-mesh is applied, often employ just one $\boldsymbol{k}$-point which, for the sake of additional

computational savings, is often chosen to be the Γ-point (i.e., the origin in reciprocal space). And inversely for small cells greater number of ***k***-points can be used. In case of metals, more ***k***-points are needed as the interaction between the conduction electrons are long ranged. By examining the convergence of total energy with ***k***-points the size of the ***k***-mesh can be determined. And for this, one can uses automatically generated, very dense ***k***-point sets that allow one to reach an accuracy of the total energy better than 1 *meV* per atom [199]. In the simplest case, a ***k***-point grid is specified by a product of three integer numbers, e.g., a 10 × 10 × 10 grid. But the number of reducible ***k***-points is given by the product of these three numbers (1,000 in the present example). Therefore, in an actual DFT calculation, only a smaller number of ***k***-points, the irreducible ***k***-points, are used. These irreducible ***k***-points that remain after all equivalences between **k**-points due to point group symmetries and time-reversal symmetry have been exploited, which helps to reduce the required computational resources considerably. Generally, ***k***-points are determined using the Monkhorst-Pack method [200]. The Monkhorst-Pack ***k***-point sets (which are defined to avoid high-symmetry points) show fast convergence, both as a function of ***k***-point density and as a function of the computational effort [199].

4.4.2 Pseudopotentials

In atoms, the electrons are classified into two groups: inner core electrons and valence electrons [197]. The inner core electrons are strongly bound to the nucleus and play a limited part in the chemical bonding with other atoms. On the other hand, the valence electrons are screened from the effects of the nucleus by the core electrons and are involved in bonding. During bonding the wavefunctions of the core electrons are only slightly affected as they remain strongly localised around their cores and for this reason, they are considered as essentially inert. These inner core electrons along with the nucleus can be treated with non-variational wavefunctions to simplify the method. This method is

known as the frozen core approximation [197]. DFT and *GW* calculations within the PAW schemes usually employ the frozen core approximation [201, 202].

The valence electrons are required to be orthogonal to the core electrons within the core region, which causes the spin orbitals of the valence electrons to oscillate in the core region [197]. And because of these oscillations, many basis functions are required to describe them correctly. Therefore, when using a plane wave basis set, a large value of the cut-off radius, i.e., G_{max} is needed (see equation (4.35)), with a high energy cut-off *E-cut* for the wavefunctions $E_{cut} = h^2 G_{max}^2 / 2m$. This enhances the computational effort.

To reduce the number of required basis sets, pseudopotentials are used to describe the Coulomb potential of the valence electrons as shown in Figure 4.2. Common forms of the pseudopotentials include the norm-conserving, ultrasoft pseudopotentials (USPP) and the projected-augmented wave method (PAW) [198]. The PAW method (used in VASP) allows an effectively all-electron calculation with frozen core orbitals (the other methods are based on valence pseudo-wavefunctions) [66, 197, 198].

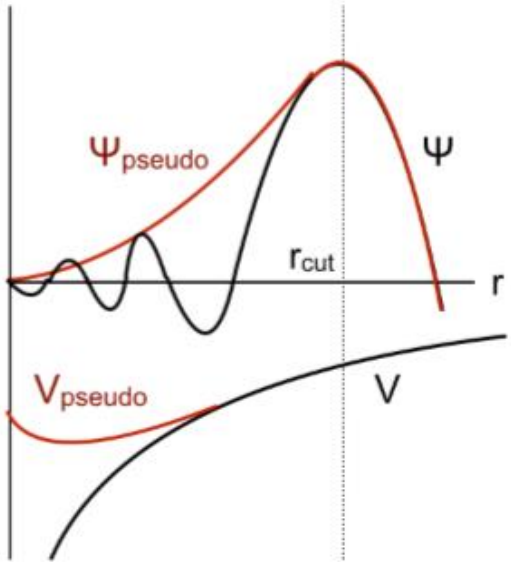

Figure 4.2: The pseudopotentials V_{pseudo} replaces the Coulomb potential V and as a result the oscillating core wavefunctions ψ are replaced by the pseudo-wavefunctions ψ_{pseudo} which are smooth inside the core region.

4.5 Optical properties calculation:

The optical processes such as absorption, reflection and transmission are observed in solids which can be quantified by several parameters [203]. At microscopic or quantum mechanical level in bulk solids the complex dielectric function is closely connected with the electronic (i.e., band structure) structure. The frequency dependent of complex dielectric function is defined as $\varepsilon(\omega)=\varepsilon_1(\omega)+i\varepsilon_2(\omega)$, where $\varepsilon_1(\omega)$ and $\varepsilon_2(\omega)$ are the real and imaginary part of the dielectric functions, respectively. The imaginary part $\varepsilon_2(\omega)$ of the dielectric function can be expressed from the momentum matrix elements between the occupied and the unoccupied electronic states and can be calculated directly using [203, 204]

$$\varepsilon_2(\omega) = \frac{4\Pi^2 e^2}{\Omega}\frac{1}{q^2}\lim_{q\to 0}\sum_{c,v,k} 2\,w_k\,\delta(\epsilon_{ck}-\epsilon_{vk}-\omega)\times\langle u_{ck+e_\alpha q}|u_{vk}\rangle\langle u_{vk}|u_{ck+e_\beta q}\rangle \quad \ldots\ldots\ldots\ldots\ldots\ldots\ldots\ldots \quad (4.37)$$

here the indices *c* and *v* refer to conduction and valence band states respectively, and $u_{c\mathbf{k}}$ is the cell periodic part of the orbitals at the $\boldsymbol{k}$-point. The real part of the dielectric function is obtained by the usual Kramers-Kronig transformation:

$$\varepsilon_1(\omega) = 1 + \frac{2}{\Pi}P\int_0^\infty \frac{\varepsilon_2(\omega')\omega'}{\omega'^2-\omega^2+i\eta}d\omega' \quad \ldots\ldots\ldots\ldots\ldots\ldots\ldots\ldots \quad (4.38)$$

where *P* denotes the principle value.

The refractive index $n(\omega)$, extinction coefficient $k(\omega)$, reflectivity $R(\omega)$, absorption coefficient $\alpha(\omega)$, and energy loss spectra $L(\omega)$, can be calculated by using the following equations [203, 205-207]:

$$\text{Refractive index, } n(\omega) = \left[\frac{\sqrt{\varepsilon_1^2+\varepsilon_2^2}+\varepsilon_1}{2}\right]^{1/2} \quad \ldots\ldots\ldots\ldots\ldots\ldots\ldots\ldots \quad (4.39)$$

Extinction coefficient, $k(\omega) = [\frac{\sqrt{\varepsilon_1^2+\varepsilon_2^2}-\varepsilon_1}{2}]^{1/2}$ …….. (4.40)

Reflectivity, $R(\omega) = \frac{(1-n)^2+k^2}{(1+n)^2+k^2}$ ……. (4.41)

Absorption coefficient, $\alpha(\omega) = 4\pi k/(ln10)$ ……..... (4.42)

Energy loss spectra, $L(\omega) = \frac{\varepsilon_2}{\varepsilon_1^2+\varepsilon_2^2}$ …….. (4.43)

Conductivity, $\sigma(\omega) = n(\omega) \times \alpha(\omega) \times c/4\pi$ ……. (4.44)

Where, c = velocity of light (i.e., $10^8 m/s$).

4.6 Molecular Dynamics

To determine the kinetics of various important chemical processes it is necessary to be able to evolve the dynamical motion of a system of atoms or molecules over an incremental time interval. A simple way to do this is utilizing a molecular dynamics (MD) simulation technique. In MD simulations, the forces on each atom are determined using density functional theory or classically with empirical potentials. If a force F_i acting on atom i, the motion will evolve with classical mechanics according to:

$$F_i = m_i \dot{v}_i \quad \& \quad v_i = \dot{r}_i \quad \text{…….. (4.45)}$$

And the forces required for solving the equations of motion are derived from the atomic potential energy field. Then the Newtonian equations of motion are solved to evolve the system of N atoms at each time step dt. This size of the time steps limits standard MD simulations to a total simulation time of microseconds when using empirical potentials and to femtoseconds or picoseconds when using DFT calculated forces.

There are different statistical ensembles i.e., NVE or NVT are used in MD simulation depending on the quantities of interest in the system. In NVE also known as microcanonical ensemble the number of particles N, the volume V, and

the total energy *E* are constrained [204]. In this ensemble the exchange between kinetic energy and potential energy of the atoms can be followed, however the total energy is constant.

The canonical ensemble known as NVT is more suitable in some scenarios as the temperature *T* may be constrained, but the pressure is allowed to vary. The NVT [204] is useful for replicating experimental scenarios where high temperatures may be required.

4.6.1 Canonical ensemble: NVT

In the canonical ensemble to maintain the correct temperature a thermostat needs to be applied to all or some of the atoms in the system [204]. This kind of simulation corresponds to the one in which a fragment of the whole system is attached to the rest of it (very large), which is treated as a heat bath at constant temperature *T*. Hence adding or removing energy from the boundaries of the system, when necessary, can be facilitated. During the simulation it is important to preserve the correct thermodynamics of the system and ensure that the dynamics is realistic. CM: The meaning of NVT should be given.

4.6.1.1 Nosé-Hoover thermostat

In the Nosé-Hoover thermostat the temperature *T* is controlled by the addition of an extra artificial degree of freedom, *s* to the equations of motion [208, 209]. This performs as a heat reservoir to exchange thermal energy with the system. The extra degree of freedom and the corresponding Hamiltonian are selected in such a way that the collective system might microcanonical; but, after the extra degree of freedom is integrated over, the system is exactly canonical. The Hamiltonian becomes as [204]

$$H_{Nose} = \sum_{i-1}^{N} \frac{\mathbf{p_i}}{2m_i s^2} + U(r^N) + \frac{p_s^2}{2Q} + nk_B T \ ln\ s \quad \text{.....(4.46)}$$

where Q is an effective mass related to the additional degree of freedom s and n is the number of degrees of freedom, $n = 3N + 1$. It then follows that the momentum p_s of s is equal to $Q\dot{s}$. In equation (3.46), the third and fourth terms are related to the "kinetic" and "potential" energy of the artificial degree of freedom, respectively. The choice the effective mass Q is important because it controls the coupling of the system to the reservoir. If Q is too large the coupling with the bath is decreased and the correct temperature will only be achieved after a long time. And if Q is too small the temperature will fluctuate significantly.

4.7 The first-principles' code VASP

Vienna *ab initio* simulation package (VASP) [204] is a package of computer programs was used for first principle DFT and MD simulation in this thesis. It has a flexibility of using either density functional theory or Hartree-Fock approximation while computing solutions of Schrödinger's equation. Further, hybrid functionals, Green's functions method and many-body perturbations theory are also available in VASP [204]. VASP uses plane wave basis set and interactions between electrons and ions are addressed using ultrasoft pseudo potentials (USPP) or projector augmented wave (PAW) method [66, 204].

VASP is accurate and efficient for relaxation and geometry optimization. VASP has few choices in controlling how the ions are updated and moved in the process of relaxation. A quasi-Newton (or variable metric) algorithm, which use forces and stress tensor to search directions to equilibrium positions, is faster but can lead to wrong results if the structure is approximate and far from the equilibrium. On the other hand, conjugate-gradient approximation is slower but is better choice for approximate structures which are far from the equilibrium.

The projector augmented wave (PAW) method [198] are used for all the calculations as supplied in the VASP distribution package in this thesis. For exchange correlation functional, a gradient correction as developed by Perdew,

Burke and Ernzerhof (PBE) [192] are used in this thesis. The exact computational details vary per system and will therefore be addressed in the respective chapters.

In general, VASP needs four basic input files named as INCAR, KPOINTS, POTCAR and POSCAR [204]. The POTCAR file contains the pseudopotential for each atomic species used in calculations. If there are two or more than two atomic species, then the pseudopotentials of atomic species are simply concatenated in POTCAR file. The order of the atomic species should be according to the POSCAR file. The POSCAR file consists of lattice vector and fractional coordinates of atomic positions of the system to be used in calculations. The KPOINTS file contains ***k***-mesh used in calculations. The INCAR file is very important file and determines what and how to calculate. It consists of relatively large number of parameters, and one always should be careful while assigning them. Most of the parameters have adequate default values so, in most cases, only a few of them need to be addressed in INCAR file. According to the purpose of any specific calculation and the corresponding tags in the INCAR file, certain output files are generated. Some of these are OUTCAR, OSZICAR, CONTCAR, CHGCAR, DOSCAR and XDATCAR [204]. The OUTCAR is the most important output file generated. It contains information of all the input files, positions of ions and the forces directed to them in each ionic relaxation step, eigenvalues of the system, the total ground state energies, and the information of the computing time it took to perform the calculation [204]. The information about the convergence speed and the current step are written to the OSZICAR file.

Chapter Five

Formation, stability, and properties of MgO and α-Al_2O_3

5.1 Introduction:

Magnesia (MgO) and α-Al_2O_3 have received a great deal of attention from both academia and industry due to their broad applications which have already been discussed in chapter one. MgO and α-Al_2O_3 form in Mg, Al metals, respectively in many Al (-Mg) alloys during melting and liquid metal handling in the casting processes [7, 22-24]. These newly-formed oxide particles have nontrivial influences on the mechanical performances of the cast parts. They may also act as nucleation sites during casting [22-24].

Chemically, both MgO and α-Al_2O_3 are ionic compounds corresponding to the large differences in the electronegativity values between the metals (1.31 for Mg and 1.61 for Al, in Pauling scale) and O (3.44) [210]. The structure and properties of a crystal is determined by the interaction of the valence electrons of the elements in the crystal. Therefore, the goal of the calculations done in this chapter is to provide a systematic procedure of first-principles density functional theory (DFT) investigation for MgO and α-Al_2O_3 and later be applied to study the θ- and γ-Al_2O_3 and Y_2O_3 as well.

Figure 5.1(a) represents the optimized rock salt type MgO crystal structure in a conventional unit cell (8 atoms). The structure consists of close packed O atoms filled by Mg atoms at the octahedral hole sites. The topological bond structure of MgO is shown in Figure 5.1 (b), where each Mg atom in MgO is bonded to six O atoms with equivalent bond distance (2.12 Å).

The crystal structure of ground-state phase α-Al_2O_3 belongs to the rhombohedral lattice with space group $R\bar{3}c$. Figure 4.1(d) shows schematically the α-Al_2O_3 structure (30 atoms) in a hexagonal lattice. The structure consists of six layers of close packed O atoms filled by Al atoms at the octahedral hole sites; the Al^{3+} cations and the O^{2-} anions are located at the 12*c* (z=0.3522) and 18*e* (x=0.3061) Wyckoff positions, respectively. The Al layer consists of 2 sublayers, the Al1 and the Al2 as labelled in Figure 5.1(d). The relaxed topological bond structure of α-Al_2O_3 is shown in Figure 5.1(c); where each Al atom in α-Al_2O_3 is bonded to six O atoms with two non-equivalent bond distances.

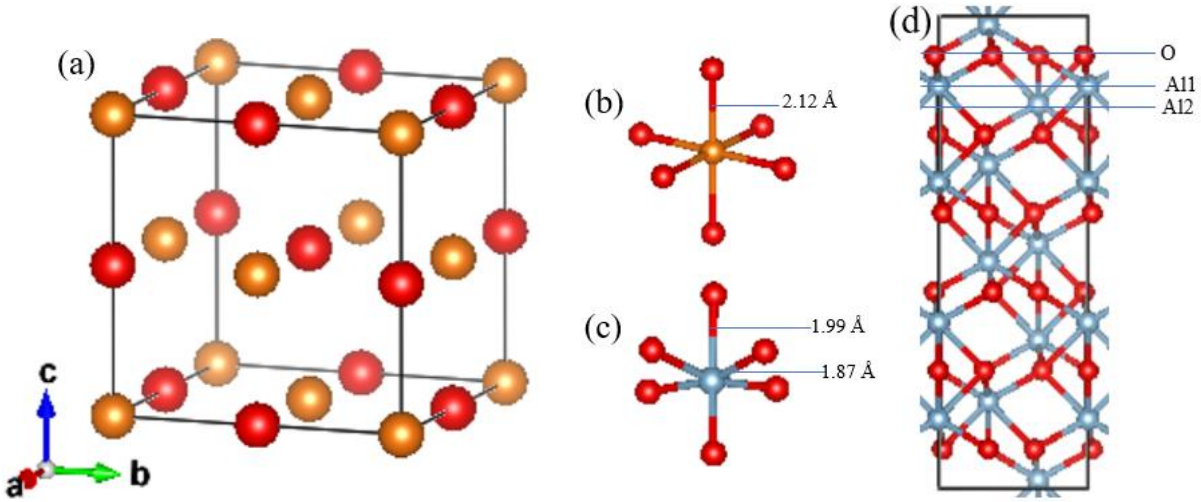

Figure 5.1: Schematic crystal structure of (a) fcc MgO unit cell, (b) and (c) the Mg-O and Al-O bonds, respectively, (d) hexagonal α-Al_2O_3 unit cell. The orange spheres represent Mg, the silvery Al and the red O. The labels Al1, Al2 in (d) represent the Al sublayers in the structure.

5.2 Methods:

5.2.1 Computational details

All the calculations were performed by first-principles density functional theory (DFT) with VASP code [204]. In electronic structures calculations of solids, the energy cut-off and the number of ***k***-points in the Brillouin zone are two important

parameters which have to be selected very carefully beyond the density functionals. Best practices in this field usually demand a convergence study of the quantity of interest with respect to these parameters prior to production runs. For this purpose, the cohesive energies and structural properties of the elemental solid Mg, Al and molecule O_2 were calculated as tests of reliability of our approach [Appendix: Table A.5.1]. The calculated results using LDA [190] and GGA-PBE [192] were compared with the experimental results.

The test calculations showed a good convergence is reached with the following settings: The cut-off energy for the wave functions (i.e., En_{cut}) is 500 eV and for the augmentation (i.e., En_{aug}) wave functions is 750 eV. The wave functions were sampled according to a Monkhorst-Pack scheme [211] with dense ***k***-meshes, e.g. 24×24×24, 22×22×22, 20×20×20 and 20×20×12 ***k***-meshes for hexagonally-close packed (hcp) Mg, fcc Al, fcc (conv) MgO, and hcp α-Al_2O_3 unit cell respectively in the irreducible Brillouin zone (BZ). Both the coordinates of atoms and the lattice parameters of the unit cells were fully relaxed. Tests for the ***k***-meshes and cut-off energies provided accuracy within 0.001 *eV*. In the case of applying *GW0* approach, the results are found to be particularly sensitive to the ***k***-point convergence and computationally expensive. Therefore, after the self-consistency convergence were achieved within 16×16×16 and 16×16×8 ***k***-points grid and a total of 192 and 416 bands are enough for fcc MgO and hcp α-Al_2O_3 structures respectively. All calculations are valid for a temperature of 0 *K* and a pressure of 0 *Pa*.

5.2.2 Formation energy:

The following chemical reactions are used as the basis for the calculation of the formation energies for magnesia and alumina:

$$Mg(s) + 1/2O_2(g) = MgO(s) \quad \ldots\ldots\ldots\ldots\ldots\ldots\ldots\ldots\ldots\ldots \quad (5.1)$$

$2Al(s) + 3/2O_2(g) = Al_2O_3(s)$ …… (5.2)

Therefore, with the help of the above equation (1) and (2) the following formulas were used to calculate the formation energy, E_F (eV/f.u.) for fcc MgO and hcp α-Al_2O_3:

$$E_F(MgO) = E_T(MgO) - \left[E_T(Mg) + \frac{1}{2}E_T(O_2)\right] \quad \ldots\ldots\ldots\ldots\ldots \quad (5.3)$$

$$E_F(Al_2O_3) = E_T(Al_2O_3) - [2E_T(Al) + \frac{3}{2}E_T(O_2)] \quad \ldots\ldots\ldots\ldots\ldots \quad (5.4)$$

Where, E_T is the total energy of the compound per formula unit.

In the present work Mg and Al were used as hcp and fcc solid, respectively and oxygen was used as O_2 molecule in a large simple cubic supercell of volume of 20×20×20 $Å^3$. Structural optimization produced a triples solution, and the O-O bond length is 1.222 Å. The results of total energy for hcp Mg is -1.804 eV/f.u. from the LDA and -1.501 eV/f.u. from the GGA-PBE approximations, for fcc Al is -4.018 eV/f.u. from the LDA and -3.756 eV/f.u. from the GGA-PBE approximations, respectively. The calculations in this work provide the triplet solution for an isolated O_2 molecule with a magnetic moment of two Bohr unit per molecule. The calculated results of total energy for O_2 molecule is -3.789 eV/f.u. from the LDA and -3.378 eV/f.u. from the GGA-PBE approximations.

5.3 Results and discussions:

5.3.1 Crystal chemistry of MgO and α-Al_2O_3

The calculated results include equilibrium lattice parameters, bond lengths, equilibrium volume, formation energies and bulk modulus obtained from the present work are listed and compared with other theoretical and experimental results in Table 5.1 for fcc MgO and hcp α-Al_2O_3.

Table 5.1: Comparison of calculated bulk properties (lattice parameters, formation energies, etc.) of fcc MgO and hcp α-Al_2O_3 with experiments and other DFT work.

fcc MgO Space group: *fm3m* (Nr 225)	LDA [This work]	GGA-PBE [This work]	DFT-HSE06 [73]	DFT-LDA [88]	Experiment [79]
Lattice parameter (Å)	4.115	4.216	4.19	4.183	4.21
Bond lengths of Mg-O (Å)	2.102	2.118	2.1	2.091	
Volume (Å^3/molecule)	17.38	18.73		18.3	
Formation energy, E_F (eV/f.u.)	-6.74	-6.10			
Bulk Modulus (*GPa*)		166.2		179.0	162.0
hcp α-Al_2O_3 Space group: *R3c* (Nr 167)	LDA [This work]	GGA-PBE [This work]	DFT-GGA, FPLAPW[a], EVA[b] [108]	DFT-GGA-PBE-HF[c] [109]	High pressure experiment [98, 214]
Lattice parameter (Å)	a=4.735, c=12.903	a=4.804, c=13.107	a=4.759, c=12.992	a=4.806, c=13.113	a=4.760, c=12.996 [98]
Bond lengths of Al-O (Å)	1.856-1.956	1.872-1.990		1.873-1.990	
Volume (Å^3/molecule)	41.756	43.445	43.8		
Formation energy, E_F (eV/f.u.)	-41.554	-37.762			
Bulk Modulus (*GPa*)		250.5	243.4		239.0 [214]

[a]Full Potential Linear Augmented Plane Waves.
[b]EVA: Engle-Vosco approximation.
[c]HF: Hybrid Functional.

From Table 5.1, the calculated lattice parameters in this work for fcc MgO is 4.115 Å and 4.216 Å from the LDA and GGA-PBE respectively. The GGA-PBE results shows closer to experimental results (within ±1%) [79] (Table 5.1). The Mg-O bond lengths are 2.102 Å and 2.118 Å from our calculated LDA and GGA-PBE results respectively. The GGA-PBE result of bond length is close to other DFT work (within 1%) [73, 88]. The calculated formation energy (E_F) from GGA-PBE is -6.10 eV/f.u. which is smaller than the LDA result i.e., -6.74 eV/f.u.

and is close to the other first principle DFT results i.e., -6.18 (eV/f.u.) and -6.30 (eV/f.u.) (within 5%) [211, 212].

For hcp α-Al_2O_3 from Table 5.1, the calculations produced the lattice parameters, a_0=4.804 Å, c_0=13.107 Å by GGA-PBE, which are close to experimental [98] and the other first principle DFT results [99, 108-110, 139, 215]. The Al-O bond lengths are in the range of 1.872-1.990 Å by our GGA-PBE calculations, which are close to the GGA-PBE (HF) result of Z. Zhang *et. al* work (1.873-1.990 Å) [109]. The calculated formation energy (E_F) off α-Al_2O_3 is -37.762 eV/f.u. for the GGA-PBE which is smaller than that from the LDA (-41.554 eV/f.u.). Such difference is not unusual in standard DFT calculation [140].

The bulk modulus was calculated using the Birch-Murnaghan Equation of States (EOS) from the energy vs volume curve [Appendix: Figure A.5.1 and A.5.2]. The calculated bulk modulus for fcc MgO from GGA-PBE is 166.2 *GPa*, which is overestimated (within 2%) from experimental results 162.2 *GPa* at 23^0C [79] and 163.93 *GPa* at 300 *K* [78] but lower from other DFT results [81-83, 87]. For hcp α-Al_2O_3 calculated bulk modulus by GGA-PBE from the present work is 250.5 *GPa*, which is overestimated (within 4%) from the high-pressure experiment measurement [214], and from DFT-GGA within FPLAPW-EVA^b method [108].

5.3.2 Electronic Properties by GGA-PBE

The electronic structure calculations are performed for fcc MgO and hcp α-Al_2O_3 using GGA-PBE approach. Analysis of the electronic density of states (DOS) curve is useful to specify the electronic properties of matter. The calculated total density of states (TDOS) and partial density of states (PDOS) for fcc MgO and hcp α-Al_2O_3 are shown in Figure 5.2.

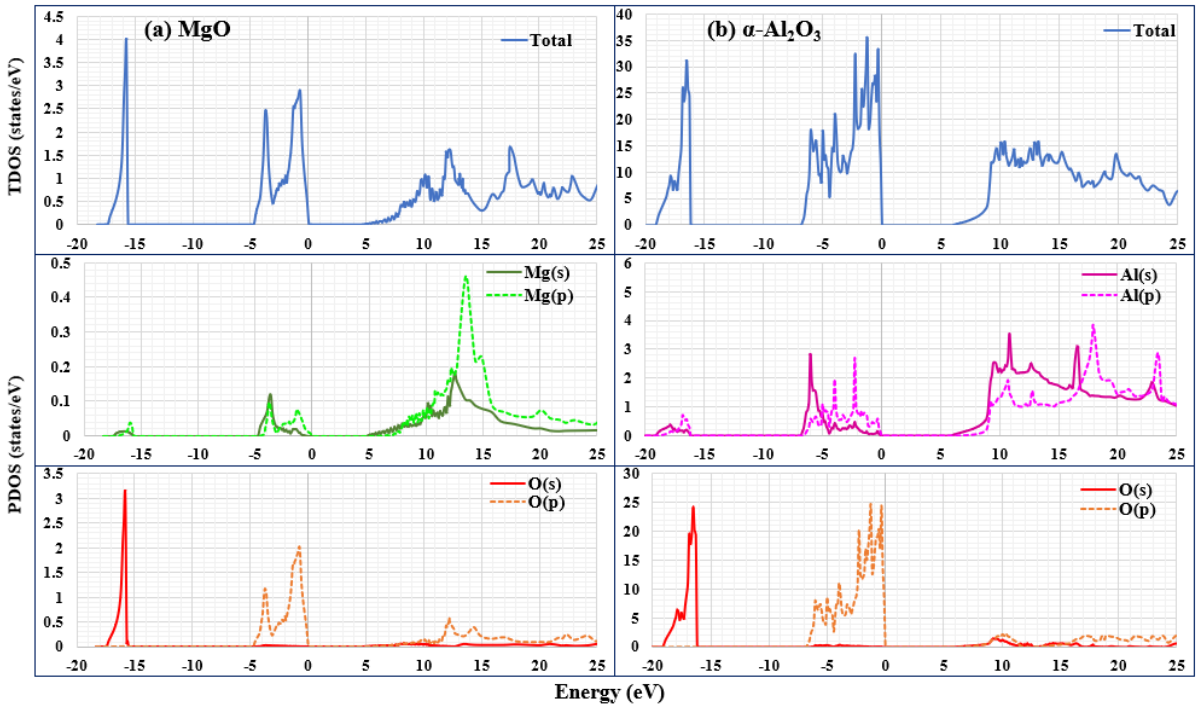

Figure 5.2: The total (TDOS) and partial (PDOS) density of states of (a) MgO and (b) α-Al_2O_3 from GGA-PBE calculations.

From partial DOS (PDOS) of Mg and O for fcc MgO in Figure 5.2 (a), it can be clearly seen that there are enormous differences between the PDOS of Mg and O. For Mg, the main differences are in the CB (conduction band), whereas for O, the differences are mostly in the VB (valence band) region. The PDOS for the O can be clearly divided into two segments, the upper *2p* band (0 to −5.0 eV) and the lower *2s* band (−15.8 to −17.4 eV). The top of the VB is derived mostly from the *2p* states of O atom/ion. The O *2p* and O *2s* states are 1.8 eV and 4.8 eV wide respectively which are close to DFT-GGA(PBE) results (1.54 and 4.51) [216]. The intervalence band gap (i.e., O *2s* - O *2p*) is 17.4 eV which is close from Electron momentum spectroscopy result 17.6 eV and DFT-GGA(PBE) calculated result 17.10 eV [216]. The peak in the lower valence band (LVB) is situated between −17.4 and −15.8 eV from the top of the valence band [Figure 5.2 (a)].

For α-Al_2O_3 [Figure 5.2(b)], the calculated width of the lower-valence-band (LVB) is 3.16 eV which are mostly from *2s* states of O atoms. The LVB has two peaks located between −19.16 and −16.00 eV from the top of the valence band.

The width of the upper valence band (UVB) is 6.9 eV and are mostly from *2p* states of O atoms [Figure 5.2(b)]. There is small amounts of Al (*3s* and *3p*) states are also observed in valence band regions [Figure 5.2(b)]. In the upper valence band (UVB) region there are many peaks [Figure 5.2 (b)], which are the sources of electrons that can make transitions to the conduction band. The width between the UVB and LVB is about 9.0 eV from GGA-PBE calculations. The conduction band presents contributions mainly from Al (*3s* and *3p*) states with some contribution from O atoms as well. The calculations indicate ionic nature of this compound as the valence bands are dominated by O *2p* and the lower part of conduction band by Al characters.

Table 5.2: The comparison of band widths and band gaps (eV) from GGA-PBE calculated results of fcc MgO and hcp α-Al_2O_3 with the previous theoretical and experimental data.

	Upper VB width (O *2p*) (eV)	Lower VB width (O *2s*) (eV)	Differences (O *2s* - O *2p*) (eV)	Band gap (eV)
fcc MgO				
This work, DFT-GGA(PBE)	4.8	1.8	17.4	4.9
Ultraviolet Spectroscopy [80]				7.7
Reflection Electron Energy Loss Spectroscopy [82]				7.8
Electron momentum spectroscopy [216]	3.3	1.1	17.6	
Spectrophotometer [217]				7.5
DFT-GGA(USPP[d]) [86]				4.5
DFT-GGA(PAW) [87]				4.8
DFT-GGA(PBE) [216]	4.51	1.54	17.10	
hcp α-Al_2O_3				
This work, DFT-GGA(PBE)	6.9	3.16	9.0	6.3
X-ray photoelectron spectroscopy [125]				9.57
Vacuum ultraviolet spectroscopy [206]		6.0		8.8
DFT-LDA-FPLMTO[e] [107]	7.2	3.0	8.8	6.6
DFT-FPLAPW-EVA [108]	6.53	3.1	9.71	7.2

[d]USPP: Ultrasoft Pseudopotentials.
[e]FPLMPO: full potential linear muffin-tin-orbital.

The calculated bandgap for fcc MgO from our DFT-GGA(PBE) between UVB and conduction band is 4.9 eV, which is close to 4.5 eV from other DFT-GGA(USPP) calculation [86]. But the band gap from our DFT-GGA(PBE) calculations is within 30% smaller than experimental results [80, 217]. For hcp α-Al_2O_3 our calculated band gap is 6.30 eV from GGA-PBE calculation. This value is close to 6.60 eV for DFT (LDA+FPLMTO) work done by R. Ahuja *et al* [107] and 6.24 eV for DFT (LDA+OLCAO) done by S -D Mo *et al* [105], whereas the experimental gap is 9.57 eV from XPS (X-ray photoelectron spectroscopy) data of B Ealet *et al* work [125] and 8.8 eV from vacuum ultraviolet spectroscopy measurement from R. H. French *et al* work [206]. In case of our electronic band gap calculations for MgO and α-Al_2O_3, there is large differences between our DFT-GGA(PBE) calculated results with experimental results from literature. This discrepancy arises, because of the inability of DFT to describe excited states [73, 85, 87]. The experimental measurements of the electronic properties, such as band gaps, are related to excitations of electrons [85, 87]. To describe such excitations another scheme needs to be used, such as the *GW* approximation (whereby the self-energy is obtained from the Green's functional *G* and the electronic screening effect *W*) which describes well the eigenstates of one-electron quasiparticle (QP) levels and relates to electronic excitations [204].

5.3.3 Accurate calculation of band gap by *GW0* correction

To improve calculations for the electronic properties of fcc MgO and hcp α-Al_2O_3 the self-consistence *GW*0 correction, a beyond-DFT approach was applied in this work. The calculations show that the *GW*0 correction has improved the K-S energy gap from DFT-GGA(PBE) significantly and about 3 iterations are enough to reach convergence [Appendix: Figure A.5.3 (a) and (b)]. The Fermi level was set at 0 *eV*.

Table 5.3: The comparison of widths and band gaps (eV) of fcc MgO and hcp α-Al_2O_3 by DFT-GGA(PBE) and *GW0* potential from our calculation with the previous experimental data.

	Upper VB (O *2p*) width (eV)	Lower VB (O *2s*) width (eV)	Differences (O *2s*-O *2p*) (eV)	Band gap (eV)
fcc MgO				
This work, DFT-GGA(PBE)	4.8	1.8	17.2	4.9
This work, *GW0*	5.1	2.0	17.8	7.3
Spectrophotometer [217]				7.5
hcp α-Al_2O_3				
This work, DFT-GGA(PBE)	7.0	3.0	9.0	6.3
This work, *GW0*	8.5	4.0	10.7	9.8
X-ray photoelectron spectroscopy [125]				9.57
Vacuum ultraviolet spectroscopy [206]				8.8

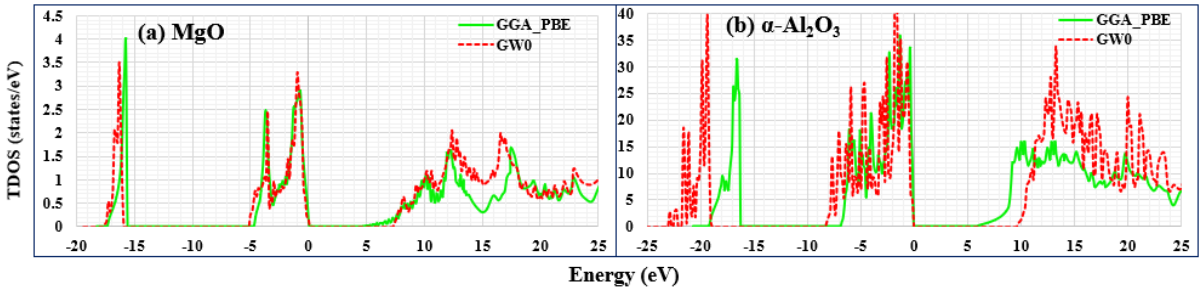

Figure 5.3: Calculated total density of states (TDOS) of (a) MgO and (b) α-Al_2O_3 using both GGA(PBE) and *GW0* functionals.

When the *GW0* approach was applied to fcc MgO and hcp α-Al_2O_3 structure [Figure 5.3 (a) and (b)] all states in the conduction band are shifted toward higher energy, which causes increasing in the band gap. The calculated band gap for fcc MgO by the *GW0* correction is 7.3 eV which is in very good agreement (within 2% smaller) with experimental one 7.5 eV measured from spectrophotometer [217]. Also, for α-Al_2O_3 the calculated band gap by the *GW*0 approach is 9.8 eV which is close to the experimental value 9.57 eV observed from X-ray photoelectron spectroscopy by B. Ealet *et. al* work [125].

5.3.4 Optical properties

The study of the optical properties of oxides with different photon energies is crucial for a better understanding of the electronic structure of that compound. Therefore, the optical properties of MgO and α-Al_2O_3 have been calculated by both GGA-PBE and sc *GW0* approach and the obtained results are compared with available experimental data in the literature. The optical functions of both oxides including real $\varepsilon_1(\omega)$ and imaginary $\varepsilon_2(\omega)$ part of dielectric constants, refractive index $n(\omega)$, extinction coefficient $k(\omega)$, reflectivity $R(\omega)$, absorption coefficient $\alpha(\omega)$, energy loss functions $L(\omega)$ and conductivity $\sigma(\omega)$ are calculated for the photon energies by using equation (4.39)-(4.44) which are described in the methodology part (i.e., Chapter Four). The calculated optical properties for MgO and α-Al_2O_3 are plotted in Figure 5.4 and Figure 5.5 respectively.

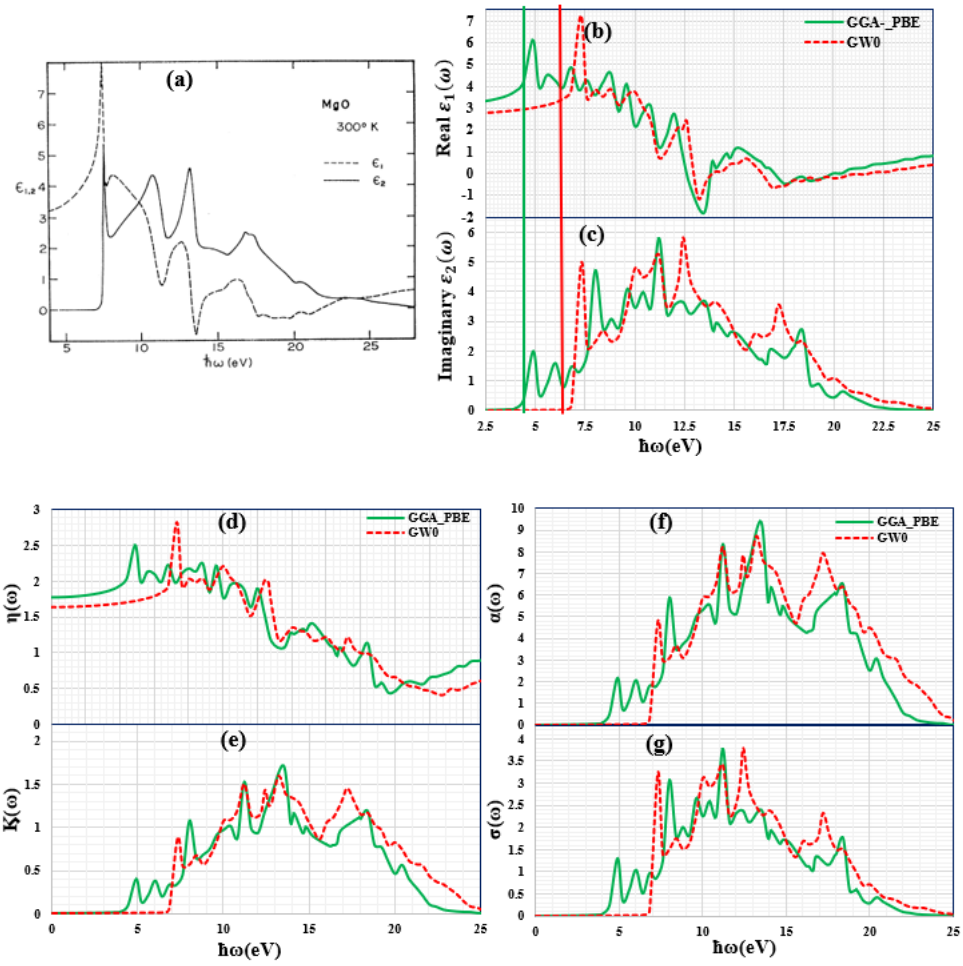

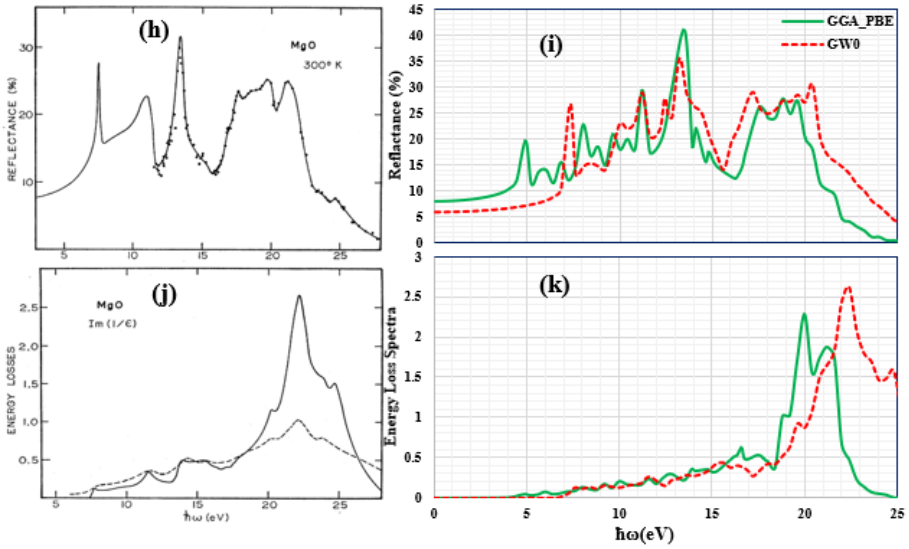

Figure 5.4: The optical functions of MgO i.e., dielectric constants of real part $\varepsilon_1(\omega)$ and imaginary part $\varepsilon_2(\omega)$ from (a) experiment [213], (b) and (c) this theoretical work, (d) refractive index $n(\omega)$, (e) extinction coefficient $k(\omega)$, (f) absorption coefficient $\alpha(\omega)$, (g) conductivity $\sigma(\omega)$, reflectance from (h) experiment [213] and (i) this theoretical work, energy loss spectra from (j) experiment [213] and (k) this theoretical work respectively. The direct band gap at 4.9 (7.26) eV for GGA_PBE (*GW0*) is marked by a vertical green (red) line in Figure 5.4 (a) and (b).

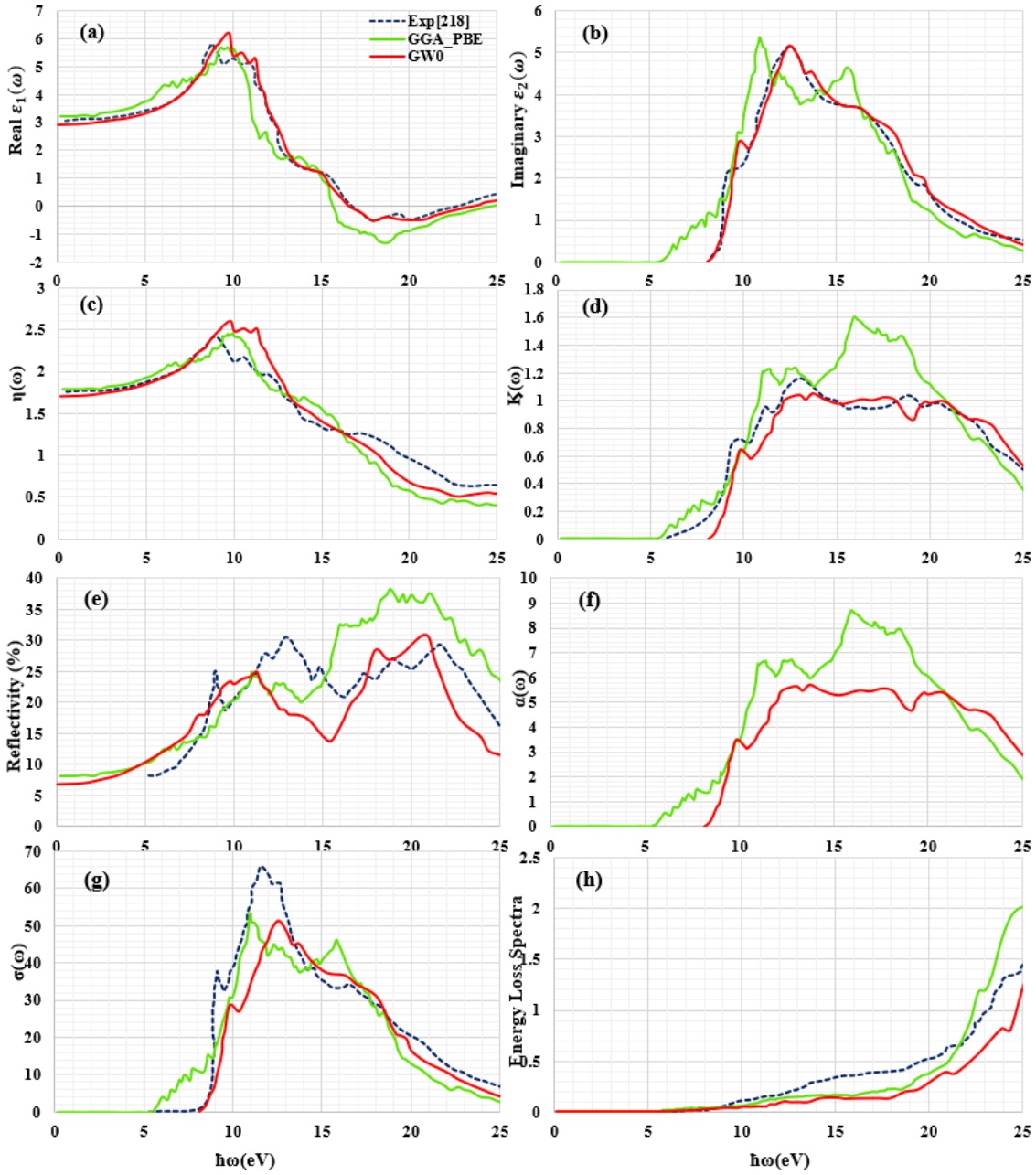

Figure 5.5: The optical functions of α-Al_2O_3 structure from experimental work [218, 219] and the present GGA_PBE and GW0 calculations: Dielectric constants of (a) real part $\varepsilon_1(\omega)$, (b) imaginary part $\varepsilon_2(\omega)$, (c) refractive index $n(\omega)$, (d) extinction coefficient $k(\omega)$, (e) reflectivity $R(\omega)$, (f) absorption coefficient $\alpha(\omega)$, (g) conductivity $\sigma(\omega)$ and (h) energy loss spectra $L(\omega)$.

The real part of the dielectric function $\varepsilon_1(\omega)$ gives information about the electronic polarizability of material. The static dielectric function is inversely dependent on the band gap values. The static dielectric constant $\varepsilon_1(0)$ under

GGA(PBE) and *GW0* for fcc MgO and hcp α-Al_2O_3 are given in Table 5.4, and for comparison with the experimental results, $\varepsilon_1(\omega)$ is also estimated at 5 eV corresponding energy. The interesting feature of the $\varepsilon_2(\omega)$ curve is its first critical point, also known as optical absorption edge. Figure 5.4 and 5.5 reveal that the optical absorption edge is found at 4.9 eV (GGA-PBE), 7.26 eV (*GW0*) for MgO and 6.3 eV (GGA_PBE), 9.8 eV (*GW0*) for α-Al_2O_3 respectively. The higher peaks spectrum of absorption edge from $\varepsilon_2(\omega)$ curves are observed in between 5.0-18.4 eV (GGA_PBE), 7.5-20.8 eV (*GW0*) for fcc MgO and 8.0-16.0 eV (GGA_PBE), 9.8-20.0 eV (*GW0*) for hcp α-Al_2O_3 respectively. From imaginary spectra, the peak positions of the distinct features and plasmonic resonance for MgO at 12.5 eV from *GW0* calculation which is close to 13.4 eV, M. L. Bortz *et al* experimental work [217]. For hcp α-Al_2O_3 the sharp peak observed from imaginary spectra at 12.5 eV from *GW0* calculation coincide with W. Tews et al experimental work [218]. For both oxides, *GW0* produced spectra shows higher absorption in UV (ultra-violet) energy region compares to GGA-PBE.

Table 5.4: The important optical parameters for MgO and α-Al_2O_3 compared with the previous theoretical and experimental results.

Parameter	fcc MgO			hcp α-Al_2O_3		
	GGA(PBE)	*GW0*	Reference	GGA(PBE)	*GW0*	Reference
$\varepsilon_1(0)$	3.00	2.80	3.20 (Exp) [213] 2.84 (DFT-GGA) [256]	3.10	2.96	3.00 (Exp) [218] 3.20 (DFT) [107]
$\varepsilon_1(5)$	4.00	3.10	-	3.80	3.30	3.30 (Exp) [218]
$R(0)$	0.08	0.06	0.08 (Exp) [213]	0.08	0.07	0.07 (Exp) [219]
$R(5)$	0.20	0.08	0.09 (Exp) [213]	0.10	0.10	0.09 (Exp) [219]
$n(0)$	1.80	1.65	1.68 (DFT-GGA) [256]	1.80	1.70	1.75 (Exp) [218] 1.79 (DFT) [107]
$n(5)$	1.90	1.70	-	1.90	1.86	1.86 (Exp) [218]

From Figure 5.5, for hcp α-Al_2O_3, there are more weak peaks are observed from *GW0* corrections for imaginary part $\varepsilon_2(\omega)$ at around 18.00-20.00 eV region which are also observed at 17.00 eV-19.00 eV from GGA-PBE calculation. These weak peaks are also observed from experimental data from E. T. Arakawa *et al*

work, and they described these peaks are due to interband transitions from Al *3p* to Al *3s* states [207].

The refractive index of an optical medium is a dimensionless number to describe how light or any other radiation propagates through the medium. The static refractive indices for MgO are 1.80 and 1.65 from GGA-PBE and *GW0* respectively. From Figure 5.4 and 5.5, it is noticed that the refractive indices of both magnesia and aluminum oxides show higher in the UV (5.00-20.00 eV) region and then gradually tend to decrease. The calculated values of the ordinary refractive index $n(0)$ for the α-Al_2O_3 is 1.70 from *GW0* calculations, which is comparable to the experimental value (1.75) from W. Tews *et al* [218].

The extinction coefficient $k(\omega)$ is also calculated under GGA-PBE and *GW0* considerations. This is evidence that the overall behavior of $k(\omega)$ is close to that of the imaginary part of the dielectric functions $\varepsilon_2(\omega)$ [Figure 5.4 and 5.5]. The extinction coefficient $k(\omega)$ shows higher energy peak around 5.0-20.0 eV and 9.0-25.0 eV energy region for MgO and α-Al_2O_3 [Figure 5.4 and 5.5] respectively from *GW0* correction. This indicates practically negligible loss of energy of electro-magnetic (EM) wave within this energy range while passing through the fcc MgO and hcp α-Al_2O_3.

From the reflectivity spectra [Figure 5.4 and 5.5] as a function of incident light energy, there few sharp peaks in between the photon energy range 5.0-22.0 eV for fcc MgO from both GGA(PBE) and *GW0* calculations, which are close to D. M. Roessler *et al* experimental work [213]. For α-Al_2O_3 from both GGA(PBE) and *GW0* calculation most of the higher peaks are observed from 9.0 eV-22.0 eV region which can be related to the excitonic peak, also close to M. L. Bortz *et al* experimental work [219]. In addition to this, for hcp α-Al_2O_3, the experimental spectrum from M. L. Bortz *et al* [219] spectrophotometer experimental work shows features at 9.0, 12.0, 13.0, 14.9, 17.4, 19.0 and 21.8 eV, which are in good

agreements with those from our *GW0* calculations 9.5, 11.5, 12.9, 18.0 and 21.0 eV respectively. Also, in Figure 5.4 and 5.5, there are a sharp peak at 21.0 eV and 20.8 eV region for MgO and α-Al_2O_3 respectively from *GW0* approach and after that the reflectance spectrum falls off rapidly because of the exhaustion of the upper valence-to-conduction band transition.

The absorption coefficient spectrum, $\alpha(\omega)$ provides important information about optimum solar energy conversion efficiency and it indicates how far light energy (wavelength) can penetrate the material before being absorbed [205]. From Figure 5.4 (f), fcc MgO has largest peaks at 8.0-18.4 eV and 6.9-20.0 eV region from GGA-PBE and *GW0* calculation respectively besides having shoulder at lower energy. From the absorption spectra of α-Al_2O_3 in Figure 5.5 (f) the consecutive peaks are observed between 11.0-18.5 eV and 10.0-23.3 eV region from the GGA-PBE and *GW0* calculation respectively. Clearly the *GW0* produced spectra shows higher absorption in UV (ultra-violet) energy region for both oxides compare to the GGA-PBE.

In case of conductivity spectrum from Figure 5.4 (g), the observed optical photoconductivity spectra have several maxima and minima from *GW0* calculation within 7.3-17.2 eV energy range whereas the GGA-PBE produced shows less peaks for fcc MgO. From the Figure 5.5 (g), the prominent peaks are at 10.0-17.5 eV energy ranges from *GW0* calculation hcp α-Al_2O_3 which is close to experimental observation 9.2-16.9 eV [219].

The electron energy loss function of materials is a key optical parameter to describe the energy loss of a fast electron passing through a material is usually large at the plasma frequency [205]. From Figure 5.4 (k), the prominent peak for fcc MgO at 20.0 eV from GGA-PBE which is increased to 22.4 eV from *GW0* calculation and close to experimental value 22.2 eV [213]. And there are some weak peaks are also observed which indicates rapid reduction in the reflectance.

The prominent peaks started for hcp α-Al_2O_3 phase after 20.0 eV [Figure 5.5 (h)] from GW0 calculation which is close to experimental spectrophotometer measurement [218]. Therefore, the calculated plasmon energy from *GW0* calculation shows close to experimental value for both oxides.

5.4 Conclusion

In this chapter the systematic bulk, electronic and optical properties for fcc MgO and hcp α-Al_2O_3 are calculated from first-principles DFT calculation within GGA_PBE approximation. The resulting equilibrium bulk properties (i.e., lattice parameters, volume, bulk modulus, formation, etc.) obtained from GGA-PBE are consistent with the available experimental and theoretical results from literature indicating the accuracy and reliability of the modeling elements used in this study.

The electronic and optical properties have been studied by GGA(PBE) and state-of-art *GW0* correction. Overall, the self-consistent *GW0* corrections described well the electronic and optical properties for both oxides that the obtained results are in excellent agreement with experimental observations.

Chapter Six

Crystal chemistry and physical properties θ- and γ-Al_2O_3

6.1 Introduction

θ- and γ-Al_2O_3 have been extensively used in protective coatings and many catalysis applications [92-95]. Recent experimental observations revealed that γ-Al_2O_3 can be used as potential nucleation sites in solidification of Al-based metals and alloys [22, 91, 133]. In the case of the stable ground state α-phase there are experimental results available, while such are absent for θ- and γ-Al_2O_3. Specially in case of metastable γ-Al_2O_3 there is still controversy about its crystal structure [28, 105, 107, 114, 119-147].

In this chapter the structural, electronic and optical properties of θ- and γ-Al_2O_3 will be investigated using the first-principles density function theory (DFT) within the GGA_PBE approximation. In previous chapter (chapter Five) the results for the electronic and optical properties of fcc MgO and hcp α-Al_2O_3 have been successfully enhanced by the *GW0* correction over DFT. Therefore, for θ- and γ-alumina phases we present the electronic and optical properties by DFT(GGA-PBE) with the state-of-art *GW0* correction. The obtained results for optical properties of alumina phases from this study will help experimentalists for various potential optoelectronic applications such as solar energy devices, semiconductor parts etc.

6.2 Methods

6.2.1 Computational details:

All the calculations were performed in this chapter using the first-principles DFT within GGA-PBE [192] approximations. The obtained results are compared with

the experimental results. According to our test calculations, the plane wave pseudopotential with energy cut-offs, En_{cut}= 500 eV and En_{aug} = 750 eV was applied. Convergence of the geometry optimization was considered when the difference of total energies between the last iterations did not exceed 1.0×10^{-4} eV and the forces on each ion was $1.0x10^{-3}$ eV/Å. The electronic wave function was sampled on 12×12×8 with 350 and 8×8×6 with 114 $\boldsymbol{k}$-mesh for θ-Al_2O_3 and γ-Al_2O_3 in the irreducible Brillouin zone (BZ), respectively generated by the Monkhorst-Pack algorithm [211] [Figure A.6.1]. In case of *GW0* approach, the self-consistency convergences were achieved within 8×8×4 k-meshes for both monoclinic θ- and hexagonal γ-alumina phases to balance the accuracy of the results and the computational capability. Numbers of 400 and 468 bands are enough for monoclinic θ-Al_2O_3 and hexagonal γ-Al_2O_3 structures respectively. All calculations are valid for a temperature of 0 K and a pressure of 0 Pa.

6.2.2 Formation energy calculation:

The following chemical reactions are used as the basis for the calculation of the formation energies for θ- and γ-alumina phases:

$2Al(s) + 3/2\ O_2(g) = Al_2O_3(s)$ …… (6.1)

Therefore, with the help of the above equation (6.1) the following formula was used to calculate the formation energy, E_F (eV/f.u.) for θ- and γ-Al_2O_3:

$$E_F(Al_2O_3) = E_T(Al_2O_3) - [2E_T(Al) + (3/2)E_T(O_2)] \text{ ……..} \quad (6.2)$$

Where, E_T is the total energy of the compound per formula unit.

The total energy for fcc Al is -3.756 eV/f.u., for an isolated O_2 molecule is -3.378 eV/f.u. for its triplet solution from GGA-PBE calculations. These energies are as references used to calculate the formation energy of alumina.

To compare the stability of different alumina phases in this work, the energy differences were calculated between the stable α-Al_2O_3 and metastable θ-, γ-Al_2O_3 using the following formula:

$$\Delta E = [E_T(\square\text{-}Al_2O_3) - E_T(\alpha\text{-}Al_2O_3)] \text{ eV/f.u.} \quad \ldots\ldots\ldots\ldots\ldots\ldots (6.3)$$

Where, E_T refers to the total ground state energy per formula unit for the α-, θ- and γ-Al_2O_3 compounds, □ denotes for θ and γ.

6.3 Results and discussions

6.3.1 Crystal structural properties

6.3.1.1 θ-Al_2O_3

The θ-Al_2O_3 has a monoclinic lattice with space group *C2/m*. All the ions located at 4i (x, 0, z) Wyckoff sites. Figure 6.1 (a) shows schematically the θ-Al_2O_3 unit cell which contains 20 atoms. The Al atoms occupy four octahedral and four tetrahedral interstitials sites [Figure 6.1 (b) and (c)]. θ-Al_2O_3 has three different types of O coordination [Table 6.1].

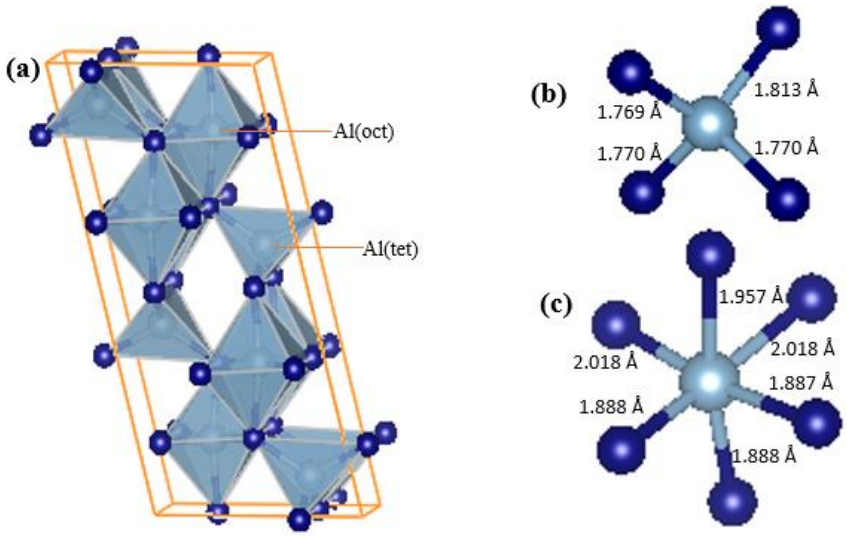

Figure 6.1: Schematic structure of lattice topology and polyhedra of the (a) monoclinic θ-Al_2O_3, where Al_{tet} and Al_{oct} bonded with four and six O anions respectively. The surrounding bond arrangements and the bond lengths are shown

for (b) Al_{tet} and (c) Al_{oct}. The silvery spheres represent Al and dark blue O atom/ion.

The calculated coordinates of Al and O atoms are listed in Table 6.1. The calculated values agree well with those by E. Husson *et. al* for Al: Al_{tet} (0.101 0 0.794) and Al_{oct}(0.352 0 0.687) and those for O: O_1 (0.163 0 0.123), O_2 (0.489 0 0.261), O_3 (0.830 0 0.439) [115].

Table 6.1: Crystallographic data for computed monoclinic θ-Al_2O_3 structure by GGA-PBE

θ-Al_2O_3: Monoclinic Space group: *C2/m* Atom	Wyckoff notation	x	y	z
Al_{tet}	4i	0.0903	0.0000	0.7958
Al_{oct}	4i	0.3422	0.0000	0.6829
O_1	4i	0.1606	0.0000	0.1092
O_2	4i	0.4948	0.0000	0.2570
O_3	4i	0.8266	0.0000	0.4331
Bond lengths (Å): Al_{tet}-O: 1.768-1.813 Al_{oct}-O: 1.888-2.018				

Table 6.2: Comparison of calculated bulk properties of θ-Al_2O_3 crystals with experiments and other DFT work

Monoclinic θ-Al_2O_3	Lattice parameter (Å) And angles (^{0})	Bond lengths of Al-O (Å)	ΔE(θ-α) (eV/f.u.)	Bulk Modulus (*GPa*)
This work, GGA-PBE	*a*=11.905 Å, *b*=2.938 Å, *c*=5.667 Å *β*=104.012^0	Al_{tet}: 1.768-1.813 Al_{oct}: 1.888-2.018	0.043	185.5
References-Experiment				
XRD [114]	*a*=11.854 Å, *b*=2.904 Å, *c*=5.622 Å *β*=103.830^0	Al_{tet}: 1.710-1.811 Al_{oct}: 1.896-2.025		
TEM, XRD [126]	*a*=11.790 Å, *b*=2.91 Å, *c*=5.620 Å *β*=103.800^0			
References-Theoretical				
DFT-GGA-PW91 [90]	*a*=11.853 Å, *b*=2.923 Å, *c*=5.631 Å *β*=104.034^0		0.030	
DFT-GGA-PBE (HF) [109]	*a*=11.922 Å, *b*=2.940 Å, *c*=5.668 Å *β*=104.000^0	Al_{tet}: 1.770-1.813 Al_{oct}: 1.888-2.021	0.047	
DFT-LDA [136]	*a*=11.860 Å, *b*=2.929 Å, *c*=5.657 Å *β*=104.000^0		0.040	

From Table 6.2, the calculations produced the lattice parameters, a=11.905 Å, b=2.938 Å, c=5.667 Å and β=104.012^0 by GGA-PBE, which are close to experimental [114, 126] and the other first principle DFT results [90, 109, 136]. The Al-O bond lengths are in the range of Al_{tet}-O: 1.768-1.813 Å and Al_{oct}-O: 1.888-2.018 Å from the GGA-PBE calculation, which are also close to the GGA-PBE (HF) result of Z. Zhang *et al* DFT within Hartree-Fock (HF) work [109]. The calculated bulk modulus in this work is 185.5 *GPa* by GGA-PBE calculation using Birch-Murnaghan EOS [Figure A.6.2].

The energy difference per formula unit between α-Al_2O_3 and θ-Al_2O_3 is 0.043 eV/f.u. from GGA-PBE calculation [Table 6.2], which is consistent with results from previous reports at Z. Zhang *et al* (0.047 eV/f.u.) [109] and C. Wolverton *et al* (0.04 eV/f.u.) [136].

6.3.1.2 γ-Al_2O_3

6.3.1.2.1 Structural model of γ-Al_2O_3

Here four different existing spinel models [122, 138, 140, 144] and one non-spinel model [145] for γ-Al_2O_3 are revisited. The dependence of total energy on the cation (Al) vacancies positions is examined. This study also includes the local structure contribution including cation (Al), anion (O) distributions to the total energetics and the charge distribution using Bader charge approach [220-222] in the spinel γ-Al_2O_3 structure.

Model-1 was built based on the primitive unit cell of γ-Al_2O_3 which is rhombohedral [138]. The lattice vectors are $a_p = a_0$ (0, 1/2, 1/2), $b_p = a_0$ (1/2, 0, 1/2) and $c_p = a_0$ (1/2, 1/2, 0) are used, where a_0=7.938 Å [122] is the lattice parameter of the cubic γ-Al_2O_3 phase [see Figure A.6.3]. The primitive unit cell then tripled c-axis to get the supercell with 40 atoms and 2 vacancies [Figure 6.2 (a)]. This model followed from the work by G. Gutiérrez *et al* [138]. The small

size of the cell may affect the chemical composition of cation, anion and vacancy distribution.

Therefore, Model-2 was prepared with a $1a_0 \times 1a_0 \times 3a_0$ supercell followed from L. Smročk *et al* [122] cubic unit cell. This supercell contains 160 atoms. It was built up by stacking three fcc $MgAl_2O_4$ cells into *z*-direction, replacing all the Mg with Al and finally extracting 8 Al atoms (i.e., vacancies) to maintain stoichiometry [Figure A.6.4]. Meanwhile, the distribution of cation (Al) at the interstitial sites requires investigations [Figure 6.2 (b)]. This Al distribution is related to several factors, including distances between Al vacancies, occupations at the tetrahedral and octahedral sites, the repulsive Coulomb interaction between vacancies, etc.

The γ-Al_2O_3 structure in a hexagonal unit cell was also prepared and named Model-3 [Figure 6.2 (c)]. The hexagonal lattice vectors are $a_h = a_0$ (-1/2, 1/2, 0), $b_h = a_0$ (0, -1/2, 1/2) and $c_h = a_0$ (1, 1, 1), here a_0 =7.938 Å is the lattice parameter of the cubic γ-Al_2O_3 phase [see Figure A.6.5]. This hexagonal unit cell contains six layers of close-packed O layers with Al atoms positioned at the tetrahedral and octahedral interstitial sites. This model contains 40 atoms with 2 vacancies. The relatively small cell might cause strong interaction between the vacancies. To avoid that issue, another Model-4 was prepared, with a hexagonal $2a_h \times 2a_h \times 1c_h$ supercell that contains 160 atoms with 8 vacancies [Figure 6.2 (d)].

In the models (1 to 4) the introduction of Al vacancies breaks the symmetry of the lattices. All the built models have the space group P1 as shown in Table 6.3.

One non-spinel γ-Al_2O_3 structure was also prepared based on a monoclinic unit cell as used by Digne *et al* [145]. The non-spinel γ-Al_2O_3 unit cell contains 40 atoms, and the structure was named as Model-5 [Figure 6.2 (e)].

The unit cells of the models considered in this work are shown in Figure 6.2 with their relevant structural aspects summarized in Table 6.3.

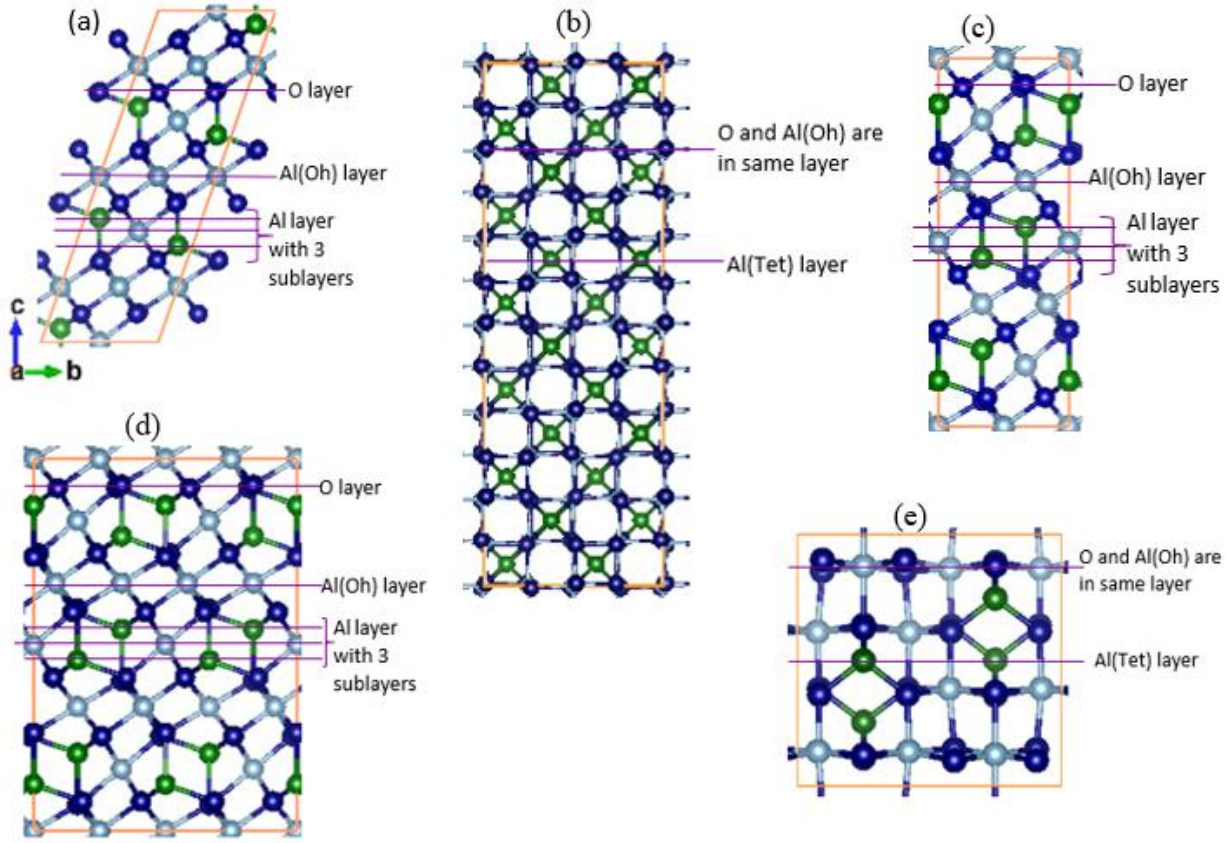

Figure 6.2: Different structural models for γ-Al_2O_3: (a) Model-1: $1a_p \times 1a_p \times 3a_p$ primitive (rhombohedral) supercell, (b) Model-2: $1a_0 \times 1a_0 \times 3a_0$ conventional fcc supercell, (c) Model-3: $1a_h \times 1a_h \times 1c_h$ hexagonal cell, (d) Model-4: $2a_h \times 2a_h \times 1c_h$ hexagonal supercell, (e) Model-5: Monoclinic non-spinel cell [145]. The green and silvery spheres represent the Al(tetrahedral) and Al(octahedral), and dark blue balls represent O atom/ion.

Table 6.3: Relevant structural details including lattice parameters (input), symmetry, number of atoms and vacancies.

Different structural Models	Symmetry	Numbers of atoms and vacancies	Lattice parameter and Angles [Inputs]	References
Model-1: Primitive (Rhombohedral) cell	*P1*	40 atoms with 2 vacancies	$a=b=5.613$ Å, $c=16.839$ Å $\alpha=\beta=\gamma=60.00^0$	G. Gutiérrez *et al* [138]
Model-2: Conventional fcc supercell	*P1*	160 atoms with 8 vacancies-oh	$a=b=7.938$ Å, $c=23.814$ Å $\alpha=\beta=\gamma=90.00^0$	L. Smročk *et al* [122]

Model-3: Hexagonal unit cell	*P1*	40 atoms with 2 vacancies	$a=b$=5.613 Å, c=13.749 Å $\alpha=\beta$=90.00^0, γ=120.00^0	E. Menéndez-Proupin *et al* [140]
Model-4: Hexagonal supercell	*P1*	160 atoms with 8 vacancies-oh	$a=b$=11.226 Å, c=13.749 Å $\alpha=\beta$=90.00^0, γ=120.00^0	F. Maglia *et al* [144]
Model-5: Non-spinel (monoclinic) cell	*P21/m*	40 atoms	a=5.576 Å, b=8.398 Å, c=8.068 Å $\alpha=\gamma$=90.00^0, β=90.53^0	M. Digne *et al* [145]

From all 4 spinel structures, total 12 different spinel structural models were created in this work with different vacancy distributions (i.e., vac-Tet, vac-Tet-Oh, vac-Oh). This work then examined the dependence of total energy for all 12 spinel models on the cation (Al) vacancies positions homogeneously and one non-spinel model. The local structure contribution including cation (Al), anion (O) distributions to the total energetics were also analysed. The following subsections 6.3.1.2.2 and 6.3.1.2.3 will describe the obtained results for all models using first principle DFT within GGA-PBE calculations in detail.

6.3.1.2.2 Formation, stability, and chemical bonding in different models

The results include equilibrium lattice parameters, bulk modulus and energy differences per unit formula for different optimized γ-Al_2O_3 structural models with respect to the α-Al_2O_3 obtained from the present work are listed and compared with other theoretical and experimental results in Table 6.4.

Table 6.4: Calculated results (lattice parameters, volume, bulk modulus etc.) of our different structural models of γ-Al_2O_3.

Different structural Models	Lattice parameter and Angles	ΔE(γ-α) eV/f.u.	Bulk modulus (*GPa*)
Model-1:			
Pr-1a (vac-Tet)	$a=b$=5.664 Å, c=17.032Å $\alpha=\beta$=60.08^0, γ=60.00^0	0.409	
Pr-1b (vac-Oh-Tet)	$a=b$=5.676 Å, c=17.042Å $\alpha=\beta$=60.03^0, γ=60.00^0	0.359	
Pr-1c (vac-Oh)	$a=b$=5.655 Å, c=16.868 Å $\alpha=\beta$=59.15^0, γ=59.80^0	0.198	
Ref: DFT-GGA(PW-91) (40 atoms cell, vac-oh) [139]	$a=b$=5.663 Å, c=13.710 Å $\alpha=\beta$=90.60^0, γ=60.40^0	0.180	209.00
Model-2:			
Conv-1a (vac-Tet)	a=8.053 Å, b=8.054 Å, c=24.061 Å	0.357	

	$\alpha=\beta=89.99^0$, $\gamma=90.00^0$		
Conv-1b (vac-Oh-Tet)	a= 8.050 Å, b=8.036 Å, c=24.167 Å $\alpha=\beta=89.94^0$, $\gamma=89.97^0$	0.332	
Conv-1c (vac-Oh)	a=7.968 Å, b=7.978 Å, c=23.943 Å $\alpha=\beta=89.78^0$, $\gamma=90.29^0$	0.129	
Ref: Experiment: XRD (vac-oh) [122]	$a=b=c$=7.938 Å	-	
Model-3:			
Hex-1a (vac-Tet)	$a=b$=5.663 Å, c=13.925 Å $\alpha=\beta=89.94^0$, $\gamma=120.05^0$	0.312	
Hex-1b (vac-Oh-Tet)	$a=b$=5.670 Å, c=13.852 Å $\alpha=\beta=89.42^0$, $\gamma=120.24^0$	0.254	
Hex-1c (vac-Oh)	$a=b$=5.642 Å, c=13.664 Å $\alpha=\beta=90.64^0$, $\gamma=119.62^0$	0.112	205.67
Ref: DFT-LDA+USPP (40 atoms cell, vac-oh) [223]	$a=b$=5.606 Å, c=13.482 Å $\alpha=\beta=90.00^0$, $\gamma=120.00^0$		204.00
Model-4:			
Hex-2a (vac-Tet)	a=12.089 Å, b=12.085 Å, c=13.920 Å $\alpha=\beta=90.24^0$, $\gamma=120.06^0$	0.313	
Hex-2b (vac-Oh-Tet)	a=12.042 Å, b=12.040 Å, c=13.877 Å $\alpha=\beta=89.88^0$, $\gamma=120.09^0$	0.220	
Hex-2c (vac-Oh)	a=11.895 Å, b=11.893 Å, c=13.442 Å $\alpha=\beta=89.96^0$, $\gamma=119.94^0$	0.086	209.73
Ref: DFT+pair potential (160 atoms cell, vac-oh-tet) [144]	$a=b$=11.190 Å, c=13.700 Å	0.390	208.00
Model-5:	a=5.576 Å, b=8.398 Å, c=8.068 Å $\alpha=\gamma=90.00^0$, $\beta=90.53^0$	0.294	
Ref: DFT-GGA(PW-91) (40 atoms cell) [145]	a=5.587 Å, b=8.413 Å, c=8.068 Å $\alpha=\gamma=90.00^0$, $\beta=90.59^0$		171.00

The energy dependences on cation (Al) vacancy positions for 12 spinel structural models with different possible configurations (vacancy sites: Tet-Tet, Oh-Tet, Oh-Oh) and for one non-spinel model are summarized in the following Figure 6.3. Figure 6.3 shows the variation of formation energy difference, ΔE (eV/f.u.), between different possible γ-Al_2O_3 structural models and α-Al_2O_3 phases as a function of vacancy positions used in DFT-GGA(PBE) approach.

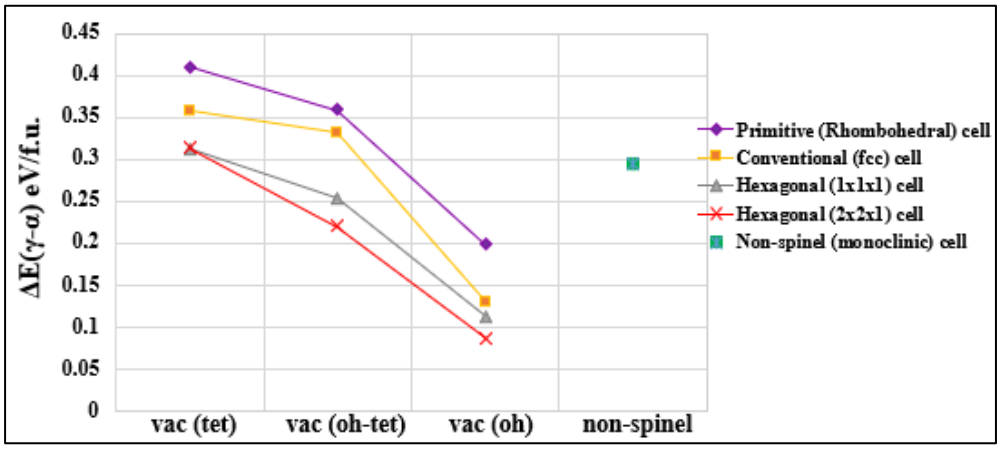

Figure 6.3: The energetics of the structural models of γ-Al_2O_3 with respect to that of α-Al_2O_3 (Equation 6.3).

From Figure 6.3 and Table 6.4, the γ-Al_2O_3 hexagonal 2×2×1 supercell (160 atoms) with octahedral (Oh) vacancies from Model-4 shows the most stable phase because of having lowest energy difference (ΔE) with stable ground state α-Al_2O_3 (i.e., 0.086 eV/f.u.), while the other models show the higher energy difference and less stable. The bulk modulus of the most stable hexagonal γ-Al_2O_3 2×2×1 supercell structure is 209.73 *GPa* [see Appendix Figure A.6.6] which is close to 208.00 *GPa* from Maglia *et al* work [144] and larger from non-spinel model (171.00 *GPa*) proposed by Digne *et al* [145].

Figure 6.4 shows the variation of formation energy difference, ΔE (eV/f.u.), between different possible γ-Al_2O_3 structural models and α-Al_2O_3 phases as a function of volume (Å^3/f.u.).

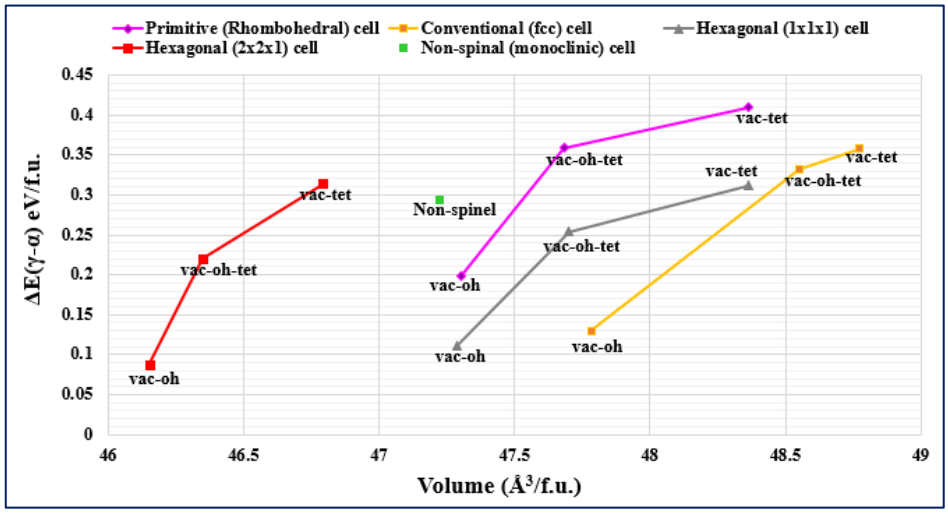

Figure 6.4: Formation energy difference, ΔE (eV/f.u.) for different γ-Al_2O_3 structural models as a function of volume (Å^3/f.u.).

From Figure 6.4, there is a strong correlation between vacancy site preference, unit cell volume and formation energies. The structure contains Oh vacancies yield smaller volume than Tet and Tet+Oh vacancies structure for all spinel

models studied in this work, in agreement with Wolverton and Hass [136]. In ideal spinel ($MgAl_2O_4$) structure, the octahedral sites are geometrically larger (Oh–O distance: 1.932 Å) than the tetrahedral sites (Tet–O distance: 1.811 Å) and the lattice, most likely, can relax and shrink to a larger extent around the Oh vacancies and yield lower volume [144]. The γ-Al_2O_3 2×2×1 hexagonal supercell (160 atoms) with Oh vacancies from Model-4 shows the most stable phase having smaller volume than other structures [Figure 6.4], also having larger Al(Oh)-O bonds (Average: 2.017 Å) than the Al(Tet)-O bonds (Average: 1.806 Å) [Figure 6.5 (b) and (c)].

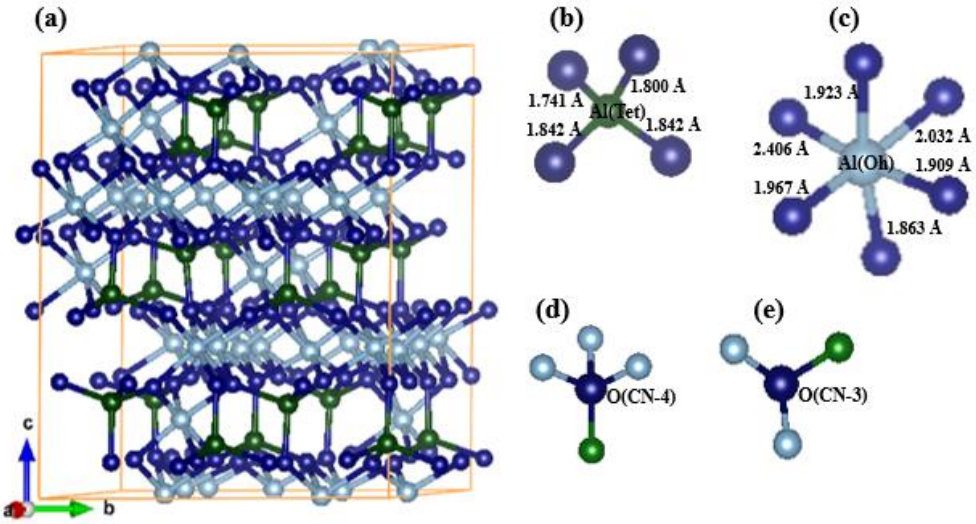

Figure 6.5: Schematic crystal structure of (a) 2×2×1 hexagonal γ-Al_2O_3 supercell with Oh vacancies (160 atoms), (b) Al_{tet} (green) and (c) Al_{oct} (silver) bonded with four and six O anions, respectively. O atom/ion (dark blue) bonded with Al(oh/tet) cations by (d) CN-4 and (e) CN-3 [here, CN-Coordination Number].

The bond valence for the proposed γ-Al_2O_3 2×2×1 hexagonal supercell (Oh vacancies) from Model-4 was also calculated to observe chemical bonding in the compounds using Brown bond theory [224, 225]. The obtained bond valence 2.64 valence units (vu) for Al(Tet) atoms and 2.96 (vu) for Al(Oh) atoms from this work which is close to 3.00 (vu) for Al(Oh) atoms in an ideal spinel $MgAl_2O_4$

[88] and is reasonable. This indicates bond valences are strong in spinel hexagonal γ-Al_2O_3 model and the structure is more ionic.

The coordination number (CN) of O atom/ion to cation is normally 4 (i.e. CN-4) in an ideal spinel $MgAl_2O_4$ structure. But in spinel γ-Al_2O_3 structure to maintain the charge balance for ionic distribution vacancy introduced and therefore, O^{2-} loses some bonds with Al^{3+} creating CN-3 of O-Al bonds [Figure 6.5 (d) and (e)] and releases some energies according to work-force law which should increases total ground state energy (i.e., more stable structure). Therefore, more CN-4 of O-Al bonds mean the structure should have lower energy and less stable. Figure 6.6 shows the energetics for all our spinel γ-Al_2O_3 structural Models after relaxing the structures as function of the ratio of CN-4:CN-3 of O anions.

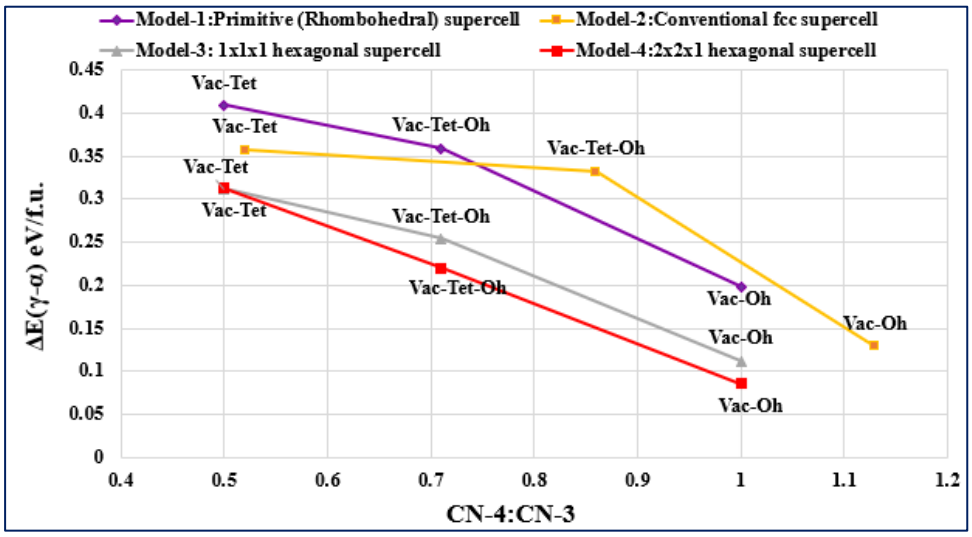

Figure 6.6: Formation energy difference, ΔE (eV/f.u.) for different γ-Al_2O_3 structural models as a function of CN-4:CN-3 of O anion.

From Figure 6.6, the coordination number (CN) of O anion affect the lattice energy and the proportion of CN-4 and CN-3 should be equal to get more stable structure. Because if we look in γ-Al_2O_3(conv) structure containing Oh vacancies, from Model-2 the CN-4 of O anion is more than CN-3 (i.e., CN-4:CN-3 is 1.13:1) and have less stable structure (energetically) compared to hexagonal γ-Al_2O_3 with

Oh vacancies from Model-3 and Model-4. Again, more CN-3 means there are more O^{2-} anions lost the bonds with Al^{3+} cations and create the structure more unstable due to charge difference. We have also done the Bader charge analysis to check charge neutrality due to CN-4 and CN-3 for our most stable hexagonal γ-Al_2O_3 2×2×1 supercell and compared with α-Al_2O_3. The calculated Bader charges of Al(Oh) is +2.14 in our hexagonal γ-Al_2O_3 2×2×1 supercell which is close to +2.19 of α-Al_2O_3. The calculated Bader charges varies for O anion, with CN-4 (i.e. -1.37 to -1.45 eV) are more negative than O atoms/ion with CN-3 (-1.34 to -1.39 eV). These different variation of charge distribution of Al(Tet), Al(Oh) and O for CN-4 and CN-3 with their total number of proportions in hexagonal γ-Al_2O_3 2×2×1 supercell makes the structure charge neutral as well as stable.

6.3.1.2.3 Distribution of vacancies between layers in the structure

In the spinel γ-Al_2O_3 unit cell of primitive (Rhombohedral) and hexagonal structure, Al consists of 2 different configuration atomic layers, the Al_1 layer, where Al ions occupy two thirds of the octahedral sites i.e. pure Al(Oh) layer. Another Al_2 i.e. mixed Al(Oh+Tet) layer is composed of three sublayers: a sublayer of octahedrally coordinated Al being sandwiched by two tetragonally coordinated Al sublayers [Figure 6.7]. Therefore, when choose the Al vacancies for octahedral (Oh) sites, the vacancies can recite either only in pure Al_1(Oh) layer or in Al_2(Oh+Tet) layer or from two mixed (Al_1 and Al_2) layers. To see the distribution of vacancies between the layers homogeneously, 9 different structures for Oh vacancy sites from primitive (Model-1), hexagonal 1×1×1 (Model-3) and hexagonal 2×2×1 supercell (Model-4) models are created and compared in this work.

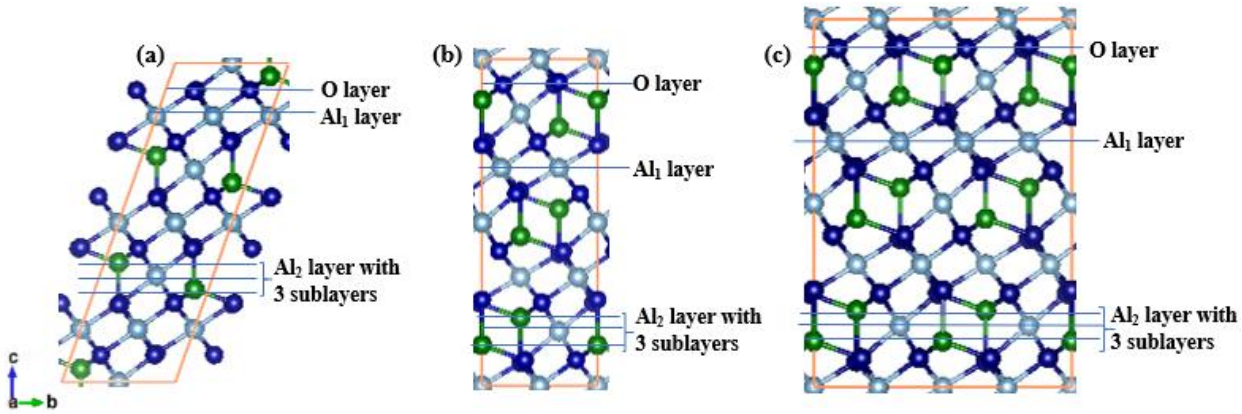

Figure 6.7: Schematic crystal structure of spinel γ-Al_2O_3 with Oh vacancies for (a) Model-1: primitive (Rhombohedral) cell, (b) Model-3: hexagonal 1×1×1 unit cell, (c) Model-4: hexagonal 2×2×1 supercell. Al_{tet} (green) and Al_{oct} (silver) bonded with four and six O anions, respectively. The dark blue represents O atom/ion. The orange lines represent the axis of the unit cell. The labels Al_1, Al_2 and O represent the Al sublayers and O layer in the structure, respectively.

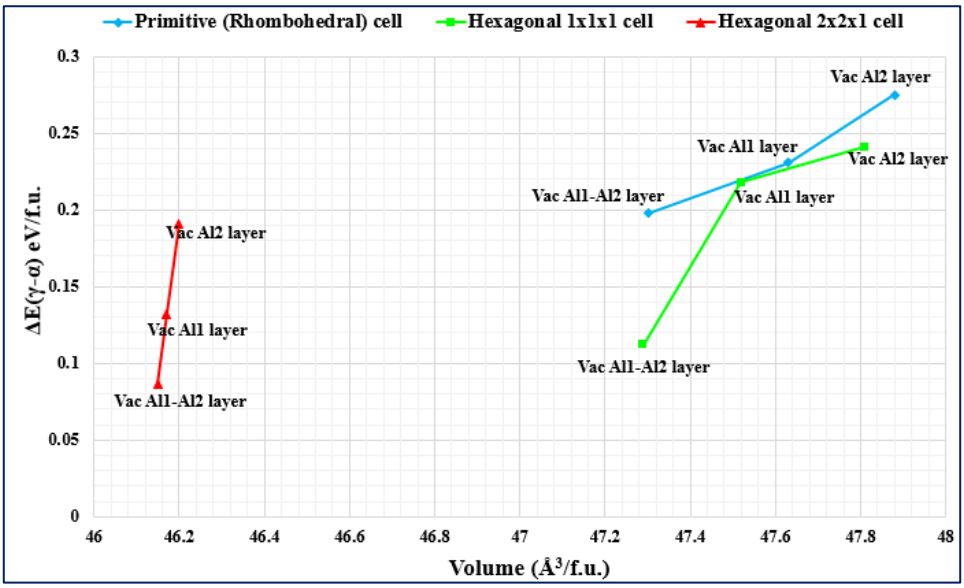

Figure 6.8: Formation energy difference, ΔE (eV/f.u.) as a function of volume (Å^3/f.u.) for Primitive (Rhombohedral), Hexagonal (1×1×1) cell and Hexagonal (2×2×1) supercell of γ-Al_2O_3 structural models respectively with Oh vacancies distributed at different layers.

From Figure 6.8, most stable structure is hexagonal γ-Al_2O_3 2×2×1 (160 atoms) supercell from Model-4 with Oh vacancies where the vacancies introduced from different atomic configurations layers (i. e., from layer Al_1 and Al_2) and yield the lower volume (46.15 $Å^3$/f.u.) as well. Therefore, the vacancies (Oh) in hexagonal γ-Al_2O_3 spinel like structure preferred to be situated different configurational layers rather than from same type of layer [Figure 6.8].

6.3.1.2.4 Summary

From all the different structural models of γ-Al_2O_3 calculation, the total energy calculations showed that spinel type γ-Al_2O_3 within the hexagonal supercell containing 160 atoms (Model 4) is intrinsically favored at ambient conditions. The vacancies are preferred in octahedral sites as well.

From present works analysis, for coordination number (CN) of O atoms with Al atoms showed that any configuration involving less or too many O-Al missing bonds in the spinel structure (i.e. O ion having more or less CN-3 than CN-4) is energetically unfavorable. The proportion of CN-4 and CN-3 for O anion/atom in spinel γ-Al_2O_3 should be 1 to have the more ionic charge neutral stable structure. The vacancies distribution between layers in the spinel γ-Al_2O_3 also shows correlation between the stability of the structures. The present study showed that γ-Al_2O_3 hexagonal supercell with octahedral (Oh) vacancies from different atomic configurations layers [i.e., from mixed Al2(Oh+Tet) layers and pure Al1(Oh) layers] is energetically favorable.

From the overall careful observations of different existing γ-Al_2O_3 structural models, present study proposed spinel γ-Al_2O_3 hexagonal structure with Oh (octahedral) vacancies have a stable uniform structure compared to traditional primitive (rhombohedral) and tetragonal cell.

According to formation energy and stability analysis it has been seen that there is very little difference (ΔE=0.026 eV/f.u.) between hexagonal 1×1×1 (40 atoms) and 2×2×1 (160 atoms) supercell which means the structures are close to each other. Therefore, the hexagonal γ-Al_2O_3 1×1×1 (40 atoms) cell were used in rest of my work in this thesis.

6.3.2 Electronic properties by GGA-PBE

The electronic structure of the monoclinic θ-Al_2O_3 and hexagonal γ-Al_2O_3 crystal structure are calculated within the GGA-PBE approximation. The following Figurer 6.9 shows the total density of states (TDOS) and partial density of states (PDOS) for both θ- and γ-Al_2O_3.

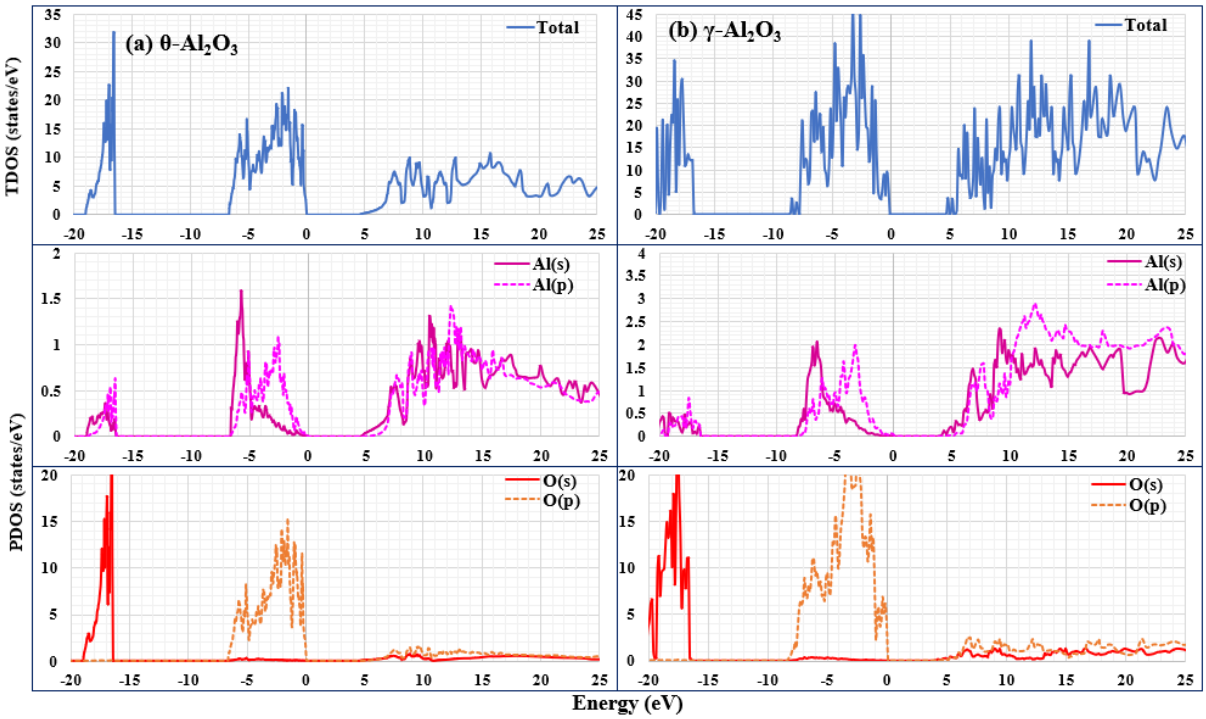

Figure 6.9: The total and partial density of states of (a) monoclinic θ-Al_2O_3 and (b) hexagonal γ-Al_2O_3 crystal structure from GGA-PBE calculations.

For both θ- and γ-Al_2O_3 the conduction bands are mainly composed from Al *3s* and *3p* states [Figure 6.9 (a) and (b)]. There are also small contribution are observed from O *2s* and *2p* states to conduction band for both alumina phases [Figure 6.9 (a) and (b)]. This indicates some covalent nature in the oxides. The

calculated lower-valence-band (LVB) are mainly from O *2s* states, and the width is 2.60 and 4.17 eV for θ-Al_2O_3 and γ-Al_2O_3 respectively from the present GGA-PBE calculation [Figure 6.9 (a) and (b)]. The upper valence band (UVB) are from O *2p* states, and the width is 6.7 and 8.5 eV for θ-Al_2O_3 and γ-Al_2O_3 respectively [Figure 6.9 (a) and (b)].

Table 6.5: The comparison of band widths and band gaps (eV) from GGA-PBE calculated results of monoclinic θ-Al_2O_3 and hexagonal γ-Al_2O_3 with the previous theoretical and experimental data.

	Upper VB (O *2p*) width (eV)	Lower VB (O *2s*) width (eV)	Differences (O *2s*-O *2p*) (eV)	Band gap (eV)
monoclinic θ-Al_2O_3				
This work, GGA-PBE	6.7	2.7	9.7	4.5
X-ray photoelectron spectroscopy [225]				5.16
DFT-LDA (OLCAO) [105]	7.41	3.14	8.86	4.64
spinel hexagonal γ-Al_2O_3				
This work, GGA-PBE	8.5	4.17	8.1	4.2
X-ray photoelectron spectroscopy [125]	9.5	-	-	8.7
DFT-GGA [140]	8.2	3.5	8.4	3.8
DFT-LDA+FPLMTO [107]	8.5	3.9	8.0	3.9

From Table 6.5 and Figure 6.9, the calculated band gap for the θ-Al_2O_3 is 4.5 eV whereas the experimental measured gap is 5.16 eV [226], which is reasonable for DFT calculation. For γ-Al_2O_3, the calculated bandgap between UVB and conduction band is 4.2 eV in the present work. This value is close to other DFT-LDA results, i.e., 3.9 eV by R Ahuja *et al* [107] and 3.8 eV by Menéndez-Proupin *et al* [140]. However, XPS (X-ray photoelectron spectroscopy) measurements by B Ealet *et al* produced band gap of 8.7 eV for γ-Al_2O_3 [125].

6.3.3 Accurate calculation of band gap by *GW0* correction

To improve the electronic structure for both θ- and γ-Al_2O_3, state-of-art *GW0* approach have been applied and discussed in this section.

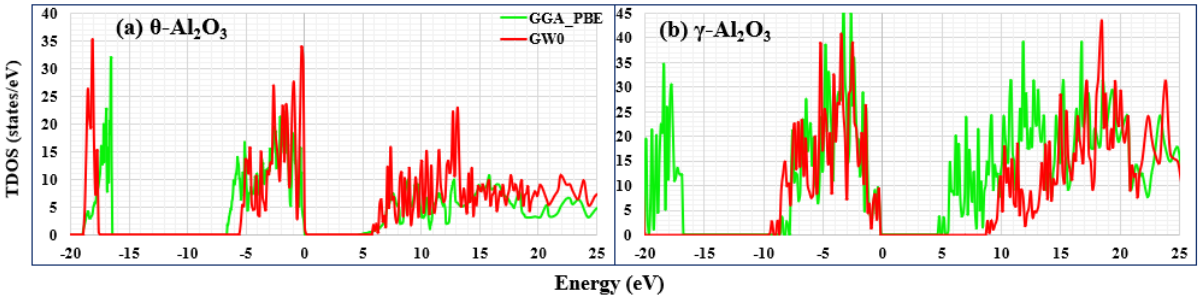

Figure 6.10: Schematic picture of the total density of states (DOS) of (a) θ-Al_2O_3 and (b) γ-Al_2O_3 structure using both GGA(PBE) and *GW0* functionals.

The spectrum of lower valence band (LVB) and the conduction band are improved for both alumina phases. From Figure 6.10, all states in the conduction band are shifted toward high energy, which causes increasing in the band gap. The calculated band gap from *GW0* correction for our monoclinic θ-Al_2O_3 crystal structure is 5.7 eV which overestimated (within 10%) to the experimental measured band gap 5.16 eV [226]. The calculated band gap from *GW0* correction for our hexagonal γ-Al_2O_3 crystal structure is 8.3 eV which is close (within 4%) to the experimental XPS (X-ray photoelectron spectroscopy) measured band gap 8.7 eV [125].

6.3.4 Optical properties

The optical properties such as real $\varepsilon_1(\omega)$ and imaginary $\varepsilon_2(\omega)$ part of dielectric constants, refractive index $n(\omega)$, extinction coefficient $k(\omega)$, reflectivity $R(\omega)$, absorption coefficient $\alpha(\omega)$, energy loss functions $L(\omega)$ and Conductivity $\sigma(\omega)$ are calculated for the photon energies of θ- and γ-Al_2O_3 by using equation (4.39)-(4.44) [from methodology i.e., Chapter Four] and are shown in Figure 6.11. For the α phase there are experimental results for several optical quantities [see Chapter Five], while such are absent for θ- and γ-Al_2O_3. Therefore, comparison between theoretical and experimental results for α-Al_2O_3 serves to give an indication of the accuracy of the present theoretical predictions for the θ- and γ-Al_2O_3. From previous chapter (i.e., Chapter Five) the analyzed *GW0* correction

over DFT(GGA-PBE) enhanced the optical properties for α-Al_2O_3. So, for θ- and γ- alumina phases the optical properties are calculated by *GW0* approach and compared with α-Al_2O_3 [Figure 6.11].

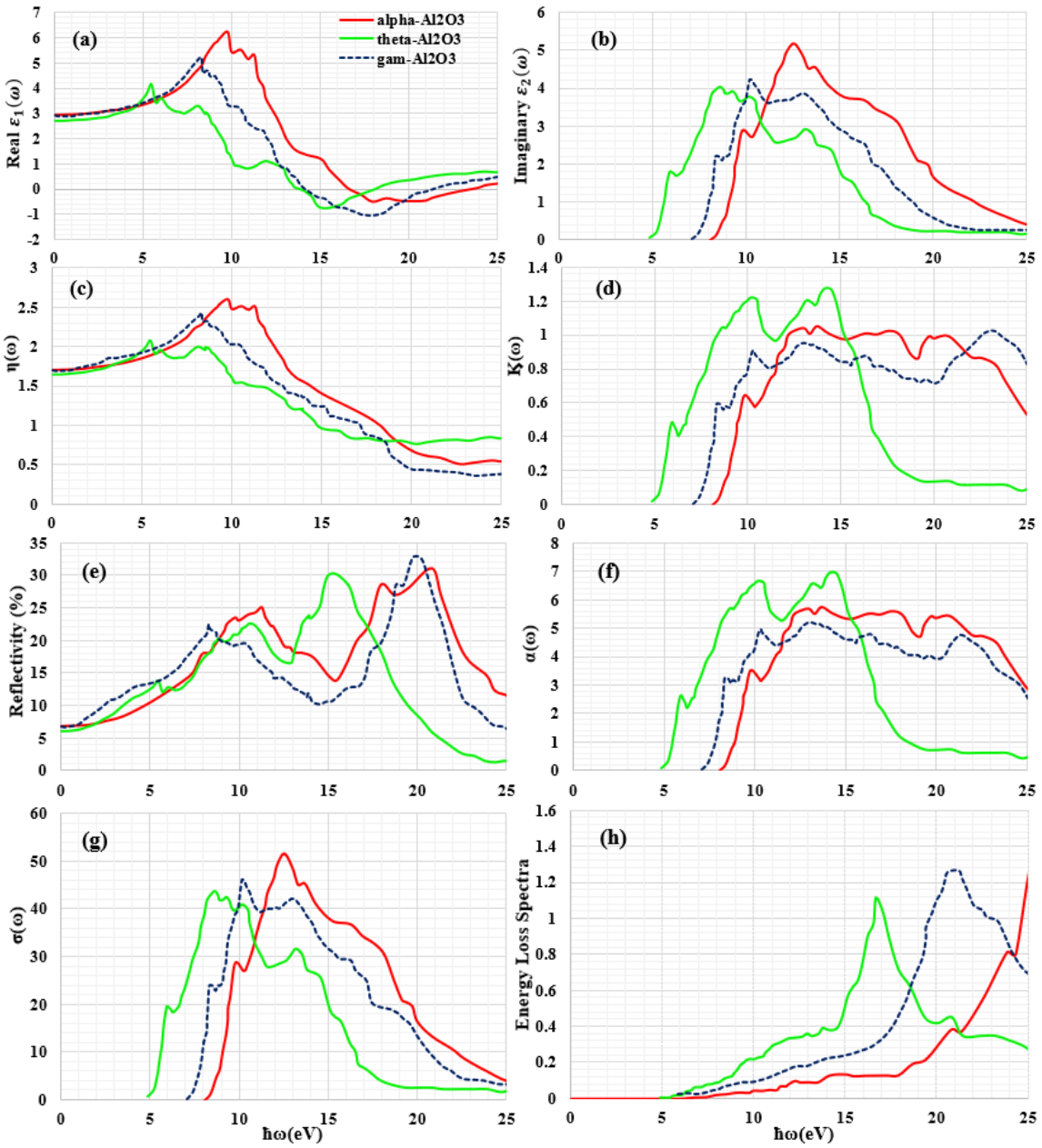

Figure 6.11: The optical functions: Dielectric constants of (a) real part $\varepsilon_1(\omega)$, (b) imaginary part $\varepsilon_2(\omega)$, (c) refractive index $n(\omega)$, (d) extinction coefficient $k(\omega)$, (e) reflectivity $R(\omega)$, (f) absorption coefficient $\alpha(\omega)$, (g) conductivity $\sigma(\omega)$ and (h) energy loss spectra $L(\omega)$ of α-, θ- and γ-Al_2O_3.

The comparison of the static dielectric constant $\varepsilon_1(0)$ and $\varepsilon_1(5)$ under *GW0* correction over DFT for α-, θ- and γ-Al_2O_3 phases are given in Table 6.6. In Figure 6.11 (b), the optical absorption edge from $\varepsilon_2(\omega)$ curve is found at 9.8 eV, 5.8 eV and 8.3 eV for α-, θ- and γ-Al_2O_3, respectively. The shift in the calculated spectra of absorption edge is in a good agreement with those from band corresponding DOS of all three alumina phases. The various peaks of this curve are also signified to different interband transitions between the conduction and valence band states. From imaginary spectra, the peak positions of the distinct features and plasmonic resonance for hcp α-Al_2O_3 the sharp peak observed from imaginary spectra at 12.5 eV from *GW0* calculation coincide with W. Tews et al experimental work [218] (also in Chapter Five, Figure 5.5). For the monoclinic θ- and hexagonal γ-Al_2O_3, the sharp peak of the peak positions of the distinct features and plasmonic resonance observed from imaginary spectra at 8.8 and 10.4 eV respectively from *GW0* calculation.

Table 6.6: The significant optical parameters for α-, θ- and γ-Al_2O_3 compared with the previous theoretical and experimental results.

Parameter	α-Al_2O_3		θ-Al_2O_3		γ-Al_2O_3	
	GW0	Reference	*GW0*	Reference	*GW0*	Reference
$\varepsilon_1(0)$	2.96	3.00 (Exp) [218] 3.20 (DFT) [107]	2.80	2.95 (DFT) [227]	2.90	3.00 (DFT) [107] 3.74 (DFT) [227]
$\varepsilon_1(5)$	3.30	3.30 (Exp) [218]	3.40	3.69 (DFT) [227]	3.35	3.25 (DFT) [227]
R(0)	0.07	0.07 (Exp) [219]	0.06	0.07 (DFT) [227]	0.07	0.10 (DFT) [227]
R(5)	0.10	0.09 (Exp) [218]	0.12	0.09 (DFT) [227]	0.13	0.08 (DFT) [227]
n(0)	1.70	1.75 (Exp) [218] 1.79 (DFT) [107]	1.75	1.72 (DFT) [227]	1.70	1.73 (DFT) [107] 1.70 (Exp) [206]
n(5)	1.86	1.86 (Exp) [218]	1.94	1.92 (DFT) [227]	1.90	1.80 (DFT) [227]

The static refractive indices of α-, θ- and γ-Al_2O_3 are 1.70, 1.65 and 1.70, respectively [Figure 6.6 (c)]. From Figure 6.11 (c), it is noticed that the refractive index $\eta(0)$ of θ-Al_2O_3 is less than α-Al_2O_3 where γ-Al_2O_3 is coincide with α-Al_2O_3 in the low energy region but then gradually decreased in the high energy region or ultraviolet region.

The extinction coefficient $k(\omega)$ shows higher energy peak around 9.0-23.0 eV, 6.0-15.0 eV, and 8.0-23.0 eV energy region for α-, θ- and γ-Al_2O_3 [Figure 6.11] respectively from *GW0* correction. This is evidence that the overall behaviour of $k(\omega)$ is close to that of the imaginary part of the dielectric functions $\varepsilon_2(\omega)$ [Figure 6.11 (d)], which affirms the established theory.

From Figure 6.11 (e), the reflectivity (%) of α- and γ-Al_2O_3 phases having nearly similar characteristics starts with a value of 6.8%, and then rise to reach maximum value of 32.0% for α- and 32.7% for γ-Al_2O_3 phases respectively between 8.0-22.0 eV energy range. The reflectivity (%) spectra of α-Al_2O_3 from present *GW0* calculation show good agreements with those from M. L. Bortz *et al* [219] spectrophotometer experimental work. But for θ-Al_2O_3, the sharpest reflectivity (%) spectra is in between 6.0-16.0 eV energy ranges, which shows lower value compared to α- and γ-Al_2O_3 phases. Thus, both the α- and γ-Al_2O_3 phases possess roughly similar reflectivity spectra showing promise as good coating materials than θ-Al_2O_3.

The absorption spectra of α-, θ- and γ-Al_2O_3 as shown in Figure 6.11 (f). From Figure 6.11 (f), α-Al_2O_3 has largest peaks at 10.0-23.3 eV region besides having shoulder at lower energy. The γ-Al_2O_3 has largest peaks at 8.4-22.0 eV region besides having shoulder at lower energy which shows closer value to α-Al_2O_3. But for θ-Al_2O_3 [Figure 6.11 (f)], largest peaks at 8.0-15.5 eV region besides having few shoulders at lower energy. Therefore, α- and γ-Al_2O_3 phases possess higher absorption in UV (ultra-violet) energy region compared to θ-Al_2O_3.

In case of conductivity spectrum from Figure 6.11 (g), the observed optical photoconductivity spectra have several maxima and minima from *GW0* calculation within for α-Al_2O_3 within the range of 10.0-17.5 eV, whereas the θ- and γ-Al_2O_3 are electrically conductive when the incident radiation has energy within the range of 6.0-13.5 eV and 8.0-16.3 eV respectively.

Figure 6.11 (h) presents the energy loss function as a function of photon energy. The prominent peaks started for α-Al_2O_3 phase after 20.0 eV and for γ-Al_2O_3 phase after 17.0 eV and 21.3 eV respectively, while the θ-Al_2O_3 has the sharpest peak at 16.7 eV, which indicates rapid reduction in the reflectance for θ-Al_2O_3 compared to α- and γ-Al_2O_3 phases.

From the above analysis of the optical properties of α-, θ- and γ-Al_2O_3, it is noted that the proposed hexagonal γ-Al_2O_3 spinel structure shows close results in dielectric properties to hcp α-Al_2O_3 rather than monoclinic θ-Al_2O_3. The present study would be helpful to provide relevant fundamental science to improve the design and application of different alumina phases i.e., θ- and γ-Al_2O_3 in the field of optoelectronics and photovoltaics.

6.4 Conclusion

The structural and electronic properties of θ- and γ-Al_2O_3 were analysed in this chapter using the first-principles DFT calculations within GGA-PBE approximation. The resulting equilibrium properties by GGA-PBE approach of θ- and γ-Al_2O_3 obtained are consistent with the experimental observations in the literature.

For γ-Al_2O_3, the physical properties related to total energy with detail local chemical structure (including cation, anion, and vacancy distribution) calculations were performed for different (spinel and non-spinel) structural models containing smaller (40 atoms unit cell) and larger supercell (160 atoms). Several important features were revealed in the present study relating to the cation (Al), anion (O) and vacancy site distribution in the spinel γ-Al_2O_3 bulk structure. The total energy calculations show that the spinel γ-Al_2O_3 structure for hexagonal lattice model [both small (40 atoms) and larger (160 atoms) supercells] with octahedral (Oh) vacancy sites having smaller volume is more stable. Any configuration involving too many O-Al missing bonds due to vacancies for spinel

structure (i.e., having more or even less CN-3 than CN-4) is unfavorable. The proportion of CN-4 and CN-3 for O anion/atom in spinel γ-Al_2O_3 should be 1 to get the more stable structure. Considering the vacancies distribution between layers, the spinel γ-Al_2O_3 structure with octahedral (Oh) vacancies from different atomic configurations layers [i.e., from mixed Al_2(Oh+Tet) layers and pure Al_1(Oh) layers] is favorable.

The electronic properties of monoclinic θ- and hexagonal γ-Al_2O_3 calculated by the self-consistent *GW0* approach were discussed in this chapter. The improved optical properties by *GW0* approaches for α-Al_2O_3 from Chapter Five are consistent with the available experimental and theoretical results in literature which indicating the accuracy and reliability of the modeling elements used in this chapter for monoclinic θ- and hexagonal γ-Al_2O_3 phases. Overall, the self-consistent *GW0* corrections enhanced the electronic structures for the monoclinic θ- and hexagonal γ-Al_2O_3 phases.

Chapter Seven

Crystal structures and properties of Al_2O_3 rich $MgO.nAl_2O_3$ spinels

7.1 Introduction

Mg-Al spinels ($MgO \cdot nAl_2O_3$) have attracted enormous attentions due to their wide applications [156, 157, 162-164]. By varying the *n* value, the existence of intermediate compositional structures for the $MgAl_2O_4$ to γ-Al_2O_3 solid solution has been reported, using the formula $Mg_{(1-x)}Al_{2(1+x/3)}O_4$ [156, 157]. But in that formula, the clear description of cation Al^{3+} and vacancy distributions in tetragonal (Tet)/octahedral (Oh) sites are absent [156, 157]. The present work proposed a new formula $[Mg_{(1-x)}Al_x]_{Tet}[Al_{(2-x/3)}V_{x/3}]_{Oh}O_4$, (here, x=0 to 1) to describe the intermediate compositional structures of $MgAl_2O_4$ to γ-Al_2O_3 solid solution. This work first investigated the distribution rules for cation Al^{3+} and vacancies at tetragonal and octahedral sites in $MgAl_2O_4$ to γ-Al_2O_3 solid solution spinel according to their energetics and with in-depth analysis of the local structure. Then seven compositions of $[Mg_{(1-x)}Al_x]_{Tet}[Al_{(2-x/3)}V_{x/3}]_{Oh}O_4$ for x = 0.0, 0.125, 0.25, 0.5, 0.75, 0.875, 1.0 have been studied by the first-principles DFT within the GGA-PBE approach. The related chemical bonding and electronic structures were also discussed for all seven compositional structures. An *ab initio* molecular dynamics (MD) simulation technique has also been applied to study the occupations of the Mg and Al atoms at the interstitial sites at high temperature in this work.

7.2 Methods:

7.2.1 Structural model for $Mg_5Al_{18}Vac_1O_{32}$ models:

The $Mg_8Al_{16}O_{32}$ [Figure 7.1 (a)] unit cell with lattice parameter 8.123 Å were used to prepare $Mg_5Al_{18}Vac_1O_{32}$ unit cell. Depending on the substation of cation Al^{3+} to Mg^{2+} and vacancy distribution, there are more than 50 possible configurations. Based on the previous analysis (the previous chapter six), around 20 structural models for $Mg_5Al_{18}Vac_1O_{32}$ were tested. The calculations revealed that the following 5 structural models have been found to be highly stable, as shown in Figure 7.1.

The atomic layers along the (001) orientation in the $Mg_8Al_{16}O_{32}$ unit cell consists of four high-density layers and four low-density layers, which alternate along the *c* direction [figure 7.1 (a)]. The low-density layer contains the tetrahedrally coordinated Mg^{2+} cations, whereas the high-density layer contains the octahedrally coordinated Al^{3+} cations, and the oxygen atoms [Figure 7.1 (a)].

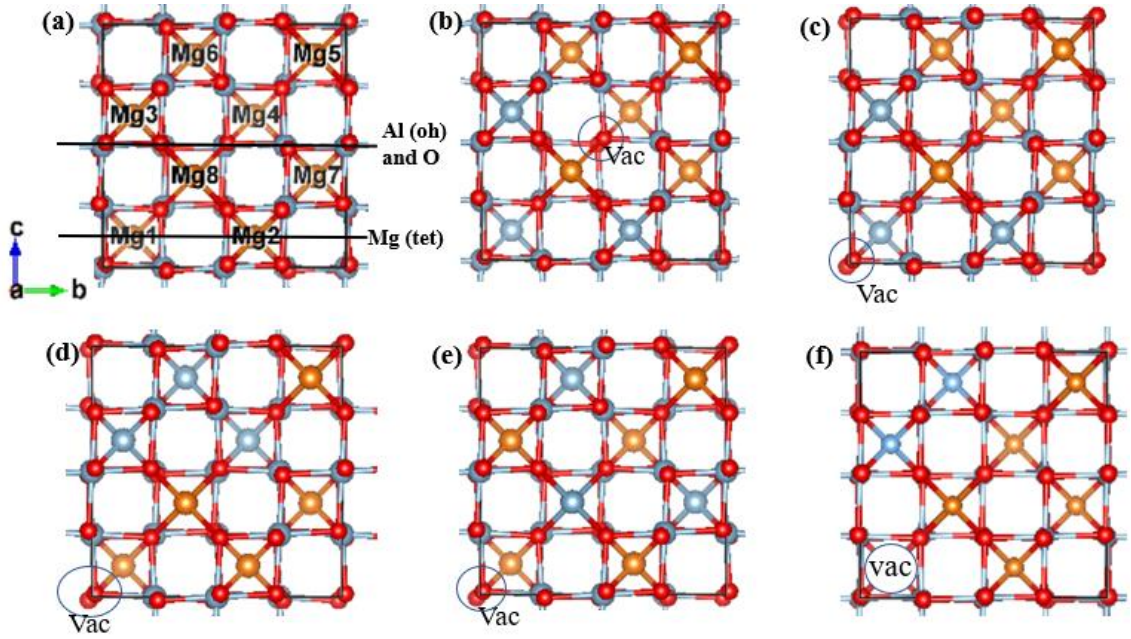

Figure 7.1: Schematic picture of (a) fcc $Mg_8Al_{16}O_{32}$ unit cell and 5 different structural models of $Mg_5Al_{18}Vac_1O_{32}$, (b) Model-1, (c) Model-2, (d) Model-3, (e) Model-4 and (f) Model-5. Orange, blue and red spheres represent the Mg, Al and

O atoms respectively. Blue circles represent the vacancies at different sites in the unit cell.

In figure 7.1, there are 5 different structural models are presented for cations (i.e., Mg^{2+}, Al^{3+}) substitution in different interstitial sites and vacancy distributions homogeneously [Table 7.1]. Model-1 to Model-4 were prepared followed by this composition $[Mg_5Al_3]_{Tet}[Al_{15}Vac1]_{Oh}[O_{32}]$. For Model-1, $3Al^{3+}$ cations were substituted to Mg1, Mg2 and Mg3 tetrahedral interstitial sites and 1 vacancy from Wyckoff (*16d*) position at Al(Oh): (½ ½ ½) which is at the center in the bulk unit cell. For Model-2, $3Al^{3+}$ in same position as Model-1, only changed 1 vacancy from Wyckoff (*16d*) position at Al: (½ 0 0) which is outer layer in the bulk unit cell. For Model-3 and -4, the vacancy was kept as same as Model-2, only $3Al^{3+}$ cations were substituted to Mg3, Mg4, Mg6 and Mg6, Mg7, Mg8 tetrahedral interstitial sites, respectively.

For Model-5, followed by this composition $[Mg_5Al_2Vac_1]_{Tet}[Al_{16}]_{Oh}[O_{32}]$, $3Al^{3+}$ cations were substituted to Mg1, Mg3 and Mg6 tetrahedral interstitial sites and then 1 vacancy in tetrahedral site from Wyckoff (*8a*) position at (1/8 1/8 -1/8) (i.e., substituted Al in Mg1) in the bulk unit cell.

Table 7.1: Fractional coordinates of the substitute Al^{3+} in Mg^{2+} tetrahedral interstitial sites and vacancy sites for 5 different Models of $[Mg_5Al_3]_{Tet}[Al_{15}Vac_1]_{Oh}[O_{32}]$ unit cell

Different Models	Coordinates of substitute Al^{3+} cations for Mg^{2+} ions in tetrahedral interstitial sites	Coordinates of Vacancy sites
Model-1 (vac-oh)	(0.1250 0.1250 0.1250) (0.6250 0.6250 0.1250) (0.6250 0.1250 0.6250)	(0.5000 0.5000 0.5000)
Model-2 (vac-oh)	(0.1250 0.1250 0.1250) (0.6250 0.6250 0.1250) (0.6250 0.1250 0.6250)	(0.5000 0.0000 -0.0000)
Model-3 (vac-oh)	(0.6250 0.1250 0.6250) (0.1250 0.6250 0.6250) (0.3750 0.3750 0.8750)	(0.5000 0.0000 -0.0000)
Model-4 (vac-oh)	(0.3750 0.3750 0.8750)	(0.5000 0.0000 -0.0000)

	(0.3750 0.8750 0.3750) (0.8750 0.3750 0.3750)	
Model-5 (vac-tet)	(0.1250 0.1250 -0.1250) (0.6250 0.1250 0.6250) (0.3750 0.3750 0.8750)	(0.1250 0.1250 -0.1250)

7.2.2 Prepare different models of $[Mg_{(1-x)}Al_x]_{Tet}[Al_{(2-x/3)}V_{x/3}]_{Oh}O_4$ spinels

For the perfect spinel structure ($MgAl_2O_4$), there are 56 atoms contained in the conventional cell ($Mg_8Al_{16}O_{32}$). From the $Mg_8Al_{16}O_{32}$ conventional cell, amounts of 1/3, 2/3, 4/3, 6/3, 7/8 and 8/3 vacancies have to be introduced for the defective spinel structure of $[Mg_{(1-x)}Al_x]_{Tet}[Al_{(2-x/3)}V_{x/3}]_{Oh}O_4$ for x=0.0, 0.125, 0.25, 0.50, 0.75, 0.875 and 1 to make the charge balance. Therefore, a redefined hexagonal cell (($Mg_6Al_{12}O_{24}$) was constructed to make sure the number of vacancies is an integer. The prepared hexagonal unit cell obtained by a transformation of the lattice vectors from conventional fcc $MgAl_2O_4$ cell with the relations, $\boldsymbol{a_h} = \boldsymbol{a_0}$ (-1/2, 1/2, 0), $\boldsymbol{b_h} = \boldsymbol{a_0}$ (0, -1/2, 1/2) and $\boldsymbol{c_h} = \boldsymbol{a_0}$ (1, 1, 1) [here $\boldsymbol{a_0}$=8.16 Å is the lattice parameter of the conventional (fcc) $MgAl_2O_4$ cell]. To avoid possible interaction between the cation, anion, and vacancies in smaller cell and to ensure the accuracy of the calculation the 2×2×1 hexagonal supercells (168 atoms) were used [Figure 7.2].

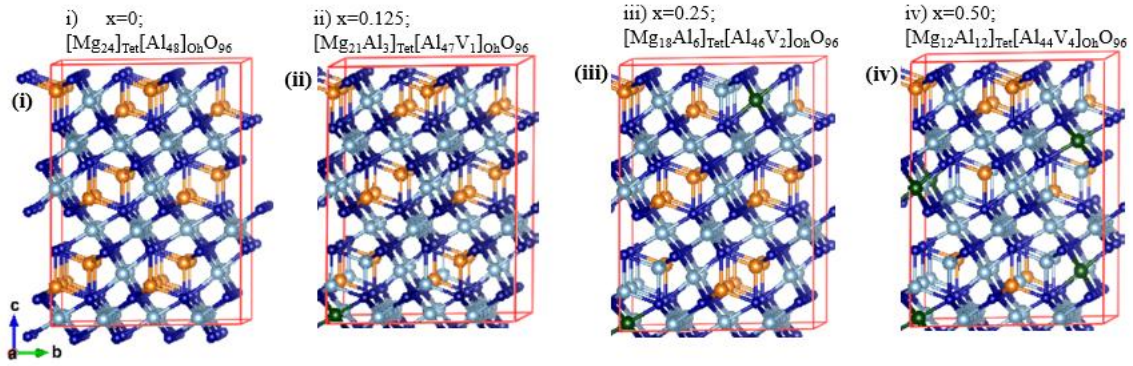

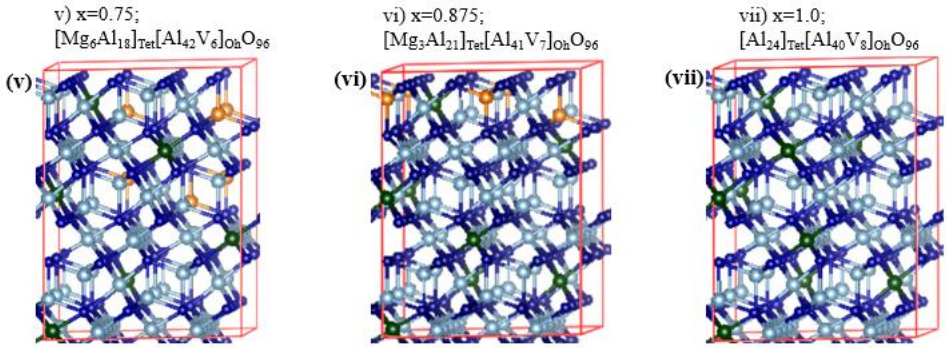

Figure 7.2: 2×2×1 hexagonal supercell models of $[Mg_{(1-x)}Al_x]_{Tet}[Al_{(2-x/3)}V_{x/3}]_{Oh}O_4$ for (i) x=0, (ii) x=0.125, (iii) x=0.25, (iv) x=0.50, (v) x=0.75, (vi) x=0.875, (vii) x=1, where orange, silver, green and dark blue balls represent Mg, Al, Vacancies and O atom/ions, respectively.

7.2.3 Computational details

All the calculations were performed by using first-principles DFT within (GGA-PBE) functionals [192]. Test calculations indicated that the plane wave pseudopotential with En_{cut}= 500 eV and En_{aug} = 750 eV is sufficient for our investigated systems. The electronic wave functions were sampled on an 8×8×3 grid with 114 ***k***-points in the irreducible Brillouin zone (BZ), generated by the Monkhorst-Pack algorithm [200]. All calculations are valid for a temperature of 0 *K* and a pressure of 0 *Pa*. The *ab initio* MD simulation uses the finite-temperature density functional theory of the one-electron states, the exact energy minimization and calculation of the exact Hellmann-Feynman forces after each MD step using the preconditioned conjugate techniques, and the Nosé dynamics for generating a canonical NVT ensemble [208]. The Gaussian smearing was employed with the width of smearing, SIGMA = 0.1 eV [204]. The *ab initio* molecular dynamics simulations were performed for 3000 steps (1.5 fs per step) at 2000 *K*.

7.2.4 Formation energy calculation

To assess the stability of the $[Mg_{(1-x)}Al_x]_{Tet}[Al_{(2-x/3)}V_{x/3}]_{Oh}O_4$ configurations, the formation energy with respect to the elemental solids and O_2 molecules, E_f (eV/f.u.) was obtained from the calculated total energy via the relation:

$$E_f = \left[E_T\left([Mg_{1-x}Al_x]_{Tet}[Al_{(2-\frac{x}{3})}V_{\frac{x}{3}}]_{Oh}[O_4]\right) - (1-x)E_T(Mg) - xE_T(Al) - \left(2-\frac{x}{3}\right)E_T(Al) - \frac{4}{2}E_T(O_2)\right]$$

…….. (7.1)

where $E_T(Mg)$, $E_T(Al)$, and $E_T(O_2)$ are the total ground state energies of elements hcp Mg, fcc Al, and O_2 molecule in their stable configurations, respectively.

7.3 Results and discussions

7.3.1 Distribution of cations in $[Mg_{(1-x)}Al_x]_{Tet}[Al_{(2-x/3)}V_{x/3}]_{Oh}O_4$

The energetics of five crystallographic non-equivalent configurations of $Mg_5Al_{18}V_1O_{32}$ were investigated to determine the distribution preference of the vacancy and substitute Al^{3+} cations in Mg^{2+} tetrahedral interstitial sites in the lattice structures. The results are shown in Figure 7.3.

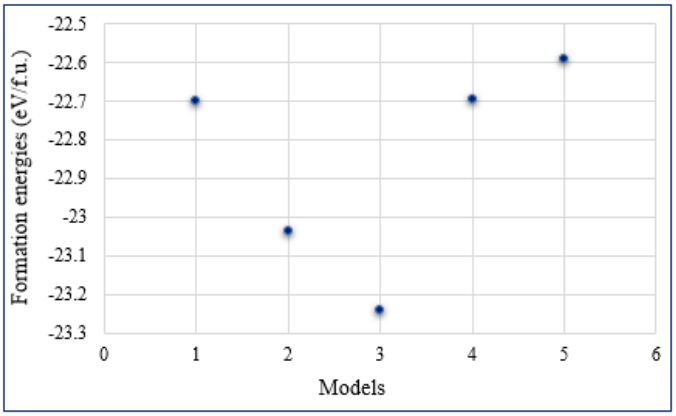

Figure 7.3: The Formation energies (eV/f.u.) of the 5 different Models of $Mg_5Al_{18}Vac_1O_{32}$ unit cell.

From Figure 7.3, our calculations showed that Model-3 has the lowest formation energy. This result indicates that the vacancy prefers to be near the outer layer of the unit cell rather than in centre of the bulk unit cell [Figure 7.3 (b) and (c)]. From comparison of Model-3 and Model-5, the vacancy also prefers to be in octahedral (Oh) interstitial site. In addition, it was proved that when there is more than one vacancy in the supercell, they should be located the most far away from each other [Chapter Six]. The substitutions of Al^{3+} cations in Mg^{2+} tetrahedral interstitial sites also show a correlation on the stability of crystal structure. In the most stable structure Model-3, substituted Al^{3+} cations for Mg^{2+} ions in tetrahedral sites preferred to situate close to outer layer along c-direction of the bulk unit cell and near vacancy [Figure 7.3 (d)]. Using the above restriction rules of cations and vacancy distribution in spinel structure the number of eligible seven configurations of stable structures using formula $[Mg_{(1-x)}Al_x]_{Tet}[Al_{(2-x/3)}V_{x/3}]_{Oh}O_4$ (x = 0.0, 0.125, 0.25, 0.5, 0.75, 0.875, 1.0) were calculated and discussed in the next section.

7.3.2 Formation, stability and chemical bonding in the series of $[Mg_{(1-x)}Al_x]_{Tet}[Al_{(2-x/3)}V_{x/3}]_{Oh}O_4$ spinels

The calculated lattice parameters, average bond lengths and formation energies of optimized $[Mg_{(1-x)}Al_x]_{Tet}[Al_{(2-x/3)}V_{x/3}]_{Oh}O_4$ (x = 0.0, 0.125, 0.25, 0.5, 0.75, 0.875, 1.0) structures are listed in Table 7.2.

Table 7.2: Calculated crystallographic parameters and formation energies (E_f) of different compositions of $MgAl_2O_4$ to γ-Al_2O_3 (x = 0.0, 0.125, 0.25, 0.5, 0.75, 0.875, 1.0), where $d_{T\text{-}O}$ and $d_{Oh\text{-}O}$ denote the average bond lengths (Å) in tetrahedral (Mg/Al-O) and octahedral (Al-O) coordination, respectively.

x	*a* (Å)	*b* (Å)	*c* (Å)	*α* (^{0})	*β* (^{0})	*γ* (^{0})	$d_{T\text{-}O}$ (Å) (average)	$d_{Oh\text{-}O}$ (Å) (average)	V (Å^3/f.u.)	E_f (eV)
0.0	11.546	11.546	14.141	90	90	120	1.964	1.937	68.109	-25.923
0.125	11.524	11.518	14.127	89.883	89.996	120.009	1.942	1.936	67.777	-25.769

0.25	11.503	11.510	14.062	89.835	89.920	120.035	1.919	1.935	67.327	-25.655
0.50	11.513	11.461	13.968	89.830	89.810	120.231	1.874	1.933	66.597	-25.547
0.75	11.391	11.383	13.869	89.884	90.153	119.966	1.830	1.931	65.283	-25.599
0.875	11.394	11.367	13.780	89.877	89.955	120.207	1.807	1.930	64.695	-25.685
1.0	11.312	11.312	13.719	89.794	90.258	120.182	1.785	1.929	63.745	-25.810

From Table 7.2, the calculated formation energies of all seven structures are negative, which indicates that the structures proposed in this work are thermodynamically stable with respect to the elemental solids and O_2 molecules.

In view of the variation of formation energies with x, it is noticed that $MgO{\cdot}nAl_2O_3$ spinel tends towards decreasing the stability up to x=0.50. But after x=0.5, increasing the Al^{3+} cations and vacancies, the formation energies tend to increase for all the models till the compositional structure of $[Mg_{(1-x)}Al_x]_{Tet}[Al_{(2-x/3)}V_{x/3}]_{Oh}O_4$ spinel completely change to γ-Al_2O_3 as x=1 [Figure 7.4 (a)].

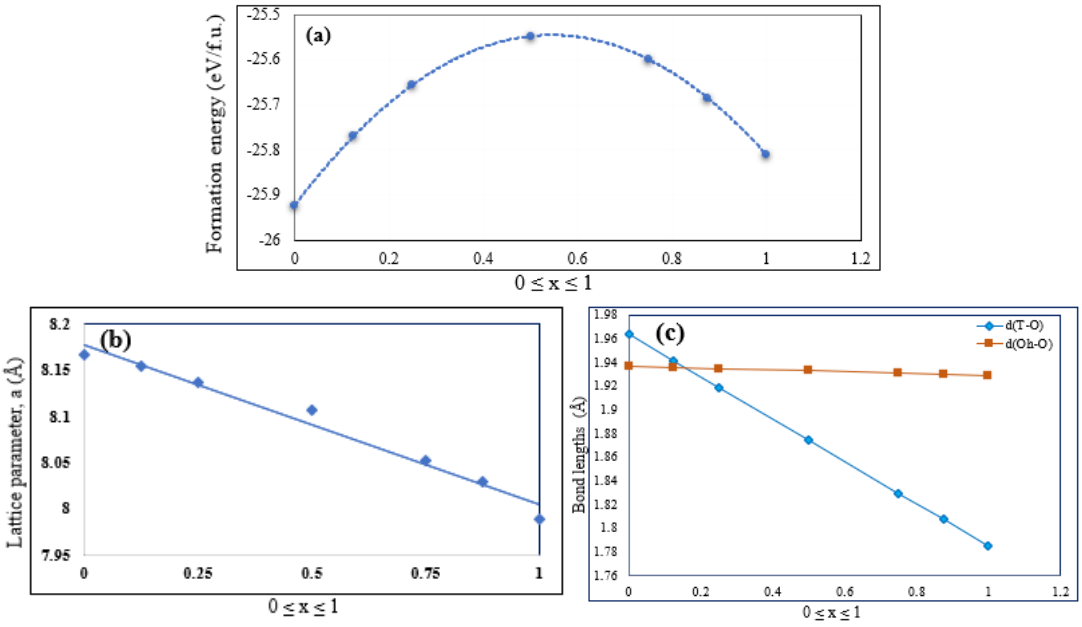

Figure 7.4: Variation of calculated (a) formation energies, E_f (eV), (b) lattice constants and (c) average bond lengths (Å) of the optimized $[Mg_{(1-x)}Al_x]_{Tet}[Al_{2-x/3}V_{x/3}]_{Oh}O_4$ (x = 0.0, 0.125, 0.25, 0.5, 0.75, 0.875, 1.0).

According to Sickafus's investigations on the structure of spinel [228], the lattice parameter [in Figure 7.4 (b)] of $MgO{\cdot}nAl_2O_3$ spinel was estimated by following formula,

$$a = 2\left(\frac{V}{Z}\right)^{1/3} \ldots\ldots\ldots\ldots\ldots\ldots (6.2)$$

Where, V is the volume of supercell after geometry optimization and Z is the number of formula unit in these supercells.

The lattice parameter as a function of composition is plotted in Figure 6.4 (b). Our calculated lattice parameter 8.16 Å of spinel $MgAl_2O_4$ is larger than 7.78 Å and 7.90 Å in the literature using DFT-LDA approaches [229, 230], but closer to experimental observed values 8.08 Å and 8.07 Å [231, 232]. With the increase of content of cation Al^{3+} and vacancies, lattice parameter of ($MgO{\cdot}nAl_2O_3$) presents a decreasing trend [Figure 7.4 (b)]. Which indicates that all seven solid solutions maintain the parent lattice structure and suggests homogeneous mixing. On the other hand, when more Mg^{2+} ions are substituted by Al^{3+} ions, the lattice is forced to contract. As a result, the bond length (Å) in octahedra (Al-O) almost keeps unchanged and the bond length (Å) in tetrahedra (Mg/Al-O) decreasing linearly with the increase in x, as presented in Figure 7.4 (c), which agrees with experimental observed results [233–235].

Therefore, the obtained results (energetics, lattice parameters and bond lengths) are comparable with experimental results. This indicates the reliability of using the formula $[Mg_{(1-x)}Al_x]_{Tet}[Al_{(2-x/3)}V_{x/3}]_{Oh}O_4$ to describe the intermediate structure by varying x from $MgAl_2O_4$ to γ-Al_2O_3 solid solution. Where, the Al^{3+} cations and vacancy distributions in tetrahedral and octahedral interstitial sites were absent in the formula $Mg_{(1-x)}Al_{2(1+x/3)}V_{x/3}O_4$ ($0 \leq x \leq 1$) used in previous literature [156, 157].

7.3.3 Electronic properties of the $[Mg_{(1-x)}Al_x]_{Tet}[Al_{(2-x/3)}V_{x/3}]_{Oh}O_4$ spinels

The effect of the composition on the electronic structure of the $[Mg_{(1-x)}Al_x]_{Tet}[Al_{(2-x/3)}V_{x/3}]_{Oh}O_4$ spinels are discussed in this section. Figure 7.5 shows the total (TDOS) and partial density of states (PDOS) for the $[Mg_{(1-x)}Al_x]_{Tet}[Al_{(2-x/3)}V_{x/3}]_{Oh}O_4$ spinels.

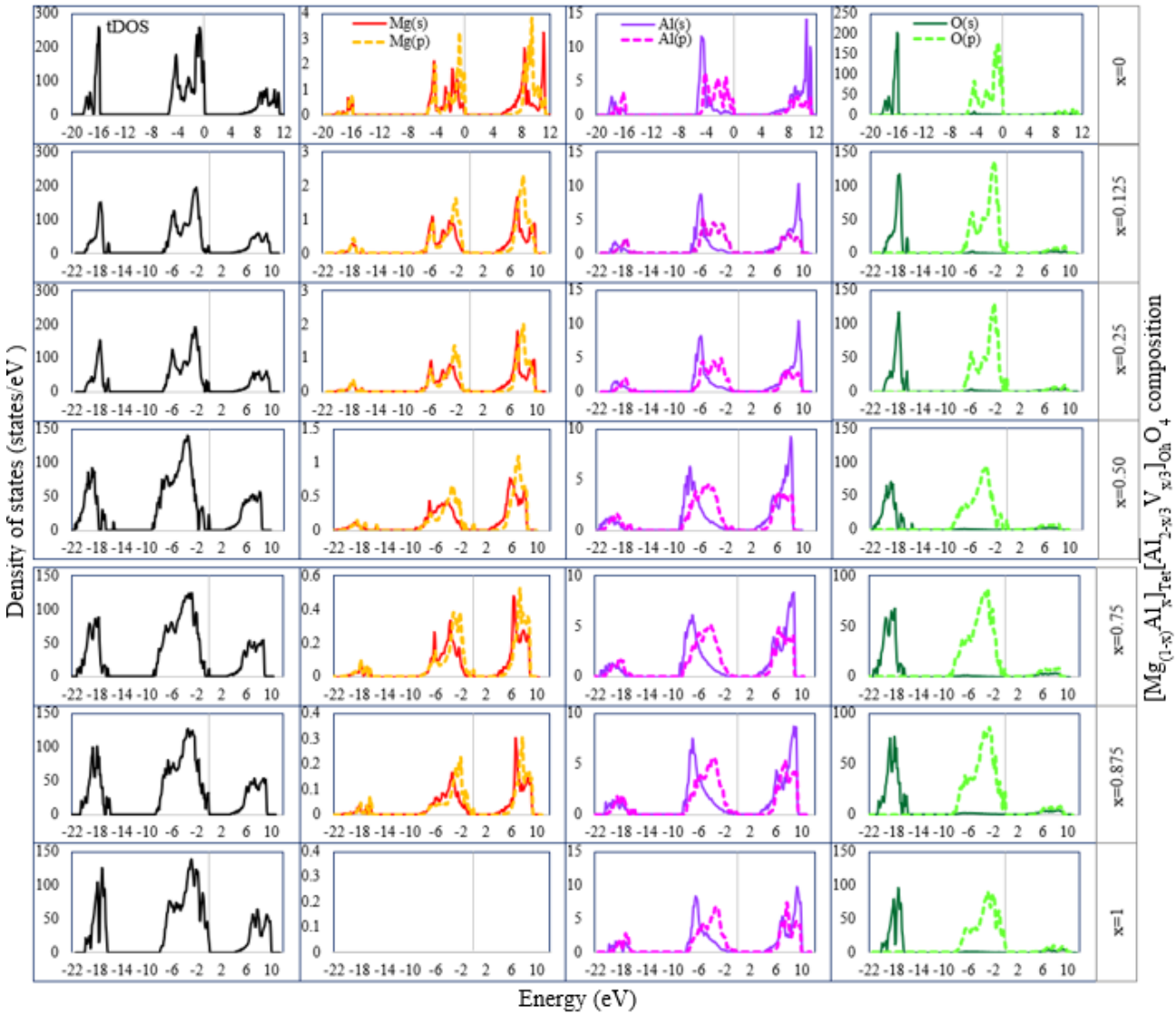

Figure 7.5: The calculated total density of states (TDOS) and partial density of states (PDOS) of the $[Mg_{(1-x)}Al_x]_{Tet}[Al_{(2-x/3)}V_{x/3}]_{Oh}O_4$ spinels.

Figure 7.5 shows the general picture of the electronic structure of the compounds. They are composed of three parts, the lower valence bands dominantly of O *2s*

states. The upper part of the valence bands are dominated by O *2p* states with some contributions from the Al-*3s 3p* or Mg-*3s 3p* states. The conduction bands are composed mainly of Al-*3s 3p* and Mg-*3s 3p* states. The bonding states in MgO·*n* Al_2O_3 spinel are formed by the interactions among the hybridization of the *2s*, *2p* orbitals from O anion and the *3s*, *3p* orbitals from Mg and Al cations.

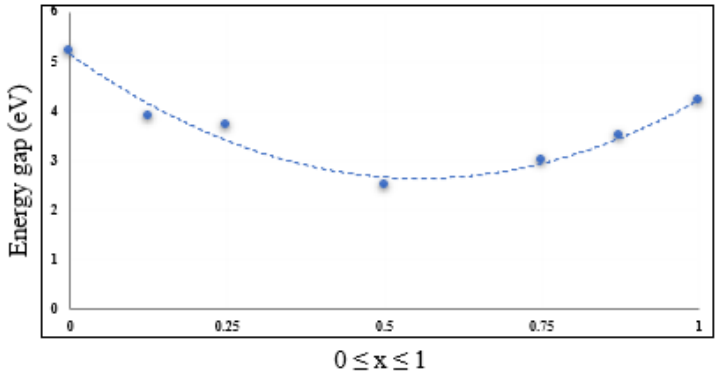

Figure 7.6: Variation of calculated energy gap as a function of x in the $[Mg_{(1-x)}Al_x]_{Tet}[Al_{(2-x/3)}V_{x/3}]_{Oh}O_4$ spinels (x = 0 to 1).

In Figure 7.6, the calculated band gaps of spinels $MgAl_2O_4$ to γ-Al_2O_3 as a function of x with different compositions are displayed. The present DFT(GGA-PBE) calculated band gap is 5.2 eV for $MgAl_2O_4$ which is smaller than the band gap (7.8 eV) observed from M. L. Bortz *et al* experimental work [218]. This smaller value is reasonable from first principle DFT calculation. From the total energy calculations [Figure 7.4 (a)] and band gaps [Figure 7.6] of $[Mg_{(1-x)}Al_x]_{Tet}[Al_{(2-x/3)}V_{x/3}]_{Oh}O_4$ shows that the most stable structure $MgAl_2O_4$ (when x=0) spinel has the largest band gap and then the spinel γ-Al_2O_3 (when x=1). The rest of intermediate structural models have the smaller band gaps which are satisfactory. And therefore, the formula $[Mg_{(1-x)}Al_x]_{Tet}[Al_{(2-x/3)}V_{x/3}]_{Oh}O_4$ is reasonable to describe the intermediate structure by varying x from $MgAl_2O_4$ to γ-Al_2O_3 solid solution.

7.3.4 *Ab initio* MD simulations of $[Mg_{(1-x)}Al_x]_{Tet}[Al_{(2-x/3)}V_{x/3}]_{Oh}O_4$ compounds

To understand the temperature effect on the stability of intermediate compositional structures of $MgAl_2O_4$ and γ-Al_2O_3 solid solution at elevated temperatures the *ab initio* MD simulation technique was applied. The resultant observations of the occupations of cations Mg, Al and vacancies at the interstitial sites at elevated temperatures were discussed in this section.

At first, *ab initio* MD simulations at temperature 1000 *K* for normal spinel $MgAl_2O_4$ (i.e., x=0) were performed. Then, equilibrated further the systems with full relaxation of the Mg, Al atoms increasing the temperature at 1500 *K* and 2000 *K*. The average temperature was examined around 1995.3 *K* for normal spinel $MgAl_2O_4$ (x = 0.0). The same method was then applied for all other compositions of $[Mg_{(1-x)}Al_x]_{Tet}[Al_{(2-x/3)}V_{x/3}]_{Oh}O_4$ (x = 0.125 to 1.0) to reach the average temperature. From the simulations, the average temperature ranges from 1991.7-1995.8 *K* were achieved for all compositions.

During the *ab initio* MD simulations at 2000 *K*, the total valence electron energies of the systems increase sharply at the first 500 steps (i.e., 0.5 ps), and then level off slowly with time [Figure 7.7]. Full relaxation of all atoms in the system causes some changes in atomic rearrangement as indicated by the energy changes [Figure 7.7]. After about 750 steps (i.e., 0.75 ps), the systems reached thermal equilibrium.

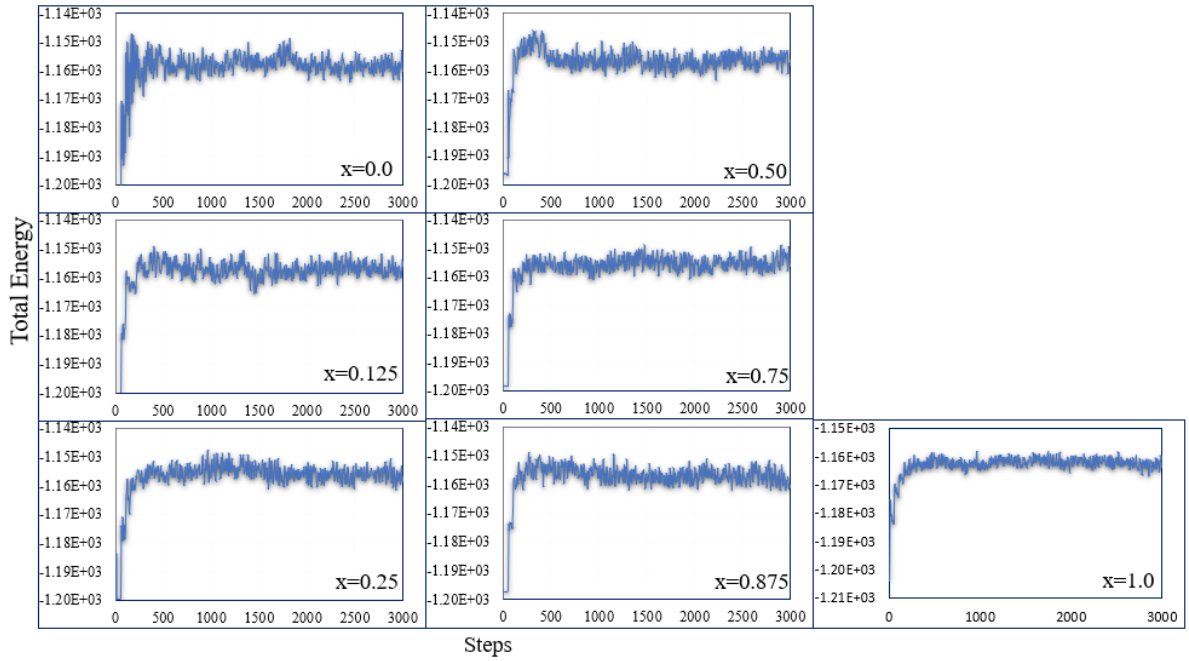

Figure 7.7. The total-valence electrons energies of the $[Mg_{(1-x)}Al_x]_{Tet}[Al_{(2-x/3)}V_{x/3}]_{Oh}O_4$ (x = 0.0, 0.125, 0.25, 0.5, 0.75, 0.875, 1.0) system as a function of steps at 2000 *K*.

From Figure 7.7, at elevated temperature, all intermediate compositional structures $[Mg_{(1-x)}Al_x]_{Tet}[Al_{2-x/3}V_{x/3}]_{Oh}O_4$ (x = 0.0, 0.125, 0.25, 0.5, 0.75, 0.875, 1.0) show average total energy ranges from -1151.3 eV to -1154.3 *eV*. Which means during *ab initio* MD simulation at elevated temperature, the Al cations and vacancies were might try to move around (i.e., even move to neighboring layers), but the numbers of Al cation and vacancies distributions at each layer were kept statistically constant [Figure 7.8 (b) and (c)].

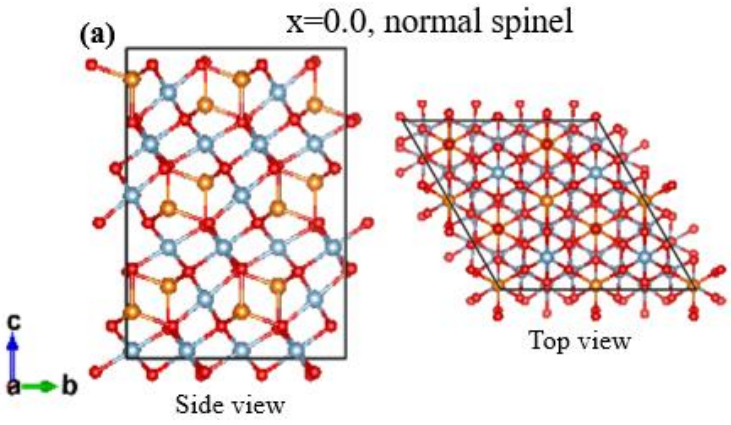

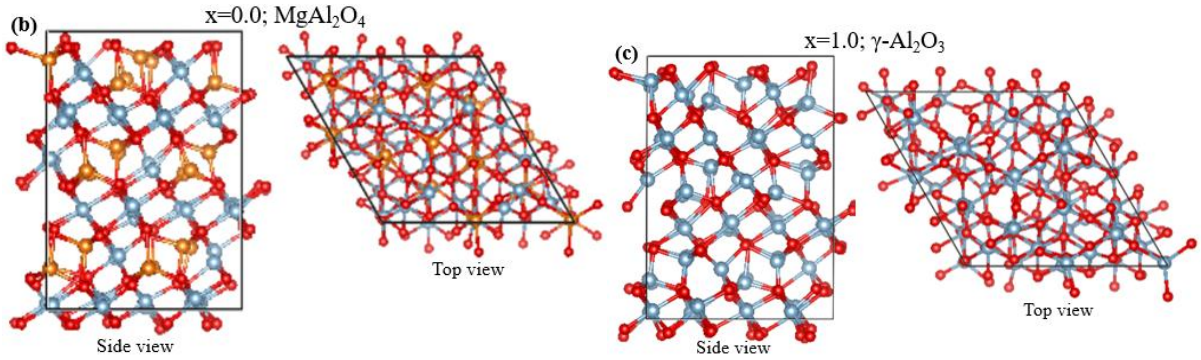

Figure 7.8: Schematic picture of (a) normal spinel $MgAl_2O_4$ at 0 *K* and 0 *P*. (b) $MgAl_2O_4$ and (c) γ-Al_2O_3 supercells after *ab initio* MD simulation at 2000 *K*. The orange, silvery and red balls represent Mg, Al and O atoms/ions respectively. The black lines represent the axis of the unit cell.

Clearly, from Figure 7.8 (b) and (c), the Mg, Al and O ions in the atomic structure are positioned orderly, close to those in the solid at 0 *K* and 0 *P* [Figure 7.8 (a)]. But at elevated temperature, the full relaxation of all atoms in the system caused some changes in atomic rearrangement i.e., created some broken bonds of cation (Mg, Al) to anion (O). A closer examination of $MgAl_2O_4$ and γ-Al_2O_3 [Figure 7.8 (b) and (c)] shows that, there are some broken bonds of Mg-O (CN-3) and Al-O (CN-3, 4 and 5) at higher temperature.

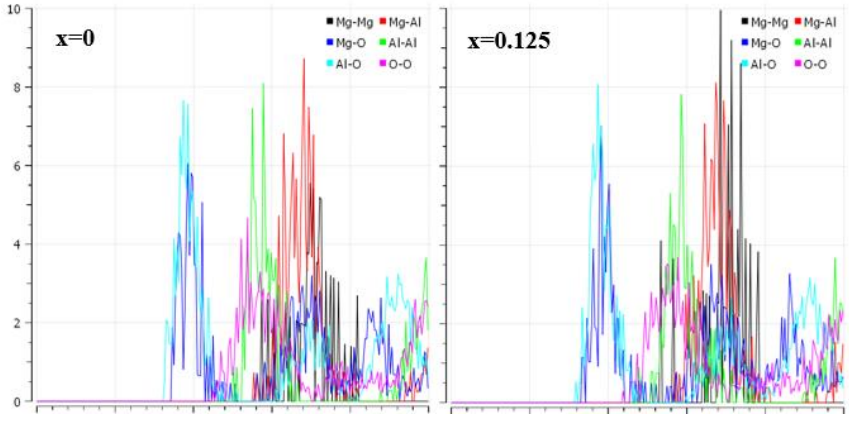

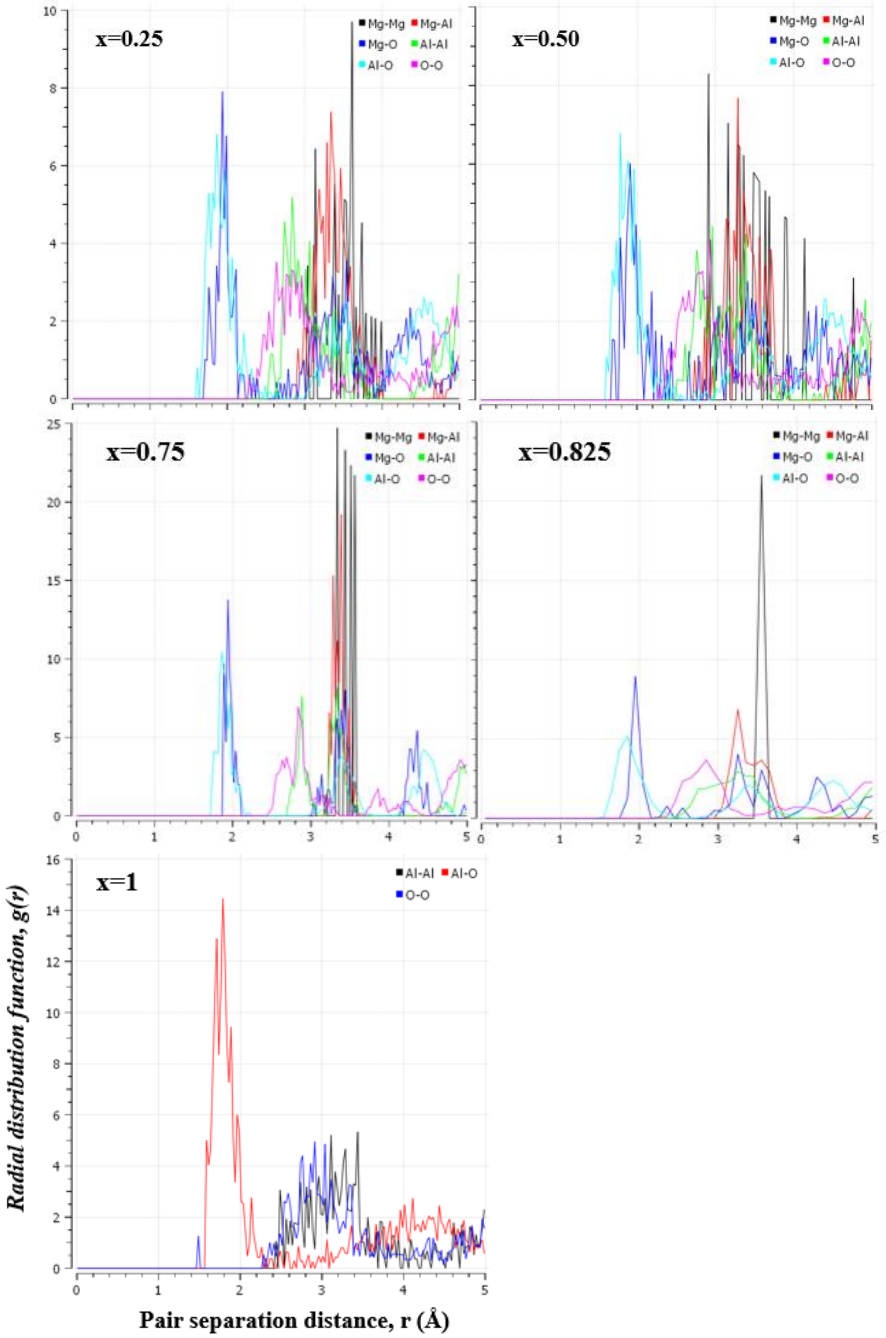

Figure 7.9: The radial distribution function *g(r)* as a function of atomic distances r (Å) of solid $[Mg_{(1-x)}Al_x]_{Tet}[Al_{(2-x/3)}V_{x/3}]_{Oh}O_4$ (x = 0.0 to 1) at 2000 *K*.

The *g(r)* provides information about interatomic distances and the coordination environment between the cation-cation, cation-anion and anion-anion in a compound structure [236]. Therefore, the radial distribution function (rdf) i.e., *g(r)* has also been calculated for all seven structures [Figure 7.9] to gain some more information about cation, anion coordination at higher temperature.

In Figure 7.9, the peak positions (different colour spectrum) indicate the distance of atomic pairs of Mg-Mg, Mg-Al, Mg-O, Al-Al, Al-O, and O-O. The cutoff distance was chosen to 5 Å, the number of histograms bins up to 200 and RDF range was 25.0. The width of peaks is related to disorder inside the material which can be structural disorder or/and atomic thermal vibration. At intermediate compositions, the peaks for M-O (here, M-Mg, Al) split into two components that can be assigned to shorter Al-O (1.6-2.2 Å) and longer Mg-O (1.7-2.3 Å) distances, indicating that the Al substitution leads to small local variations in the Mg coordination environment. During x increases, the peak intensities of Mg-Mg pairs generally decrease which is reasonable because of the Al^{3+} increases. The peaks corresponding to the Mg–Mg, Mg-Al and Mg–O pairs in close shell (< 3.2 Å) barely change after x increasing (i.e., $Al3^{+}$ increasing), implying that the local coordination environment of the transition metal mostly maintains at elevated temperature. Upon x=0.75 and x=0.875 all the peaks for Mg-Mg bond distances above 3.2 Å essentially disappear. The short Al-O pair distance is between 1.6 Å-2.2 Å which mostly stays the same for x increasing (i.e., $Al3^{+}$ increasing) in $[Mg_{(1-x)}Al_x]_{Tet}[Al_{(2-x/3)}V_{x/3}]_{Oh}O_4$ structures during the elevated temperature. The coordination number (CN) of Mg-O and Al-O can be calculated from the integral of over their first peak respectively from the Figure 7.9 for all compositions. For x=0, i.e., spinel $MgAl_2O_4$ (when, x=0), the calculated average CN for Mg-O is 2.5-3 at elevated temperature, which is smaller than the crystalline coordination of 4. This indicates that there are some broken bonds of Mg-O are created during such higher temperature. Same CN disorder observed for Al-O (i.e., 4.5-5) which is smaller than the crystalline coordination 6 indicating broken bonds. These presented radial distribution function analysis indicates that Mg, Al cations and vacancies were distributed homogeneously in computed intermediate structures of $MgAl_2O_4$ to γ-Al_2O_3 lattice framework using the formula $[Mg_{(1-x)}Al_x]_{Tet}[Al_{(2-x/3)}V_{x/3}]_{Oh}O_4$ even at higher temperature.

Finally, the mean squared displacement (MSD) of spinel $MgAl_2O_4$ and γ-Al_2O_3 were also calculated to describe thermal stability. The Open Visualization Tool (OVITO) was used for data visualization and post-processing analysis. and the MSD of every atom in the system was calculated from these trajectories.

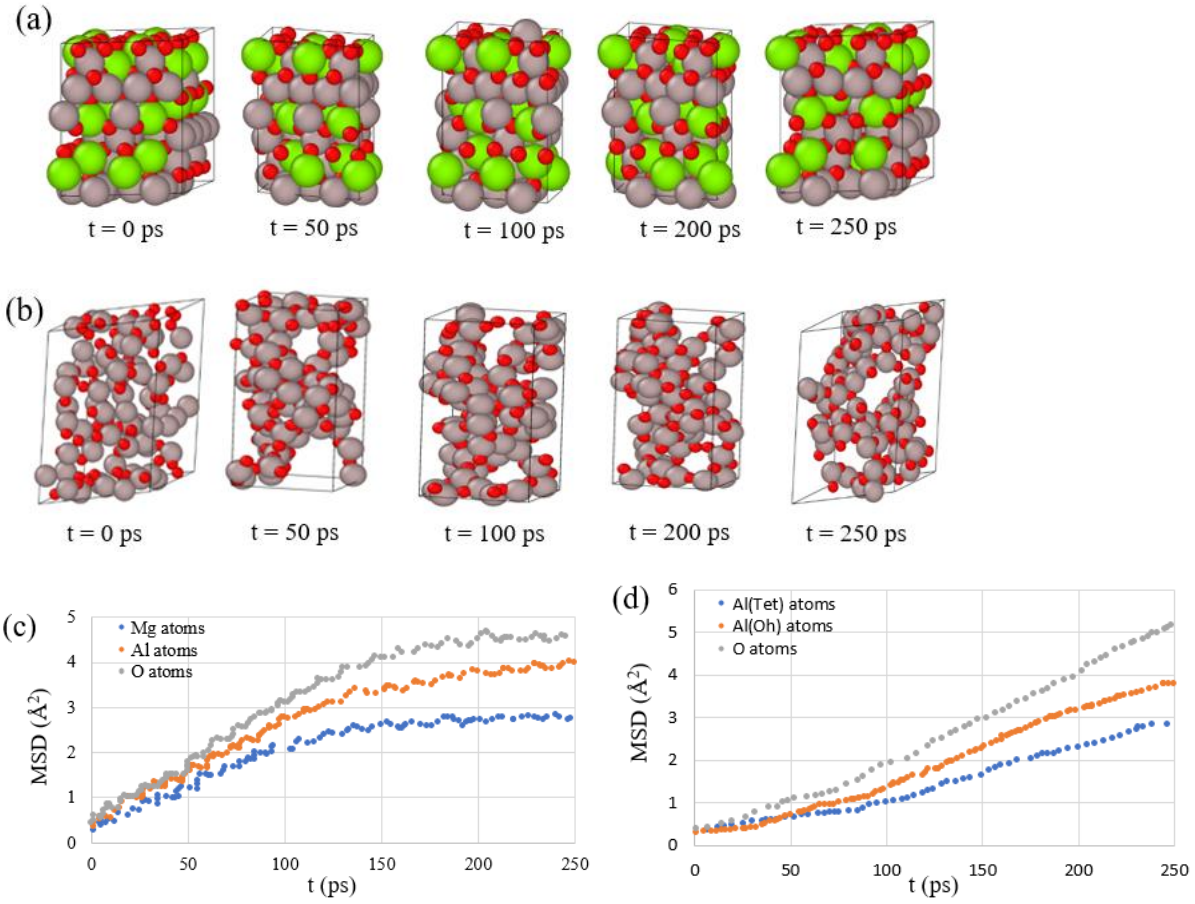

Figure 7.10: Snapshots of (a) $MgAl_2O_4$ and (b) γ-Al_2O_3 during MD simulations. Green, silver, and red spheres are Mg, Al, and O atoms respectively. Mean squared displacements of Mg, Al, and O atoms in (c) $MgAl_2O_4$ and (d) γ-Al_2O_3 spinels.

The structures were reached at the end of the thermal equilibration (i.e. after 250 ps) was compared. As shown in figure 7.10 (c) for T = 2000 K, the MSD increases with time, indicating that the atoms are migrating through the simulation cell. For $MgAl_2O_4$, for all atoms, the MSD increase slowly with time until 150 ps. After that time all atoms are found to be stable situations. But for γ-Al_2O_3, the MSD

increases linearly for all atoms with time. This increasing is happening because inside γ-Al_2O_3 structures there are some vacancies which causes the migration of Al(Tet), Al(Oh) and O atoms at higher temperature. Therefore, from the MSD analysis there is some diffusion was also happening.

7.4 Conclusions

In this work, the Al_2O_3 rich spinels in the $MgAl_2O_4$ to γ-Al_2O_3 solid solution was described with molecular formula $[Mg_{(1-x)}Al_x]_{Tet}[Al_{(2-x/3)}V_{x/3}]_{Oh}O_4$ (here, x=0 to 1). The first- principles DFT calculations verified that Mg and substitute Al atoms occupy the tetrahedral sites while the cation vacancies tend to reside on octahedral sites in the intermediate compositional structural models of $MgAl_2O_4$ to γ-Al_2O_3 solid solution spinel. Moreover, the vacancies prefer to situate around outer layer rather than the centre of the bulk unit cell and position of substituted Al^{3+} ions for Mg^{2+} ions in tetrahedral sites prefer to situate near the vacancies. Restricted by these rules of cations Mg^{2+}, Al^{3+} and vacancies in tetrahedral and octahedral sites, with reasonable formula $[Mg_{(1-x)}Al_x]_{Tet}[Al_{(2-x/3)}V_{x/3}]_{Oh}O_4$ (x = 0.0, 0.125, 0.25, 0.5, 0.75, 0.875, 1.0) seven redefined supercells were built efficiently. A series of first principle DFT calculations have been performed to investigate the composition dependence of structure and properties in intermediate compositions of $MgAl_2O_4$ to γ-Al_2O_3 solid solution. The calculated results demonstrated that the lattice parameter decreased with the increase of x in the composition of $MgAl_2O_4$ to γ-Al_2O_3 solid solution spinel. From the electronic structure calculations, the bonding states in alumina-rich spinel were formed by the interaction among the hybridization of *2s*, *2p* orbitals from O anion and *3s*, *3p* states of both Mg and Al cations. The conduction bands (CB), which mainly originated from *3s*, *3p* states of both Mg and Al atoms, showed a similar profile in TDOS of these models, while the valence bands (VB) presented a downward shift to low energy with the increasing of x.

Ab initio MD simulation also applied to see the temperature effect on the Mg, Al cation and vacancy distribution in the $[Mg_{(1-x)}Al_x]_{Tet}[Al_{(2-x/3)}V_{x/3}]_{Oh}O_4$ solid solution spinels (x =0 to 1) at high temperature. After full relaxations at elevated temperature the radial distribution function *g(r)* analysis shows that Mg, Al cations and vacancies distributed homogeneously in present computed seven redefined supercell models. The cation (i.e., Mg and Al atoms) and anion (i.e., O atoms) migration in spinel $MgAl_2O_4$ and γ-Al_2O_3 were also discussed by the mean squared displacement (MSD) analysis. The outcome of MD simulation indicates regular, periodic solid solution homogeneously even at higher temperature.

The overall theoretical research presented in this work offers a deep insight into the relationship among composition, structure and electronic properties of the $MgAl_2O_4$ to γ-Al_2O_3 solid solution spinels using the formula $[Mg_{(1-x)}Al_x]_{Tet}[Al_{(2-x/3)}V_{x/3}]_{Oh}O_4$. This present understanding offer guidance for the rational compositional design of not only for $MgAl_2O_4$ to γ-Al_2O_3 composition, but also other dependent spinel-type disordered solid solution structures with desirable properties.

Chapter Eight

Structural chemistry and electronic properties of MgO and γ-Al_2O_3 surfaces

8.1 Introduction

The metastable phase γ-Al_2O_3 have been intensively studied in recent years and is regarded as one of most prominent materials in various industrial applications [10-13, 120, 121]. Most of these applications depend on the nature of specific γ-Al_2O_3 surfaces and their properties. Therefore, knowledge about the surface structure is crucial for many related applications.

Revisiting the existing structural models of γ-Al_2O_3 in the literature [28, 105, 107, 114, 119-147] the present study (Chapter Six) proposed that spinel γ-Al_2O_3 in the hexagonal lattice with Al vacancies at the octahedral sites is a preferred model. Figure 8.1 (a) shows the hexagonal γ-Al_2O_3 lattice structure along its (0001) orientation. The oxygen sublattices has the (ABCABC….) stacking series [Figure 8.1 (b)]. The Al ions occupy the interstitial sites of the neighbouring O layers in two different ways and thus, there are two types of Al layers [Figure 8.1 (a)]. At the Al1 layer, which is below the O1 layer, the Al ions occupy two thirds of the octahedral sites. The Al2 layer below the O2 layer [Figure 8.1 (a)] is composed of three sublayers: a sublayer of octahedrally coordinated Al being sandwiched by two tetragonally coordinated Al sublayers [Figure 8.1 (a)]. Such rich Al/O arrangements in the γ-Al_2O_3 phase shall have impacts on the catalyst and catalytic support activities in experiments as well as surface related applications.

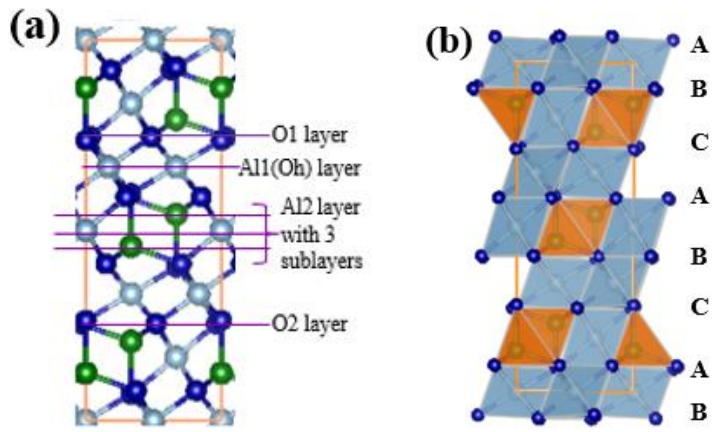

Figure 8.1: Schematic structure of (a) hexagonal γ-Al_2O_3 along its (0001) orientation and (b) the ABCABC stacking series. Al[Tet] and Al[Oh] bonded with four and six O anions, respectively. The green, silver and dark blue spheres represent the Al(Tet), Al(Oh) and O atom/ion respectively. The orange lines represent the axis of the unit cell. The labels Al1(Oh), Al2, O1 and O2 represent the Al sublayers and O layers in the structure, respectively.

In this chapter the first-principles DFT method was applied within GGA-PBE approximation [192] to investigate the stability of hexagonal γ-Al_2O_3 along (0001) polar and defective non-polar surfaces with possible Al/O terminations.

First, the MgO (001) surfaces of different thickness with their stability were investigated as tests. The first-principles DFT calculations were performed with relaxation of atomic coordinates with the settings based on the convergence test of the corresponding surface unit cell. The MgO (111) surface contains either Mg or O atoms in each atomic layer at the surface known as polar surface. Such polar surfaces are not stable for large crystal sizes [240]. Then, MgO (111) polar and defective-polar surfaces were discussed with Mg/O termination to validate the method. The reason of using MgO surfaces in the present work was that MgO has the simple rocksalt-type structure and has been used as a model system in the study of surfaces for several decades [169, 237-239].

The theoretical simulations based on first-principles DFT in the present work will provide a potential possibility to give a new aspect to surface structures of γ-Al_2O_3. The stability and electronic structures of MgO and γ-Al_2O_3 surfaces were analysed in detail in this chapter.

8.2 Methods

8.2.1 Preparing MgO (001) and (111) Surfaces:

To calculate the energies of the MgO surfaces using quantum mechanics-based methods, appropriate supercells need to be constructed which are always stoichiometric and periodic in three dimensions. These cells include two surfaces, separated by a slab of vacuum which is thick enough to render the interaction between the surfaces negligible.

For the MgO (001) surfaces 1×1 fcc (conventional) bulk unit cell was used based on its bulk structure with a lattice parameter, a=4.22 Å from the first-principles DFT(GGA-PBE) calculation as shown in chapter five [Figure 8.2 (a)]. A MgO (001) surface model-1 [Figure 8.2 (b)] was built which has a length of c-axis over 19.23 Å (3 atomic layers slab and 15 Å vacuum), each layer has 2 Mg atoms and 2 O atoms. For model-2, -3 and -4 [Figure 8.2 (c), (d) and (e)], the 3 atomic layers supercell slab were kept but increased the vacuum thickness in c-direction to 18, 20 and 22 Å respectively to test the influence of vacuum thickness on the calculations. For model -5, -6 and -7, then 6, 8 and 10 atomic layers slab were used respectively with 22 Å vacuum thickness [Figure 8.2 (f), (g) and (h)]. These different surface models will help to get insight into convergence of the MgO slab.

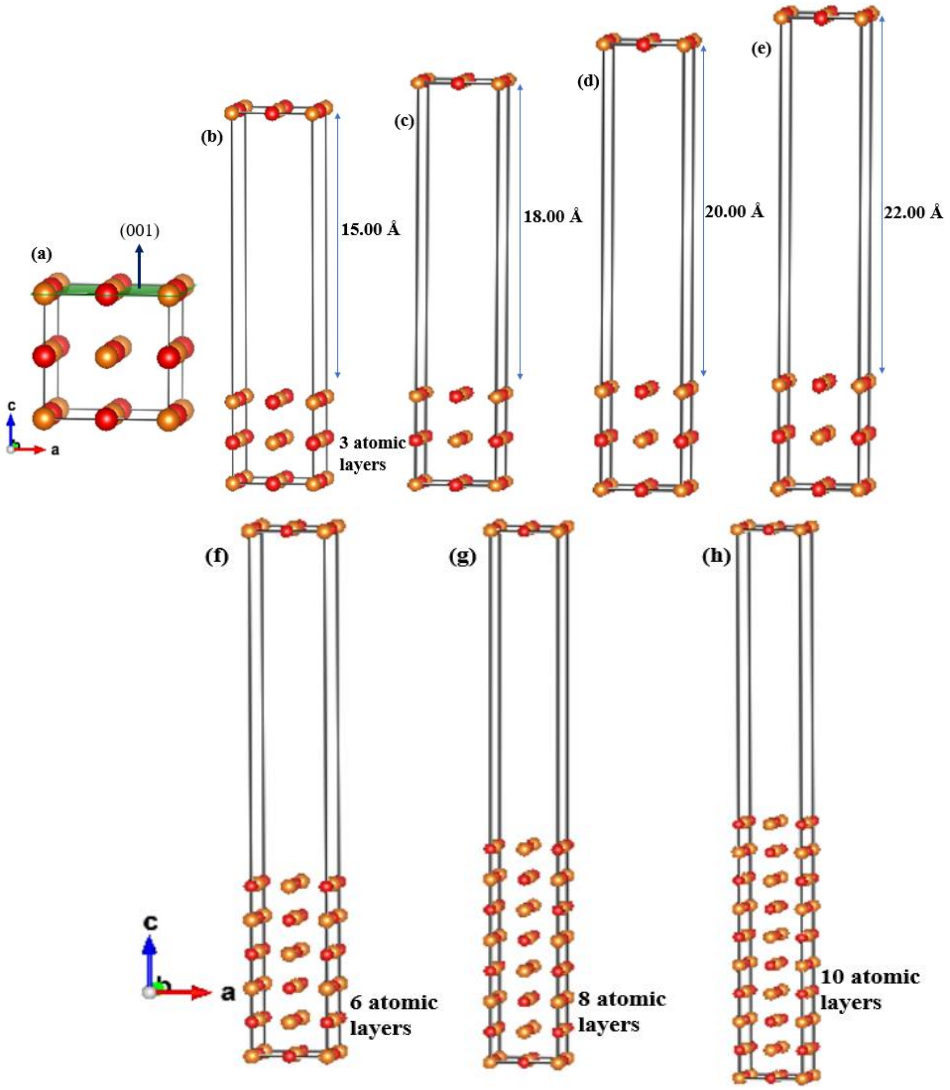

Figure 8.2: Configuration of (001) MgO surfaces. Subfigure (a) 1×1 fcc (conventional) bulk unit cell. MgO (001) surfaces of 3 atomic layers slab where (b) model-1: 15 Å vacuum, (c) model-2: 18 Å vacuum, (d) model-3: 20 Å vacuum and (e) model-4: 22 Å vacuum, thickness respectively. For (f) model-5: 6 atomic layers slab, (g) model-6: 8 atomic layers slab and (h) model-7: 10 atomic layers slab, respectively with 22 Å vacuum thickness. Orange and red balls represent Mg and O atoms, respectively.

The polar MgO (111) surface is shown in Figure 8.3 (a). The stacking order along the <111> axis is ...AcBaCb..., whereby A, B, C represent Mg atoms and a, b, c represent O atoms. Therefore, the MgO (111) atomic layers consist entirely of either Mg or O atoms and are alternating as ...MgOMgOMgO... [Figure 8.3 (a)

and (b)]. To investigate feasible (111) defective surfaces, first 2×2×4 supercell [Figure 8.3 (b)] was built which has length of c-axis over 29.362 Å based on 1×1×1 hexagonal unit cell [Figure 8.3 (a)]. Then from 2×2×4 supercell, removed ¾ of atoms from bulk structure and created a polar (111) surface slab contains 6 atomic layers and 22.022 Å vacuum (i.e., 3/4 of the length of the c-axis) [Figure 8.3 (c)]. Here the polar (111) surface slab has two fully occupied surfaces, one surface contains only 4-Mg atoms and the other only 4-O atoms. Half the Mg atoms from the Mg top layer are moved to the other side of the slab and added in the empty Mg layer on top of the O surface layer, as shown in Figure 8.3 (d). This MgO (111) surface was referred as to MgO (111)-Mg terminated defective surface. Both surfaces in the calculation cell are now equivalent and partially Mg-terminated. For MgO (111)-O terminated defective surface can be constructed analogously. Half the O atoms from the O top layer are moved to the other side of the slab and added in the empty O layer on top of the Mg surface layer, as shown in Figure 8.3 (e). The defective (111) surfaces were created by followed from C. Fang *et al* work [240].

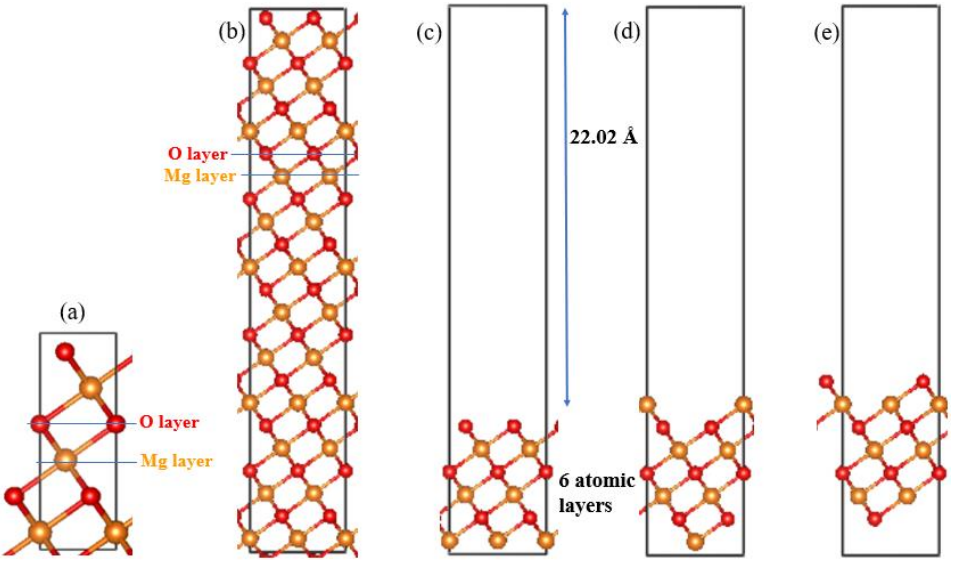

Figure 8.3: Configuration of (111) MgO surfaces. Subfigure (a) 1×1×1 hexagonal unit cell, (b) 2×2×4 supercell, (c) polar (111) surface slab contains atoms 1/4 of

the slab and a vacuum ¾ of slab along c-direction. The subfigures (d) MgO (111)-Mg and (e) MgO (111)-O terminated defective surfaces.

8.2.2 Preparing hexagonal γ-Al_2O_3 (0001) Surfaces:

Based on the hexagonal γ-Al_2O_3 cell with homogeneously distributed Al(Oh) vacancies from Chapter Six, first a 2×2×3 bulk supercell [Figure 8.4 (a)] was built which has length of c-axis being 40.818 Å. Then from 2×2×3 bulk supercell 2/3 of atoms were removed and created a polar (001) surface contains 12 atomic layers slab (160 atoms) and a vacuum of 2/3 (27.212 Å) of the length of the c-axis [Figure 8.4 (b)]. In Figure 8.4 (b), the polar hexagonal γ-Al_2O_3 (0001) surface slab has 4 different fully occupied surfaces, (i) one surface contains only 12 Al atoms in pure octahedral sites named Al1(Oh) terminated surface, (ii) one contains 8 Al atoms in tetrahedral sites and 4 Al atoms in octahedral sites named Al2(Oh_Tet) terminated surface, (iii) one contains 16 O atoms on top of Al1(Oh) layer [i.e., on bottom of Al2(Oh_Tet) layer] named O1 terminated surface and (iv) the other contains 16 O atoms on top of Al2(Oh_tet) layer [i.e., on bottom of Al1(Oh) layer] named O2 terminated surface. Therefore, several defective surfaces are possible with different surface termination layers.

To create the defective surfaces, from the Al1(Oh) top layer surface of polar surface slab in Figure 8.4 (b), half of the Al1(Oh) atoms are moved to the other side of the slab i.e., added in the empty Al1(Oh) layer on top of the O2 surface layer in two different ways, as shown in Figure 8.4 (c) and (d). These surfaces were referred as 1Al1(Oh)_surface [Figure 8.4 (c)] and 2Al1(Oh)_surface [Figure 8.4 (d)]. Both surfaces in the calculation cell are now equivalent and partially Al1(Oh)-terminated.

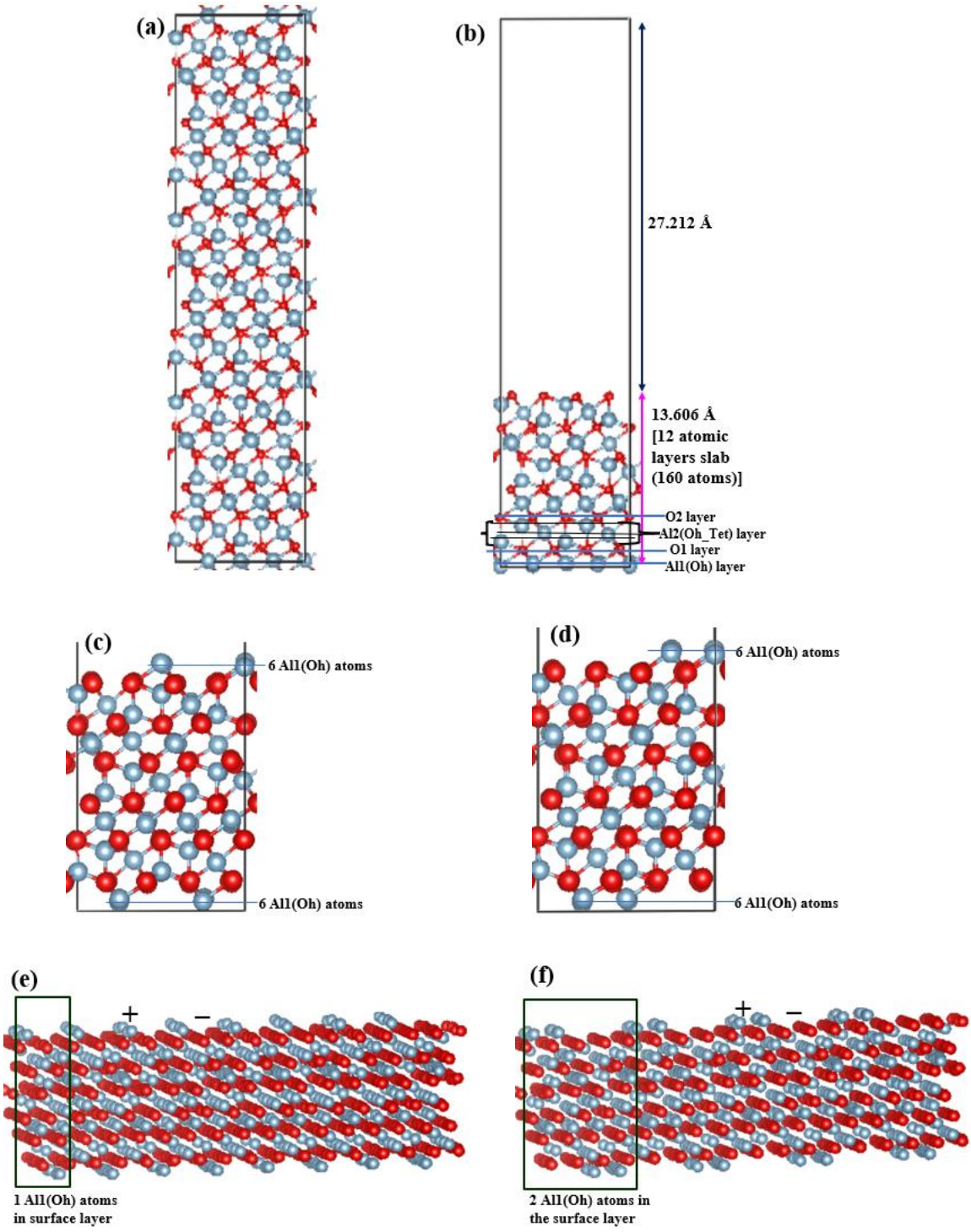

Figure 8.4: Side view of hexagonal γ-Al_2O_3 along (0001) surfaces. Subfigures: (a) 2×2×3 hexagonal bulk supercell, (b) polar surface slab contains 1/3 length of c-axis filled with the atoms and 2/3 of vacuum, (c) 1Al1(Oh) defective surface, (d) 2Al1(Oh) defective surface, (e) and (f) Three-dimensional schematic showing

the nanopatterning based on the domain model 1Al1(Oh) and 2Al1(Oh) defective surfaces respectively.

To create the Al2(Oh_Tet) defective surfaces, the surface slab named Al2(Oh_Tet) polar surface slab [Figure 8.5 (a)] was used. 4 Al(Tet1) atoms from the top layer of Al2(Oh_tet) polar surface slab are moved to the other side on top of O1 layer of the slab and named Al2(Tet1) defective surface [Figure 8.5 (b)]. For the next defective surface, 4 Al(Tet2) atoms from the top layer of Al2(Oh_tet) polar surface slab are moved to the other side on top of O1 layer of the slab and named Al2(Tet2) defective surface [Figure 8.5 (c)]. To create Al2(Oh) defective surface, 4 Al(Oh) atoms from the top layer of Al2(Oh_tet) polar surface slab are moved to the other side on top of O1 layer of the slab [Figure 8.5 (d)]. The Al2(Oh_Tet) defective surface was created by moving half of Al(Oh) and Al(Tet) atoms from the top layer of Al2(Oh_tet) polar surface the other side on top of O1 layer of the slab [Figure 8.5 (e)]

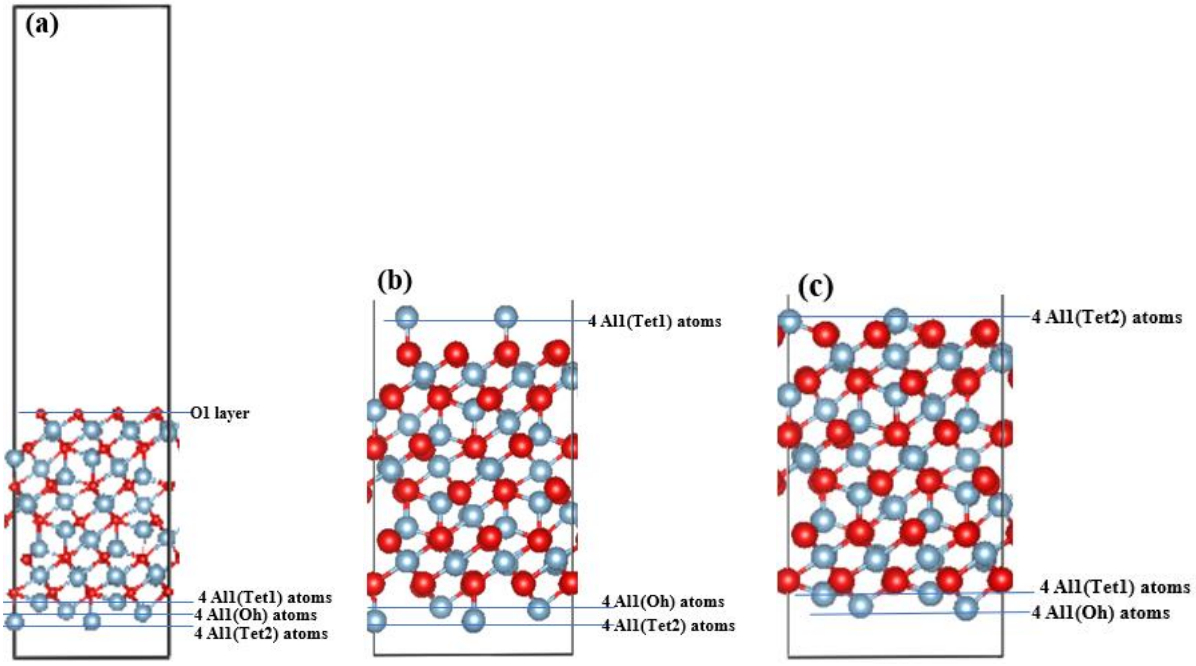

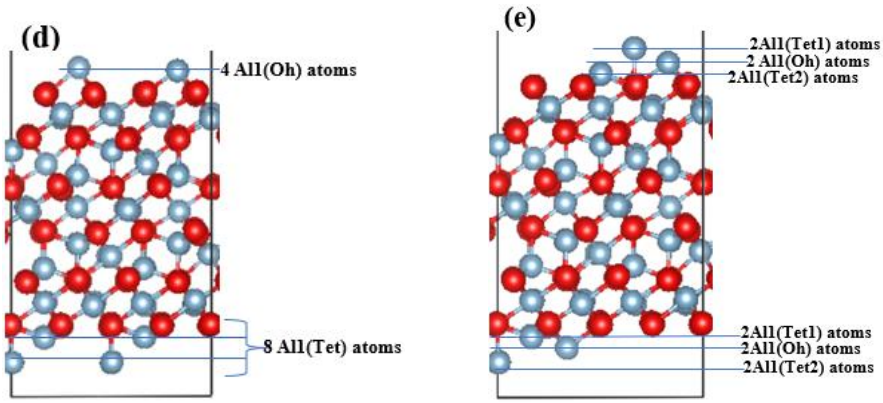

Figure 8.5: Configuration of side view of (a) polar surface slab used to prepare Al2(Oh_Tet) defective surfaces, (b) Al2(Tet1) defective surface, (c) Al2(Tet2) defective surface, (d) Al2(Oh) defective surface and (e) Al2(Oh_Tet) defective surface.

The surface slabs named O1 and O2 polar surface slab [Figure 8.6 (a) and (d)] were used to create the O1 and O2 defective surfaces respectively. Half of the O 1 and O2 atoms (i.e., 8 atoms) moved to the other side of the top layers in two different ways for each surface [Figure 8.6 (a)-(f)]. These defective surfaces are named as 1O1 defective surface [Figure 8.6 (b)], 2O1 defective surface [Figure 8.6 (c)], 1O2 defective surface [Figure 8.6 (e)]and 2O2 defective surface [Figure 8.6 (f)].

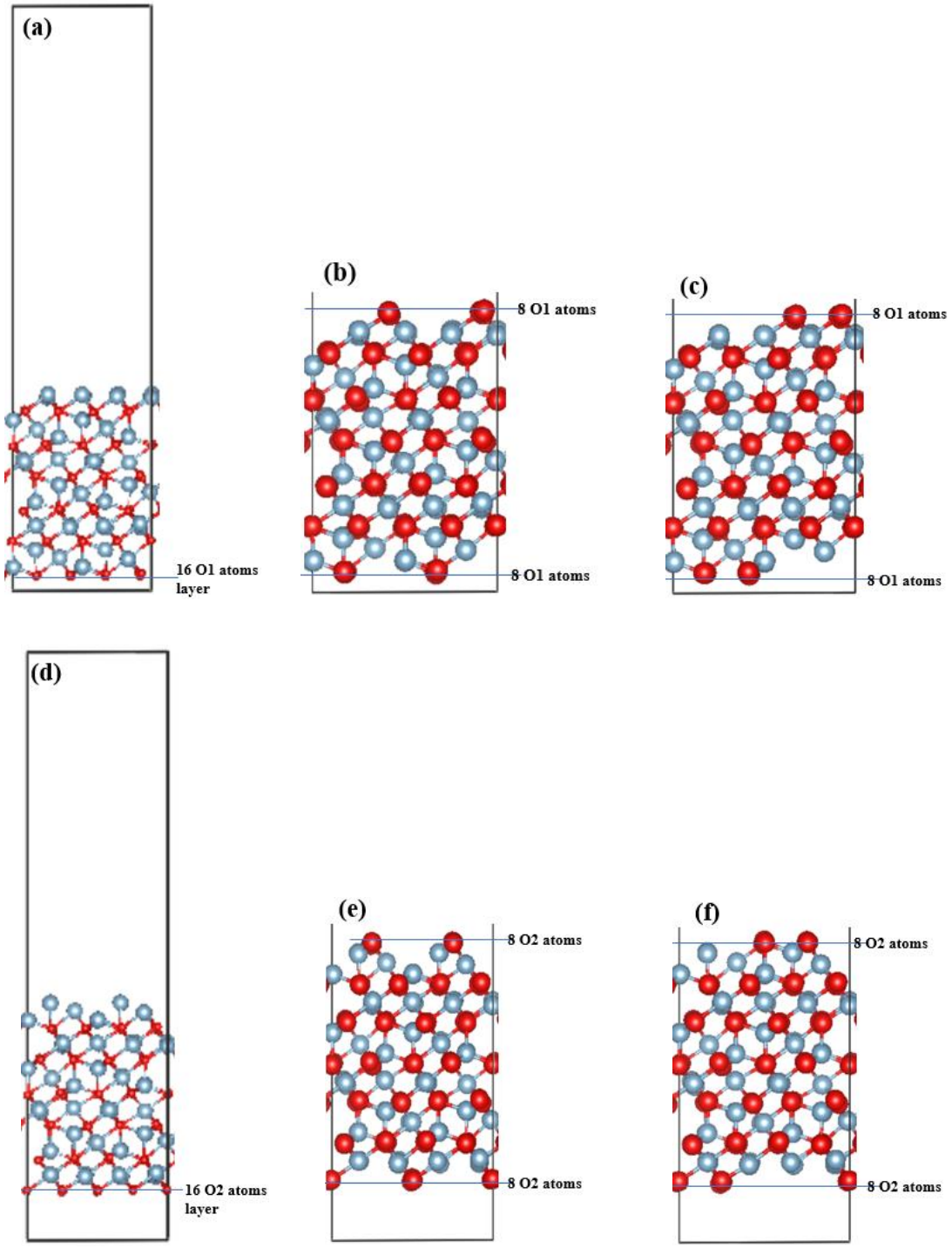

Figure 8.6: Configuration of side view of (a) polar surface slab used to prepare O1 defective surfaces, (b) 1O1 defective surface, (c) 2O1 defective surface, (d) polar surface slab used to prepare O2 defective surfaces (e) 1O2 defective surface and (f) 2O2 defective surface.

8.2.3 Computational details:

All calculations have been performed using the first-principles DFT within the GGA-PBE approximations [192]. The cut-off energies of the wave functions and the augmentation functions were set to be En_{cut} = 400.00 eV and En_{aug} = 650.00 eV, respectively. The electronic wave functions were sampled on 20×20×1, 16×16×1, and 8×8×1 ***k***-meshes in the irreducible Brillouin zone (BZ) for MgO (001) and (111) surfaces and hexagonal γ-Al_2O_3 along (0001) surfaces respectively using the Monkhorst and Pack method [200] in correspondence with that of the bulk. Different ***k***-meshes for supercell slab, as well as cut-off energies and augmentation waves were tested. The tests of ***k***-mesh and cut-off energies showed good convergences (within 1meV/atom). The atomic coordinates of the surface models have been fully relaxed in the DFT total energy calculations.

8.2.4 Calculate surface energies and surface relaxation energies:

The surface energies for MgO (001) and (111) were calculated for the relaxed surface structures. Using the standard method [241], the surface energy γ_{surf} was calculated from the following formula,

$$\gamma_{surf} = \frac{1}{A} \lim_{N\to\infty} \frac{1}{2} (E_{slab}^{N} - NE_{bulk}) \qquad \text{.....} \qquad (8.1)$$

Where, A is the slab area, E_{slab}^{N} is the total energy of the N-atom relaxed slab and E_{bulk} is the bulk total energy. Here the limit is approximated with the Nth term. The surface energy is normally used to predict the stability of the surface. The larger the value is, the less stable is the surface.

The surface relaxation energy E_{relax} per unit volume was also calculated for the surfaces in this work is defined according to D.-N. Zhang *et al* [243] by following relationship:

$$E_{relax} = \frac{1}{2A}(E_{unrelaxed} - E_{slab}) \qquad \ldots\ldots\ldots\ldots\ldots\ldots \qquad (8.2)$$

Where $E_{unrelaxed}$ is the energy of the unrelaxed surface without relaxation which is half of the related cleavage energy of the crystal.

8.3 Results and discussions:

8.3.1 MgO (001) and (111) surfaces:

8.3.1.1 Energetics and local Structure:

To determine thickness effect for simulating MgO (001) surface slab, on the surface energies (equation 8.1) 7 different structures of MgO (001) surfaces were calculated. And the thickness of a slab can be expressed in terms of a number of atomic layers. The effects of these variables on the surface energy were presented to determine the model structure. Calculations have been performed for a variety of different vacuum widths (15-22 Å) and slab thicknesses of 3, 6, 8 and 10 layers [Figure 8.7 (a) and (b)].

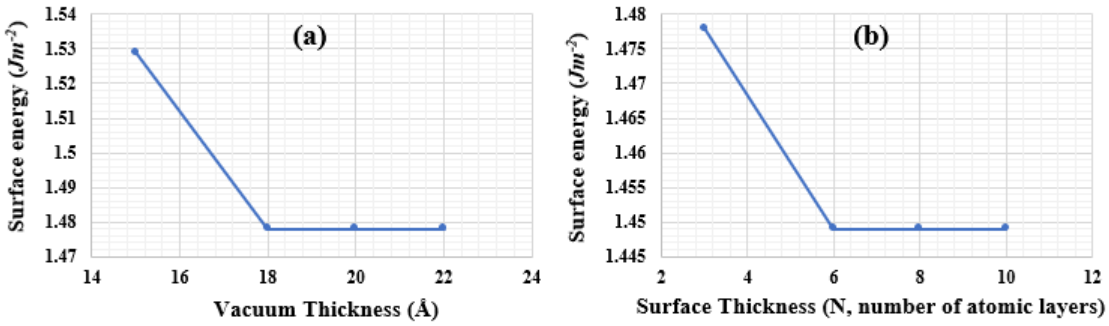

Figure 8.7: The variation of surface energy, γ_{surf} of MgO (001) surfaces as a function of (a) vacuum thickness and (b) slab thickness.

From Figure 8.7 (a) and (b), the surface energy for different MgO (001) slabs converged rapidly to a certain value with increasing the vacuum and slab thickness. From Table 8.1, the surface energy of MgO (001) surface with 22 Å vacuum and 6 layers atomic thickness is 1.449 Jm^{-2} which 4% larger than D.-N.

Zhang *et al* DFT work (1.38 Jm^{-2}) [243] where they used 15 Å vacuum and 13 atomic layers of thickness. From Figure 8.7 and following Table 8.1, the surface energies for vacuum thickness of 22 Å with 6, 8 and 10 atomic layers of slabs are identical. Therefore, for MgO (111) surfaces slabs 6 atomic layers and 22.02 Å vacuum thickness were used for DFT calculation.

Table 8.1: Convergence of the surface relaxation energy for MgO (001) slabs with respect to the vacuum and slab thickness.

MgO (001) surfaces	Vacuum thickness (Å)	Slab (N, number of atomic layers)	Surface energy (Jm^{-2})	Surface relaxation energy (Jm^{-2})
Model-1	15	3	1.529	0.051
Model-2	18	3	1.478	0.048
Model-3	20	3	1.478	0.048
Model-4	22	3	1.478	0.048
Model-5	22	6	1.449	0.045
Model-6	22	8	1.449	0.045
Model-7	22	10	1.449	0.045
Experiment [242]			1.12	
Other DFT(FPLAPW[1]) -GGA [243]	15	13	1.38	0.046

[1]full potential linearized augmented plane wave (FPLAPW) method

The first-principles DFT(GGA-PBE) calculated results of MgO (001) and (111) surface models are summarized in Table 8.2.

Table 8.2: Calculated results of MgO (001), polar (111), defective (111)-Mg and defective (111)-O terminated surfaces.

MgO surfaces	Mg-O atomic distances (Å) in top surface and subsurface layer	Surface energy (Jm^{-2})	Surface relaxation energy (Jm^{-2})
Present work			
(001)	-	1.449	0.045
Polar (111)	unstable	unstable	-
defective (111)-Mg Figure 7.3 (d)	Mg-O:1.896 Å, 1.858 Å	2.364	0.038
defective (111)-O Figure 7.3 (d)	O-Mg: 1.895 Å, 1.878 Å	2.360	0.036
Other DFT(FPLAPW[1]) -GGA [243]			
(001)	-	1.38	0.046
(111)-Mg	-	2.04	0.033
(111)-O	-	3.39	0.040

From Table 8.2, the MgO (001) is the most stable one with the lowest surface energy of 1.449 Jm^{-2}. The surface energy of the MgO (001) is close to D.-N. Zhang *et al* DFT work [243]. The MgO (111) polar surface found to be very unstable. But for MgO (111) surfaces, (111)-O terminated defective surface have slightly less energies compare to (111)-Mg terminated defective surface [Table 8.2]. Therefore MgO (111)-O defective surface shows more stable than MgO (111)-Mg defective surface. For MgO (111)-surfaces, these results are quite different from the early theoretical results (from DFT) by D.-N. Zhang *et al* [243]. They found that the MgO (111)-Mg surface is the most stable with a surface energy as low as 2.04 Jm^{-2}. Therefore, the defective (111)-Mg and MgO (111)-O surfaces with half occupied Mg or O surface layer [Figure 8.3 (d) and (e)] were used in the present work affects the surface stability. However, for the surface relaxation energy, MgO (001) has the larger energy than surfaces. This is largely since MgO (001) has the highest number of adjacent atoms in its topmost layer [Figure 8.2 (b-h)], where the MgO (111)-Mg and (111)-O both defective surfaces have the least adjacent atoms in the outmost layer [Figure 8.3 (d) and (e)].

The structural optimizations for MgO (111)-Mg and MgO (111)-O surfaces showed strong relaxation, occurring mainly along the direction perpendicular to the surface [Figure 8.8]. After fully relaxations of the optimized structure, from MgO (111)-Mg surface, the top Mg atom moves inward from the vacuum about 0.24 Å from the top layer and toward (i.e., upward) the vacuum 0.275 Å from the bottom layer [Figure 8.8 (a)]. These different types of moving distances of Mg atoms cause more interactions between the cation and anion, therefore might cause larger surface energy and make the MgO (111)-Mg terminated defective surface less stable.

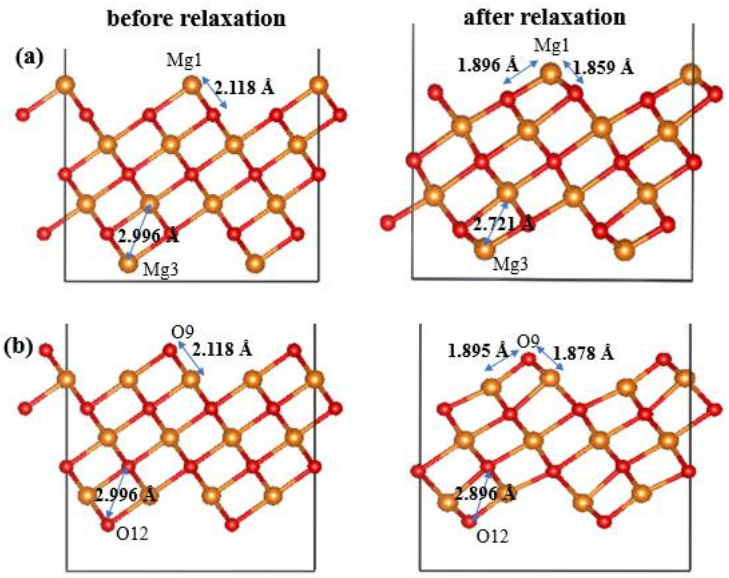

Figure 8.8: The side view of the MgO (a) (111)-Mg and (b) (111)-O defective surfaces respectively before and after relaxations. Color legends: orange for Mg and red for O, black line for unit cell.

On the other hand, after relaxations, the top O atoms from MgO (111)-O surface moves upward 0.23 Å from surface layer and toward (i.e., upward) the vacuum 0.10 Å from the bottom layer [Figure 8.8 (b)]. The lower values of atomic movements distances cause less interactions between atoms which makes the MgO (111)-O terminated defective surface more stable. The obtained calculation results in this section show reasonable and good indication of the method to build the defective surfaces. For MgO (111) surfaces only 6 atomic layers were used which is smaller thickness, but the obtained information might be useful to understand the formation and stability of nanocrystalline facets.

8.3.1.2 Electronic structure of MgO (111) surfaces

The electronic structure within the GGA-PBE approximation was calculated for both MgO (111)-Mg and (111)-O defective surfaces. The calculated total density of states (TDOS) and partial density of states (PDOS) for both surfaces are shown in Figure 8.9.

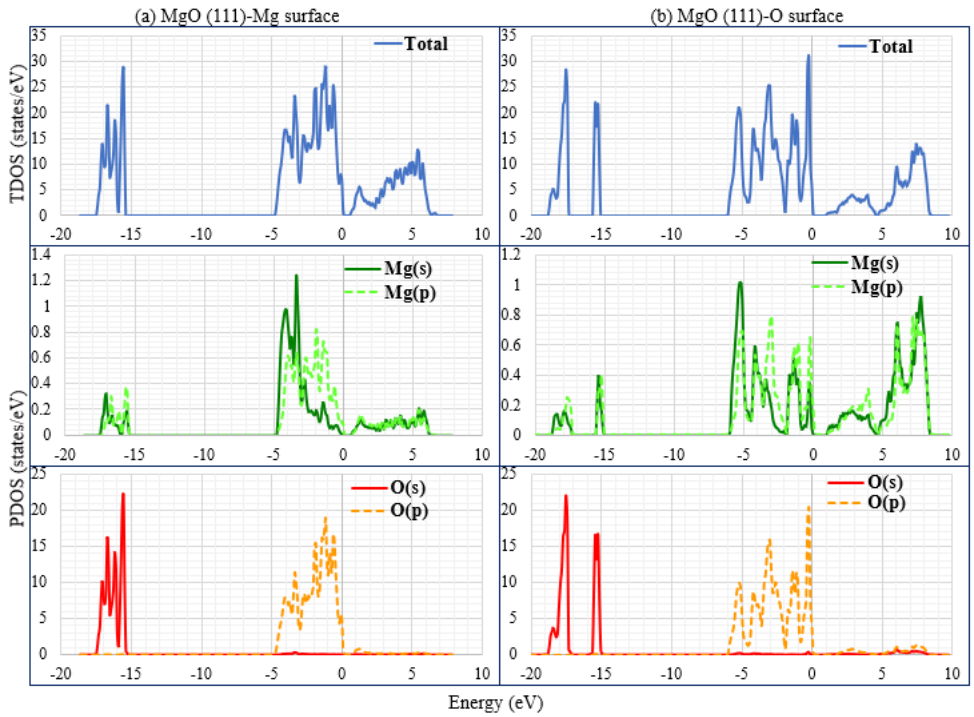

Figure 8.9: The total (TDOS) and partial (PDOS) density of states for MgO (a) (111)-Mg defective and (b) (111)-O defective surfaces.

From the Figure 8.9, the energy gap between UVB and conduction band is within 0.8-1.1 eV by DFT-GGA(PBE) when the fermi energy (E_F) is set to be 0 for both MgO (111) defective surfaces. This lower bandgap is mainly due to the states at the top of the valence band and conduction band [Figure 8.9 (a) and (b)]. The calculated energy gap of MgO (111)-O defective surface is 1.1 eV which is slightly larger than the MgO (111)-Mg defective surface (0.8 eV). In MgO (111)-Mg defective surface [Figure 8.9 (a)], the upper valence band region is mainly from O *2p* states and there is also some contribution from Mg *2s* and Mg *2p* states. But in lower valence band which are mostly causes from the O *2s* states, the contribution from Mg *2s* and Mg *2p* states are absent. The main reasons of having smaller energy gap in the surface structure is increasing the conduction band produced from Mg *2s* and Mg *2p* states towards fermi region which are larger amount in MgO (111)-Mg defective surface. The inward and upward movement of Mg atoms upon relaxation, to decrease the surface charge, appears to be linked to this phenomenon.

8.3.2 Hexagonal γ-Al_2O_3 (0001) surfaces:

8.3.2.1 Energetics and local structure:

The first-principles' structural optimizations were performed for 10 different hexagonal γ-Al_2O_3 (0001) surfaces. Based on calculations, the related surface energies were obtained by following equation 8.1.

The calculated surface energies, as well as details about chemical bonding were summarized in Table 8.3.

Table 8.3: Calculated surface energies of one polar smooth and 10 different hexagonal γ-Al_2O_3 along (0001) defective surfaces with 160 atoms slab size.

Hexagonal γ-Al_2O_3 along (0001) Surfaces	Al-O atomic distances (Å) in top surface and subsurface layer	Surface energies (Jm^{-2})
Polar	Al(Tet)-O: 1.74-1.85 Al(Oh)-O: 1.79-2.07	Unstable
1Al1(Oh) defective surface	Al(Tet)-O: 1.65-1.77 Al(Oh)-O: 1.66-1.78	1.77
2Al1(Oh) defective surface	Al(Tet)-O: 1.69-1.83 Al(Oh)-O: 1.69-1.84	1.52
Al2(Tet1) defective surface	Al(Tet)-O: 1.69-1.75 Al(Oh)-O: 1.78-1.86	1.98
Al2(Tet2) defective surface	Al(Tet)-O: 1.69-1.77 Al(Oh)-O: 1.85-2.10	1.31
Al2(Oh) defective surface	Al(Tet)-O: 1.71-1.75 Al(Oh)-O: 1.78-1.95	2.28
Al2(Oh_Tet) defective surface	Al(Tet)-O: 1.65-1.74 Al(Oh)-O: 1.71-2.03	1.71
1O1 defective surface	Al(Tet)-O: 1.64-1.89 Al(Oh)-O: 1.74-1.90	1.93
2O1 defective surface	Al(Tet)-O: 1.66-1.78 Al(Oh)-O: 1.76-2.08	1.69
1O2 defective surface	Al(Tet)-O: 1.66-1.83 Al(Oh)-O: 1.73-1.99	1.27
2O2 defective surface	Al(Tet)-O: 1.67-1.80 Al(Oh)-O: 1.69-1.89	1.51

From Table 8.3, the surface energy of polar γ-Al_2O_3 (0001) surface is very large, which means the polar smooth surface is less stable. The defected surfaces with half-occupied Al(Oh), or Al(Oh_Tet) or O terminated surface layers were found to be structurally stable. These defected surfaces can be considered non-polar because the net dipole moment at the surface is small due to the defective surfacial atomic layers. The structural optimizations showed strong relaxation, occurring

mainly along the direction perpendicular to the surface. The calculations show that the hexagonal γ-Al_2O_3 (0001)-1O2 defective surface having lowest surface energy 1.27 Jm^{-2} is significantly more stable compared to other defective surfaces [Table 8.3]. The hexagonal γ-Al_2O_3 (0001)-Al2(Tet2) defective surface, where 4Al2(Tet) atoms on the top of surface layer from Al2(Oh_Tet) defected termination layer, having 1.31 Jm^{-2} surface energy. This result is about 2.7% higher than that of the most stable hexagonal γ-Al_2O_3 (0001)-1O2 defective surface, and slightly lower than that of the other possible defected surfaces. Therefore, the calculations predict stability of these charged surfacial domains.

The most stable hexagonal γ-Al_2O_3 (0001)-1O2 defective surface is composed of 8 oxygen (O2) atoms on top of the Al2(Oh_Tet) layer where each oxygen atom coordinated with 2 Al atoms [Figure 8.10 (a)]. After relaxations, each O atom from the top layer moves 0.044 Å upward from surface layer. And each O atom from bottom layer moves toward the vacuum 0.028 Å. Al(Tet) from the top subsurface layer moves to about 0.20 Å upward. From the subsurface layer each Al(Tet) and Al(Oh) atom loses some bonds with O atoms and is coordinated by 3 and 5 O atoms respectively.

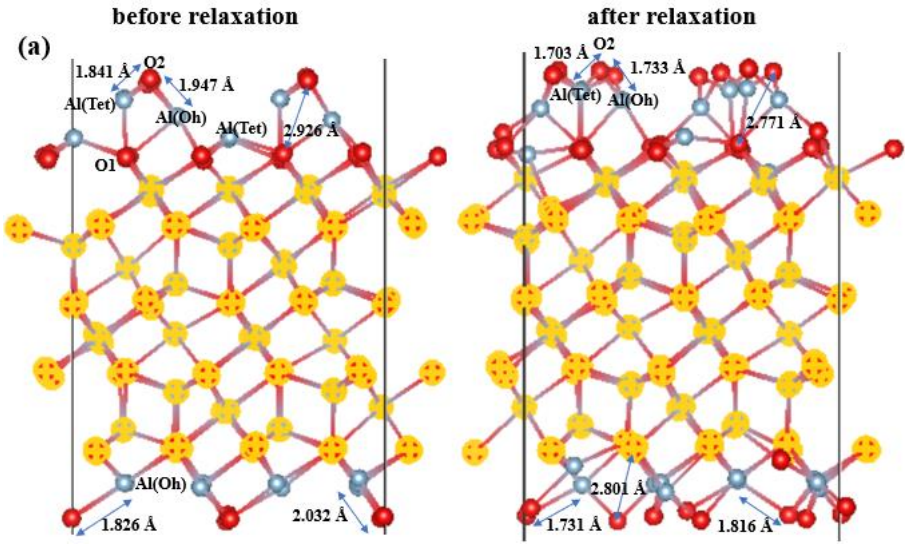

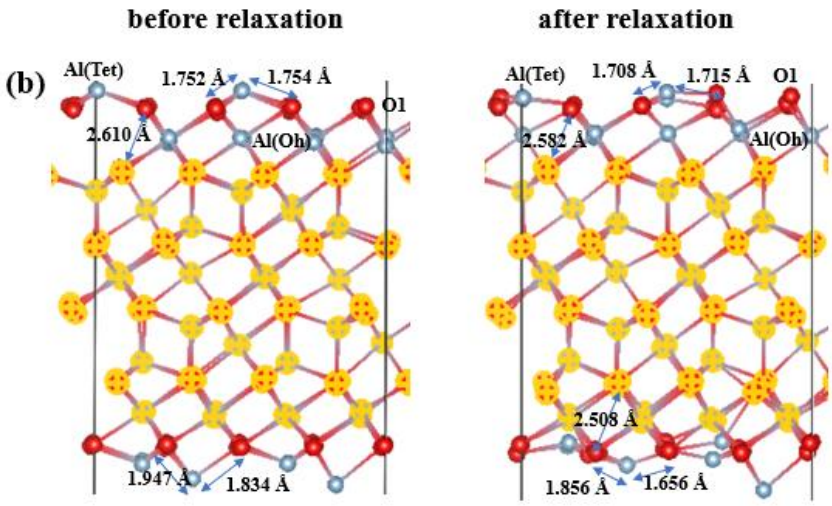

Figure 8.10: The side view of hexagonal γ-Al_2O_3 (0001) (a) 1O2 and (b) Al2(Tet2) defective surfaces respectively. Atoms underneath the surfaces have been yellow colored for clarity. Color legends: red for O and light blue for Al.

The hexagonal γ-Al_2O_3 (0001)-Al2(Tet2) surface is composed of 4 Al(Tet) atoms on top of the O1 layer where each Al(Tet) atom coordinated with 3 O atoms [Figure 8.10 (b)]. After full relaxations, in γ-Al_2O_3 (0001)-Al2(Tet2) surface structure, each Al(Tet) moves to 0.15 Å upwards from surface and O1 from the top subsurface layer moves toward the vacuum 0.13 Å [Figure 8.10 (b)]. From the subsurface O1 layer 4 O atoms are coordinated by 2 Al atoms and 8 O atoms are coordinated by 3 Al atoms after full relaxations. In this surface, there are more losing bonds observed between Al and O atoms. These different types of moving distances, directions and coordination number of Al and O atoms cause more interactions between the cation and anion which increases the surface energy and make the γ-Al_2O_3 (0001)-Al2(Tet2) defective surface less stable compared to γ-Al_2O_3 (0001)-1O2 defective surface.

There is not enough available experimental work have been done for γ-Al_2O_3 surfaces, therefore the stable hexagonal γ-Al_2O_3 (0001)-1O2 defective surface in the present work was compared with well characterized α-Al_2O_3 (0001) [139] and $MgAl_2O_4$ (111) [171] surfaces from literature [Table 8.4].

Table 8.4: Calculate surface energy and slab size of the hexagonal γ-Al_2O_3 (0001)-1O2 defective surface and available theoretical results of α-Al_2O_3 (0001) [139] and $MgAl_2O_4$ (111)-O [171].

Surface structure	Slab size (no. of atoms)	Vacuum thickness (Å)	Surface energy (Jm^{-2})
hexagonal γ-Al_2O_3 (0001)-1O2 defective surface	160	27.2	1.27
α-Al_2O_3 (0001) [139]	60	13.1	1.54
γ-Al_2O_3 (111)*a* *[139]	40	-	0.95
γ-Al_2O_3 (111)*b* *[139]	40	-	1.85
$MgAl_2O_4$ (111)-O [171]	-	-	3.06

*cleaving through the V_{1Oh}-Al(3)$_{Td}$ plane yields (111)*a* and while the V_{2Oh}-Al(4)$_{Oh}$ plane is denoted (111)*b*.

From Table 8.4, the surface energy of the hexagonal γ-Al_2O_3 (0001)-1O2 defective structure from the present work is smaller than $MgAl_2O_4$ (111)-O surface from C. Fang *et al* work [171]. But this difference is reasonable because of two different spinels (i.e., γ-Al_2O_3 and $MgAl_2O_4$) surfaces are compared. In their calculation they found that stable $MgAl_2O_4$ (111)-O surface is composed of seven oxygen atoms on top of a Mg layer and surface reconstruction occurred [171]. The cation Al(Oh) vacancies and surfacial O atoms in the structure of the hexagonal γ-Al_2O_3 (0001)-1O2 defective surface from this work could occur this surface energy differences compared to $MgAl_2O_4$ (111)-O surface from C. Fang *et al* work [171]. The surface energy of the hexagonal γ-Al_2O_3 (0001)-1O2 defective structure from this work is also smaller compared to the Al-terminated α-Al_2O_3 (0001) surface from H. P. Pinto *et al* work [139]. H. P. Pinto *et al* [139] also calculated two types of γ-Al_2O_3 (111) surfaces, where they found their γ-Al_2O_3 (111) with cleaving through the V_{1Oh}-Al(3)$_{Td}$ [i.e., one octahedral vacancy and 3Al(Tet)] plane yields the lowest surface energy 0.95 Jm^{-2} [139]. But in their calculations, they used very small supercell slab (40 atoms). But in the present work, larger and defective supercell slab of γ-Al_2O_3 (160 atoms slab) were used.

8.3.2.2 Electronic structure for surfacial atoms/ions:

The total and partial density of states (DOS) for the most stable hexagonal γ-Al_2O_3 (0001)-1O2 defective surface has been calculated within GGA-PBE approximation [Figure 8.11]. The calculated bandgap between top of the valence band and the bottom of the conduction band is 1.8 eV by DFT-GGA(PBE). This value is notably smaller than that of bulk γ-Al_2O_3 4.2 eV using the same method [Figure 8.11 (a) and (b)]. This lower bandgap is mainly due to surficial states from conduction bands being present at gap of the surface structure as shown in Figures 8.11 (b).

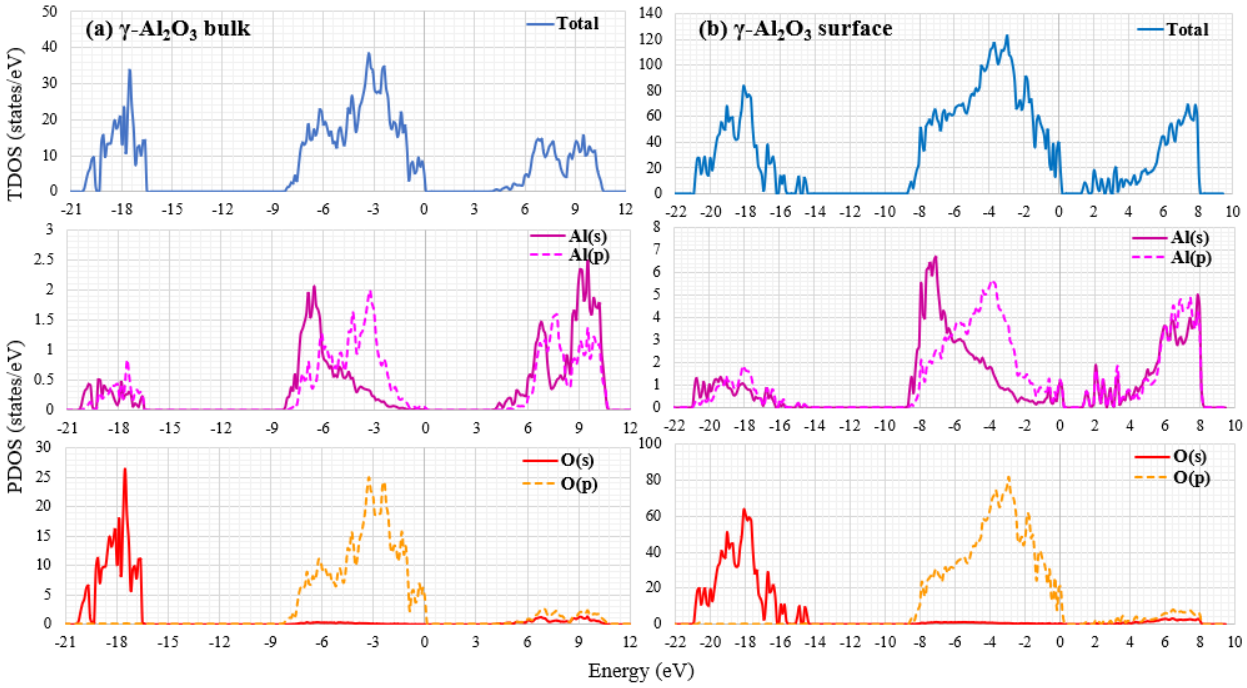

Figure 8.11: The total (TDOS) and partial (PDOS) density of states for hexagonal (a) bulk γ-Al_2O_3 and (b) the most stable hexagonal γ-Al_2O_3 (0001)-1O2 defective surface. The Fermi level is set at 0 eV.

From the PDOS of hexagonal γ-Al_2O_3 (0001)-1O2 defective surface [Figure 8.11 (b)], the conduction band is produced mainly from contribution of Al *3s* and *3p* states. The PDOS for the O can be clearly divided into two segments, the upper valence band contributed mostly by *2p* states (0 to −8.7 eV) and the lower valence

band contributed mostly by *2s* states (−14.5 to −21.0 eV). The O 2p and O 2s states are 8.7 eV and 6.5 eV wide respectively [Figure 8.11 (b)]. The valence bands (LVB and UVB) from O *2s* and *2p* states shows normal as bulk structure.

8.4 Conclusion:

First-principles density-functional theory has been applied to the quantitative elucidation of structure and energetics of MgO (111) and hexagonal γ-Al_2O_3 along (0001) defective surfaces.

First test calculations were performed to investigate the stability of MgO (001) surfaces according to energetics with different vacuum and slab thicknesses. From the test calculations, the 6 atomic layers slab with 22.0 Å vacuum thickness is enough to study MgO surfaces. Therefore, the MgO (111) polar and defective surfaces were created with 22.02 Å vacuum and 6 atomic layers thickness and then tested. The MgO (111)-Mg and (111)-O terminated defective surfaces were calculated to exhibit surface energy values of 2.364 Jm^{-2} and 2.360 Jm^{-2}, respectively. Fully polar surface was found to be unstable. Electronic structure was also calculated for both MgO (111)-Mg and MgO (111)-O terminated defective surfaces. The electronic band gap of MgO (111)-O defective surface (1.1 eV) is slightly larger than MgO (111)-Mg defective surface (i.e., 0.8 eV). The calculated band gaps of both surfaces are smaller compared to the bulk structure value which is reasonable. The detailed analysis here as served as good indication of the accuracy and reliability of the method for developing non-polar defective surfaces for ionic oxides.

Based on analysis about MgO (111) surfaces, possible hexagonal γ-Al_2O_3 along (0001) defective surfaces were created. The surfaces with half-occupied Al (Tet), Al(Oh) or O surface layers were found to be structurally stable. These defective surfaces can be considered non-polar because the net dipole moment at the surface is small. The first-principles DFT structural optimizations were

performed, and total energy calculations have been done for these surface systems. The calculations revealed that the γ-Al_2O_3 (0001)-1O2 defective and γ-Al_2O_3 (0001)-Al2(Tet2) terminated defective surfaces have high stability with surface energy of 1.27 Jm^{-2} and 1.31 Jm^{-2}, respectively. The structural optimizations showed strong relaxation, occurring mainly along the direction perpendicular to the surface. The electronic structure of most stable hexagonal γ-Al_2O_3 (0001)-O2 defective surface was also described in this chapter. The surface states lower the value of band gap compared to bulk structure which is reasonable for the surface structure.

The present work expected to provide useful information to reach a better understanding about the γ-Al_2O_3 surface structure and encourage new theoretical and experimental work for nanocrystalline facets.

Chapter Nine

Crystal chemistry and physical properties of Y_2O_3

9.1 Introduction:

Yttrium oxide (Y_2O_3) or yttria has attracted attention in the scientific community due to its rich variety of properties and potential applications [42-47]. To have better applications, the knowledge of crystal structural and physical properties of this oxide is prerequisite. Many experimental techniques [244-246] include X-ray photoelectron spectroscopy, spectroscopic ellipsometry, reflection high-energy electron diffraction (RHEED) and X-ray diffractometer, micro-Raman spectrometer, and theoretical approaches include DFT within LDA, GGA and HSE06 approximations [247-250] have been applied to study this compound with emphasis on the cubic phase of Y_2O_3. In this work, first-principles DFT calculations within GGA-PBE approximation have been applied to study the crystal structural properties of Y_2O_3 phases. The stability of six different possible structural models of Y_2O_3 (i.e., cubic, monoclinic, hexagonal, and fcc) will be discussed in this chapter. The crystal structural properties i.e., lattice parameter, volume, bulk modulus etc. along with their energetics and local bonding and electronic properties will be describe in detail.

9.2 Methods:

9.2.1 Structural models of Y_2O_3:

The cubic C-Y_2O_3 unit cell prepared followed from F. Hanic *et al* work [176]. The structure belongs to the body centred cubic (BCC) and space group *Ia3*. The unit cell contains 80 atoms [Figure 9.1(a)] with two nonequivalent yttrium cation sites, Y1 and Y2, occupying the 8*b* (1/4 1/4 1/4) and 24*d* (0.28261 0.0000 0.2500) crystallographic positions, respectively, and one type of O atom at the 48*e*

(0.09834 0.35913 0.12985) site. Y1 (Y2) is surrounded by six oxygen atoms in the form of a perfect (distorted) octahedron (Y1O6 and Y2O6 polyhedral units), and the O atom is surrounded by four Y atoms in the form of a distorted tetrahedron, respectively.

The structure of the monoclinic M-Y_2O_3 phase was reported by I. Halevy *et al* [177]. The structure has the space group *C2/m*. The unit cell contains 30 atoms, with all the ions located at 4i (x, y, z) Wyckoff positions [Figure 9.1(b)]. Our calculated coordinates for Y are: (0.0323 -0.0000 0.8136), (0.6352 0.0000 0.4883), (0.6911 0.0000 0.1371) and for O are: (0.5294 0.0000 0.6573), (0.6276 0.5000 0.2818), (0.6745 0.5000 0.9695), (0.7067 0.5000 0.6229), (0.0000 0.5000 -0.0000). CM: please use the same digital, typically three to four after point.

A hexagonal H-Y_2O_3 phase was reported by K. Kuribayashi *et al* [178]. The space group of this structure is *P3m1*. The prepared H-Y_2O_3 primitive cell contains 5 atoms [Figure 9.1(c)], and the coordinates are for Y are: (2/3 1/3 0.7503), (1/3 2/3 0.2497) and for O are: (2/3 2/3 0.3534), (1/3 2/3 0.6466), (0.0000 0.0000 0.0000).

Another F-Er_2S_3-type monoclinic Y_2O_3 phase was based on the structure of Er_2S_3 [251]. The space group of this structure is $P2_1/m$. The unit cell contains 20 atoms [Figure 9.1(d)], with four types of Y atoms, four in six coordination (0.06134 1/4 0.1714), two in seven coordination (0.8197, 1/4, 0.4871) and two in eight coordination (0.4517, 1/4, 0.3162) by O atoms.

The α-Al_2O_3-type hexagonal Y_2O_3 structure is based on the hexagonal α-Al_2O_3 structural model from chapter five. The structure belongs to the space group *R3c*. The hexagonal cell contains 30 atoms [Figure 9.1(e)] with six layers of close packed O atoms filled by Y atoms at the octahedral interstitial sites. The Y layer consists of 2 sublayers, the Y1 and the Y2, the Y cations and the O anions are

located at the 12*c* (0.0000 0.0000 0.3591) and 18*e* (0.2924 0.0000 1/4) Wyckoff positions, respectively.

The fcc-Y_2O_3 structure is based on the recent experiments by S. H. Wang [180]. It contains 10 atoms [Figure 9.1(f)]. The space group of this structure is *Pn3m* where the atomic coordinates are: Y (3/4 3/4 3/4) and O (1/2 1/2 0.000). In fcc-Y_2O_3 unit cell, each Y atom coordinated by 6 O atoms and each O atoms coordinated by four Y atoms.

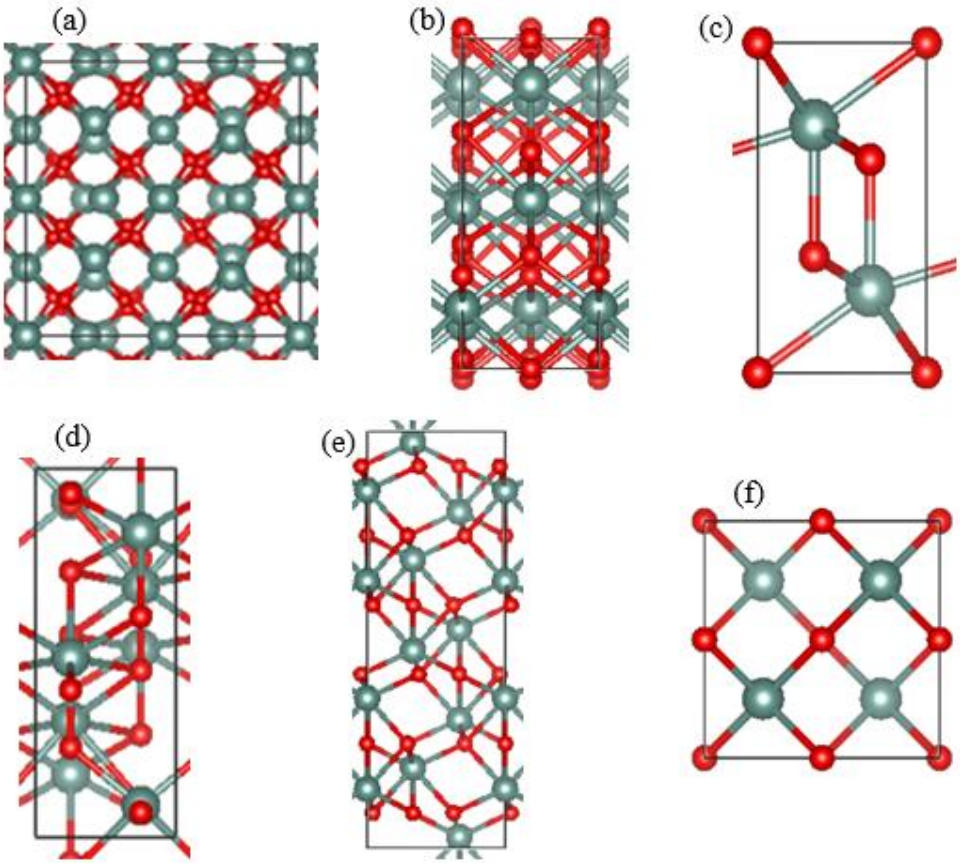

Figure 9.1: Schematic structure of the Y_2O_3 phases. Subfigure (a) cubic (80 atoms-$Y_{32}O_{48}$), (b) monoclinic (30 atoms-$Y_{12}O_{18}$), (c) hexagonal (5 atoms-Y_2O_3), (d) F-Er_2S_3-type monoclinic (20 atoms-Y_8O_{12}), (e) α-Al_2O_3-type hexagonal (30 atoms-$Y_{12}O_{18}$) and (f) fcc (10 atoms-Y_4O_6) Y_2O_3 unit cell. The green sphere represents Y atom and red sphere represents O atom.

9.2.2 Computational details:

All the calculations were performed using first-principles DFT within the GGA-PBE functional [192]. The test calculations indicated that the plane wave pseudopotential with En_{cut}= 450 eV and En_{aug} = 600 eV is sufficient to obtain convergence in both the total energy differences and the geometries for our investigated systems. The electronic wave functions were sampled on 8×8×8 ***k***-points for C-Y_2O_3, 4×20×4 ***k***-points for M-Y_2O_3, 4×20×8 ***k***-points for F-Er_2S_3-type-Y_2O_3, 16×16×10 ***k***-points for H-Y_2O_3, 16×16×7 ***k***-points for α-Al_2O_3-type Y_2O_3 and 10×10×10 ***k***-points for fcc-Y_2O_3 respectively in the irreducible Brillouin zone (BZ), generated by the Monkhorst-Pack algorithm [200].

9.3 Results and Discussions:

9.3.1 Energetics and chemical bonding of the Y_2O_3 phases:

The obtained results include optimized lattice parameters, volumes, and total valence electrons energies for the structural models of Y_2O_3 (cubic, monoclinic, hexagonal, and fcc) which are summarised in Table 9.1.

Table 9.1: Calculated bulk properties of the Y_2O_3 phases

Y_2O_3 structural models	Space group	Lattice Parameters (Å)	Lattice Angles	Volume (Å^3/f.u.)	Energy (eV/f.u.)
Cubic	*Ia3* (nr206)	a=10.653	α=β=γ=90.00^0	75.566	-45.768
Monoclinic	*C2/m* (nr12)	a=14.057, b=3.501, c=8.653	α=γ=90.00^0 β=106.41^0	69.798	-45.527
Hexagonal	*P3m1* (nr164)	a=b=3.671, c=5.886	α=β=90.00^0 γ=120.00^0	68.680	-45.413
[a]F-Er_2S_3-type monoclinic,	*P2$_1$/m* (nr11)	a=9.154, b=3.403, c=9.315	α=γ=90.00^0 β=106.49^0	69.560	-45.317
α-Al_2O_3-type Hexagonal	*R3c* (nr161)	a=b=5.692, c=14.893	α=β=90.00^0 γ=120.00^0	69.645	-44.783
fcc	*Pn3m* (nr224)	a=b=c=5.341	α=β=γ=90.00^0	76.185	-43.367

[a]F-type erbium sesquisulfide [251]

The relations between the total energies and their volumes of the six Y_2O_3 phases are plotted in figure 9.2.

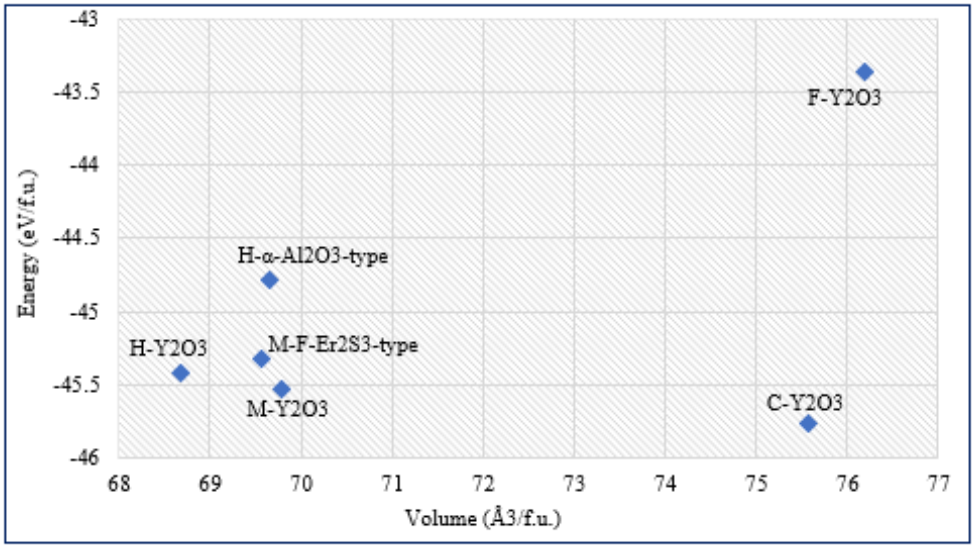

Figure 9.2: Calculated total energies as a function of their volumes for the Y_2O_3 Phases.

From Table 9.1 and Figure 9.2, the H-Y_2O_3 phases has the smallest volume, where the cubic i.e., C-Y_2O_3 having a larger volume but lowest energy which means it being the most stable one. Also, the F-Y_2O_3 having the largest volume and the highest energy, indicating its meta-stability at ambient conditions. The calculations reproduced the experimental observations that the cubic C-Y_2O_3 phase is the ground state phase. Our calculated lattice parameter of the cubic C-Y_2O_3 is 10.653 Å which is close to the experimental work (i.e., 10.603 Å) obtained from X-ray analysis by F. Hanic *et al* [176].

The coordination number (CN) and interatomic distances between Y cations and O anions in all six phases of Y_2O_3 have also been analyzed and shown schematically in Figure 9.3.

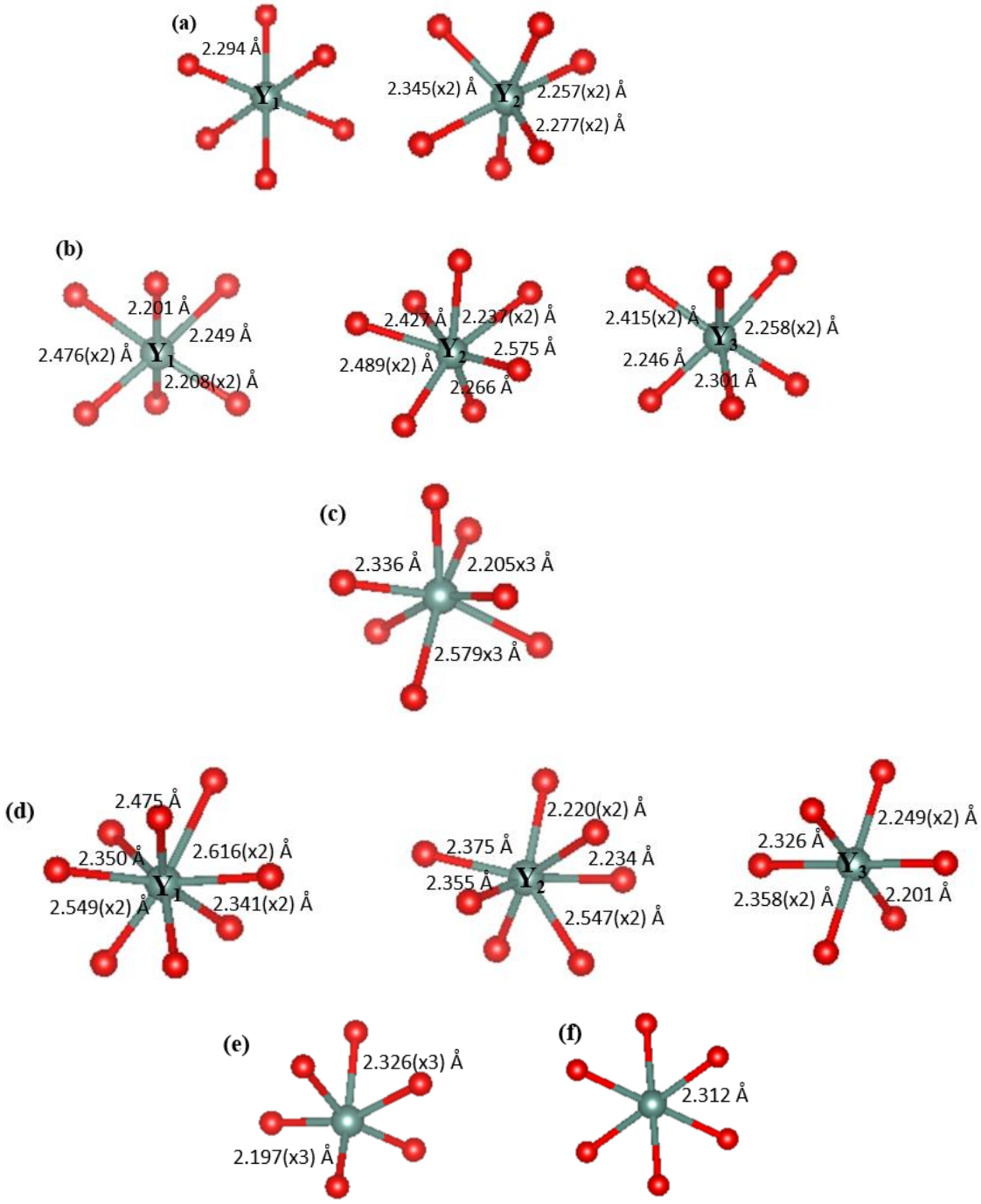

Figure 9.3: Schematical coordination of Y by O and the related Y-O bond lengths (a) C-Y_2O_3, (b) M-Y_2O_3, (c) H-Y_2O_3, (d) F-Er_2S_3-type monoclinic-Y_2O_3, (e) α-Al_2O_3-type hexagonal-Y_2O_3 and (f) fcc-Y_2O_3. The green and red spheres represent Y and O atom respectively.

As shown in Figure 9.3, in the C-Y_2O_3 structure Y cation bonded with 6 O anions i.e., the coordination number (CN) of Y is 6. In the M-Y_2O_3 there are two different

CN of Y i.e., 6 and 7. The H-Y_2O_3 structure has CN = 7 for Y. In the F-Er_2S_3-type monoclinic Y_2O_3 three different CNs of Y have been observed i.e., CN = 6, 7 and 8, respectively. The α-Al_2O_3-type hexagonal Y_2O_3 and fcc Y_2O_3 has CN = 6 for Y. The interatomic distances between the Y-O bonding have been summarized in Table 9.2.

Table 9.2: Comparison of the interatomic distances in Y_2O_3 structures.

Different phases of Y_2O_3	CN of Y with O	Bonding distances between Y-O (Å)
cubic	6	Y1-O: 2.294 (×6) Y2-O: 2.345 (×2), 2.257 (×2), 2.277 (×2)
monoclinic	6 and 7	Y1-O: 2.201, 2.208 (×2), 2.249, 2.476 (×2) Y2-O: 2.237 (×2), 2.266, 2.427, 2.489 (×2), 2.575 Y3-O: 2.246, 2.258 (×2), 2.301, 2.415 (×2)
hexagonal	7	2.205(×3), 2.336, 2.579(×3)
[a]F-Er_2S_3-type monoclinic,	6, 7 and 8	Y1-O: 2.341(×2), 2.350, 2.475, 2.549(×2), 2.616(×2) Y2-O: 2.220(×2), 2.234, 2.355, 2.375, 2.547(×2) Y3-O: 2.201, 2.249(×2), 2.326, 2.358(×2)
α-Al_2O_3-type hexagonal	6	2.197(×3), 2.326(×3)
fcc	6	2.312(×6)

From Table 9.2, rich variety of chemical bonding have been observed between all six different structures of Y_2O_3. The cubic, α-Al_2O_3-type hexagonal and fcc structures of Y_2O_3 only have 6 CN of Y with O. The C-Y_2O_3 structure also has the CN 6 of Y with O but there are largest distance has been observed between Y-O bonding which might cause less interactions between cation to anion, and makes the structure more stable. The calculated bulk modulus by first principle DFT(GGA-PBE) for stable C-Y_2O_3 structural model is 154.7 *GPa* using birch Murnaghan equation of states (EOS) [Appendix: Figure A.9.1], which is close to the experimental value 149.5±1.0 *GPa* [252].

9.3.2 Electronic Properties of cubic Y_2O_3

The electronic properties of C-Y_2O_3 were calculated within GGA-PBE approximation. The density of states are shown in Figure 9.4.

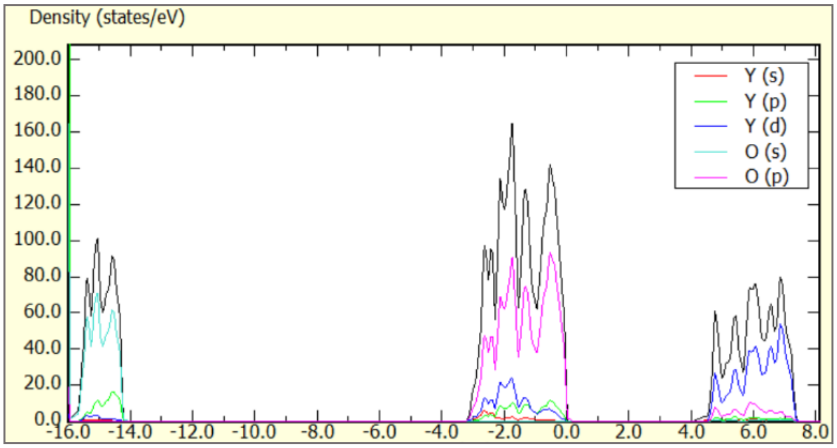

Figure 9.4: Total (black line) and partial (colored lines) density of states of the ground state C-Y_2O_3 phase.

From the partial density of states (pDOS) of Y and O for the C-Y_2O_3 phase [Figure 9.4] show that the upper valence band (-3.2 to 0.0) are dominated by O *2p* state and the lower valence band (−14.2 to −16.2 eV) by O *2s* states. The O *2p* and O *2s* states dominated bands have widths of 3.2 and 2.0 eV, respectively. The lower part of the conduction band is dominated by Y *4d* states, whereas Y *5s* and Y *5p* states are all over the valence band. There is small contribution from O *2p* states have been observed in the lower part of the conduction band. The calculated band gap is 4.2 eV as shown in Table 9.3 and Figure 9.4.

Table 9.3: Calculated electronic energy gap (E_g) in eV of C-Y_2O_3.

Method	Energy gap (E_g) in eV
DFT(GGA-PBE) [Our work]	4.2
Exp: Spectrophotometry [245]	5.91-6.15
Exp: Photoelectron spectroscopy [252]	6.0
DFT-HSE06 [249]	6.0
DFT(GGA-PBE) [250]	4.8

The calculated electronic energy gap (4.2 eV) from the first-principles DFT(GGA-PBE) calculations [is notably smaller than the experimental value from the photoelectron spectroscopy (6.0 eV) [252]. This discrepancy arises, because of the inability of DFT to describe excited states [193, 204].

9.4 Conclusions

In conclusion, six different structures of Y_2O_3 have been studied by the first-principles DFT calculations within the GGA-PBE approximation. The calculations show that C-Y_2O_3 is the ground state phase. The calculated chemical bonding of cation Y and anion O in all six phases were discussed. The electronic properties of C-Y_2O_3 have also been calculated. The calculated electronic energy gap is 4.2 eV which is smaller than experimental value 6.0 eV [252] but reasonable for the first-principles DFT calculations.

Chapter Ten

Final Remarks

10.1 Conclusions

A systematic theoretical study about the crystal structural properties of MgO, Al_2O_3 (α-, θ-, and γ-phases) and Y_2O_3 phases is presented in this thesis by mean of the first-principles density functional theory. For the bulk properties (i.e., lattice parameters, volumes, chemical bonding nature, bulk modulus, etc), the calculated results from the GGA-PBE were reasonable with available experimental and theoretical results in the literature. Meanwhile, there are some differences between the experimental obtained results for the electronic properties, especially the band gaps. The experimental measurements were related to excitonic states, which could not be described accurately by means of the standard DFT functionals, e.g. the GGA approximations. Therefore, the state-of-art *GW0* corrections have been applied to predict the electronic and optical properties for the oxides in this thesis.

In chapter five, the crystal structural properties include local chemical bonding, bulk modulus, and electronic properties of fcc MgO and hcp α-Al_2O_3 have been calculated by the first-principles DFT within both LDA and GGA-PBE approximations. The resulting equilibrium structural properties obtained from GGA-PBE are in good agreement with the experimental and theoretical results in the literatures. But the electronic properties in particular the band gaps calculated by the GGA-PBE approximation are notably smaller than the corresponding experimental values [82, 125]. The self-consistent *GW0* corrections over DFT produced electronic band gaps that are in excellent agreement with the experimental observations [82, 125]. The optical properties include dielectric constants i.e., real part $\varepsilon_1(\omega)$, imaginary part $\varepsilon_2(\omega)$, refractive index $n(\omega)$,

extinction coefficient $k(\omega)$, absorption coefficient $\alpha(\omega)$, conductivity $\sigma(\omega)$, reflectivity $R(\omega)$, and energy loss spectra $L(\omega)$ of the oxides were calculated by means of both GGA-PBA and *GW0*methods. The calculated optical properties of the oxides by *GW0* correction show good agreement with the experimental observations in the literature as well.

Chapter six presented the first-principles results for the monoclinic θ-Al_2O_3 and γ-Al_2O_3 in a hexagonal lattice. For γ-Al_2O_3, the several existing models were revisited. We explored the distribution and interactions between cation vacancies with possible vacancy configurations. The present study revealed that the spinel-type γ-Al_2O_3 in the hexagonal lattice have Al vacancies distributing at the octahedral sites. There are variation of coordination numbers (CN) of O by Al, i.e., CN-3 and CN-4. The CN variation also effects the stability. From the self-consistent *GW0* calculations, the band gaps of θ-Al_2O_3 and the γ-Al_2O_3 are 5.7 eV and 8.3 eV, respectively, which are close to experimental observations (5.16 eV and 8.7 eV) [225, 125]. For α- Al_2O_3 there have been available experimental results in the literature, while such are absent for θ- and γ-Al_2O_3. So, for the θ- and γ- alumina phases the calculated optical properties were compared with α-Al_2O_3.

By investigating the optical properties of MgO, Al_2O_3 (α-, θ-, and γ-Al_2O_3) oxide materials by means of the *GW0* calculations, the present study provides a roadway to extend the applications of these materials into the UV regions in many optoelectronic devices.

In chapter seven the detailed analysis of composition-dependent structure and properties of Al_2O_3 rich $MgAl_2O_4$-*n*.Al_2O_3 spinels are presented. A structural formula, $Mg_{(1-x)}Al_x]_{Tet}[Al_{(2-x/3)}V_{x/3}]_{Oh}O_4$ (x= 0 to 1) was developed with distribution rules of cations, vacancies and anions in this work. Restricted by distribution rules along with the number of substituted Al^{3+} ions for Mg^{2+} ions in

tetrahedral sites, seven $[Mg_{(1-x)}Al_x]_{Tet}[Al_{(2-x/3)}V_{x/3}]_{Oh}O_4$ (x = 0.0, 0.125, 0.25, 0.5, 0.75, 0.875, 1.0) supercells were built. The calculations produced a dependence of formation energy on chemical composition for the solid solution. The influences of temperature effect on the stability of $[Mg_{(1-x)}Al_x]_{Tet}[Al_{(2-x/3)}V_{x/3}]_{Oh}O_4$ (x= 0 to 1) at higher temperature also observed by the ab initio molecular dynamics (AIMD) simulations. The resultant compositional structure of $[Mg_{(1-x)}Al_x]_{Tet}[Al_{(2-x/3)}V_{x/3}]_{Oh}O_4$ shows Mg, Al cations and vacancies distributed homogeneously at high temperatures.

The detail analysis of structural chemistry and electronic properties of MgO and γ-Al_2O_3 surfaces are presented in chapter eight. The stability and atomic structure of the MgO (001), polar MgO (111) and defected MgO (111) surfaces have been studied. By means of the first-principles calculations, the non-polar MgO (111)-O terminated defective surface was found to be as stable (2.360 Jm^{-2}) energetically as the MgO (111)-Mg terminated defective surface (i.e., 2.364 Jm^{-2}). Fully polar surface was found both structurally and energetically unstable. Electronic structure was also calculated for both MgO (111)-Mg and MgO (111)-O terminated defective surfaces. The results thus may serve as good indication of the accuracy and reliability of the method and settings for investigation of the surfaces of the complex oxides. The methods then were applied to study surfaces of hexagonal γ-Al_2O_3 cleaved perpendicular to its (0001) axis. We built 10 different (non-polar) defective surfaces with Al(Tet), Al(Oh), Al(Oh_Tet), O termination of hexagonal γ-Al_2O_3 perpendicular to its (0001) . From the local bonding, energetics, and electronic properties analysis of the 10 defective surfaces we concluded that hexagonal γ-Al_2O_3 {0001}-O non-polar surface has a high stability than those with Al terminations. The present study provides some insight into the γ-Al_2O_3 surface structures and may help new applications for this important oxide.

Chapter nine focused on the crystal chemistry and properties of Y_2O_3. Six different phases i.e., cubic C-Y_2O_3, monoclinic M-Y_2O_3, Hexagonal H-Y_2O_3, F-Er_2S_3-type monoclinic Y_2O_3, α-Al_2O_3-type hexagonal Y_2O_3, and fcc-Y_2O_3 have been investigated. The calculated results concluded that the cubic C-Y_2O_3 structural phase is the most stable. The electronic structure of stable cubic Y_2O_3 phase has also been studied.

10.2 Future Work

Interfaces between liquid Mg/Al and oxides' substrates, including MgO, $MgAl_2O_4$, Al_2O_3 (α-, and γ-Al_2O_3) have shown growing importance as potential nucleation sites during solidification of the light metals and alloys [7, 20-22]. Therefore, more efforts on the atomic ordering at the interfaces need to be made for the developments of new alloys of fine uniform microstructures and desirable mechanical and chemical properties.

From the literature, an improvement in tensile properties and hardness of Mg metals with the addition of Y_2O_3 was reported [253, 254]. Another experimental observation revealed that the added yttrium has influences on both the microstructures and properties of the surfaces of α-Al_2O_3 particles, which is called yttrium effect [173]. Thus, the information about Y_2O_3 surfaces might be important to understand the yttrium effect. The influence of temperature effect on the stability of cubic Y_2O_3 phase and surfaces will also be observed in future work by the first-principles molecular dynamics simulations.

References

[1] R. Stewart McWilliams, D. K. Spauldingjon, J. H. Eggert, P. M. Celliers, D. G. Hicks, R. F. Smith, G. W. Collins and R. Jeanloz. Science, 338, 6112, pp. 1330-1333, (2012).

[2] W. A. Deer, R. A. Howie, J. Zussman. *An Introduction to the Rock-Forming Minerals*, 3rd ed. (2013). ISBN 978-0903056-33-5.

[3] C. Kittel. *Introduction to Solid State Physics*. New Jersey. John Wiley & Sons, 8th ed. (2005). ISBN: 9780471415268.

[4] H. Abu-Farsakh, I. Al-Qasir, A. Qteish, Comp. Mate. Sci. 154, 159-168 (2018).

[5] C. Noguera, *Physics and chemistry of oxide surfaces*, Cambridge University Press (1996).

[6] J. F. Schifo and J. T. Radia, *Theoretical/best practice energy use in metal casting operations*, Advanced Technology Institute North Charleston, SC (2004).

[7] Z. Fan, Proc. The 11th international conference on magnesium alloys and their applications, 24-27 July 2018, Beaumont Estate, Old Windsor, UK. Ed. By Z. Fan and C. Mendis, p 7 (2018).

[8] Handbook Committee, *Metal Handbook. Vol. 2, Properties and Selection: Nonferrous Alloys and Special-Purpose Materials*, Materials Park, OH, ASM International (1990).

[9] W. J. Joost, *Magnesium Technology*, Wiley, New York (2014).

[10] K. Wefers and C. Misra, *Alcoa Technical Paper No 19* (revised), Alcoa Laboratories (1987).

[11] A. Stierle, F. Renner, R. Streitel, H. Dosch, W. Drube and B. C. Cowie, Science, 303, 1652 (2004).

[12] Z. Łodziana, N. Y. Topsoe and J. K. Norskov, Nat. Mater. 3, 289 (2004).

[13] G. Kresse, M. Schmid, E. Napetschnig, M. Shishkin, L. Köhler and P. Varga, Science, 308, 1440 (2005).

[14] Y. Shimizu, H. Arai and T. Seiyama, Sensors and Actuators, 7, 11 – 22 (1985).

[15] H. Cynn, S. K. Sharma, T. F. Cooney, and M. Nicol, Phys. Rev. B 45, 500(R) (1992).

[16] Y. Urita, K. Yamaguchi, I. Takita, K. Furuta and Y. Natsuo, Taikabutsu 45, 664-672 (1993).

[17] Z. Haijun, J. Xiaolin, Y. Yongjie, L. Zhanjie, Y. Daoyuan, and L. Zhenzhen, Mater. Res. Bull. 39, 839 (2004).

[18] M. F. Zawrah, H. Hamaad, and S. Meky, Ceram. Int. 33, 969 (2007).

[19] G. Cole, A. Glove, R. Jeryan, G. Davies, Steel World 2, 75–83 (1997).

[20] Z. Fan, F. Gao, B. Jiang and Z. P. Que, Sci. Rep. 10, 9448 (2020).

[21] Z. Fan, Metal. Mater. Trans. A 44, 1409-1418 (2013).

[22] H. T. Li, Y. Wang, Z. Fan, Acta Materialia 60, 1528-1537 (2012).

[23] S. F. Wang, J. Zhang, D. W. Luo, F. Gu, D. Y. Tang, Z. L. Dong, G. E. B. Tan, W. X. Que, T. S. Zhang, S. Li, L. B. Kong, Progress in Solid State Chemistry 41, 20-54 (2013).

[24] P. Dragic, T. Hawkins, P. Foy, S. Morris, and J. Ballato, Nature Photonics 6, 627 (2012).

[25] J. M. Zahler and C. J. Petti, "*Mobile electronic device comprising an ultrathin sapphire cover plate*," (2016), US Patent 9,369,553.

[26] H. Knozinger and P. Ratnasamy, Catal. Rev. - Sci. Eng. 17, 31 (1978).

[27] B. C. Gates, J. R. Katzer, and G. A. Schuit, *Chemistry of Catalytic Processes*, McGraw-Hill, New York (1979).

[28] E. J. W. Verwey, Z. Kristallogr. 91, 65-69 (1935).

[29] B. Hallstedt, J. Am. Ceram. Soc. 75, 1497– 1507 (1992).

[30] A. C. Sutorik, G. Gilde, J. J. Swab, C. Cooper, R. Gamble, E. Shanholtz, J. Am. Ceram. Soc., 95, 636-643 (2012).

[31] A. Krell, K. Waetzig, J. Klimke, J. Eur. Ceram. Soc. 32, 2887– 2898 (2012).

[32] A. B. Belonoshko, G. Gutierrez, R. Ahuja, B. Johansson, Phys. Rev. B 64, 607–611 (2001).

[33] S. J. MillS, P. M. KartaShov, C. Ma, G. R. Rossman, M. I. Novgorodova, A. R. Kampf, and M. Raudsepp, American Mineralogist, 96, 1166–1170, (2011).

[34] M. I. Novgorodova, N. N. Nedashkovskaya, A. V. Rassdazov, N. V. Trubkin, E. I. Semenov and B. L. Koshelev, Doklady RAN, 340, 681–684 (in Russian) (1995).

[35] D. G. W. Smith and E. H. Nickel, Canadian Mineralogist, 45, 983–1055 (2007).

[36] M. K. Bera, Y. Liu, L. M. Kyaw, Y. J. Ngoo, S. P. Singh, E. F. Chor, ECS J. Solid State Sci. Technol. 3, 120–126 (2014).

[37] J. X. Zhao, Y. J. Zhang, H.Y. Gong, Y.B. Zhang, X.L. Wang, X. Guo, Y.J. Zhao, Ceram. Int. 41, 5232–5238 (2015).

[38] X. Zhanga, W. Guia, Q. Zeng, Ceramics International 43, 3346–3355 (2017).

[39] M. Ju, L. Pan, C. Zhang, Y. Jin, M. Zhong, So. Li, Shi. Li, T. Yang, X. Wang, R. Soc. Chem. Adv., 10, 28674 (2020).

[39] F. C. Palilla, and A. K. Levine, Applied Optics, 1467–1468 (1996).

[40] K. S. Hong, R. S. Meltzer, S.P. Feofilov, R. I. Zakharchenya, W. Jia, H. Lui and B. Yuan, Journal of Luminescence, 83, 393–398 (1999).

[41] J. Yang, X. Houa, P. Zhang, Y. Zhou, Y. Yang, X. Ren, Q. Yang, Materials Science & Engineering A 655, 346–354 (2016).

[42] X.-R. Hou, S.-M. Zhou, W.-J. Li, Y.-K. Li, J. Eur. Ceram. Soc. 30, 3125–3129 (2010).

[43] J. Zhang, L.-Q. An, M. Liu, S. Shimai, S.-W. Wang, J. Eur. Ceram. Soc. 29, 305–309 (2009).

[44] C. Greskovich, S. Duclos, Annu. Rev. Mater. Sci. 27, 69–88 (1997).

[45] D. C. Harris, Infrared Phys. Technol. 39, 185–201 (1998).

[46] L. Lou, W. Zhang, A. Brioude, C.L. Luyer, J. Mugnier, Opt. Mater. 18, 331–336 (2001).

[47] R. Korenstein, P. Cremin, T.E. Varitimos, R. Tustison, Proc. SPIE 5078, 169–178 (2003).

[48] G. E. Moore. Electronics, 38, 8 (1965).

[49] M. C. Gutzwiller. *Chaos in Classical and Quantum Mechanics*. Springer-Verlag New York Inc (1990).

[50] M. Born and J. Mayer Z. Phys., 75, 1 (1932).

[51] M. Born and J. Mayer J. Chem. Phys., 1, 270 (1933).

[52] A. D. Becke. The journal of Chemical Physics, 140(18):18A301 (2014).

[53] R. Martin. *Electronic Structure: Basic Theory and Practical Methods*. Cambridge University Press, 2004. ISBN 9780521782852.

[54] E. Schrödinger. Phys. Rev., 28, 1049 (1926).

[55] R. Car, M. Parinello. Phys. Rev. Lett. 55, 2471–2474 (1985).

[56] J. S. Wang, A. Horsfield, U. Schwingenschlogl, P.D. Lee, Phys. Rev. B, 82, 184203 (2010).

[57] J. S. Wang, A. Horsfield, P.D. Lee, P. Brommer, Phys. Rev. B, 82, 144203 (2010).

[58] P. Elliott, F. Furche and K. Burke, *Reviews in Computational Chemistry*, John Wiley & Sons, Inc., Hoboken, NJ, USA, vol. 26, pp. 91–165 (2008).

[59] L. Hedin, Phys. Rev., 139(3A), A796 (1965).

[60] M. S. Hybertsen and S. G. Louie, Phys. Rev. B, 34(8), 5390 (1986).

[61] F. Aryasetiawan and O. Gunnarsson, Rep. Prog. Phys., 61(3), 237–312 (1998).

[62] L. Hedin. J. Phys.: Condens. Matter 11 R489–R528 (1999).

[63] G. Onida, L. Reining and A. Rubio, Rev. Mod. Phys., 74(2), 601 (2002).

[64] P. Liao and E. A. Carter. Phys. Chem. Chem. Phys .,13,15189–15199 (2011).

[65] C. Friedrich and A. Schindlmayr. *John von Neumann Institute for Computing*, Jülich, NIC Series, Vol. 31, ISBN 3-00-017350-1, pp. 335-355, (2006).

[66] D. Golze, M. Dvorak and P. Rinke. Front. Chem. 7, 377 (2019).

[67] J. Redinger and K. Schwarz, Z. Phys. B 40, 269 (I981).

[68] M. Causà, R. Dovesi, C. Pisani, and C. Roetti, Phys. Rev. B 33, 1308 (1986).

[69] K. M. Neyman and N. Rösch, Chem. Phys. 168, 267 (1992).

[70] G. Pacchioni, C. Sousa, F. Illas, F. Parmigiani, and P. S. Bagus, Phys. Rev. B 48, 11573 (1993).

[71] U. Birkenheuer, J. C. Boettger and N. Rösch, J. Chem. Phys. 100, 6826 (1994).

[72] A. Subramanian, L. D. Marks, O. Warschkow, and D. E. Ellis, Phys. Rev. Lett. Vol. 92, 2, DOI: 10.1103/PhysRevLett92.026101 (2004).

[73] J. G. Smith, J. Naruse, H. Hiramatsu and D. J. Siegel. Chem. Mater. 29, 7, 31523163 (2017).

[74] R. W. G. Wyckoff. American Journal of Science 1(2): 138-152 (1921).

[75] B. J. Skinner, *X-ray crystallographic data of minerals*. In: S. P. Clark, Handbook of Physical Constants. Geological Society of America, New York, pp 30-55 (1966).

[76] R. M. Hazen. American Mineralogist, 61, 266-271 (1976).

[77] S. Sasaki, K. Fujino, and Y. Takéuchi. Proc. Japan Acad., 55, Ser. B (1979).

[78] D. G. Isaak, O. L. Anderson, T. Goto. Phys Chem Miner. 16(7), 704–713 (1989).

[79] O. L. Anderson, P. Andreatc (Jr). J Am Ceram Soc. 49, 8 (1966).

[80] D. M. Roessler and W. C. Walker. Phys. Rev. 159, 733 (1967).

[81] B. A. Petersen, B. Liu, W. J. Weber, and Y. Zhang, Journal of Nucl. Mat. Vol. 486, 122-128 (2017).

[82] S. Heo, E. Cho, H.-Ik Lee, G. Su Park, H. J. Kang, T. Nagatomi, P. Choi, and B.-D. Choi. AIP ADVANCES5, 077167 (2015).

[83] M. Mehl, R. Cohen, H. Krakauer. J Geophys Res-Solid Earth Planets. 93(B7), 8009-8022 (1988).

[84] J. E. Jaffe, J. A. Snyder, Z. Lin, A. C. Hess. Phys. Rev. B 62, 1660 (2000).

[85] G. Cappellini, S. B. -Russo, B. Amadon, C. Noguera and F. Finocchi. J. Phys.: Condens. Matter 12, 3671–3688 (2000).

[86] I. Tanaka, F. Oba, K. Tatsumi, M. Kunisu, M. Nakano and H. Adachi. Mat. Trans., 43, 1426-1429 (2002).

[87] B. Nourozia, A. Aminianb, N. Filic, Y. Zangeneh, A. Boochani, P. Darabi. Res. in Phys. 12, 2038-2043 (2019).

[88] C. M. Fang and G. D. With. Philosophical Magazine A, 82, 15, 28852894 (2002).

[89] I. Levin and D. Brandon, J. Am. Ceram. Soc., 81, 8, 1995–2012 (1995).

[90] Z. Łodziana and K. Parlinski, Phys. Rev. B: Condens. Matter Mater. Phys., 67, 174106 (2003).

[91] Y. Wang, H. T. Li and Z. Fan. Trans. Indian Inst. Met. 65, 653 (2012).

[92] K. M. N. Prasanna, A. S. Khanna and R. Chandra, Oxid. Met., 46, 465–480 (1996).

[93] J. Doychak and M. Röhle, Oxid. Met., 31, 431–452 (1989).

[94] S. H. Cai, S. N. Rashkeev, S. T. Pantelides and K. Sohlberg, Phys. Rev. B: Condens. Matter Mater. Phys., 67, 224104 (2003).

[95] J. M. McHale, A. Auroux, A. J. Perrota and A. Navrotsky, Science, 277, 788 (1997).

[96] L. Pauling and S. B. Hendricks, J. Am. Chem. Soc. 47, 781–790 (1925).

[97] R. W. G. Wyckoff, Crystal Structures, 2nd ed., 2, 6-8 (1964).

[98] L. Lutterotti and P. Scardi, J. Appl. Cryst. 23, 246-252 (1990).

[99] W. Lu, Y. Dai, F. Wang, F. Yang, C. Ma, X. Zhang, and X. Jiang, AIP Advances 7, 125001 (2017).

[100] C. Rohmann, J. B. Matson, H. Idriss. Surf. Scien. 605, 1694-1703 (2011).

[101] C. V. Chandran, C. E. A. Kirschhock, S. Radhakrishnan, F. Taulelle, J. A. Martens and E. Breynaert. Chem. Soc. Rev. 48, 134 (2019).

[102] H. d'Amour, D. Schiferl, W. Denner, H. Schulz, and W. B. Holzapfel, J. Appl. Phys. 49, 4411 (1978).

[103] N. Ishizawa, T. Miyata, I. Minato, F. Marúmo and S. Iwai. Acta Chrysta. B36, 228-230 (1980).

[104] R. H. French, D. J. Jones, and S. Loughin, J. Am. Ceram. Soc. 77, 412 (1994).

[105] S.-Di. Mo, Y.-N. Xu, and W.-Y. Ching, J. Am. Ceram. Soc. 80, 1193 (1997).

[106] L. Ouyang and W. Y. Ching, J. Am. Ceram. Soc. 84, 801 (2001).

[107] R. Ahuja, J. M. Osorio-Guillen, J. Souza de Almeida, B. Holm, W. Y. Ching and B. Johansson, J. Phys.: Condens. Matter 16, 2891–2900 (2004).

[108] S. J. Mousavi, M. R. Abolhassani, S. M. Hosseini, and S. A. Sebt, Chine. J. Phys. 47, 6 (2009).

[109] Z. Zhang, Z. H. Fu, R. F. Zhang, D. Legut and H. B. Guo, RSC Adv., 6, 12885 (2016).

[110] T. Biswas and M. Jain. Phys. Rev. B 99, 144102 (2019).

[111] S. J. Wilson and J. D. C. McConnell, J. Sol. State Chem. 34, 315 (1980).

[112] J. D. Kohn, J. A. Katz and G. Broder, Am. Mineral. 42, 398 (1957).

[113] G. Yamaguchi, I. Yasui, W. -C. Chiu. Bull. Chem. Soc. Jpn. 43, (1970).

[114] R. -S. Zhou and R. L. Snyder, Acta. Cryst. B 47, 617-630 (1991).

[115] E. Husson and Y. Repelin, Eur. J. Solid State Inorg. Chem. 33, 1223 (1996).

[116] R. Franchy, G. Schmitz, P. Gassmann, and F. Bartolucci, Appl. Phys., 65, 551–566 (1997).

[117] A. P. Borosy, B. Silvi, M. Allavena, and P. Nortier. J. Phys. Chem. 98, (1994).

[118] S. -Di Mo and W. Y. Ching, Phys. Rev. B, 57, 24 (1998).

[119] M. F. Peintinger, M. J. Kratz and T. Bredow, J. Mater. Chem. A, 2, (2014).

[120] A. R. Ferreira, M. J. F. Martins, E. Konstantinova, R. B. Capaz, W. F. Souza, S. S. X. Chiaro, A. A. Leitão, Jour. of Sol. State Chem. 184, 1105–1111 (2011).

[121] G. Busca, Catal. Today 226, 2-13 (2014).

[122] L. Smroček, V. Langer and J. Křestan, Acta Cryst. C, 62, i83-i84 (2006).

[123] H. O. Ayoola, S. D. Housea, C. S. Bonifacio, K. Kisslinger, W. A. Saidi, J. C. Yang, Acta Materialia 182, 257-266 (2020).

[124] R. Dupree, M. H. Lewis, and M. E. Smith, Philos. Mag. A 53, L17 (1986).

[125] B. Ealet, M. H. Elyakhlouffi, E. Gillet and M. Ricci, Thin Solid Films 250, 92 (1994).

[126] Y. G. Wang, P. M. Bronsveld, and J. Th. M. DeHosson. J. Am. Crem. Soc., 81, 1655-60 (1998).

[127] G. N. Kryukova, D. O. Klenov, A. S. Ivanova and S. V. Tsybulya, J EUR CERAM, 20(8), 1187-1189 (2000).

[128] H. Saalfeld, B. Mehrotra, Ber. Dtsch. Keram. Ges., 42, 161 (1965).

[129] C. S. John, N. C. M. Alma and G. R. Hays, Applied Catalysis, 6, 341-346 (1983).

[130] V. Jayaram and C. G. Levi, Acta Metall. Vol. 37, No. 2, 569-578 (1989).

[131] C. Pecharromán, I. Sobrados, J. E. Iglesias, T. Gonzáles-Carrenõ, and J. Sanz, J. Phys. Chem. B, 103, 6160–70 (1999).

[132] J. Wang, X. Bokhimim, A. Morales, O. Novaro, T. Lopez and R. Gomez, J. Phys. Chem. B, 103, 299-303 (1999).

[133] K. Kim. Metall. Mater. Trans. A 45, 3650 (2014).

[134] G. Paglia, C.E. Buckley, A.L. Rohl, B.A. Hunter, R.D. Hart, J.V. Hanna, L.T. Byrne, Phys. Rev. B 68, 144110 (2003).

[135] V. P. Pakharukova, D. A. Yatsenko, E. Yu. Gerasimov, A. S. Shalygin, O. N. Martyanov, S. V. Tsybulya, Journal of Solid State Chemistry 246, 284–292 (2017).

[136] C. Wolverton and K. C. Hass, Phys. Rev. B: Condens. Matter Mater. Phys., 63, 024102, 1-16 (2000).

[137] F. H. Streitz and J. W. Mintmire, Phys. Rev. B., 60, 2, 773–7 (1999).

[138] G. Gutiérrez, A. Taga and B. Johansson, Phys. Rev. B, 65, 1, 012201, 1-4 (2001).

[139] H. P. Pinto, R. M. Nieminen and S. D. Elliott, Phys. Rev. B 70, 125402 (2004).

[140] E. Menéndez-Proupin and G. Gutiérrez, Phys. Rev. B., 72, 035116 (2005).

[141] Y. Liu, B. Cheng, K.-Kai Wang, G.-Ping Ling, J. Cai, C.-Lu Song, G.-Rong Han, Solid State Communications 178, 16-22 (2014).

[142] S. Blonski and S. H. Garofalini, Surface Science, 195, 263-274 (1993).

[143] M.-H. Lee, C.-F. Cheng, V. Heine, and J. Klinowski, Chem. Phys. Lett., 265, 673-676 (1997).

[144] F. Maglia and S. Gennari, J. Am. Ceram. Soc., 91, 283–290 (2008).

[145] M. Digne, P. Stautet, P. Raybaud, P. Euzen and H. Toulhoat, Journal of Catalysis 226, 54-68 (2004).

[146] G. Paglia, A. L. Rohl, C. E. Buckley, and J. D. Gale, Phys. Rev. B 71, 224115 (2005).

[147] S. Blancka, S. Loehlé, S. N. Steinmann and C. Michel, Tribology International 145, 106140 (2020).

[148] R. J. Hill, J. R. Craig, and G. V. Gibbs. Phys. Chem. Minerals 4, 317, 339 (1979).

[149] S. Hafner and F. Laves. Z. Kristallogr., vol.115, 331 (1961).

[150] C. Liu, Y. Li, T. Shi, Q. Peng and F. Gao. Jour. of Nucl. Mate. 527, 151830 (2019).

[151] F. Colin. Rev. Int. Hautes Temp. Refract., 5, 269 (1968).

[152] A. C. Sutorik, G. Gilde, J. J. Swab, C. Cooper, R. Gamble, E. Shanholtz, J. Am. Ceram. Soc., 95, 636-643 (2012).

[153] A. Krell, K. Waetzig, J. Klimke, J. Eur. Ceram. Soc. 32, 2887– 2898 (2012).

[154] P. Fu, Y. Xu, X. Wang, W. Lu, W. Lei, X. Ruan. Int. J. Appl. Ceram. Technol.; 12, 116–23 (2015).

[155] A. Ibarra, R. Vila, M. Jiménez de Castro. Philos. Mag. Lett., 64, 45 (1991).

[156] B. Tu, H. Wang, X. Liu, W. Wang, Z. Fu, J Eur. Ceram. Soc. 36, 1073–9 (2016).

[157] L. Ren, H. Wang, B. Tu, X. Zong, W. Wang, Z. Fu, J. Am. Ceram. Soc. 102, 6913–6924 (2019).

[158] M. Leskelä and M. Ritala, Thin Solid Films 409, 138 (2002).

[159] J. Joubert, A. Salameh, V. Krakoviack, F. Delbecq, P. Sautet, C. Coperet, J. M. Basset. J. Phys. Chem. B, 110, 23944−23950 (2006).

[160] R. Wischert, C. CopØret, F. Delbecq, and P. Sautet. Angew. Chem. Int. Ed., 50, 3202 –3205 (2011).

[161] L. J. Álvarez, J. F. Sanz, M. J. Capitán and J. A. Odriozola. Chem. Phys. Lett., 192, 5,6, 463-468 (1992).

[162] L. J. Álvarez, J. F. Sanz, M. J. Capitan, M. A. Centeno and J. A. Odriozola. Jour. of the Chem. Soc., Fara. Trans., 89, 19, 3623-3628 (1993).

[163] L. J. Álvarez, L. E. León, J. F. Sanz, M. J. Capitán and J. A. Odriozola. Jour. of Phys. Chem., 99, 17872-17876 (1995).

[164] S. Blonski and S. H. Garofalini. Surf. Sci. 295, 263 (1993).

[165] C. Y. Ouyang, Ž. Šljivančanin, and A. Baldereschi. Phys. Rev. B 79, 235410 (2009).

[166] G. Fenga, C.-F. Huoa, C.-M. Denga, L. Huanga, Y.-W. Lia, J. Wanga, H. Jiaoa. Jour. of Mol. Cat. A: Chem. 304, 58-64 (2009).

[167] R. Prins. Journal of Catalysis 392, 336-346 (2020).

[168] Y. Rozita, R. Brydson, T.P. Comyn, A.J. Scott, C. Hammond, A. Brown, S. Chauruka, A. Hassanpour, N.P. Young, A.I. Kirkland, H. Sawada, R.I. Smith. Chem Cat Chem 5, 2695–2706 (2013).

[169] P. W. Tasker, Phil. Mag. A, 39, 119–136 (1979).

[170] J. Goniakowski, F. Finocchi, C. Noguera. Rep. Prog. Phys.,71, 016501 (2008).

[171] C. M. Fang, S. C. Parker, G. de With. J. Am. Ceram. Soc., 83, 2082–2084 (2000).

[172] F. Bertaut. Comput. Rendu. 246, 3447 (1998).

[173] M. K. Loudjani, A. M. Huntz, and R. Cortés, Jour. of Mater. Sci. 28, (1993).

[174] J. Bruley, J. Cho, H.M. Chan, M.P. Harmer, and J.M. Rickman, J. Am. Ceram. Soc. 82, 2865 (1999).

[175] L. Pauling and M. D. Shappel, Z. Kristallogr. 75, 128-131 (1930).

[176] F. Hanic, M. Hartmanová, G. G. Knab, A. A. Urusovskaya and K. S. Bagdasarov, Acta Crystal. B 40, 76-82 (1984).

[177] I. Halevy, R. Carmon, M.L. Winterrose, O. Yeheskel, E. Tiferet and S. Ghose, J. Phys.: Conf. Ser. 215, 012003 (2010).

[178] K. Kuribayashi, M. Yoshimura, T. Ohta and T. Sata, J. Am. Ceram. Soc. 63, 644-647 (1980).

[179] S. Jiang, J. Liu, X.-D. Li, Y.-C. Li, S.-M. He, J.-C. Zhang, Chin. Phys. Lett. 36, 4, 046103 (2019).

[180] S. H. Wang unpublished data.

[181] P. Atkins, Physical Chemistry. W. H. Freeman & Company, 5th ed. (1994).

[182] D. J. Griffiths.; (2017). *Introduction to quantum mechanics* (2nd ed.). Cambridge: Cambridge University Press. ISBN 978-1-107-17986-8. OCLC 952389109.

[183] M. Born and R. Oppenheimer. Annalen der Physik (Leipzig), 84, 457 (1927).

[184] P. Hohenberg, W. Kohn, Phys. Rev., 136, 864–B871 (1964).

[185] W. Kohn, L. J. Sham, Phys. Rev. 140, 1133–1138 (1965).

[186] E. Wigner. Phys. Rev., 46, 1002–1011, (1934).

[187] M. Gell-Mann and K. A. Brueckner. Phys. Rev., 106, 364–368, (1957).

[188] J. P. Perdew and A. Zunger. Phys. Rev. B, 23, 5048–5079, (1981).

[189] R. O. Jones and O. Gunnarsson. Rev. Mod. Phys., 61, 689–746, (1989).

[190] K. Capelle, Brazilian Journal of Physics 36, 1318 (2006).

[191] J. P. Perdew, and Y. Wang, Phys. Rev. B 33, 8800 (1986).

[192] J. P. Perdew, K. Burke, and M. Ernzerhof. Phys. Rev. Lett., 77, 3865– 3868, (1996).

[193] M. van Schilfgaarde, Takao Kotani, and S. Faleev. Phys. Rev. Lett., 96, 226402, (2006).

[194] L. Hedin and S. Lundqvist. In F. Seitz, D. Turn bull, and H. Ehrenreich, editors, Solid State Physics, Advanced in Research and Applications, 23, 1–181. Academic Press, New York, (1969).

[195] F. Aryasetiawan and O. Gunnarsson. Reports on Progress in Physics, 61, 237, (1998).

[196] A. Ernst and M. Luders. In M. Dane W. Hergert and A. Ernst, editors, Computational Materials Science, 642, 23–54. Springer Berlin Heidelberg, (2004).

[197] L. Kantorovich. *Quantum Theory of the Solid State: An Introduction*. Kluwer, (2004).

[198] P. E. Blöchl. Phys. Rev. B 50, 17953– 17979 (1994).

[199] P. Kratzer and J. Neugebauer, Frontiers in Chemistry, 7, 106, (2019).

[200] H. J. Monkhorst and J. D. Pack. Physical Review B, 13, 5188–5192, (1976).

[201] M. Shishkin and G. Kresse. Phys. Rev. B 74, 035101 (2006).

[202] P. Liu, M. Kaltak, J. Klimeš, and G. Kresse. Phys. Rev. B 94:165109 (2016).

[203] M. Gajdoš, K. Hummer, G. Kresse, J. Furthmüller, and F. Bechstedt, Phys. Rev. B 73, 045112 (2006).

[204] G. Kresse, http://cms.mpi.univie.ac.at/VASP/

[205] Md. L. Ali, Md. Z. Rahaman, Md. A. Rahman, Int. J. Comp. Mat. Sci. Eng. 5, 1650024-16 (2016).

[206] R. H. French, H. Mullejans, and D. J. Jones, J. Am. Ceram. Soc. 81, 2549–57 (1998).

[207] E. T. Arakawa and M. W. Williams. J. Phys. Chem. Solids 29, 735 (1968).

[208] S. Nosé. The Journal of Chemical Physics, 81(1), (1984).

[209] W. G. Hoover. Phys. Rev. A, 31, 1695–1697, (1985).

[210] C. Fang and Z. Fan. Comp. Mat. Scie. 171, 109258 (2020).

[211] M. W. Chase, Jr., *NIST-JANAF Thermochemical Tables*, Fourth Edition, J. Phys. Chem. Ref. Data Monograph No. 9, American Chemical Society and American Institute of Physics (1998).

[212] Yu Liu, Y. Huang, Z. Xiao, C. Yang and X. Reng. Int. J. Mod. Phys. B 30, 1650085 (2016).

[213] D. M. Roessler and W. Walker, Phys. Rev. 159, 733 (1967).

[214] Y. Sato and S. Akimoto, J. Appl. Phys. 50, 5285–5290 (1979).

[215] M. S. Mahabal, Dr. M. D. Deshpande, IJCPS 7, Special Issue, ISSN:2319-6602 (2018).

[216] V. A. Sashin, H. E. Dorsett, M. A. Bolorizadeh and M. J. Ford. Journ. Of Chem. Phys. 113, 18 (2000).

[217] M. L. Bortz, R. H. French, D. J. Jones, R. V. Kasowski and F. S. Ohuchi. Physica Scripta. 41, 537-541 (1990).

[218] W. Tews and R. Gründler, phys. stat. sol. (b) 109, 255 (1982).

[219] M. L. Bortz and R. H. French. Appl. Phys. Lett. 55, 1955 (1989).

[220] G. Henkelman, A. Arnaldsson, H. Jónsson, Comput. Mater. Sci. 36, 254-360 (2006).

[221] E. Sanville, S. D. Kenny, R. Smith, G. Henkelman, J. Comput. Chem. 28, 899908 (2007).

[222] W. Tang, E. Sanville, G. Henkelman, J. Phys.: Condens. Matter 21, 084204 (2009).

[223] W. Y. Ching, Lizhi Ouyang, Paul Rulis, and Hongzhi Yao, Phys. Rev. B 78, 014106 (2008).

[224] I. D. Brown, *The Chemical Bond in Inorganic Chemistry*. IUCr Monographs in Crystallography 12, Oxford Science Publications, Oxford University Press, Oxford, U.K. (2002).

[225] I. D. Brown, Chem. Rev. 109, 6858-6919 (2009).

[226] J. Gangwar B. K. Gupta, P. Kumar, S. K. Tripathi, and A. K. Srivastava, Dalton Transactions 43(45), 17034 17043 (2014).

[227] A. S. Jbara, Z. Othaman1, H. A. R. Aliabad4 and M. A. Saeed, Adv. Sci. Eng. and Med. 9, 287–293 (2017).

[228] K. E. Sickafus, J. M. Wills, N. W. Grimes, J. Am. Ceram. Soc. 82, 3279-3292 (1999).

[229] R. H. French, J. Am. Ceram. Soc. 73, 3, 477-489 (1990).

[230] T. Pascal, G. Francois, J. Phys. Condens. Matter 14, 3543-3552 (2002).

[231] L. Zhang, G.-F. Ji, F. Zhao, C.-M. Meng, D.-Q. Wei, Physica B. 406, 335-338 (2011).

[232] A. Navrotsky, B. A. Wechsler, K. Geisinger, F. Seifert, J. Am. Ceram. Soc. 69, 418-422 (2002).

[233] Y. Okuyama, N. Kurita, N. Fukatsu, Solid state Ionics 177, 59-64 (2006).

[234] S. Lucchesi, A. Della Giusta, Z Kristallogr Cryst Mater. 209, 714–719 (1994).

[235] R. I. Sheldon, T. Hartmann, K. E. Sickafus, A. Ibarra, B. L. Scott, D. N. Argyriou, A. C. Larson, and R. B. Von Dreele, J. Am. Ceram. Soc. 82, 3293–8 (1999).

[236] X. Wang, S. Tan, X. -Q. Yang, E. Hu. Chine. Phys. B 29, 028802 (2020).

[237] P. A Cox, F. W. H. Dean and A. A. Williams. 33, 389 (1983).

[238] A. Gibson, R. Haydock and J. P. LaFemina. J. Vac. Sci. Technol. A 10, 2361 (1992).

[239] R. Plass, K. Egan, C. C. -Davila, D. Grozea, E. Landree, L. D. Marks, and M. G. -Josifovska. Phys. Rev. Lett. 81, 22 (1998).

[240] C. Fang, M. A. van Huis, D. Vanmaekelbergh, and H. W. Zandbergen. *ACS Nano*, 4, 1, 211–218 (2010).

[241] J. C. Boettger, Phys. Rev. B 49, 16 798 (1994).

[242] J. J. Gilman. Jour. of App. Phys. 31, 12 (1960).

[243] D.-N. Zhang, L. Zhao, J.-F. Wang and Y.-L. Li. Surf. Rev. Lett. 22, 3 (2015).

[244] E. J. Rubio, V. V. Atuchin, V. N. Kruchinin, L. D. Pokrovsky, I. P. Prosvirin, C. V. Ramana, J. Phys. Chem. C 118, 13644–13651 (2014).

[245] V. H. Mudavakkat, V. V. Atuchin, V. N. Kruchinin, A. Kayani, C. V. Ramana, Opt. Mater. 34, 893–900 (2012).

[246] M. V. Abrashev, N. D. Todorov, J. Geshev, J. Appl. Phys. 116, 103508-1-7 (2014).

[247] Y.-N. Xu, Z.-q Gu, W.Y. Ching, Phys. Rev. B 56, 14993–15000 (1997).

[248] J. X. Zheng, G. Ceder, T. Maxisch, W.K. Chim, W.K. Choi, Phys. Rev. B 73, 104101–104107 (2006).

[249] M. Ramzan, Y. Li, R. Chimata, R. Ahuja, Comput. Mat. Sci 71, 19–24 (2013).

[250] H. A. Badehian, H. Salehi, and M. Ghoohestani. J. Am. Ceram. Soc., 1–9 (2013).

[251] C.M. Fang, A. Meetsma and G.A. Wiegers, Journal of Alloys and Compounds. 201, 1-2 (1993).

[252] J. W. Palko, W. M. Kriven, S. V. Sinogeikin, J. D. Bass, A. Sayir, J. Appl. Phys. 89, 7791–7796 (2001).

[253] S. F. Hassan, and M. Gupta, Materials Science and Technology, 20, 1383–1388 (2004).

[254] C. S. Goh, J. Wei, L. C. Lee, and M. Gupta, Nanotechnology, 17, 7–12 (2006).

Appendix

Table A.5.1: Calculated physical properties of hcp Mg and fcc Al crystals at temperature of 0 *K* and a pressure of 0 *Pa*.

hcp Mg: Space group (*d_h*) *P63/mmc*[194]	Lattice constant a_0 (Å)	 c/a_0	Energy (E) (eV/f.u.)	Bulk modulus(B_0) (GPa)
<u>Method:</u>				
This work, LDA	3.13	1.633	-1.804	41.3
LDA [i]	3.16	1.610	—	35.0
LDA [ii]	3.16	1.590	—	39.0
This work, GGA(PBE)	3.18	1.615	-1.501	35.84
Other GGA [ii]	3.20	1.660	—	30.0
Experiment [iii]	3.21	1.624	—	35.4
fcc Al: Space group (*o_h*) *fm3m*[225]	Lattice constant a_0(Å)		Energy (E) (eV/f.u.)	Bulk modulus(B_0) (GPa)
<u>Method</u>				
This work, LDA	3.97		-4.018	85.85
LDA [iv]	3.98		—	84.00
This work, GGA(PBE)	4.04		-3.756	76.06
GGA [v]	4.05		—	76.70
Experiment[a]	4.03 [vi]		—	76.20 [vii]

[a]experimental values were obtained for temperature interval 273-298 K.

[i] M. Y. Chou and M L Cohen, Solid State Commun. 57 785, 1986.

[ii] M. Fuchs, M. Bockstedte, E. Pehlke and M. Scheffler, Phys. Rev. B 57 2134, 1997.

[iii] N. W. Ashcroft and N. D. Mermin, Solid State Physics (New York: Holt, Rinehart and Winston), 1976.

[iv] S. Kurth et al., Int. J. Quant. Chem. 75 889-909, 1999.

[v] P.W.M. Jacobs, Y. F. Zhukovski, Y. Mastrikov, Y. N. Shunin, Computer Modelling & New Technologies, Volume 6, No.1, 7-28, 2002.

[vi] M. E. Straumanis, C. L. Woodard, Acta Cryst. A 27, 549, 1971.

[vii] J. L. Tallon, A. Wolfenden, J. Phys. Chem. Solids 40, pp 831-837, 1979.

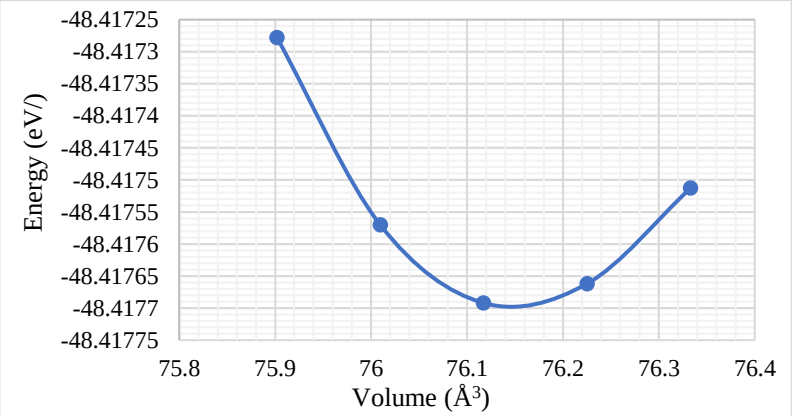

Figure A.5.1: Calculated total energy as a function of volume for FCC MgO. Performing Birch-Murnaghan EOS (equation of state) fitting we estimate the bulk modulus for MgO is 166.294 *GPa*.

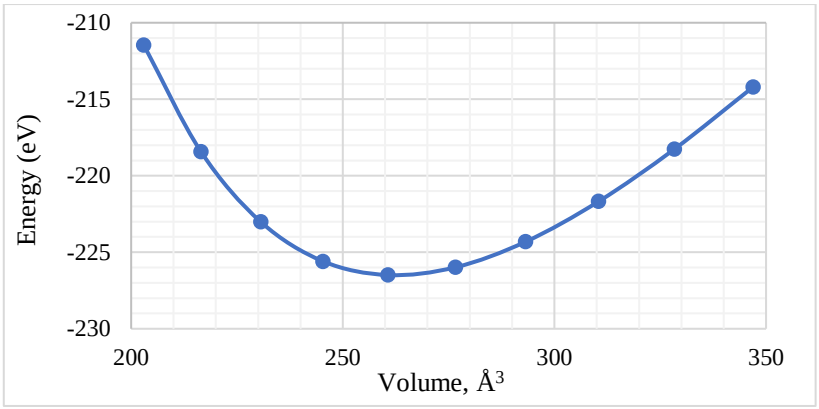

Figure A.5.2: Calculated total energy as a function of volume for conventional hcp α-Al_2O_3 unit cell. Performing Birch-Murnaghan EOS (equation of state) fitting we estimate the bulk modulus is 250.5 *GPa*.

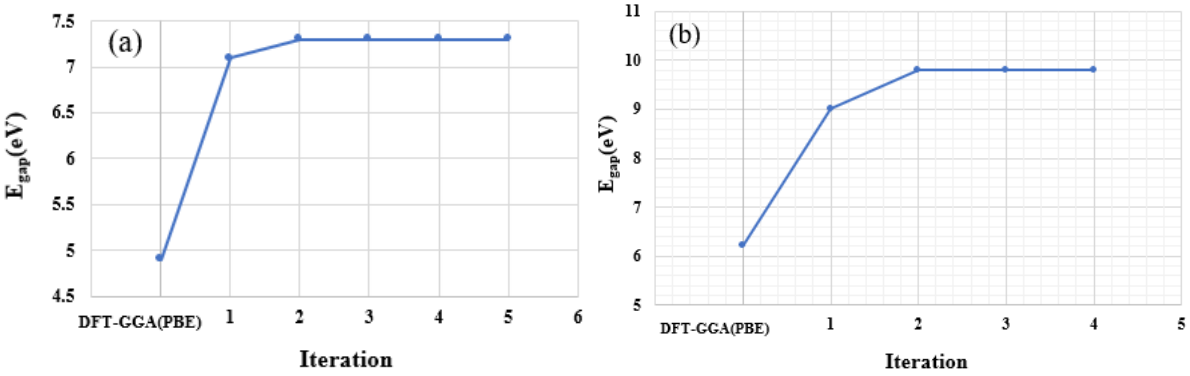

Figure A.5.3: Convergence of the partially self-consistence *GW0* calculations for (a) fcc MgO and (b) hcp α-Al_2O_3.

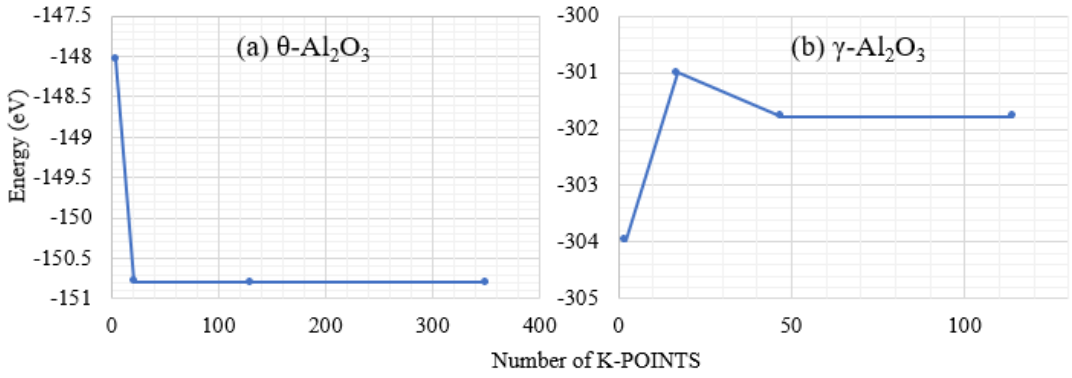

Figure A.6.1: The convergence of total energy with respect to the K-POINTS sampling for (a) θ-Al_2O_3 and (b) spinel hexagonal γ-Al_2O_3. From the Figure,

12×12×8 grid with 350 k-points for θ-Al_2O_3 and 8×8×6 grid with 114 k-points for spinel hexagonal γ-Al_2O_3 is sufficient to obtain convergence in both the total energy differences and the geometries for our investigated systems.

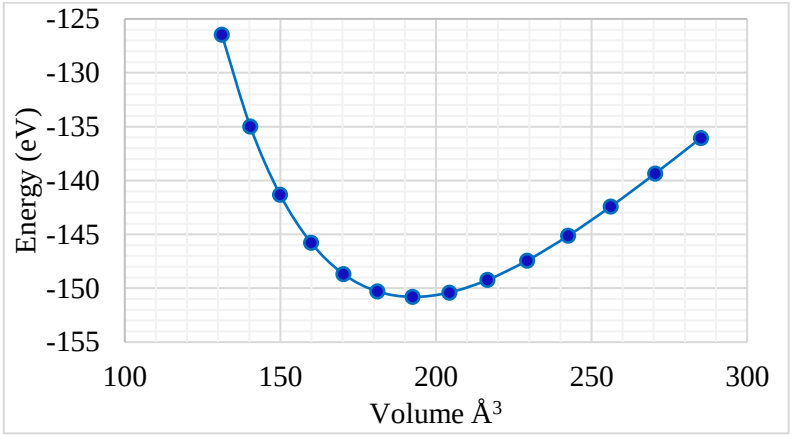

Figure A.6.2: Calculated total energy as a function of volume for conventional monoclinic θ-Al_2O_3 unit cell. Performing Birch-Murnaghan EOS (equation of state) fitting we estimate the bulk modulus is 185.5 *GPa*.

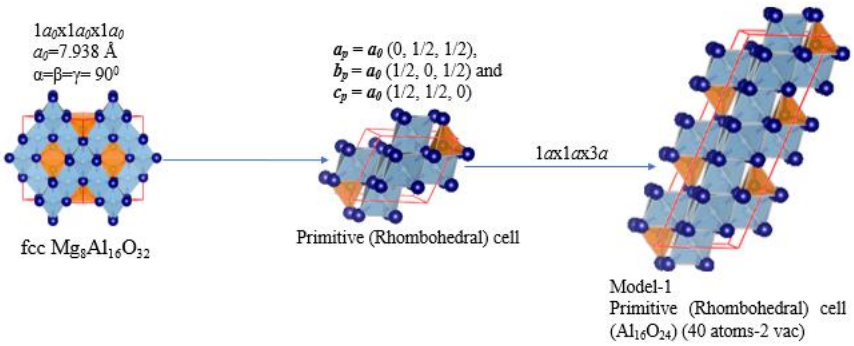

Figure A.6.3: Schematic structure of Model 1, Primitive (rhombohedral) γ-Al_2O_3 unit cell constructed from fcc spinel $MgAl_2O_4$.

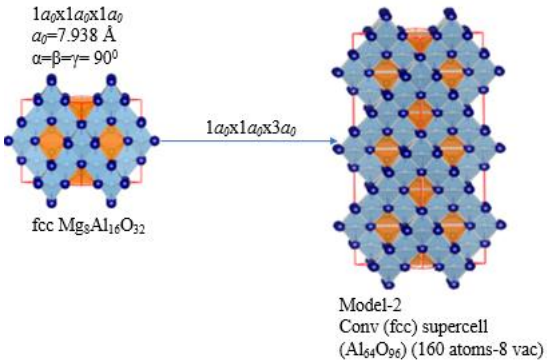

Figure A.6.4: Schematic structure of Model 2, conventional fcc γ-Al_2O_3 supercell constructed from fcc spinel $MgAl_2O_4$.

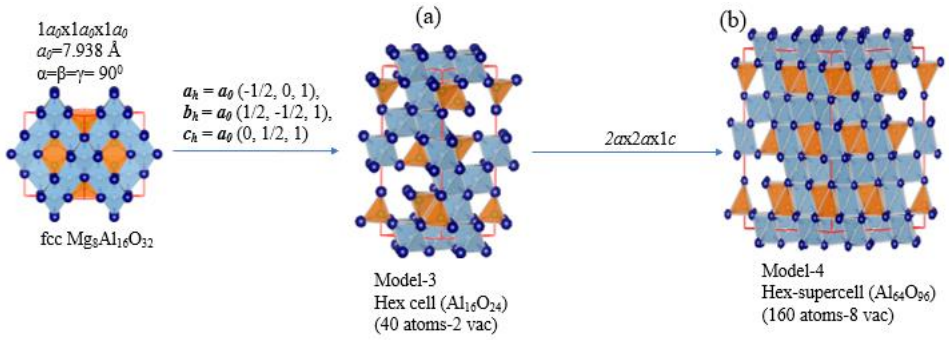

Figure A.6.5: Schematic structure of (a) Model 3, hexagonal γ-Al_2O_3 unit cell and (b) Model-4, hexagonal γ-Al_2O_3 supercell constructed from fcc spinel $MgAl_2O_4$.

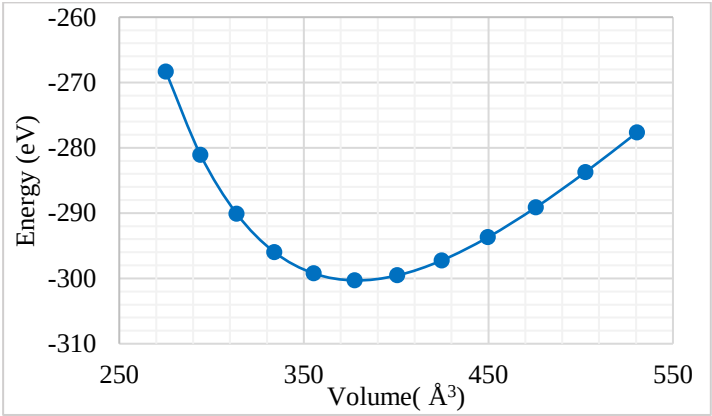

Figure A.6.6: Calculated total energy as a function of volume for conventional monoclinic γ-Al_2O_3 unit cell. Performing Birch-Murnaghan EOS (equation of state) fitting we estimate the bulk modulus is 209.73 *GPa*.

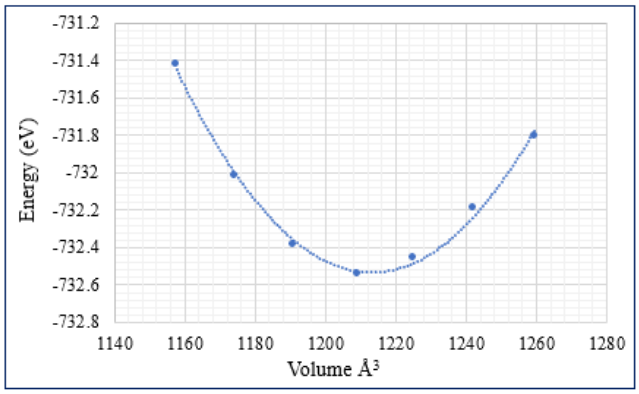

Figure A.9.1: Calculated total energy as a function of volume for conventional cubic Y_2O_3 unit cell. Performing Birch-Murnaghan EOS (equation of state) fitting we estimate the bulk modulus is 154.7 *GPa*.